DOCTOR OF PHILOSOPHY

Theoretical investigation of self-pulsating laser diodes for optical storage applications

Jones, Dewi Robert

Award date:
2001

Awarding institution:
University of Wales, Bangor

Theoretical Investigation of Self-Pulsating Laser Diodes for Optical Storage Applications

by

Dewi Robert Jones

A thesis submitted in candidature for the degree of
Doctor of Philosophy

School of Informatics
University of Wales
Bangor
Gwynedd

May 2001

To my family and in memory of Nain.

Summary

Self-pulsating laser diodes emitting at 650 and 420 nm are currently in demand in the optical storage industry. Such lasers offer emission with a low temporal coherence length, thereby providing a cheap and efficient mechanism of reading data from an optical disc. Laser diodes operating at 650 nm are fabricated in the AlGaInP material system; however, material properties hinder self-pulsation at 70 °C, an operating constraint that must be satisfied. To overcome this problem the use of alternative, more expensive, techniques are utilised to achieve pulsation and satisfy the emission criteria. Research involving 420 nm emission, using either GaN or ZnSe material systems, is still in its infancy with self-pulsation having been somewhat neglected. It is therefore desirable to achieve high temperature self-pulsation at both operating wavelengths in order to provide economic and compact mechanisms of reading data from optical discs.

This thesis offers a theoretical investigation of visible emitting self-pulsating laser diodes to provide an insight into the viability of the use of such lasers in optical storage devices. The work is split into two sections. The first part gives a thorough, detailed study of self-pulsation, analysing the theory required to understand the mechanisms behind such unstable output. The design and attributes of self-pulsating laser diodes are discussed combined with the theory used to model the dynamics of such lasers when operating at different wavelengths. Attention will be directed towards two of the most advanced self-pulsating structures, namely the real refractive index guided laser and the laser diode with epitaxial absorber layers.

The second part implements the theoretical models to study and optimise the emission characteristics of different self-pulsating lasers for optical storage applications. Three lasers are considered – two operating at 650 nm and the other at 420 nm. In each case the laser is initially investigated for self-pulsation at 70 °C. If successful the cavity design is then optimised subject to other well-defined operating constraints, thereby providing an assessment of the most desirable structures. As a result, the work offers a clear indication of the suitability of short wavelength self-pulsating laser diodes as economical read-out mechanisms within optical storage devices.

Acknowledgements

Having spent three years at the School of Informatics I'd like to thank a number of people, all of whom have contributed towards my academic and social life at Bangor. I must firstly thank my tutor Paul Rees for his help and encouragement during my postgraduate studies. Having arrived in the department with a very limited knowledge of the field of opto-electronics he has provided me with the guidance and support that has allowed my confidence in the subject to grow. I am also indebted to Iestyn Pierce. Without his help and expertise (and the use of his DEC Alpha computer) I would have struggled to finish this work on time. Indeed, I have benefited immensely from the relaxed and friendly environment in which both Paul and Iestyn work – thanks again to you both.

I'd like to express my appreciation to all the members of the Opto-electronics group at Bangor. In particular, many thanks to Guy Barlow for his invaluable help with the waveguiding analysis. Thanks also to the head of the group Alan Shore and other past and present group members including Paul Spencer, post-docs Jianming, Colleen, Siva and Yanhua and fellow postgraduate students Andrea, Robin, John, Dave, Marta and Javi.

Outside the workplace I would like to say thanks to all those friends with whom I have enjoyed many a night out in Bangor. The Wednesday nights in the Skerries and/or Students Union were an ideal release from the pressures of work. However, these indulgences did hamper the performance of a few "athletes" in the five-a-side football on Thursday!

Last, but by no means least, I'd like to thank my family. Each family member has, in their own way, always provided me with their love and support in whatever adventure that I have undertaken. Indeed, during the good and bad times they have been the ones who have believed in me, something for which I am forever grateful.

Contents

Chapter 1

Introduction

1.1 Historical development of the semiconductor laser

The word *laser* is an acronym for *l*ight *a*mplification by *s*timulated *e*mission of *r*adiation. There are many different kinds of lasers but they all share one thing in common – each contains material capable of amplifying radiation. This material is called a gain medium because radiation gains energy by passing through it and is generated by making use of the discrete energy levels that exist within matter (at an atomic level). The discovery of the laser dates back to 1958 when Schawlow and Townes developed the ruby laser [1]. In the following years various lasers using different gain media were created [2, 3], including the semiconductor laser [4-7]. Semiconductor laser diodes have subsequently revolutionised the electronics industry. They have become the most widely used of all lasers, are manufactured in the largest quantities and are an essential part of many electronic devices such as compact disc (CD) players and laser printers.

The semiconductor laser concept was suggested in 1961 [4]. It was stated that gain could be generated via electron-hole recombination by forward biasing a GaAs p-n junction [4, 5]. The discrete nature of the energy bands that electrons occupy

combined with the band-gap associated with semiconductor materials could therefore be manipulated to create an active region where recombination takes place. This area of population inversion creates/absorbs photons as electrons cross the band-gap to recombine with holes, as predicted by the Einstein relations [8]. Cleaving the facets perpendicular to the junction plane provides the optical feedback required for amplification. This earliest form of the laser diode has become known as the homojunction.

Although easy to fabricate the performance of the homojunction laser proved to be quite unsatisfactory, primarily due to the very high threshold currents. This was essentially caused by poor carrier confinement; i.e. injected carriers found it far too easy to "escape" from the active region. A solution to the problem was suggested in the mid 1960's. It was put forward that a material of low band-gap "sandwiched" between a material of higher band-gap would confine the carriers more effectively and therefore improve the efficiency of the laser. Optical confinement would also be improved as the relationship between band-gap, E_g, and refractive index, n, i.e. $E_g \propto^{-1} n$, enables the cavity to behave as an optical waveguide. The device was subsequently developed and would become known as the heterostructure laser [6, 7].

To create such a structure one must join two semiconductor materials of different lattice constant. If this process is poorly controlled then numerous dislocations arise resulting in an inefficient laser with a high threshold current. Due to the infancy of the growth technology available in the 1960's it wasn't until the end of the decade that the first successful heterostructure laser operating at room temperature was presented [9]. Such a device was fabricated using the liquid-phase epitaxial (LPE) growth technique. Subsequent work gave researchers an even deeper insight into the properties of such light emitters, enabling the crystal grower to create laser diodes with better operating characteristics. These improvements are demonstrated in the reduction of the threshold current density. From the discovery of the first homojunction laser in 1963 to the design of an optimised heterostructure in the 1970's the threshold current density was reduced by two orders of magnitude, i.e. from 50 kA/cm^2 to 0.5 kA/cm^2. By the mid seventies the laser diode therefore provided a compact, coherent light source that was useful for numerous applications.

A superior growth technique (to LPE) was demonstrated in the early 1970's. The method, known as molecular beam epitaxy (MBE), enabled thinner films to be grown [10, 11]. This development led to research into quantum confined laser diodes. It was found that when the active layer thickness is reduced to a length comparable to the deBroglie wavelength of the carriers then they behave in a quantum mechanical nature and occupy discrete energy levels (in the growth direction) [12, 13]. The structure, known as a quantum well, offers an active region that enables the laser to display superior operating characteristics to those offered by unconfined bulk lasers. Improvements include a lower threshold current, higher differential gain and a shorter operating wavelength. The first quantum well laser was demonstrated in 1975 [14], however, in a similar manner to the changes from homojunction to heterostructure, the predicted improvements took years to materialise due to problems in growth technology.

The problems originated from the fact that the popular growth processes at the time, i.e. LPE and MBE, produced thin films with too many defects, resulting in threshold currents that were far higher than predicted. However, in 1977 a new process called metalorganic chemical vapor deposition (MOCVD) successfully demonstrated the growth of high quality thin films [15]. The development of this procedure combined with improvements in the MBE technique [16] culminated in low threshold quantum well lasers in the 1980's with optimised structures offering superior performance characteristics to those offered by the old heterostructure devices [17, 18]. The subsequent introduction of strained quantum well devices [19, 20], where materials of different lattice constant are grown to enhance the device performance, led to even lower threshold currents [21].

Quantum wells provide confinement in only one direction. As the beneficial consequences of such active regions became apparent, higher dimensional confinement was suggested. Indeed, theoretical predictions provided evidence that quantum wire (2-d confinement) and quantum dot (3-d confinement) active regions would improve the laser's operating characteristics even further [22], with lower threshold currents being amongst the many advantages [23]. So, once the design of the quantum well was pushed to its limit, numerous research groups moved on to investigate these highly confined structures [24, 25]. Unfortunately progress has been

slow due to the limited growth technology that is on offer. Indeed, even now in the year 2001 the strained quantum well active region is usually the active region of choice. Fabrication technologies must therefore improve once again if these new multi-dimensional quantum confined structures are to be realised on a commercial scale. However, with research moving forward day by day it seems that it is only a matter of time before such new technology is fully developed.

1.2 Laser application: optical storage

1.2.1 Optical storage: technological details

Since the introduction of the audio CD in 1982 by Philips and Sony the optical disc industry has advanced rapidly to keep up with the consumer demand of higher density storage capability. Indeed, current state-of-the-art technology can offer the customer digital versatile disc (DVD) systems that can store over seven times more information than the CD. This storage improvement allows much more than 75 minutes of audio to be stored on disc, as is the case with a CD. DVD-ROM (Read-Only Memory) systems capable of playing pre-recorded movies at twice the resolution of a video cassette recorder (VCR) with 8 channels of audio and up to 32 channels of subtitles are already commercially available and various recordable systems will be introduced soon. Just as the CD has surpassed vinyl records and analogue audiocassettes in the music industry, it is only a matter of time before the DVD replaces the VCR as the dominant in-home video device.

Both CD and DVD systems operate under the same principles. To read the data, a focused 5 mW semiconductor laser shines onto a rotating disc [26]. Patterns of pits are concealed within the transparent disc, as shown in fig. 1.1. These pits reflect less light than the areas between them creating a pattern of strong and weak reflections. A pickup lens then gathers the reflected light and directs it to a photodiode, where the pattern of light fluctuations are converted to a pattern of voltage fluctuations. These analogue voltage fluctuations are then converted to a digital bit-stream by an analogue-to-digital converter.

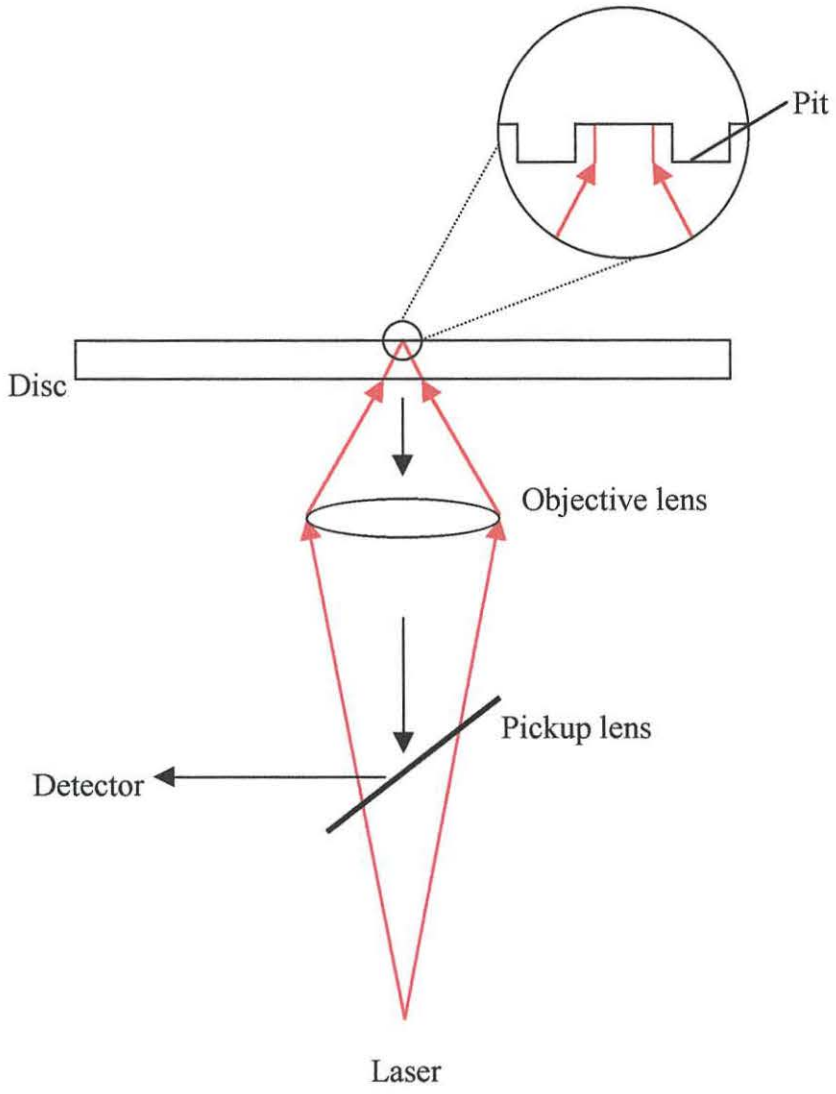

Fig. 1.1 *Simple illustration of an optical disc system.*

One of the main differences between CD and DVD systems is the diameter of the focused laser beam when it strikes the disc. A compact disc system uses a GaAs semiconductor laser operating at a wavelength, λ, of 780 nm to read the data, whilst the DVD uses a 650 nm laser fabricated in the AlGaInP material system. The minimum focused spot diameter is approximately $\lambda/2N_A$ where N_A is the numerical aperture of the focusing lens [27], i.e. the lens's light focusing capacity. In CD players, the N_A value is typically 0.45 ensuing a diameter of approximately 1 μm, whilst a numerical aperture of 0.6 in a DVD system offers a diameter of 0.5 μm. The smaller spot size allows smaller pits and a shorter distance between pits, permitting

greater storage capacity. This spot size reduction combined with improvements in data compression techniques adds up to a DVD-ROM being able to store 4.7 Gbytes of information compared with the 650 Mbytes capacity of the CD-ROM i.e. approximately seven times more information.

To be attractive as a home entertainment system it is essential for the optical storage device to be able to record and playback data. A CD-Recordable (CD-R) system was developed in the late 1980's [26]. This device allows data to be recorded by using a 30 mW semiconductor laser to "burn" pits into the disc. However, data can be recorded only once. In 1996 CD-Rewritable (CD-RW) technology became commercially available, using a technique called phase-change recording [26]. This method uses laser pulses to form "dots" (similar to pits) of erasable digital data within a specially designed disc material. Although the data is stored differently to conventional discs they can be played on standard CD-ROM or CD players and are a natural successor to the standard floppy disc. Current research is concentrating on developing recordable and rewritable DVDs for the commercial market. The methods outlined above will probably be modified or perhaps new techniques will need to be introduced so that DVD-R and DVD-RW systems will be available to challenge the VCR.

1.2.2 Future developments

To develop a DVD system that will be capable of utilising on-line multimedia technology, such as digital video by cable, a storage capacity greater than 10 Gbytes is thought to be required combined with the ability to read and record data at high speeds [26]. One possibility is to use double-sided discs where two discs are "sandwiched" together thus offering two layers of pits and double the amount of information storage. Unfortunately the methods of retrieving the data indicate that a device of this nature will be expensive so an alternative, cheaper method will probably be required. The answer may well lie in laser diodes fabricated in the Gallium Nitride (GaN) material system [28]. These nitride lasers have been extensively researched over the last few years and are able to emit light in the blue range of the electromagnetic spectrum, i.e. $\lambda \approx 400$ nm, which would offer a storage

	CD	*DVD (red)*	*DVD (blue)*
Data capacity (Gbytes)	0.65	4.7	18
Laser wavelength (nm)	780	650	420
N_A of objective lens	0.45	0.6	0.85
Minimum pit length (μm)	0.83	0.4	0.2
Disc diameter (mm)	120	120	120

Table 1.1 *Specifications for three read-only optical storage systems using a single sided, single-layered disc [26, 29].*

capacity of at least 18 Gbytes on a single sided disc, as summarised in table 1.1. However, further research is being carried out to optimise the operating characteristics of these lasers and will have to be adapted further to be used in optical storage devices.

So just as the DVD has surpassed the CD in storage capacity, the chances are that a new "next generation" DVD will take over from the VCR and DVD in the not too distant future. Once the relevant technologies, e.g. GaN lasers and recordable discs, have been fully developed the prices of DVD systems should reduce making them more accessible to the general public.

1.3 Optical storage and self-pulsation

1.3.1 Optical feedback

The use of semiconductor laser diodes to extract information from an optical disc had been suggested as early as the 1970's [30]. However, it was found that when a standard continuous wave (*cw*) laser beam shines onto a disc not all of the light is collected by the detector. Some of the light is reflected back into the cavity, resulting in feedback that can cause deleterious effects due to the coherent nature of the laser beam [31], as shown in fig. 1.2. High optical feedback results in multiple external

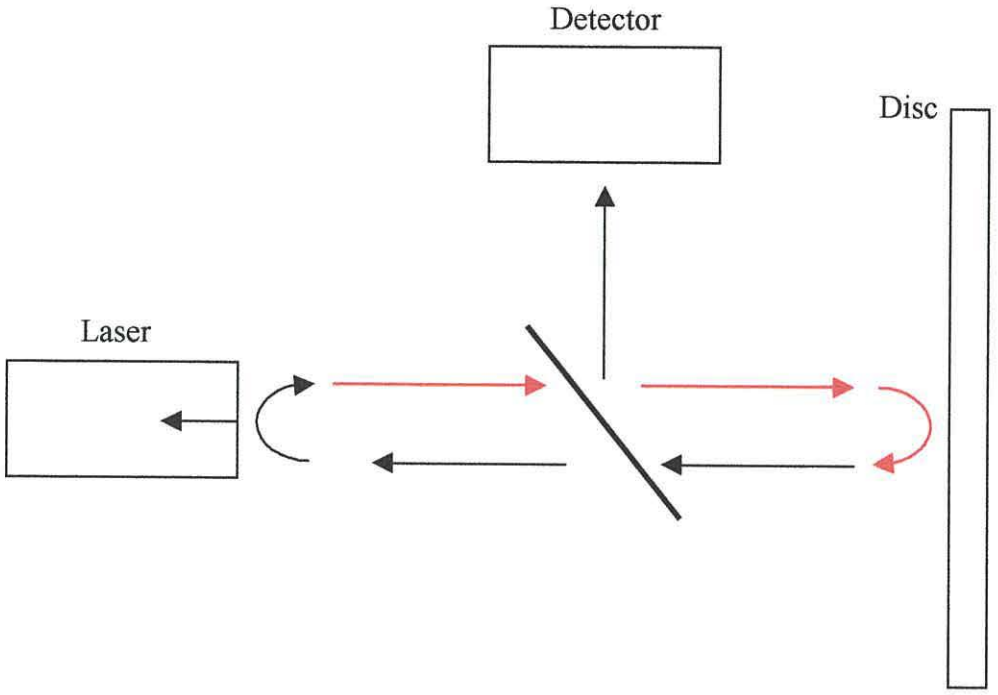

Fig. 1.2 *Problems of optical feedback from the surface of an optical disc.*

cavity modes being created, leading to undesirable linewidth broadening. When the feedback becomes too high coherence collapse and chaos can occur where the coherence length of the laser beam decreases rapidly and the power of the laser varies unpredictably [31]. Several mechanisms have been used to explain this excess noise but are beyond the scope of this work, so the reader is referred to references [31, 32].

It was soon found that a pulsating laser beam could be used to reduce the sensitivity of the laser to optical feedback [33]. Such emission has a low coherence length making it relatively insensitive to backward reflections, i.e. spontaneous emission is observed between pulses, so an incoherent beam (with no phase) dominates the output which gives rise to a stream of incoherent pulses. As a result the excess noise due to mode competition amongst lasing modes (within the cavity) and external modes (formed by reflections) is well suppressed [32], making such emission ideal for use in an optical storage system. A very effective method of achieving this desirable output is to design the laser diode so that it "self-pulsates". Such a device offers pulsation in the lasers optical output under d.c. bias, thereby providing a compact and economical method of reading information from an optical disc.

1.3.2 Device specifications

When using a pulsating laser beam to read data from an optical disc there are a number of operating conditions that the semiconductor device must satisfy. Specifications demand that the laser diode must operate at [34-36]

- temperatures greater than 70 °C;
- an output power of 5 mW for read-only systems;
- 30 mW for a read/write device.

It is also desirable to design a structure that operates at a low threshold current and over a wide operating current range, thereby optimising the performance of the device.

Due to the benefits of pulsation self-pulsating lasers are now commonly used in CD devices, where the GaAs material system is used to construct "narrow stripe" laser diodes that self-pulsate at 780 nm and satisfy the above-mentioned conditions [37]. To achieve pulsation at 650 nm the laser is fabricated in the AlGaInP material system. Unfortunately the output of a conventional AlGaInP narrow stripe laser degrades at high temperatures and subsequently fails to self-pulsate at 70 °C [38]. As a results current DVD systems use high frequency current modulation to reduce the sensitivity of the laser to feedback which adds additional circuitry and amounts to extra costs. For emission at even shorter wavelengths lasers fabricated in the GaN material system now seem desirable. However, due to the infancy of research into nitride materials no literature has been released about controllable self-pulsation in the blue range of the electromagnetic spectrum.

With these points in mind, self-pulsating laser diodes that operate at 650 and 420 nm and satisfy the high temperature operating conditions are required for optical storage devices. The work in this thesis will therefore investigate the most advanced structures on offer to try and achieve such emission. The development of such short wavelength lasers would provide a step towards improvements in current DVD systems and also provide a notable contribution towards a "next generation" DVD device.

1.4 Self-pulsation

When the semiconductor laser diode was discovered self-pulsating emission was considered undesirable, yielding unwanted fluctuations in the power output. Considerable efforts were made to eliminate these pulses to achieve the more desirable *cw* emission. In time, applications were found for self-pulsating devices and significant research was conducted into understanding the process in an attempt to devise structures that offered controllable self-pulsation. In 1974 it was suggested that the phenomenon was associated with age induced defects [39]. Subsequent work concentrated on trying to determine precisely how these defects gave rise to pulsating emission [40]. This led to Dixon and Joyce suggesting that self-pulsation was a result of the interplay between the gain and defect induced areas of absorption within the cavity [41]. It was therefore determined that the introduction of saturable absorption into the laser cavity is the key factor in achieving self-pulsation. With this knowledge and improvements in fabrication techniques, the subsequent years yielded numerous devices that offered controllable self-pulsation [37, 42-44].

Self-pulsation could be described as being an extension of the relaxation oscillations that are observed when the laser is trying to stabilise after turn-on. By introducing saturable absorption into the laser cavity the steady state that is eventually achieved in a *cw* laser is disrupted, resulting in a system where the carrier densities in the respective regions oscillate around their steady state, as shown in fig. 1.3(b). The process can therefore be described using a coupled system of three variables – carrier densities in the amplifying and absorbing regions and the light intensity. Changes in one about its steady state value gives rise to changes in the others. An unstable situation is created when the absorber absorbs stimulated photons giving rise to a laser that has more net gain than is required to sustain steady state emission, thus emitting a pulse. This happens as follows:

1) The carrier density in the active region, N_{qw}, is increased by the injection current.
2) As N_{qw} approaches threshold, i.e. when the gain overcomes the losses within the cavity, photons are generated that are absorbed in the absorber section.
3) Absorption of carriers increases the carrier density in the absorber region, N_{α}.

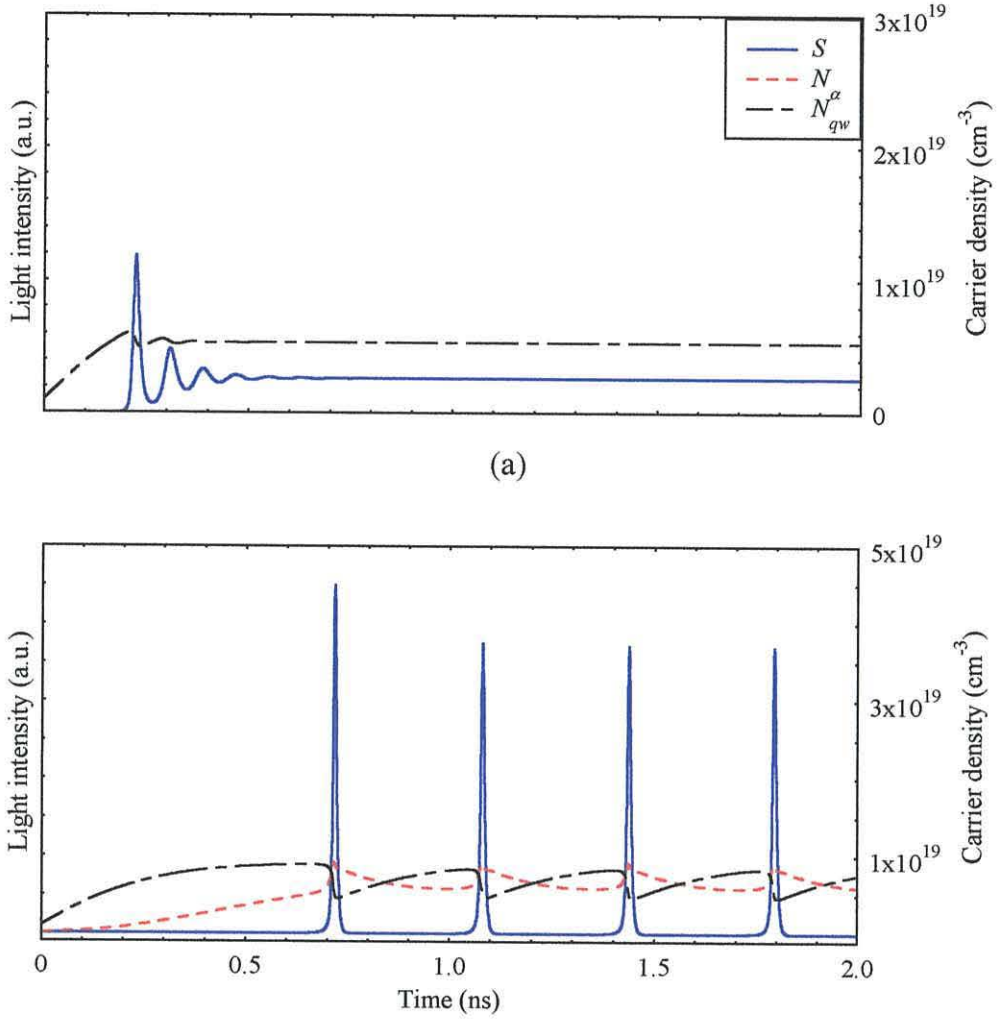

Fig. 1.3 *Typical temporal evolution of the various carrier densities in (a) cw and (b) self-pulsating laser diodes (S=photon density, N_{qw}=carrier density in the gain region and N_{α}=carrier density in the absorber).*

4) As N_{α} increases the rate of absorption decreases. As a result there exists more gain than loss in the cavity so there is a rapid increase in the photon density, S.
5) N_{qw} decreases with increasing stimulated emission until no light is emitted, i.e. when N_{qw} is low enough to be below threshold.
6) The process is repeated, i.e. return to1).

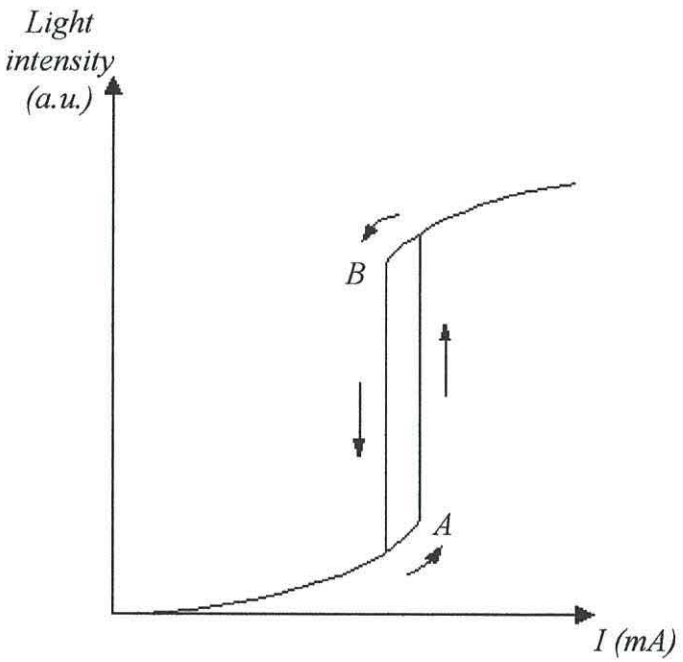

Fig. 1.4 *Typical variation of light output as a function of current for a bistable laser (with arrows indicating the level of bias current).*

A consequence of adding a saturable absorber into the cavity is that bistable operation is observed [42, 45], resulting in a hysterisis loop which offers two states for the same current, as displayed in fig. 1.4. The route through point *A* indicates the influence of the absorption; i.e. the absorber increases the threshold value. This corresponds to an "on state" (pulse peak) and a coherent light output. After turn-on, the return trip through *B* displays the light output without the influence of the absorber as the carriers attempt to return to equilibrium. This route offers an "off state" (pulse trough) which gives rise to incoherent output, i.e. spontaneous emission. It is also known that the width of the loop can influence the device characteristics [46], i.e. a narrow hysterisis is essential for self-pulsation.

1.5 Overview of thesis

This chapter has described the basic operation of the semiconductor laser and outlined one of its main applications, namely reading data from an optical disc. A key method of increasing the storage capacity is to reduce the wavelength of the laser and the most efficient way of reading information from an optical disc involves using a self-pulsating laser diode. Unfortunately the older, more traditional methods of achieving self-pulsation have failed to offer the high temperature, short wavelength emission required for DVD systems. With this in mind, the work in this thesis theoretically investigates newer, more advanced, self-pulsating laser diodes for 650 and 420 nm emission, with the devices being optimised subject to the high temperature operating constraints stipulated in section 1.3.2.

Chapter 2 gives a more thorough description of the semiconductor laser, describing the key material and optical properties that are required for successful lasing. To accurately assess the dynamical output of the device it is important to use a detailed gain model that calculates the material gain of the active region. A gain equation will therefore be derived, explaining how gain is generated in bulk and quantum confined devices with key material properties, such as many-body effects, being included. The optical properties of the semiconductor laser are then investigated, with a derivation of the basic equations that simulate the propagation of the optical field within the laser cavity. The optical and material properties of the device are then combined, giving rise to an equation for the threshold gain within a semiconductor laser.

The third chapter introduces the methods required to model the dynamical properties of the laser diode, with an emphasis on self-pulsation. To start, a review of different self-pulsating laser diodes is given, offering an insight into the various designs that enable controllable amounts of saturable absorption to be included in the cavity. This is followed by a more thorough investigation of two of the devices, i.e. the real refractive index guided laser and laser diode with epitaxial absorber layers. It is the emission of these two lasers that will be investigated in this thesis, so a rate equation model is derived for each device. The chapter concludes with an outline of

the conditions for self-pulsation, with attention being paid to the key differential gain/absorption relationship that must be satisfied for the emission to self-pulsate.

The first three chapters will give the reader an understanding of the semiconductor laser and the process of self-pulsation. The remaining chapters implement the rate equations in order to study and optimise the emission of three different self-pulsating laser diodes, specifically for optical storage applications. Chapter 4 uses a rate equation model to simulate a 650 nm real refractive index guided laser diode and investigate the emission subject to the temperature, power and current conditions stated in section 1.3.2. To achieve the desired operating wavelength the device is fabricated in the AlGaInP material system. This material gives rise to an unwanted leakage current at high temperatures, so the active region is configured to minimise this deleterious effect. By investigating numerous design parameters the quantity of absorption within the cavity is optimised. As a result, the work gives an indication of the suitability of such laser diodes for use in optical storage devices.

Chapter 5 uses a different structure, a laser diode with epitaxial absorber layers, to investigate self-pulsation at 650 nm. Again, the AlGaInP material system is used to achieve emission at the desired wavelength so the problematic nature of the leakage current comes to the fore. This device offers absorption in a different manner to the laser described in the previous chapter. Using gain/absorption calculations for the gain and absorber regions and the relevant rate equation model, the emission of the laser is studied. In particular, the design of the absorber and the cavity parameters are investigated for self-pulsation subject to the temperature, power and current specifications stipulated in section 1.3.2. As a result, two optimised structures are presented, one suitable for use in a read-only DVD and another for use in a read/write DVD.

The benefits of 420 nm self-pulsation have already been stated so the penultimate chapter studies a nitride self-pulsating laser for optical storage applications. Assessing the results in chapters 4 and 5 it is decided to design and investigate a GaN laser diode with epitaxial absorber layers. The material properties of the material system are introduced, followed by the design of the various epitaxial layers. Gain calculations are presented then the rate equation model is implemented

to investigate the emission. In particular, the gain and absorber sections are optimised subject to the high temperature operating constraints with the cavity parameters also being assessed. The design of two optimised cavity configurations are then presented, giving an indication of the suitability of nitride self-pulsating lasers for use in "next generation" DVD systems.

The final chapter summarises the results presented in the thesis and discusses their implications. The benefits of using the different laser structures and material systems are given with an assessment of whether self-pulsation is feasible for short wavelength optical storage. Possible future work will then be assessed.

References

[1] A. L. Schawlow and C. H. Townes, "Infrared and optical masers," *Phys. Rev.*, vol. 112, pp. 1940-1949, 1958.

[2] T. H. Maiman, "Stimulated optical radiation in ruby masers," *Nature*, vol. 187, pp. 493-494, 1960.

[3] A. Javan, W. R. Bennett Jr. and D. R. Herriot, "Population inversion and continuous optical maser oscillation in a gas discharge containing a He-Ne mixture," *Phys. Rev. Lett.*, vol. 6, pp. 106-110, 1961.

[4] N. G. Basov, O. N. Krokhin and Y. M. Popov, "Production of negative temperature states in p-n junctions of degenerate semiconductors," *Sov. Phys. JETP*, vol. 13, pp. 1321-1330, 1961.

[5] M. I. Nathan, W. P. Dumke, G. Burns, F. H. Dill Jr., and G. Lasher "Stimulated emission of radiation from GaAs p-n junctions," *Appl. Phys. Lett.*, vol. 1, pp. 62-64, 1962.

[6] H. Kroemer, "A proposed class of heterojunction laser," *Proc. IEEE*, vol. 51, pp. 1782-1783, 1963.

[7] Zh. I. Alferov and R. F. Kazarinov, "Semiconductor laser with electric pumping," (U.S.S.R.) Patent 181737, 1963.

[8] C. C. Davis, *Lasers and Electro-Optics: Fundamentals and Engineering*, Cambridge University Press, 1996.

[9] I. Hayashi, M. B. Panish and P. W. Foy, "Low-threshold room-temperature injection laser," *IEEE J. Quantum Electron.*, vol. 5, pp. 211-212, 1969.

[10] A. Y. Cho, "Film deposition by molecular beam techniques," *J. Vac. Sci. Technol.*, vol. 8, pp. S31-S38, 1971.

[11] A. Y. Cho, "Growth of periodic structures by the molecular-beam method," *Appl. Phys. Lett.*, vol. 19, pp. 467-468, 1971.

[12] L. L. Chang, L. Esaki, R. Tsu, "Resonant tunnelling in semiconductor double barriers," *Appl. Phys. Lett.*, vol. 24, pp. 593-595, 1974.

[13] R. Dingle, W. Wiegmann and C. H. Henry, "Quantized states of confined carriers in very thin $Al_xGa_{1-x}As$-GaAs-$Al_xGa_{1-x}As$ heterostructures," *Phys. Rev. Lett.*, vol. 33, pp. 827-830, 1974.

[14] J. P. van der Ziel, R. Dingle, R. C. Miller, W. Wiegmann and W. A. Norland Jr., "Laser oscillation from quantum states in very thin GaAs-$Al_{0.2}Ga_{0.8}As$ multilayer structures," *Appl. Phys. Lett.*, vol. 26, pp. 463-465, 1975.

[15] R. D. Dupuis and P. D. Dapkus, "Room temperature operation of $Ga_{1-x}Al_xAs$/GaAs double-heterostructures grown by metalorganic chemical vapor deposition," *Appl. Phys. Lett.*, vol. 31, pp. 466-468, 1977.

[16] W. T. Tsang, F. K. Reinhart and D. Ditzenberg, "The effect of substrate temperature on the current threshold of GaAs-$Al_xGa_{1-x}As$ double-heterostructure lasers grown by molecular beam epitaxy," *Appl. Phys. Lett.*, vol. 36, pp. 118-120, 1980.

[17] W. T. Tsang, "Extremely low threshold (AlGa)As modified multiquantum well heterostructure lasers grown by molecular-beam epitaxy," *Appl. Phys. Lett.*, vol. 39, pp. 786-788, 1981.

[18] W. T. Tsang, "Extremely low threshold (AlGa)As graded-index waveguide separate-confinement heterostructure lasers grown by molecular-beam epitaxy," *Appl. Phys. Lett.*, vol. 40, pp. 217-219, 1982.

[19] A. R. Adams, "Band structure engineering for low threshold high efficiency lasers," *Electron. Lett.*, vol. 22, pp. 249-251, 1986.

[20] E. Yablonovich and E. O. Kane, "Reduction of lasing threshold current density by the lowering of valence band effective mass," *J. Lightwave Technol.*, vol. 4, pp. 504-506, 1986.

[21] E. Kapon, S. Simhony, J. P. Harbison, L. T. Florez and P. Worland, "Threshold current reduction in patterned quantum-well semiconductor-lasers grown by molecular-beam epitaxy," *Appl. Phys. Lett.*, vol. 56, pp. 1825-27, 1990.

[22] Y. Arakawa and H. Sakaki, "Multidimensional quantum well lasers and temperature-dependence of its threshold current," *Appl. Phys. Lett.*, vol. 40, pp. 939-941, 1982.

[23] A. Yariv, "Scaling laws and minimum threshold currents for quantum-confined semiconductor-lasers," *Appl. Phys. Lett.*, vol. 53, pp. 1033-1035, 1988.

[24] K. Vahala, Y. Arakawa and A. Yariv, "Reduction of the field spectrum linewidth of a multiple quantum-well laser in a high magnetic-field – spectral properties of a quantum dot laser," vol. 50, pp. 365-367, 1987.

[25] H. T. Johnson, L. B. Freund, C. D. Akyuz and A. Zaslavsky, "Finite element analysis of strain effects on electronic and transport properties in quantum dots and wires," *J. Appl. Phys.*, vol. 84, pp. 3714-3725, 1998.

[26] H. van Houten and J. Schleipen, "Optical data storage," *Physics World*, vol. 11, pp. 33-37, 1998.

[27] S. M. Mansfield, W. R. Studenmund, G. S. Kino and K. Osato, "High-numerical aperture lens system for optical storage," *Optics Lett.*, vol. 18, pp. 305-307, 1993.

[28] S. Nakamura and G. Fasol, *The Blue Laser Diode*, Springer-Verlag, Berlin, 1997.

[29] T. R. Halfhill, "CDs for the gigabyte era," *Byte*, October 1996.

[30] A. Seko, Y. Mitsuhashi, T. Morikawa, J. Shimada and K. Sakurai, "Self-quenching in semiconductor lasers and its application in optical memory readout," *Appl. Phys. Lett.*, vol. 27, pp. 140-141, 1975.

[31] D. Lenstra, B. H. Verbeek and A. J. Denboef, "Coherence collapse in single-mode semiconductor-lasers due to optical feedback," *IEEE J. Quantum Electron.*, vol. 21, pp. 674-679, 1985.

[32] M. Yamada, "Theoretical analysis of noise-reduction in semiconductor laser with help of self-sustained pulsation phenomena," *J. Appl. Phys.*, vol. 79, pp. 61-71, 1996.

[33] S. Matsui, H. Takiguchi, H. Hayashi, S. Yamamoto, S. Yano and T. Hijikata, "Suppression of feedback-induced noise in short-cavity v-channelled substrate inner stripe lasers with self-oscillation," *Appl. Phys. Lett.*, vol. 43, pp. 219-221, 1983.

[34] H. D. Summers, C. H. Molloy, P. M. Smowton, P. Rees, I. Pierce and D. R. Jones, "Experimental analysis of self-pulsation in 650-nm-wavelength AlGaInP laser diodes with epitaxial absorbing layers," *IEEE J. Select. Topics Quantum Electron.*, vol. 5, pp. 745-749, 1999.

[35] M. Ohya, H. Fujii, K. Doi and K. Endo, "Low current and highly reliable operation at 80°C of 650 nm 5 mW LDs for DVD applications," *Electron. Lett.*, vol. 35, pp. 46-48, 1999.

[36] Y. Ueno, H. Fujji, H. Sawano, K. Kobayashi, K. Hara, A. Gomyo and K. Endo, "30-mW 690-nm high-power strained-quantum-well AlGaInP laser," *IEEE J. Quantum Electron.*, vol. 29, pp. 1851-1856, 1993.

[37] M. Yuri, S. Harris, T. Takayama, O. Imafuji, H. Naito, M. Kume, K. Itoh and T. Baba, "Two-dimensional analysis of self-sustained pulsation for narrow-stripe AlGaAs lasers," *IEEE J. Select. Topics Quantum Electron.*, vol. 1, pp. 473-479, 1995.

[38] H. Adachi, S. Kamiyama and I. Kidoguchi, "Current spreading effects in 680-nm-band self-sustained pulsating AlGaInP visible laser diodes," *Opt. Quantum Electron.*, vol. 28, pp. 541-546, 1996.

[39] E. S. Yang, P. G. McMullin, A. W. Smith, J. Blum and K. K. Shih, "Degradation-induced microwave oscillations in double-heterostructure injection lasers," *Appl. Phys. Lett.*, vol. 24, pp. 324-326, 1974.

[40] T. L. Paoli, "Changes in optical properties of *cw* (AlGa)As junction lasers during accelerated ageing," *IEEE J. Quantum Electron.*, vol. 13, pp. 351-359, 1977.

[41] R. W. Dixon and W. B. Joyce, "A possible model for sustained oscillations (pulsations) in (Al,Ga)As double-heterostructure lasers," *IEEE J. Quantum Electron.*, vol. 15, pp. 470-474, 1979.

[42] H. Kawaguchi and G. Iwane, "Bistable operation in semiconductor lasers with inhomogeneous excitation," *Electron. Lett.*, vol. 17, pp. 167-168, 1981.

[43] J. P. van der Ziel, "Pulsating output of separate confinement buried optical guide lasers due to the deliberate introduction of saturable loss," *Appl. Phys. Lett.*, vol. 39, pp. 376-378, 1981.

[44] R. C. P. Hoskens, T. G. van de Roer, C. J. van der Poel and H. P. M. Ambrosius, "Self-pulsating lasers with quantum well saturable absorber," *Appl. Phys. Lett.*, vol. 67, pp. 1343-1345, 1995.

[45] C. Harder, K. Y. Lau and A. Yariv, "Bistability and pulsations in *cw* lasers with a controlled amount of saturable absorption," *Appl. Phys. Lett.*, vol. 39, pp. 382-384, 1981.

[46] C. Harder, K. Y. Lau and A. Yariv, "Bistability and pulsations in semiconductor laser with inhomogeneous current injection," *IEEE J. Quantum Electron.*, vol. 18, pp. 1351-1361, 1982.

Chapter 2

Semiconductor lasers

2.1 Introduction

Having described an application for the semiconductor laser in the previous chapter it is now desirable to delve somewhat deeper into the internal properties of the device. With this in mind, the purpose of this chapter is to introduce the reader to the basic, fundamental processes required to understand the material and optical properties of a semiconductor laser. The work begins with a description of the formation of a solid at an atomic scale. This leads to the classification of a direct band-gap semiconductor, a material with useful characteristics that can be manipulated to achieve lasing. Concepts are introduced that describe how electron-hole pairs are created and destroyed, including equations that enable one to model such features. Improvements in fabrication methods have led to new quantum structures being devised over the past 20 years. The benefits of quantum confinement can significantly improve the performance of a semiconductor laser and will therefore be introduced, concentrating on quantum well and strained quantum well devices.

The majority of the chapter considers the material properties of the semiconductor. However, to achieve lasing the semiconductor material must form a cavity that allows an optical field to be amplified. A section is included that describes the propagation of such a field within a dielectric waveguide. The chapter concludes by combining the optical and material components of a semiconductor laser cavity to construct an equation for the threshold gain within such a device.

2.2 Semiconductor diodes

2.2.1 Band structure

When atoms combine to form a solid the interaction between an atom and its neighbours cause a broadening of the sharply defined atomic energy states, resulting in a series of broad energy bands. The outermost electrons of the atoms combine to form the valence band. At absolute zero the bands above the valence band are empty, the lowest and nearest to the valence band being the conduction band. The forbidden energy gap between these two bands is called the band-gap, E_g, the width of which changes for different materials. The classifications of conductor, semiconductor and insulator are determined by the size of the band-gap. In this work the interest is in semiconductors, i.e. materials that have a relatively small band-gap that carriers can cross given sufficient energy. This means that unlike metals the resistance of a semiconductor decreases with increasing temperature.

A more detailed description of a semiconductor crystal is given by its band structure. This picture shows the variation of the electron energy, E, with wave vector, $\mathbf{k}$., as displayed in fig. 2.1. Visualising the electron distribution in this manner allows the bands in the semiconductor to be approximated crudely by parabolic functions of $\mathbf{k}$. When the minima of the conduction band lies directly above the highest point of the valence band a direct band-gap material is given. If this is not the case, an indirect band-gap is available. For a complete description of the valence band it must be noted that it splits into three – the heavy-hole (HH), light-hole (LH) and split-off (SO) bands. This originates from the discrete energy levels of the atoms that

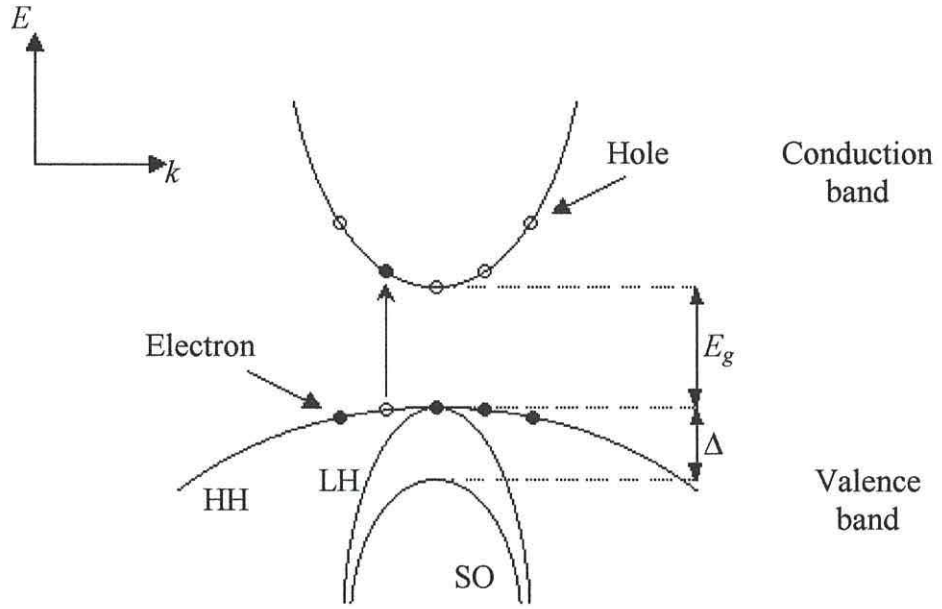

Fig. 2.1 *Parabolic energy band diagram of a semiconductor where an electron has been excited into the conduction band, leaving a vacant state (hole) in the valence band.*

compose the crystal. The uppermost degenerate valence bands, i.e. the heavy and light-hole bands, and the split-off band are separated by another energy gap, defined as Δ.

At absolute zero all electrons occupy the valence band, i.e. in discrete energy states, thus obeying Pauli's exclusion principle. However, if the temperature is increased, thermal excitation can give rise to electrons crossing the band-gap into the conduction band, leaving a vacancy in the bonding behind. This vacancy behaves like a positive charge and is called a hole. Transitions occur primarily between the upper two valence bands and the conduction band because of the smaller transition energy required in comparison with the split-off-conduction band transition.

To model this energy-momentum relationship one must start by investigating the electron as it propagates within the semiconductor crystal. The electrons wavefunction, ψ, can be found for a carrier in either the conduction or valence band by solving the Schroedinger equation [1]

$$H_0\psi = \left[\frac{\mathbf{p}^2}{2m_0} + V(\mathbf{r})\right]\psi = E\psi \tag{2.1}$$

which relates the system Hamiltonian of the crystal lattice, H_0, to the energy of the electron, E. The momentum operator is represented by $\mathbf{p}$, $\mathbf{r}$ is the electrons position vector, $V(\mathbf{r})$ is the potential created by the crystal lattice and m_0 is the free electron mass. A generalised approximate solution for ψ in a given energy band is given by the following expression

$$\psi = F(\mathbf{r})u(\mathbf{r}) \tag{2.2}$$

which consists of two components, the band edge Bloch function, $u(\mathbf{r})$, which is periodic with the crystal lattice multiplied by a slowly varying envelope function, $F(\mathbf{r})$ [2]. Assuming a parabolic band structure the energy, E, and momentum, k, of the carrier may then be related by

$$E = \frac{\hbar^2 k^2}{2m^*} \tag{2.3}$$

where m^* is the effective mass. This value is dependent on which band that the carrier may reside and is approximated by

$$m^* = \hbar^2\left(\frac{d^2E}{dk^2}\right)^{-1} \tag{2.4}$$

showing that the effective mass is inversely proportional to the curvature of the band.

2.2.2 Carrier populations

Electrons are fermions and therefore obey Fermi-Dirac statistics. So, at a given temperature, T, the occupation probability of an electron with energy E is given by the Fermi-Dirac distribution

$$f(E) = \frac{1}{\exp[(E - E_F)/kT] + 1} \tag{2.5}$$

where E_F is known as the Fermi level and exists at the centre of the band-gap at absolute zero. At this point the probability of occupancy is always 1/2, i.e. $f(E_F)$=1/2. When carriers are injected into the structure non-equilibrium conditions are generated. The Fermi level is then replaced by an electron quasi-Fermi level, E_{Fn}, and a hole quasi-Fermi level, E_{Fp}, giving a measure of the deviation from equilibrium, i.e. the level will move from the centre of the band-gap.

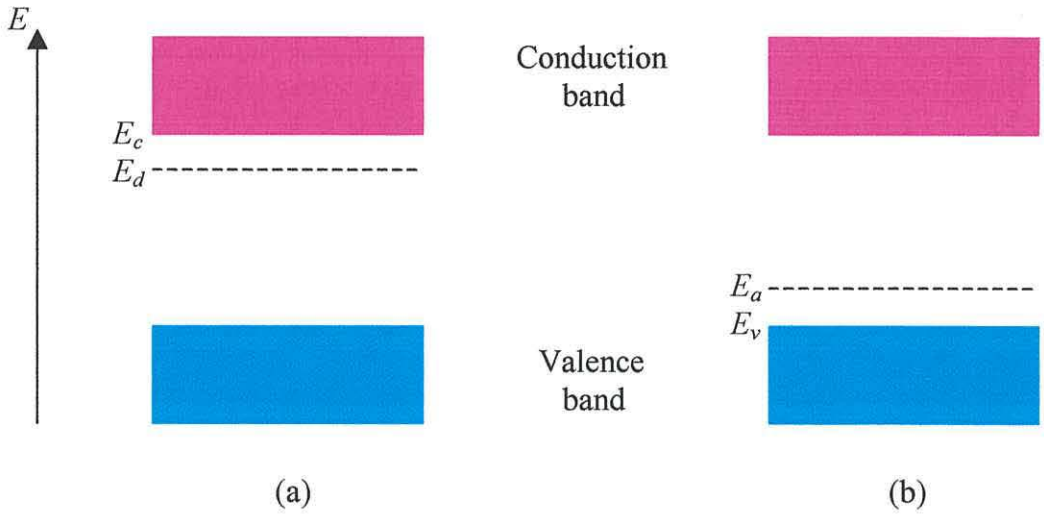

Fig. 2.2 *Schematic band diagrams showing the position of (a) donor and (b) acceptor energy levels in extrinsic semiconductor materials.*

2.2.3 Doping

A perfect semiconductor crystal is said to be intrinsic. Changes in conductivity can be obtained by doping the material with another element, forming an extrinsic semiconductor. Important impurities are those which align themselves in the lattice structure whether they have one valence electron too many or one too few. The first type contributes a free electron to the semiconductor, increasing the materials conductivity. This kind of impurity is called a donor as it donates an electron to the material. The electron density is increased and so the semiconductor is said to be n-type. In the energy band picture, the donor atoms occupy energy levels in the forbidden band, just below the conduction band, represented as E_d in fig. 2.2(a). When a small amount of energy is applied to the lattice, i.e. $\geq E_c - E_d$, the electrons in the donor atoms can occupy the conduction band, thus leaving a positively ionised atom. The addition of donor impurities can therefore increase electron conductivity significantly when enough energy is applied.

The second kind of impurity element compensates for its deficiency of a valence electron by acquiring an electron from its neighbour. Because these materials accept an electron they are called acceptor impurities. In this case the density of holes increases, so a p-type semiconductor is constructed. This kind of impurity atom

occupies energy levels in the forbidden gap near the valence band, shown as E_a in fig. 2.2(b). When enough energy is applied, i.e. $\geq E_a - E_v$, electrons will leave the valence band and occupy the hole states that are now available. This causes the acceptor atom to become negatively ionised. Beyond a certain temperature each donor atom provides a free electron to the conduction band and every acceptor atom generates a hole in the valence band. When an intrinsic semiconductor is doped the Fermi level moves from the centre of the band-gap, upwards for n-type and downwards for p-type, the precise location being a function of doping.

2.2.4 P-n junction

Joining a p- and n-type semiconductor forms a basic p-n junction diode. When such a structure is formed the Fermi levels of the two materials align with each other and a thin depletion layer exists at the junction. Within this depletion region holes and electrons are sparse with positively ionised donor atoms on one side of the band-gap and negatively ionised acceptors on the other side. At this point, when the carriers are in equilibrium, all the electrons lie below the Fermi level whilst all empty energy states lie above it.

In a semiconductor light emitting device population inversion is required, i.e. electrons are required in the conduction band and holes in the valence band. The situation is obtained by applying a large forward bias, i.e. applying a voltage, V, across the semiconductor, as shown in fig. 2.3. The two ends of the sample then have different Fermi levels, allowing population inversion to occur within an area known as the active region where electrons lie directly above empty energy states (holes). In this area there exists a high probability of an electron traversing the energy band-gap and recombining with a hole. This results in the excess energy being released as a photon of energy hv. The band-gap energy is proportional to the wavelength of the stimulated light via the equation

$$E_g = hv \tag{2.6}$$

where h is Plancks constant and v is the frequency of the emitted light. If charge neutrality is assumed within the active region then

$$n_c + N_a = p_v + N_d \tag{2.7}$$

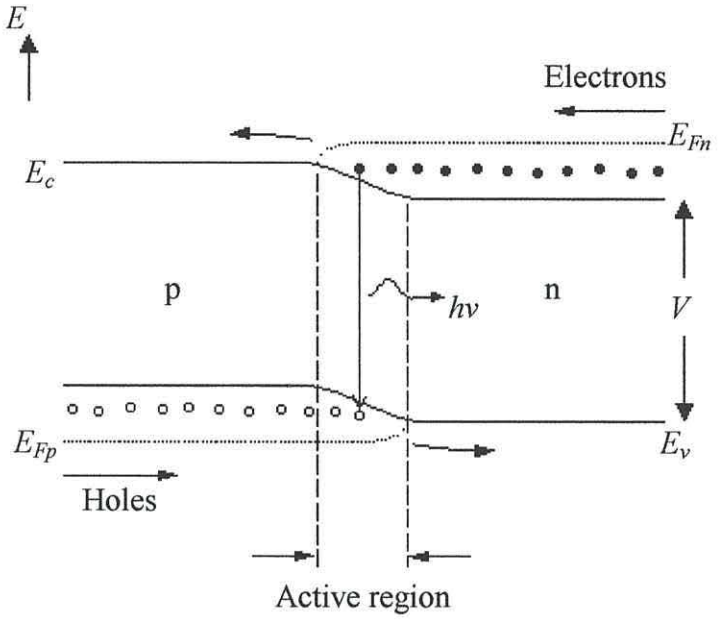

Fig. 2.3 *Energy band diagram as a function of distance through a forward biased p-n homojunction.*

where n_c represents the electron density in the conduction band and p_v denotes the hole density in the valence band. The number of donor and acceptor atoms are given by N_d and N_a, respectively.

The homojunction is the simplest p-n junction, made up of the same material on both sides of the junction. Unfortunately the carrier confinement in such a structure is quite poor, i.e. the carriers "leak" out of the active region for too easily. This led to the design of a more efficient active region, called the p-n heterojunction, shown in fig. 2.4. To obtain population inversion three different materials are "sandwiched" together and a forward bias is applied. The changes in material band-gap form a potential energy discontinuity resulting in an active region with improved carrier confinement. This increases the probability of electrons and holes recombining. The structure is also designed so that the active region has a higher refractive index, n, than neighbouring sections following the relationship $E_g \propto^{-1} n$. This ensures that the device behaves as a dielectric optical waveguide in the growth direction, thus offering good optical confinement (see section 2.4).

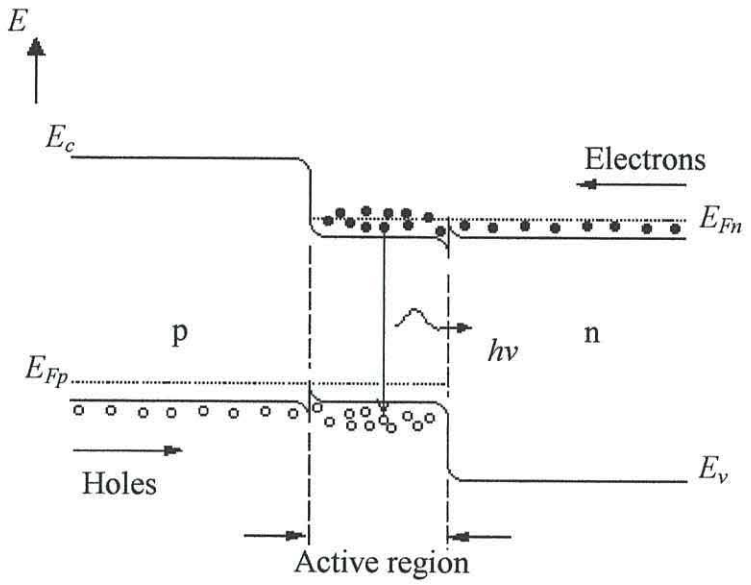

Fig. 2.4 *Band diagram of a double heterostructure p-n junction under forward bias.*

Improvements in growth techniques have led to quantum confined devices. These structures offer further improvements in carrier confinement resulting in an even higher probability of carrier transitions. Electron states for bulk crystalline solids consist of continuous energy bands, as displayed in fig. 2.1. By reducing the thickness of the material to a value comparable to the de Broglie wavelength of the carriers ($\lambda \sim h/p$) it is possible to enter the quantum regime and use non-classical rules to improve various operating characteristics. The simplest quantum confined structure is known as the quantum well, which restricts the movement of carriers in the growth (x) direction creating a very thin active region, as displayed in fig. 2.5(b). A well layer is formed when a monolayer of low band-gap material is sandwiched between a material of higher band-gap. In the y and z directions the energy levels form a continuum of states. However, in the x-direction the energy levels are quantized resulting in discrete energy levels that the carriers must occupy whilst obeying Pauli's exclusion principle, as shown in fig. 2.6. [*Note*: The quantized direction in a quantum well is usually denoted as the "z-direction". However, for consistency with the other co-ordinate systems used in this work the quantized direction will remain as the "x-direction" throughout this thesis.]

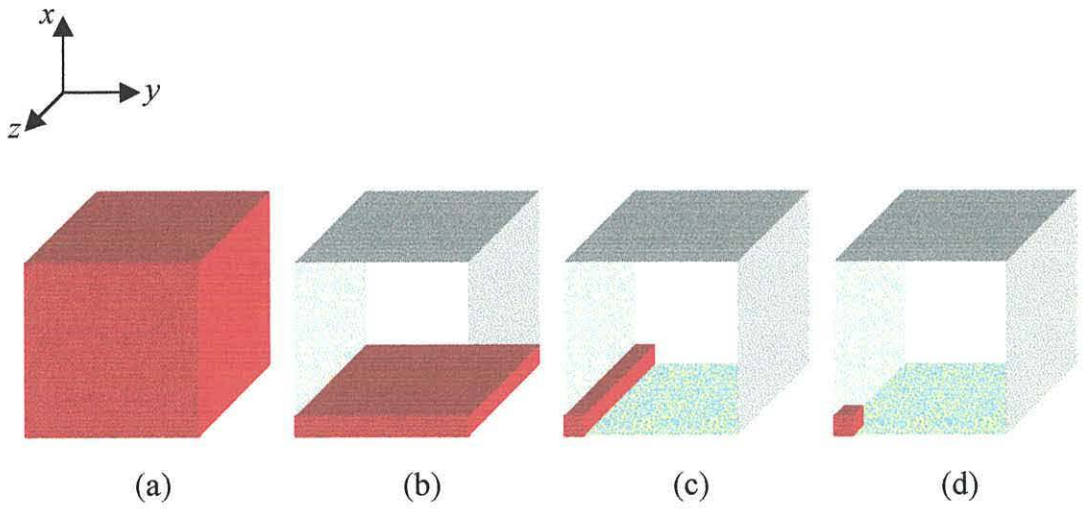

Fig. 2.5 *Crystal geometry's of the (a) bulk, (b) quantum well, (c) quantum wire and (d) quantum dot structures.*

Unfortunately the small active region widths that are used in quantum well devices give rise to poor optical confinement. This problem is overcome by growing additional waveguiding layers between the active and cladding regions. These layers can have different designs but the most popular is known as the separate confinement heterostructure (SCH). This addition results in a structure that offers excellent carrier and optical confinement, properties that are essential if lasing is to be achieved.

By introducing multi-dimensional confinement other quantum confined structures may be fabricated. Two-dimensional confinement results in a quantum wire where a wire-like potential well allows freedom in only one direction. A quantum dot is formed when the whole three-dimensional active region in reduced to a size below the de Broglie wavelength of the carriers, offering a box-like confinement. These structures are shown in figs. 2.5, however, both are very hard to fabricate and aren't understood as well as the quantum well structure. Only quantum well active regions will be used in this work, so the interested reader will find more information about quantum wires and dots in references [1, 3].

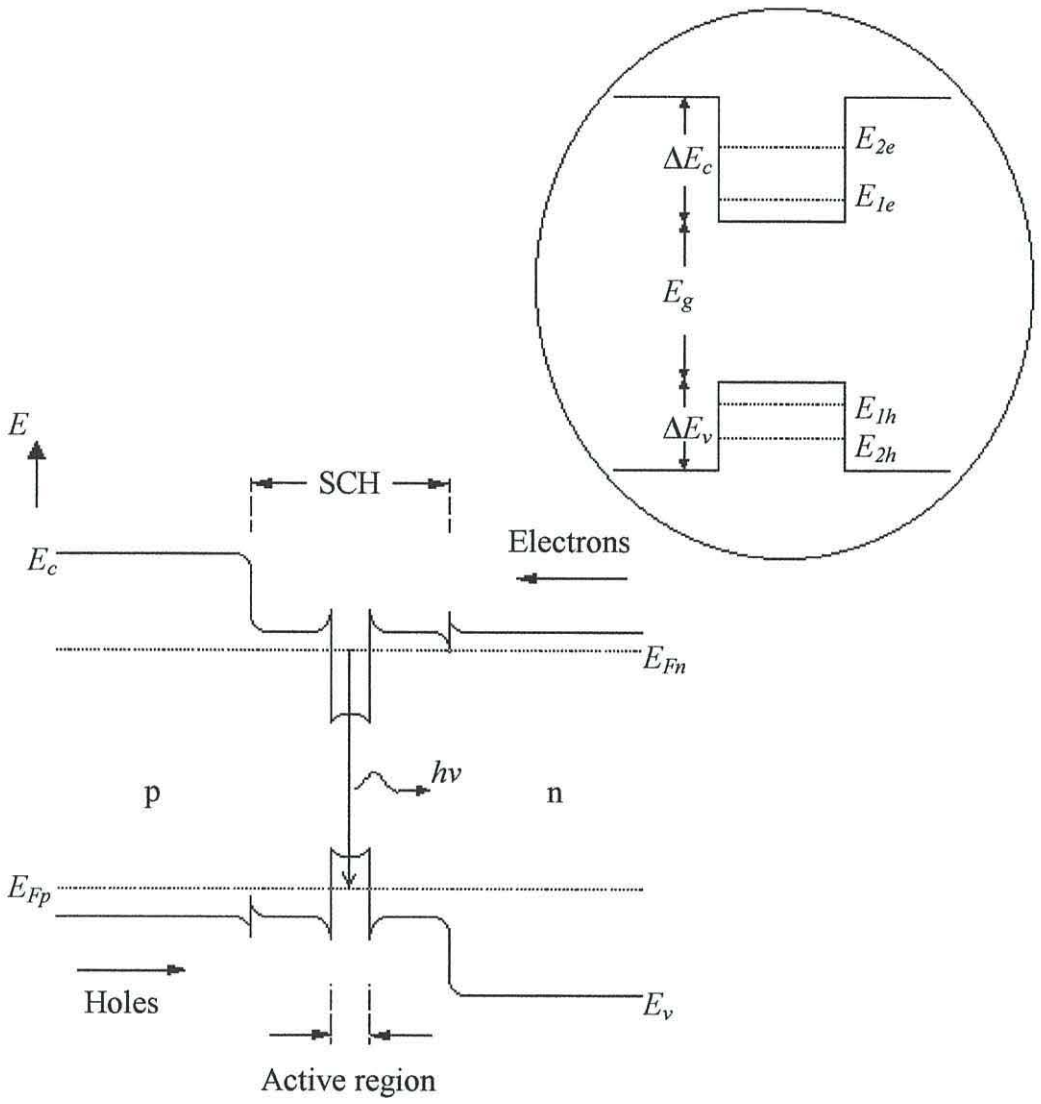

Fig. 2.6 *Band diagram of a single quantum well separate confinement heterostructure (SCH) and (inset) an energy band diagram of the quantum well structure with two confined energy levels in the conduction and valence bands.*

2.2.5 Energy states in quantum wells

The quantised, or "sub-band", energy levels for the motion of carriers in the x-direction are obtained by solving equation (2.1) for carriers in both the well and the barrier regions of the structure. For the 1-dimensional confinement associated with a quantum well one can assume the envelope function solutions to be of the form

$$F(x,y,z) = F(x)\exp\{i(k_y y + k_z z)\}. \tag{2.8}$$

To find the energy levels in the quantum well one must therefore solve [1]

$$EF(x) = -\frac{\hbar^2}{2m_w^*}\frac{d^2F(x)}{dx^2} \tag{2.9}$$

and for the barrier

$$EF(x) = -\frac{\hbar^2}{2m_b^*}\frac{d^2F(x)}{dx^2} + VF(x) \tag{2.10}$$

where V is the height of the potential well which is given by the band-offsets for that semiconductor interface; ΔE_c for electrons in the conduction band and ΔE_v for holes in the valence band, as shown in fig. 2.6. The effective masses of the carriers at the band edge within the quantum well and the barrier are denoted by m_w^* and m_b^*, respectively.

For a finite quantum well the solutions for the electron wavefunctions in the well are given by

$$F_e(x) = A\sin(k_w x) \qquad \text{(odd solutions)} \tag{2.11a}$$

$$F_e(x) = C\cos(k_w x) \qquad \text{(even solutions)} \tag{2.11b}$$

and the solutions for the wavefunctions in the barrier are represented by

$$F_e(x) = B\exp(-k_b|x|) \qquad \text{(odd solutions)} \tag{2.12a}$$

$$F_e(x) = D\exp(-k_b|x|) \qquad \text{(even solutions).} \tag{2.12b}$$

where $k_w = \sqrt{2m_w^* E/\hbar^2}$ and $k_b = \sqrt{2m_b^*(V-E)/\hbar^2}$.

The confined energy levels and the constants ($A \rightarrow D$) may now be calculated. At the junction of the well and barrier the carrier wavefunction must be continuous, so, assuming current continuity

$$F_w = F_b \tag{2.13}$$

and

$$\frac{1}{m_w^*}\frac{dF}{dx} = \frac{1}{m_b^*}\frac{dF}{dx}. \tag{2.14}$$

For even modes the confined energies are then obtained by solving

$$\sqrt{\left(\frac{m_b^*}{m_w^*}\right)\left(\frac{V-E}{E}\right)} = \tan\sqrt{\frac{m_w^* L_x^2 E}{2\hbar^2}} \tag{2.15}$$

and similarly for odd modes

$$\sqrt{\left(\frac{m_b^*}{m_w^*}\right)\left(\frac{V-E}{E}\right)} = \cot\sqrt{\frac{m_w^* L_x^2 E}{2\hbar^2}} \tag{2.16}$$

where L_x is the width of the quantum well. These transcendental equations apply for both the calculation of electron and hole sub-band energies. The equations assume a "square well" where the conduction and valence bands are flat at operating bias. This is a reasonable approximation when the well and barrier regions are undoped. However, if the structure is doped then "band bending" is observed which destroys the square well and leads to a more complicated solution.

Varying the well width can change the wavelength of the emission so a certain amount of control can be utilised over the output, i.e. the band-gap between the lowest sub-band in the conduction band and highest sub-band in the valence band is approximately inversely proportional to the well width. The introduction of additional quantum well layers and variations in width can also change the carrier confinement. For instance, the lowest sub-band in the conduction band of a narrow well is usually higher than that in a wider well, making recombination between bands less likely (due to the weaker overlap between wavefunctions) and increasing the probability of carriers leaking out of their respective wells.

2.2.6 Density of states

Electrons in a semiconductor material occupy certain "allowed states". To determine the number of such states the density of states function is used. This concept is very important in semiconductor theory, so a full derivation of the function is required. Consider an unconfined electron within a bulk crystal of dimensions L_x, L_y and L_z with the boundary condition that its wavefunction must tend to zero at the edges of the crystal. It can then be shown that the discrete set of **k** vector states that the electron can have can be represented by [1]

$$\mathbf{k} = n_x\mathbf{K}_x + n_y\mathbf{K}_y + n_z\mathbf{K}_z \tag{2.17}$$

where $|\mathbf{K}_i| = \pi/L_i$ and the n_i's are the quantum numbers of the system. In this bulk material the total volume of states in k-space with a value less than some constant value of k is given by a sphere of radius k and volume V_k. The volume of k-space occupied by a single **k**-vector is given by a cube of volume V_s. The total number of states can then be written as

$$N_s = \frac{V_k}{V_s} = \frac{\left(4\pi k^3/3\right)}{\left(2\pi/L\right)^3} = \frac{L^3 k^3}{6\pi^2} \tag{2.18}$$

where $L = L_x L_y L_z$. If the density of **k** vector states is known throughout all of *k*-space, then the total number of **k** vector states per unit volume of the crystal, or density of states, is given by

$$\rho(k) = \frac{1}{V}\frac{dN_s}{dk} = \frac{k^2}{2\pi^2} \tag{2.19}$$

where V is the volume of the crystal. The equation is usually required as a function of energy. Using the relation [1]

$$\rho(E)dE = \rho(k)dk \rightarrow \rho(E) = \frac{\rho(k)}{dE/dk} \tag{2.20}$$

it is possible to transform equation (2.19) into energy space. So, for a bulk semiconductor material with parabolic energy bands the density of states function for free electrons about an energy level E is given by

$$\rho(E) = \frac{\sqrt{E}}{4\pi^2}\left(\frac{2m^*}{\hbar^2}\right)^{3/2}. \tag{2.21}$$

When plotted, the equation gives rise to the curve displayed in fig. 2.7(a) indicating that more states are available at the higher energy levels.

In the case of a quantum well structure, the length in the *x*-direction is reduced significantly, i.e. $L_x << L_y L_z$. This results in a modified volume for all **k** states with the component in the *x*-direction, i.e. k_x, forming discrete steps in *k*-space. For each step, or sub-band, the total volume is now represented by a circle of radius *k*, resulting in the following expression for the total number of states

$$N_s = \frac{\pi k^2}{\left(2\pi/L\right)^2} = \frac{L^2 k^2}{4\pi}. \tag{2.22}$$

Following the same procedure as for the bulk case the total number of **k** vector states per unit volume for this modified crystal is given by

$$\rho(k) = \frac{1}{V}\frac{dN_s}{dk} = \frac{k}{2\pi L_x} \tag{2.23}$$

which is transformed into the following equation in terms of energy

$$\rho(E) = \frac{m^*}{2\pi\hbar^2}\left(\frac{1}{L_x}\right) \tag{2.24}$$

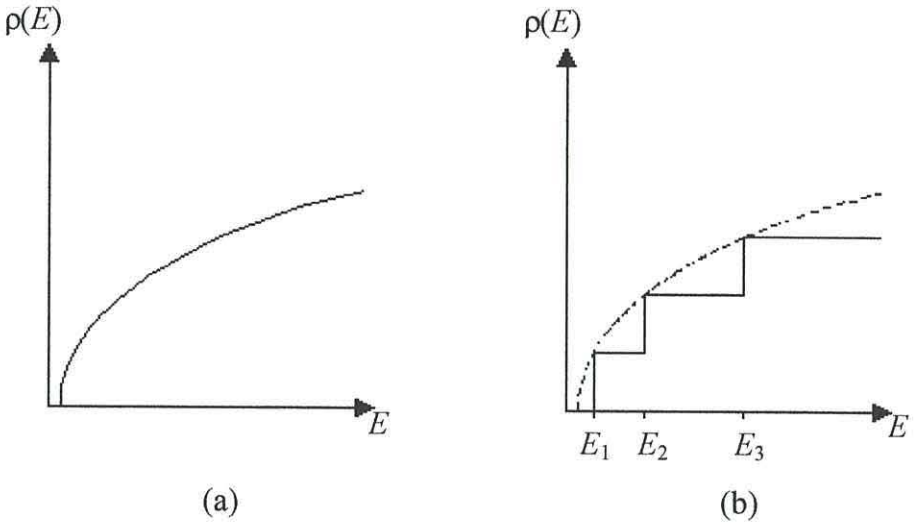

Fig. 2.7 *Density of states versus energy curves for (a) bulk and (b) quantum well structures.*

(similar expressions can be derived for structures with higher dimensional confinement). The density of states equation for a single sub-band is therefore given by

$$\rho_i(E_i) = \frac{m_i^*}{2\pi\hbar^2}\left(\frac{1}{L_x}\right). \tag{2.25}$$

where E_i is the confined particle energy level in the i^{th} sub-band as the function is independent of energy within any one sub-band (unlike the bulk case). Fig. 2.7(b) illustrates how equation (2.25) results in a step-like function as opposed to the continuous curve for the bulk case. This is due to the quantization of the energy levels, as displayed in fig. 2.6(inset).

The number of carriers injected into states at an energy E can now be calculated. Using the probability of occupancy at a specific energy level (as given by equation (2.5)) multiplied by the density of states for that energy results in an expression for the carrier density within the band. For example, if the density of electrons in the conduction band is required the following expression is used

$$n_c = \int_{E_c}^{\infty} \rho_n(E) f_c(E) dE . \tag{2.26}$$

where $f_c(E)$ is the probability of the conduction band state being occupied. Similarly, the density of holes in the valence band is given by

$$p_v = \int_{-\infty}^{E_v} \rho_p(E) f_v(E) dE \tag{2.27}$$

where $f_v(E)$ is the probability of a vacant state in the valence band. Assuming charge neutrality (equation (2.7)) it is possible to calculate the electron and hole quasi-Fermi levels from the number of injected carriers. For a bulk material equations (2.26) and (2.27) are solved numerically. In a quantum well structure, equation (2.26) may be simplified to give the following expression

$$n_c = \sum_i \frac{k_B T m_e}{\pi \hbar^2 L_x} \ln\left[1 + \exp\left(\frac{E_{fc} - E_i}{k_B T}\right)\right] \tag{2.28}$$

where E_i is now the sub-band edge energy. This expression may be used to calculate the number of holes in a specific valence band by substituting values for the hole mass and valence Fermi-level.

2.2.7 Strained quantum wells

Early work involving semiconductor heterostructures combined cladding and active layer materials of the same crystal structure and nearly the same lattice constants. As a result defect free films are formed, thus avoiding unwanted non-radiative recombination centres. In the mid 1980's research by Adams [4], and independently by Yablonovich *et. al.* [5], combined materials of different lattice constants to form strained layer structures; yielding some desirable opto-electronic properties.

Growing a quantum well layer of different lattice constant to the surrounding barrier material forces the well layer to either compress or enlarge in order to match the barriers lattice spacing. If the quantum wells lattice constant, a_l, is greater than the surrounding lattice constant, a_s, the quantum well lattice will compress in the plane, giving a structure under compressive strain, as shown in fig. 2.8(a). In an attempt conserve its volume the lattice also becomes elongated in the direction normal to the plane. If the opposite is true, i.e. $a_l < a_s$, then the quantum well is said to be under tensile strain, as shown in fig. 2.8(b). However, it must be stressed that only certain

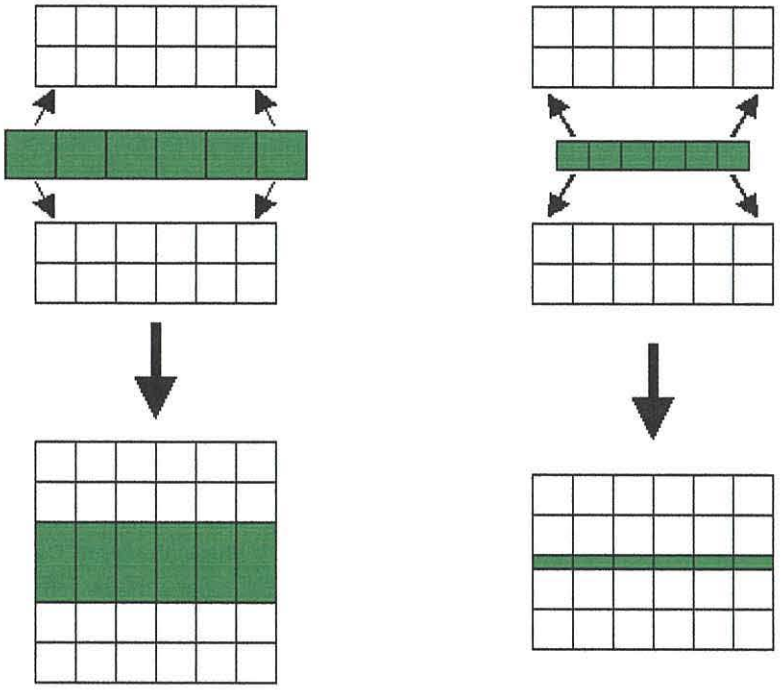

Fig. 2.8 *Crystal lattice deformation resulting from (a) compressive ($a_l > a_s$) and (b) tensile ($a_l < a_s$) strain.*

lattice mismatches are of use. Indeed, the lattice mismatch has a limit beyond which the strained lattice will revert back to its native state, causing large amounts of lattice defects and device failure.

Under both kinds of strain the band structure is affected. Assuming a material with an unstrained band-gap of E_{unstr}^{bg}, the bulk energy band-gap between the heavy-hole and the conduction band, $E_{str}^{C,HH}$, when influenced by strain is given by

$$E_{str}^{C,HH} = E_{unstr}^{bg} + \delta E_H - \delta E_S . \tag{2.29}$$

The energy separation between the light-hole and conduction band, $E_{str}^{C,LH}$, when under strain is given by

$$E_{str}^{C,LH} = E_{unstr}^{bg} + \delta E_H + \delta E_S - (\delta E_S)^2 / 2\Delta_0 . \tag{2.30}$$

The term, δE_H, named hydrostatic-pressure shift, affects only the unstrained band-gap and is defined by

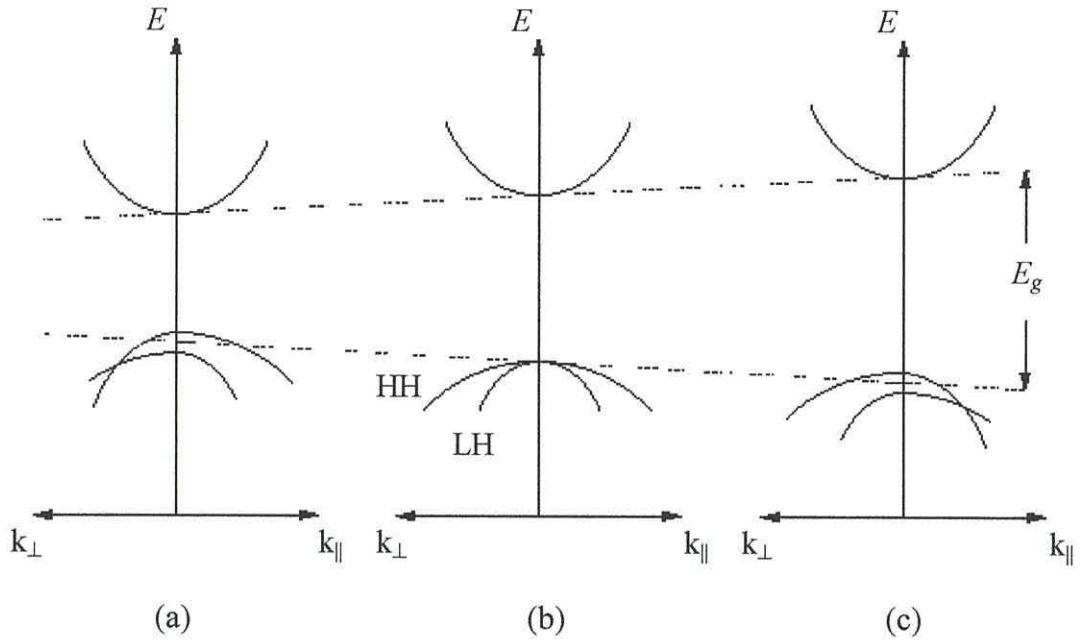

Fig. 2.9 *The changes in band-structure and the associated heavy- and light-hole sub-bands resulting from (a) tensile strain, (b) no strain and (c) compressive strain.*

$$\delta E_H = 2a\left[(C_{11} - C_{12})/C_{11}\right]\varepsilon . \tag{2.31}$$

The uniaxial stress induced valence band splitting, δE_S, is given by

$$\delta E_S = b\left[(C_{11} + 2C_{12})/C_{11}\right]\varepsilon \tag{2.32}$$

where the parameters a and b are the interband hydrostatic pressure and uniaxial deformation potentials, respectively. The term, ε, gives the amount of strain as defined by

$$\varepsilon = \frac{a_s - a_l}{a_l} . \tag{2.33}$$

The elastic-stiffness constant of the quantum well layer is denoted by C_{11} and C_{12} represents the elastic-stiffness constant of the substrate.

As is shown in fig. 2.9, the introduction of strain changes the band structure of the material. Under tensile strain, the hydrostatic component of the tension reduces the band-gap. The axial component splits the degeneracy of the valence bands and introduces an anisotropic structure, with the highest band being light along the strain axis, $k_\perp$, and comparatively heavy perpendicular to the strain axis, $k_\parallel$. When the well

layer is compressed the band-gap is increased, whilst the degeneracy of the valence band splits in a somewhat different manner. In this case the valence band splitting is reversed, resulting in the highest band being heavy along the strain axis, $k_{\perp}$, and the light in the perpendicular direction, $k_{\parallel}$.

For an unstrained structure, the energy levels associated with both heavy- and light-hole valence bands is the same due to the degenerate nature of the band structure. The heavy-hole band has a higher associated effective mass, so the resulting heavy-hole sub-bands occupy the deepest states within the well. When strain is introduced the valence band splitting results in two separate energy levels associated with the heavy- and light-hole bands. In the case of tensile strain the resulting quantum well structure increases the influence of the light-hole sub-bands, therefore increasing the amount of carriers required for gain. For a compressively strained active region the removal of the degeneracy splits the light and heavy-hole sub-bands even further than the unstrained case. This results in favourable conditions for low threshold current operation as there are less redundant sub-bands to inject carriers into with the uppermost heavy-hole band becoming light-hole like in the plane of the strained layer. When strain is introduced a number of characteristics are therefore affected. The change in band-gap will naturally influence the wavelength of the emitted light, whilst the changes in the valence band affects the density of states and the differential gain offered by the quantum well structure.

To calculate the sub-band energies for a strained layer quantum well the effective mass must be that perpendicular to the strained layer. For the calculation of the density of states (and therefore the gain and spontaneous emission, as will be shown later) the following in-plane masses are used

$$m_{hh}^{in-plane} = \left(\frac{\hbar^2}{2}\right)(\gamma_1 + \gamma_2)^{-1} \tag{2.34}$$

$$m_{lh}^{in-plane} = \left(\frac{\hbar^2}{2}\right)(\gamma_1 - \gamma_2)^{-1} \tag{2.35}$$

where γ_1 and γ_2 are known as Luttinger parameters [6] and are related to the heavy and light hole effective masses perpendicular to the well, m_{hh}^{perp} and m_{lh}^{perp}.

2.3 Gain in semiconductor heterostructures

2.3.1 Methods of recombination

The operation of almost all opto-electronic devices is based on the creation and annihilation of electron-hole pairs. Any photon that is incident on a semiconductor, which can impart energy at least equal to the band-gap energy, will create pairs. Within the crystal lattice this process is equivalent to breaking a covalent bond. For the highest probability of recombination a direct band-gap material is used. The creation and annihilation of pairs is dominated by three processes: spontaneous emission, stimulated emission and absorption. Spontaneous emission occurs randomly within the diode. Electrons from the conduction band cross the band-gap at random (to the valence band), releasing energy in the form of photons. A high proportion of the photons that are emitted in this manner are out of phase with one and other and the spectral output is fairly wide. This type of emission does not require the presence of any electromagnetic energy.

Stimulated emission requires a photon to stimulate the transmission of an electron from the conduction band to the valence band. When this happens, in order to conserve energy, the electron releases an identical photon that is in phase and of the same energy as the stimulating light packet. This results in photon emission of very narrow frequency range. As well as making stimulated transitions in the downward direction electrons may gain energy and cross the band-gap in the opposite direction as well, i.e. from the valence to conduction band. This process is known as absorption and requires the electron to absorb the energy of a passing photon in order to traverse the band-gap. When the number of downward transitions exceeds the number of upward transitions gain is achieved. This is of fundamental importance in laser theory.

In general, the recombination mechanisms can be thought of as being radiative and non-radiative. Radiative transitions, i.e. those described above, give rise to excess energy being dissipated as photons. The more undesirable non-radiative recombination is usually caused by crystal defects, causing unwanted recombination traps to form within the lattice giving energy that is usually imparted to phonons and

dissipated as heat. Taking R_r to be the radiative recombination rate and R_{nr} as the rate of non-radiative recombination the total recombination rate is given by

$$R_{total} = R_r + R_{nr}. \tag{2.36}$$

Both processes have an associated carrier lifetime, giving the average time that a carrier can exist before recombining radiatively or non-radiatively within a particular material. The total lifetime is therefore given by

$$\frac{1}{\tau_{total}} = \frac{1}{\tau_r} + \frac{1}{\tau_{nr}}. \tag{2.37}$$

2.3.2 Fermi's golden rule

Photon induced transitions therefore form the basis of semiconductor laser theory. The interaction of the electromagnetic wave and an electron may be incorporated into the Schroedinger equation, i.e. equation (2.1), via a new operator

$$H = H_0 + H_1(\mathbf{r}) \tag{2.38}$$

where H_0 is the Hamiltonian described by equation (2.1). The time-dependent perturbation term is given by

$$H_1(\mathbf{r}) = \left(\frac{e}{m_0}\right) A(\mathbf{r})\hat{\mathbf{e}} \cdot \mathbf{p} \tag{2.39}$$

where A is the vector potential of the electromagnetic radiation and $\hat{\mathbf{e}}$ is the unit polarisation vector in the direction of A. Using this new perturbed operator in the Schroedinger equation it is possible to derive an approximate expression for the transition rate of an electron from the conduction band state, ψ_e, to a particular valence band state, ψ_h. The equation is known as Fermi's golden rule and is given by

$$W_{e\to h} = \frac{2\pi}{\hbar}|H_{eh}|^2 \delta(E_e - E_h - \hbar\omega) \tag{2.40}$$

where

$$H_{eh} \equiv \langle \psi_h | H_1(\mathbf{r}) | \psi_e \rangle = \int_V \psi_h^* H_1(\mathbf{r}) \psi_e d^3\mathbf{r}, \tag{2.41}$$

E_c and E_v represent the energies of the electron and hole states whilst the delta function, δ, indicates that conservation of energy is enforced when a photon causes a transition.

Fermi's golden rule offers an expression for the transition rate between a single pair of conduction and valence band states. However, from the discussion involving the density of states it is known that there exist many k states in both conduction and valence bands. Equation (2.40) must therefore be summed over all allowed transition pairs to find the total transition rate. Assuming strict **k**-selection rules for all optical transitions, i.e. only carriers with the same k value may recombine, by considering a state in the conduction band one already knows which state in the valence band it recombines with. This allows a single density of states function to be used to describe the number of allowed transitions, as opposed to one for the conduction band and one for the valence band. For bulk semiconductor crystals, this reduced density of states function is given by

$$\rho_{red}(E_{tr}) = \frac{(E_{tr} - E_{sep})^{1/2}}{4\pi^2}\left(\frac{2m_r}{\hbar^2}\right)^{3/2} \tag{2.42}$$

where $E_{tr} \equiv E_e - E_h$ is the transition energy and $E_{sep} \equiv E_c - E_v$ is the energy separation between the conduction and valence sub-band edges. The reduced mass, m_r, is used to determine the individual energies that are related to the transition energy [1]. An analogous equation for a quantum well is given by

$$\rho_{red}(E_{tr}) = \frac{m_r^{qw}}{2\pi\hbar^2}\left(\frac{1}{L_x}\right) \tag{2.43}$$

where m_r^{qw} is a new reduced mass, specific for such a quantum confined structure.

Using equations (2.26) and (2.27) it is now possible to calculate the density of carriers in the various bands. In response to a flux of photons the total downward transition rate is given by

$$W_{c\to v} = \frac{2\pi}{\hbar}|H_{eh}|^2 \rho_{red} f_c f_v . \tag{2.44}$$

The transition rate of the reverse process, i.e. an electron transition from the valence band to the conduction band, is given by

$$W_{v\to c} = \frac{2\pi}{\hbar}|H_{eh}|^2 \rho_{red}(1 - f_c)(1 - f_v) \tag{2.45}$$

where the Fermi-functions have changed to reflect the probability of an electron existing in the valence band and a hole in the conduction band.

2.3.3 Transition matrix element

To evaluate Fermi's golden rule in its entirety equation (2.41) must be evaluated. Substituting the wave function approximation, i.e. equation (2.2), into equation (2.41) gives the following expression

$$|H_{eh}|^2 = \left(\frac{eA_0}{2m_0}\right)^2 |M_T|^2 \tag{2.46}$$

where

$$|M_T|^2 \equiv \left|\langle u_v|\hat{\mathbf{e}}\cdot\mathbf{p}|u_c\rangle\right|^2 \left|\langle F_h|F_e\rangle\right|^2 \tag{2.47}$$

is known as the transition matrix element, an important factor that determines which transitions are allowed within a particular structure, so will be looked at carefully during the remainder of this section.

Now the $\left|\langle F_h|F_e\rangle\right|$ term is the overlap integral of the envelope function and is used to specify which transitions between the conduction and valence band states are allowed. For the case of a bulk semiconductor crystal the slowly varying envelope functions given by

$$F(\mathbf{r}) = \frac{1}{\sqrt{V}} e^{i\mathbf{k}\cdot\mathbf{r}} \tag{2.48}$$

are the same for the conduction and valence band states. The overlap integral for any two states is therefore unity, so there exists an equal probability of a transition between the conduction band and any one of the valence bands.

In the case of a quantum well structure the transition probabilities are somewhat different due to the introduction of sub-bands. Consider the transition of carriers in an infinite quantum well, from a conduction band state with quantum number n_c to a valence band state with quantum number n_v, as displayed in fig. 2.10. Now for this infinite quantum well structure the envelope functions are independent of the carrier effective mass and also form an orthogonal set of functions. Transitions are allowed when the envelope functions of both states are equal, resulting with an overlap integral equal to unity. In this particular structure the envelope functions are equal when $n_c=n_v$, so transitions are forbidden when the converse is true, i.e. $n_c\neq n_v$. For quantum wells with finite barriers the envelope functions become a weak function

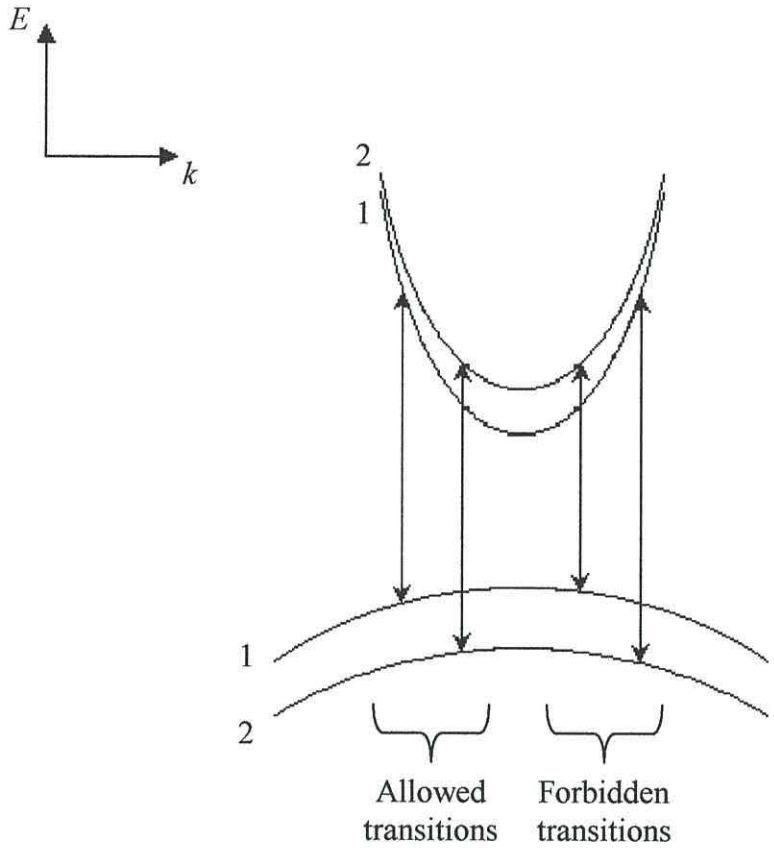

Fig. 2.10 *Allowed and forbidden transitions between two of the conduction and valence sub-bands in a quantum well.*

of effective mass. This results in a slight variation with a small probability of forbidden transitions occurring and a small probability of allowed transitions not occurring. However, this probability is very small.

The other part of the transition matrix, i.e. $\left|\langle u_v|\hat{\mathbf{e}}\cdot\mathbf{p}|u_c\rangle\right|$, is related to the Bloch function, $u(\mathbf{r})$. This element considers the polarisation of the radiation that interacts with the carriers. When evaluated this factor can be reduced to give the following expression for the transition matrix element [1]

$$|M_T|^2 = 2|M|^2 \alpha_{pol} \times |\langle F_h|F_e\rangle|^2 \tag{2.49}$$

where α_{pol} considers all polarisation's for a specified valence band and the factor of two takes into account all possible spin combinations. For a bulk material the basis

function momentum matrix element, $|M|$, can be obtained by relating it to the curvature of the conduction band and is given by [7]

$$|M|^2 = \left(\frac{m_0}{m^*} - 1\right)\frac{(E_g + \Delta)}{2(E_g + 2\Delta/3)} m_0 E_g \tag{2.50}$$

In such a material α_{pol} has a value of 1/3 for each band in each polarisation. The envelope function condition for allowed transitions is represented by $\left|\langle F_h | F_e \rangle\right|^2 = 1$ (as described above). The transition matrix element is then given by

$$|M_{TB}|^2 = \frac{1}{3}\left(\frac{m_o}{m^*} - 1\right)\frac{(E_g + \Delta)}{(E_g + 2\Delta/3)} m_0 E_g . \tag{2.51}$$

For a quantum well structure the basis matrix and the value for α_{pol} are different [1]. This is a consequence of the quantum confinement restricting the *k*-vector to lie on a circle around the k_x axis, resulting in only one TE component as TE_y=TE_z. With the overlap integral equal to unity, the quantum well matrix element is then given by

$$|M_{TQW}|^2 = 2|M|^2 \alpha_{pol} \tag{2.52}$$

where α_{pol} is given in reference [1] for the two different polarisation's. These matrix element equations can now be used in Fermi's golden rule to estimate the transition probabilities between the conduction and valence bands (and vice-versa).

2.3.4 Gain and spontaneous emission rates

Equations (2.44) and (2.45) give an estimate of the number of downward and upward transitions that occur within the semiconductor in response to an incoming flux of photons. If the number of photons being generated via downward transitions exceed the number being absorbed through upward transitions, the net increase in photons is given by

$$Net_{c\to v} = W_{c\to v} - W_{v\to c} . \tag{2.53}$$

Optical gain is defined as the fractional increase in the number of photons per unit length moving through a sample. Now the photon flux may be given by [1]

$$\Phi(\omega) = \frac{1}{\hbar\omega}\left(\frac{c}{n_g}\right)\left[\frac{n n_g \varepsilon_0 \omega^2 A_0^2}{2}\right] \tag{2.54}$$

where n denotes the refractive index of the crystal, n_g the group refractive index and ε_0 the permittivity of free space. So, by using equations (2.44), (2.45) and (2.54) the following expression for gain may be derived [1]

$$g(\hbar\omega) = \frac{Net_{c\to v}}{\Phi}$$

$$= \left(\frac{1}{\hbar\omega}\right)\frac{\pi e^2\hbar}{\varepsilon_0 c m_0^2 n}|M_T|^2 \rho_{red}(\hbar\omega)(f_c + f_v - 1) \tag{2.55}$$

Equation (2.55) only considers two stimulated transition processes, i.e. stimulated emission and absorption. However, as was explained earlier, there exists a third transition mechanism that doesn't require any photon interaction whatsoever. This spontaneous emission gives rise to downward transitions, thus releasing photons, and occurs randomly within the crystal. The process may be represented by the product of the downward transition rate, $W_{c\to v}$, and the number of modes within a given energy range, defined by [1]

$$\rho_{opt}(\hbar\omega) = \frac{1}{\pi^2}\frac{n^2 n_g}{(\hbar c)^3}(\hbar\omega)^2. \tag{2.56}$$

This results in the following expression [1]

$$R_{sp}(\hbar\omega) = \left(\frac{1}{\hbar\omega}\right)\frac{\pi e^2\hbar}{\varepsilon_0 m_0^2 n n_g}|M_{av}|^2 \rho_{red}(\hbar\omega) f_c f_v \tag{2.57}$$

where $|M_{av}|^2$ is the average strength of the transition matrix element over all three polarisations.

2.3.5 Many-body effects

The gain and spontaneous emission equations assume that the only way electrons and holes may change state is through interactions with photons. However, other factors must be considered, in particular the effects associated with the interaction of the excited carriers in the semiconductor material. These "many-body effects" play a key role in determining the material gain characteristics of a semiconductor (especially in wide band-gap materials) [8-11]. A full description of the topic is beyond the scope of this thesis, however, an outline of these events will now be given.

There are three main effects associated with many-body interactions [8, 9]. The first mechanism that will be considered is band-gap narrowing, or

"renormalisation". The band-gap is related to the amplitude of the interatomic Coulomb potential. As the number of injected carriers is increased the potential is screened, thereby reducing the band-gap, with the magnitude of such effects being scaled by the strength of the Coulomb interaction, i.e. depends on the magnitude of the screening. As a result, the influence of this renormalisation increases with band-gap, so is an important factor when modelling lasers that emit at short wavelengths.

The second many-body effect is spectral broadening. Now the gain and spontaneous emission equations assume that the only way electrons and holes may change state is through interactions with photons. However, other factors must be considered, in particular the scattering of carriers with other carriers and phonons. This results in the carriers remaining in their states for a finite amount of time, so there is an associated broadening of the carrier states and therefore of any optical transitions involving that state. At low carrier densities the broadening energy increases with the carrier density, however, at higher carrier densities, the dependence on broadening is much weaker due to the screening of the carrier interactions.

The final process is Coulomb enhancement. Due to the mutual attraction between electron and holes, the probability of recombination is increased over that for independent particles, with the strength of the attraction being scaled by the "effective Rydberg" of the material ($\propto E_g$) [8, 9]. When the Coulomb attraction is strong bound electron-hole pairs, or excitons, are formed which are depicted by introducing "exciton levels" in the forbidden band that are separated from the conduction band by a binding energy. Many pairs are formed at low carrier densities and low temperatures when a strong Coulomb attraction exists with band to exciton transitions dominating the absorption spectrum. However, as the carrier density value is increased the exciton lifetime diminishes due to collisions with other particles allowing the degree of enhancement to be reduced.

From the outline described above it is apparent that many-body effects become more influential as the band-gap is increased [8-11]. In this thesis visible emitting laser diodes are considered, so it is very important to incorporate many-body effects in the gain and spontaneous emission equations. Now the absorption, α, i.e. negative gain, is related to the susceptibility, χ, through the equation [8]

$$\alpha(v) = \frac{4\pi v}{n_b c} \mathrm{Im}\{\chi(v)\} \tag{2.58}$$

where v is the field frequency, n_b is the background refractive index and c is the speed of light. The absorption spectrum can then be determined from the imaginary part of the optical susceptibility, given by [9]

$$\chi(\hbar\omega) = \sum_k d_k \chi_k \tag{2.59}$$

where

$$\left[\hbar\omega - E_{e,k} - E_{h,k} + i\hbar\gamma\right]\chi_k = \left(1 - f_{e,k} - f_{h,k}\right)\left[d_k + \sum_{k'} V_s(k-k')\chi_{k'}\right] \tag{2.60}$$

which is derived using the Hartree-Fock approximation, which is reasonable at high carrier densities and high temperatures. The electron and hole Fermi functions are represented by f_e and f_h, respectively, and V_s is the screened two-dimensional Coulomb potential within the single plasmon pole approximation. The momentum dependent optical transition matrix, which may be linked to $|M|$ [8, 9], is represented by d_k whilst $E_{e,k}$ and $E_{h,k}$ are the renormalised electron and hole energies at the momentum k. Setting the potential to zero in equation (2.60) gives the free carrier result where the Coulomb interaction is neglected. Using the above-mentioned equations to construct the gain spectrum enables one to assess how such interactions affect the spontaneous emission characteristics [8-11].

As will be shown later, many-body effects do have a significant influence on the performance of wide band-gap materials, giving rise to an exciton peak in the absorption spectrum at low temperatures and Coulomb enhancement and band-gap renormalisation in the gain spectrum at high carrier densities. To accurately model these interactions the gain/absorption calculations used in this thesis were generated using a simulation developed by Dr P. Rees [10, 11].

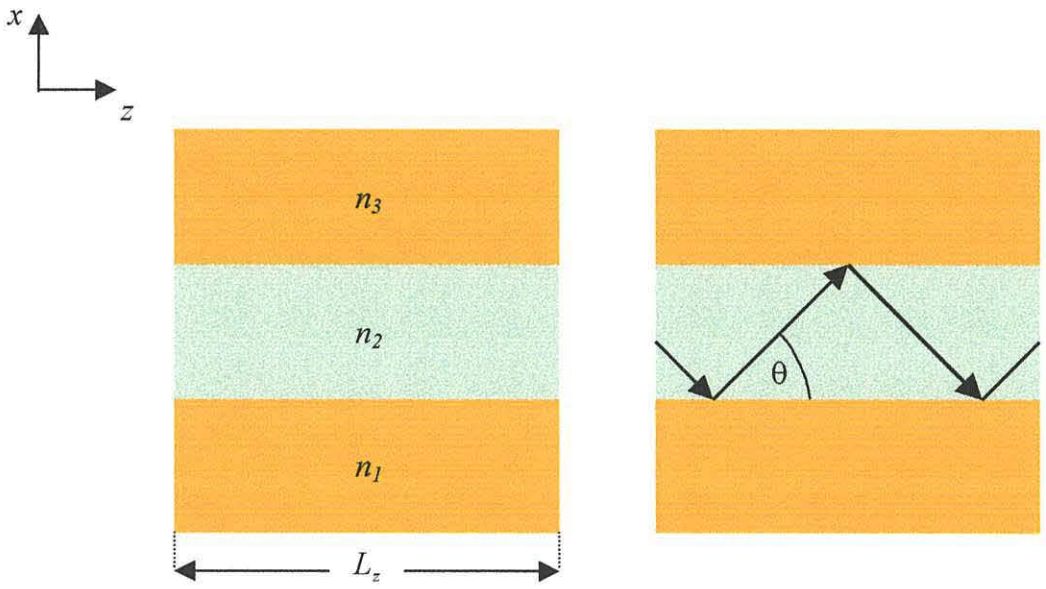

Fig. 2.11 *Dielectric waveguiding in a slab waveguide. (a) The refractive indices of a three-layer structure and (b) the ray trajectory of a guided wave displaying total internal reflection.*

2.4 Optical field propagation within the cavity

2.4.1 Waveguiding in the semiconductor laser

A laser consists of a gain medium placed within an optical cavity that provides the necessary feedback. Radiative recombination takes place within the active region giving an area where gain occurs (outside the active region losses dominate). Now that the recombination process has been discussed it is important to understand how a laser beam is amplified within an optical cavity.

Consider a two-dimensional slab waveguide structure of length L_z with refractive indices n_1, n_2 and n_3 as shown in fig. 2.11(a), such that $n_2 > n_1 \geq n_3$. The behaviour of the light depends on the angle of incidence, θ, as displayed in fig. 2.11(b). It follows from Snell's law that for total internal reflection at each interface the following must hold

$$\cos(\theta) \geq \frac{n_1}{n_2} \geq \frac{n_3}{n_2}, \tag{2.61}$$

showing that there exists a critical angle, θ_c, above which total internal reflection occurs.

For an oscillation to take place a standing wave pattern must arise within the cavity. In a slab waveguide structure the light is guided longitudinally as a zig-zag pattern, as shown in fig. 2.11(b). Ignoring phase changes due to reflections, the phase change after a round trip is given by

$$d\varphi = \frac{2\pi}{\lambda}(2L_z) \tag{2.62}$$

where λ represents the wavelength of the light. So, for laser oscillations to occur the following must hold

$$\frac{2\pi}{\lambda}(2L_z) = 2m\pi \tag{2.63}$$

or when simplified

$$L_z = m\lambda/2 \tag{2.64}$$

where m is an integer. Every value of m that satisfies this equation defines a longitudinal mode within the cavity. [*Note*: From now on the cavity length, L_z, will be denoted by L.]

The modes propagating in the cavity are three-dimensional and have components in the transverse and lateral directions as well as the longitudinal component described above. Using Maxwell's equations, these standing waves can be described by [12-14]

$$\nabla^2 \mathbf{E} = \mu_0 \varepsilon \frac{\partial^2 \mathbf{E}}{\partial t^2} \tag{2.65}$$

where **E** is the electric field vector, μ_0 denotes the vacuum permeability and ε represents the material permittivity. The modes propagating in the dielectric structure must therefore be solutions of this equation subject to the boundary conditions at the dielectric interfaces (note that a similar equation can also be derived for the magnetic field, **H**).

A semiconductor laser cavity supports two specific types off modes, known as transverse electric (TE) and transverse magnetic (TM), that are distinguished on the

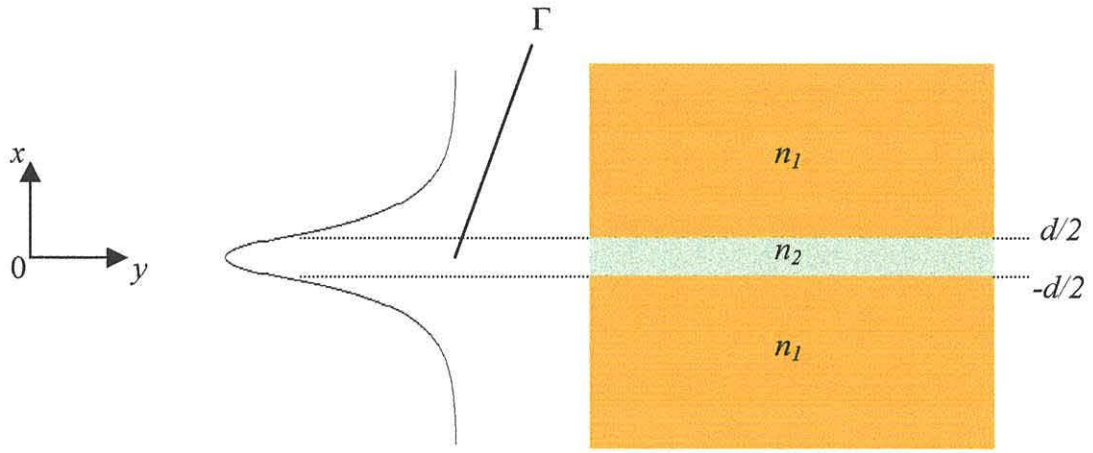

Fig. 2.12 *A three-layer symmetric slab waveguide with active layer width, d, and the corresponding transverse optical field profile.*

basis of their polarisation. The TE field describes the propagation of the electric field polarised along the junction plane whilst the TM field is the magnetic field polarised along the junction plane. The dominant polarisation is dependent on the design of the active region, e.g. TE emission is dominant in strained lasers under biaxial compression whilst TM gain is favoured in structures experiencing tensile strain [1].

2.4.2 Confinement factor calculations

It is usually desirable to be able to estimate the overlap of the optical field with the active region in the transverse direction, giving a value known as the confinement factor, Γ, as displayed in fig. 2.12. During this thesis compressively strained quantum wells will be used to generate gain/absorption in the active region. The single mode rate equations (derived in chapter 3) used to study the dynamics of the devices under investigation will assume that the optical field takes the form of the fundamental TE mode (TE_0). It is therefore the confinement factor of this transverse field profile that is required.

Consider a dielectric slab that is infinite in the y-direction such that $\delta/\delta y=0$. For TE waves $E_z=0$, so from Maxwell's equations it is possible to deduce that

E_x=H_y=0 [12-14]. The wave equation given by equation (2.65) can therefore be simplified for TE modes and rewritten as

$$\frac{\partial^2 E_y}{\partial x^2}+\frac{\partial^2 E_y}{\partial z^2}=\mu_0\varepsilon\frac{\partial^2 E_y}{\partial t^2} \tag{2.66}$$

which indicates that the field is dependent on the x and z co-ordinates and the time, t. Assuming that solutions are plane waves propagating in the z-direction, i.e. of the form

$$E_y(x,z,t)=E_y(x)\exp[j(\omega t-\beta z)]. \tag{2.67}$$

it is possible to reduce the wave equation to [12-14]

$$\frac{\partial^2 E_y}{\partial x^2}+\left(k_0^2 n^2-\beta^2\right)E_y=0 \tag{2.68}$$

where β is the propagation constant and ω represents the lasing frequency. The refractive index is given by n, k_0 is the wave number and $k_0^2 n^2=\omega^2\mu_0^2\varepsilon$. For a multi-layered waveguide, such as a semiconductor laser, solutions of equation (2.68) are therefore required for every layer with the electric field in the x-direction matching at the boundaries.

As was explained earlier, it is sufficient to calculate the field propagating in a simple three-layer symmetric slab waveguide, as displayed in fig. 2.12. The structure consists of an active layer of width d and refractive index n_2 embedded within a medium of smaller index, n_1, i.e. the cladding layers. For the analysis consider a structure that extends to infinity in the y- and z-directions. The TE_0 mode is therefore uniform in the y-direction and propagates in the z-direction. It is then required to obtain the solution for the fundamental mode from the wave equation, i.e. equation (2.68), subject to the boundary conditions that are offered by this particular waveguide.

A number of mathematical techniques have been developed to find the solution to this problem [15-20]. The most popular method involves using the effective index approximation [15-18]. This estimate uses the fact that the variation in the dielectric constant is much greater in the transverse (x) direction than the lateral (y) dimension. So, by varying the refractive index in the wave equation by $\delta n(x)$ a differential equation is constructed of the form [16]

$$\frac{\partial^2 \delta E_y}{\partial x^2} + \left(n^2(x) - n_{eff}^2\right)k_0^2 \delta E_y + \left(\delta n^2(x) - \delta n_{eff}^2\right)k_0^2 E_y = 0 \qquad (2.69)$$

which yields the field solutions. The effective refractive index for a particular solution is then linked to the propagation constant through the following equation

$$n_{eff}(z) = \beta\ (z)/k_0\ . \qquad (2.70)$$

Numerous equations have been derived to offer a simplified estimate of the effective index for various waveguiding structures [14, 18]. One investigation has led to the following equation for the effective index of the TE_0 mode within a symmetric three-layer slab waveguide [18]

$$n_{eff}^2 \approx n_2^2 - \left(\frac{1}{a}\right)\ln\left(1 + a\left(n_2^2 - n_1^2\right)\right) \qquad (2.71)$$

where $a = (k_0 d)^2 / 2$. This equation offers a small error which is adequate when the refractive index step between layers is reasonably large as the condition $n_2 > n_{eff} > n_1$ must be satisfied.

Using the effective index approximation combined with the wave equation allows the confinement factor to be calculated. Such an expression determines the overlap between the optical field and active layer and is given by [14]

$$\Gamma = \frac{\int_{d/2}^{d/2} E_y^2(x)dx}{\int_{-\infty}^{\infty} E_y^2(x)dx}. \qquad (2.72)$$

2.5 Threshold gain in a semiconductor laser

The structure of the laser diode using either bulk or quantum well heterostructures, can be grown using a semiconductor epitaxial growth technique. The wafer is then cut into individual lasers. This is achieved by scribing two parallel lines in one direction and cleaving along crystal planes perpendicular to the direction of these scribes, resulting in rectangular laser chips. The cleaved edges produce the smooth end mirrors or facets and the scribed edges are rough (which encourages the cavity to support just one lateral mode).

Lasing takes place when a sufficiently large current, known as the threshold current, is reached. At this point the round trip gain of the cavity equals the cavity losses. This threshold gain is given by [13]

$$G_{th} = \frac{1}{\Gamma}\left[\alpha_i + \frac{1}{L}\ln\left(\frac{1}{R}\right)\right], \tag{2.73}$$

where α_i represents the intrinsic loss caused by scattering and free electron absorption and R denotes the facet reflectivity. It is therefore evident that these cavity parameters can have a significant effect on the threshold characteristics of the laser device.

As one increases the injection, the semiconductor laser must first be driven hard enough to reach transparency, i.e. where gain=absorption. The current then has to be increased further until the gain required to overcome the cavity losses is reached. At this point lasing occurs and any further carriers injected recombine by very fast stimulated recombination, so the steady state populations become fixed and the spontaneous emission saturates at threshold.

2.6 Conclusions

The work in this chapter has introduced the basic theory required to understand the lasing process within a semiconductor laser. Having outlined important properties that encourage the creation and annihilation of electron-hole pairs within semiconductor materials, additional concepts such as quantum confinement and strain were discussed. These material properties were then studied in more detail, with a derivation of equations for the material gain and spontaneous emission within a semiconductor heterostructure. The propagation of an optical field within a dielectric medium was assessed then the material and optical properties were combined, leading to an equation for threshold gain within a semiconductor laser.

References

[1] P. Zory Jr., *Quantum Well Lasers*, Academic Press, 1993.

[2] G. Bastard, *Wave Mechanics Applied to Semiconductor Heterostructures*, Edition de Physique, Les Ulis, France, 1998.

[3] M. A. Reed, "Quantum dots," *Scientific American*, vol. 268 , pp. 118-123, 1993.

[4] A. R. Adams, "Band structure engineering for low threshold high efficiency lasers," *Electron. Lett.*, vol. 22, pp. 249-251, 1986.

[5] E. Yablonovich and E. O. Kane, "Reduction of lasing threshold current density by the lowering of valence band effective mass," *J. Lightwave Technol.*, vol. 4, pp. 504-506, 1986.

[6] E. P. O'Reilly and G. P. Witchlow, "Theory of the hole subband dispersion in strained and unstrained quantum-wells," *Phys. Rev. B*, vol. 34, pp. 6030-6033, 1986.

[7] E. O. Kane, "Band structure of indium antimonide", *J. Phys. Chem. Solids.*, vol. 1, p. 249, 1957.

[8] W. W. Chow, S. W. Koch and M. Sargent III, *Semiconductor Laser Physics*, Springer-Verlag, Berlin, 1994.

[9] H. Haug and S. W. Koch, *Quantum Theory of the Optical and Electronic Properties of Semiconductors*, World Scientific, Singapore, 1990.

[10] F. P. Logue, P. Rees, J. F. Heffernan, J. F. Donegan, C. Jordan, J. Hegarty, F. Hiei, and A. Ishibashi, "Effects of Coulomb enhancement on optical gain in (Zn, Cd)Se/ZnSe multiple quantum wells," *Phys. Rev. B, Condens. Matter*, vol. 54, pp. 16417-16420, 1996.

[11] P. Rees, F. P. Logue, J. F. Donegan, J. F. Heffernan, C. Jordan and J. Hegarty, "Calculation of gain-current characteristics in ZnCdSe-ZnSe quantum well structures including many body effects," *Appl. Phys. Lett.*, vol. 67, pp. 3780-3782, 1995.

[12] M. J. Adams, *An Introduction to Optical Waveguides*, Wiley, New York, 1981.

[13] H. C. Casey Jr. and M. B. Panish, *Heterostructure Lasers (Part A)*, Academic Press, 1978.

[14] G. P. Agrawal and N. K. Dutta, *Long-Wavelength Semiconductor Lasers*, Van Nostrand Reinhold, 1986.

[15] J. Buus, "The effective index method and its application to semiconductor-lasers," *IEEE J. Quantum Electron.*, vol. 18, pp. 1083-1089, 1982.

[16] J. K. Butler and D. Botez, "Mode characteristics of nonplanar double-heterojunction and large-optical-cavity laser structures," *IEEE J. Quantum Electron.*, vol. 18, pp. 952-961, 1982.

[17] S. W. Corzine and L. A. Coldren, *Diode Lasers and Photonic Integrated Circuits*, John Wiley and Sons, 1995.

[18] K. L. Chen and S. Wang, "An approximate expression for the effective refractive-index in symmetric DH lasers," *IEEE J. Quantum Electron.*, vol. 19, pp. 1354-1356, 1983.

[19] M. Munowitz and D. J. Vezzetti, "Numerical procedures for constructing equivalent slab wave-guides – an alternative approach to effective-index theory," *J. Lightwave Technol.*, vol. 9, pp. 1068-1073, 1991.

[20] R. E. Smith, S. N. Houde-Walter and G. W. Forbes, "Mode determination for planar waveguides using the four-sheeted dispersion relation," *IEEE J. Quantum Electron.*, vol. 28, pp. 1520-1526, 1992.

Chapter 3

Dynamics of self-pulsating laser diodes

3.1 Introduction

The purpose of this thesis is to investigate the suitability of different self-pulsating laser diodes for short wavelength operation, then attempt to optimise the structures for optical storage applications. The previous chapter described the basic material and optical properties required for successful lasing. The aim of this chapter is to give the reader an understanding of how self-pulsation can be achieved, including an insight into the mathematical methods that are used to model the dynamical properties of such lasers.

The chapter starts with a description of the evolution of the self-pulsating laser diode, outlining the methods that have been developed over the years to incorporate extra absorption into the cavity and therefore offer controllable self-pulsation. The two devices that will be investigated in this thesis, namely the real refractive index guided laser and laser diode with epitaxial absorber layers, are then described in more detail with a rate equation model derived for each device. These equations will be implemented in future chapters when they are used to study the suitability of the

above-mentioned lasers for optical storage applications. With this in mind a thermally activated leakage current equation is presented and included in the rate equation models in order to have a realistic estimate of the high temperature performance of either device. The chapter concludes with a more detailed description of the self-pulsation mechanism, offering an insight into the conditions that must be obeyed for self-pulsation to proceed.

3.2 The development of the self-pulsating laser diode

During the early years of semiconductor laser research, self-pulsation was seen as a deleterious effect. It was desirable to achieve *cw* emission, however, the poor fabrication processes on offer ensured vast amounts of defects, resulting in areas of saturable absorption and hence self-pulsation [1]. Fabrication techniques were therefore constantly being improved in an attempt to minimise the density of defects within these structures. As applications for pulsed emission became apparent methods of including controllable amounts of absorption into the cavity were investigated.

Probably the most popular of these early devices was the twin section laser [2-4]. This broad area double section laser was designed to intentionally create pulses by pumping currents into two sections such that one region is amplifying and the other absorbing. This is done when the amplifying section is biased above threshold and the absorber biased considerably below, resulting in a short absorber carrier lifetime as required for self-pulsation (see section 3.6). The twin section laser was therefore regarded as a very effective self-pulsating device; however, a more compact laser diode was required for commercial applications.

A number of single section lasers with controllable absorber regions were developed during the latter part of the 1970's [5-7]. A popular concept at the time involved creating a region of absorption using a method known as proton bombardment [6, 7]. By deliberately implanting protons into the structure centres of fast non-radiative recombination and saturable absorption are created. This gives rise to regions of high electrical resistance and low excitation, thus greatly reducing the radiative efficiency and carrier lifetime of emission, as required for self-pulsation. Although more compact than the twin section laser, the control over the saturable absorption and hence the self-pulsation characteristics isn't as reliable. The laser was

therefore not suitable for reproduction on a commercial scale, so the search went on for a more appropriate source of self-pulsation.

An alternative structure that came to fruition in the late 1970's was the narrow stripe laser diode [8]. Due to its use in CD systems, the laser has subsequently become the most commercially successful self-pulsating device. The cavity is designed to offer a weakly guided lateral optical field. Self-pulsation is achieved by ensuring that the lateral field extends beyond the central, electrically pumped, active region to the neighbouring unpumped region which acts as an absorber. As the stripe width increases, the amount of absorption decreases, thus offering excellent control over the absorber characteristics. Grown in the GaAs material system the device provides a cheap and simple method of achieving self-pulsation at 780 nm, hence the reasons why such laser diodes are used in CD players.

Unfortunately the self-pulsation mechanism offered by the narrow stripe laser does lead to some drawbacks. In particular, the performance of the device is restricted in that the absorber characteristics cannot be varied independently of the gain parameters as both absorption and gain are produced in the same epitaxial layers. This led to the development of the most recent self-pulsating structure, the laser diode with epitaxial absorber layers. Using the fabrication techniques that have allowed quantum confinement to be realised, this particular laser is constructed with an epitaxial absorber layer grown parallel to the active layer [9]. The absorber may be grown as a quantum well, providing the crystal grower with several design parameters, such as well width, height, number, etc... that can be varied to give optimum absorption. This laser is therefore the most advanced of all the self-pulsating devices, however, due to the fact that research is still being conducted into such structures the more well-developed narrow stripe laser diode is still, in general, the laser of choice.

The summary outlined above indicates that the two best methods of achieving compact, controllable self-pulsation involves using the narrow stripe laser and laser diode with epitaxial absorber layers. It is the emission of these two devices that will be investigated in the remainder of this thesis. The next two sections will therefore offer a more detailed description of each structure with a rate equation model derived for each device, thereby providing a method of evaluating the emission characteristics.

3.3 Narrow stripe laser diode

3.3.1 Gain-guiding devices

The narrow stripe laser diode is ideal for optical storage systems as it offers a cheap and efficient method of producing self-pulsation. The device is characterised by the planar and continuous nature of the active layer, resulting in a structure that is very easy to fabricate. As there is no lateral index guiding, the laser uses the area that is experiencing gain to guide the electromagnetic wave, and is suitably called a gain-guided laser. Unfortunately, high threshold currents and low differential quantum efficiency are a performance characteristic, a consequence of the small carrier induced refractive index changes within the cavity. This also gives rise to a movement of the optical mode along the junction plane.

Carriers enter the cavity through a stripe contact, as displayed in fig. 3.1. When current is injected through the stripe, the combined influence of carrier diffusion in the active region and current spreading creates a carrier density profile in the active layer. Since optical gain is a function of carrier density a gain profile is also established. The saturable absorption required for self-pulsation is then given by the interaction of the optical field with the loss region of the active layer in the lateral (y) direction. Pulsed output is emitted when the gain/absorption interaction is at a suitable level. A change in stripe width, W, varies the amount of absorption within the cavity. An element of control is therefore offered and an optimum cavity structure should be available that emits self-pulsation at the lowest possible injection current.

The optical field distribution in the transverse (x) direction is reasonably stable with the associated confinement factor, $\Gamma(x)$, only changing as one varies the configuration of wells in the active region. Optical confinement in the lateral direction isn't as straightforward. The electromagnetic field is guided by the area generating gain as it continually creates radiation to replace that lost to the outer, absorbing areas. This gain-guiding then confines the lateral mode to an area under the stripe. The diffusion of carriers during self-pulsation therefore changes the lateral refractive index profile, which subsequently adds a time dependency to the lateral component of the optical field, as shown in fig. 3.1(b). This factor must be carefully considered when modelling the device [10].

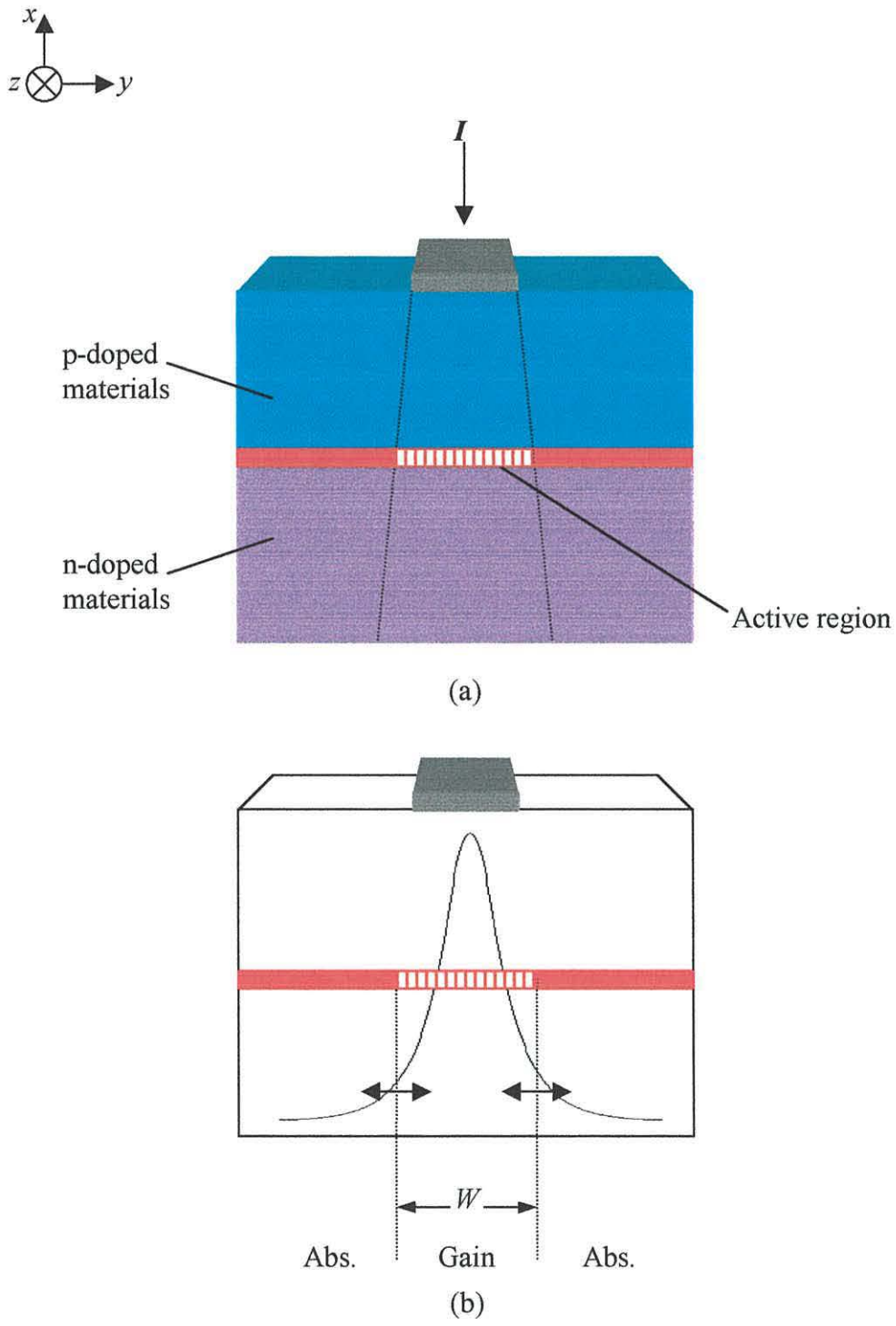

Fig. 3.1 *Schematic diagram of the narrow stripe laser showing time varying (a) carrier diffusion and (b) lateral optical field within the cavity.*

3.3.2 Derivation of the rate equation model

To calculate the dynamical properties of the narrow stripe laser diode a set of coupled rate equations are commonly used. The equations describe the exchange of energy between electrons and photons in the cavity by stimulated and spontaneous emission and absorption. These processes have been described earlier but a number of other events must be considered to give an accurate description of the amplification process. In general, the continuity equations for both electrons and holes should be considered, however, the two are related due to charge neutrality, so the consideration of the electron evolution is sufficient. Throughout this work only single mode emission will be considered, i.e. it is assumed that only the dominant TE_0 longitudinal mode propagates within the cavity.

For an accurate estimate of the dynamical properties of the narrow stripe laser it is important to consider the lateral diffusion of carriers. Two mathematical models are commonly used. One method uses a carrier density rate equation that includes a carrier diffusion term, coupled with a standard rate equation for photon generation [10, 11]. It is assumed that the carriers are confined in a uniform manner within the transverse (x) and longitudinal (z) dimensions of the active layer, whilst varying in density in the lateral (y) direction. The evolution of the lateral carrier density profile is then modelled by solving a partial differential equation, which subsequently allows the calculation of the photon density within the cavity.

The alternative method uses three rate equations that describe the evolution of the carrier densities in the gain section, absorber section and the photon generation, with the absorber volume being a function of stripe width. Two "diffusion terms" are included to model the carrier diffusion between the gain and absorber sections during emission [8]. The changing optical field is calculated continuously and entered into the simulation. This modelling technique will be applied in chapter 4, so a derivation of a set of coupled rate equations is required for this narrow stripe laser diode.

It is of use to start with equations that describe the time evolution of the number of carriers and photons in the cavity. Three are required, one representing the number of carriers that exist within the active region, another evaluating the number of carriers in the absorber section and the final equation denoting the number of photons being generated. Now, the two carrier number equations have the form [12]

change in carrier reservoir	=	carriers going in	-	carriers lost due to nr. & spon. recomb.	-	carriers gained/lost due to radiative recomb. & abs.	-	carriers lost due to leakage

whilst the photon number equation is defined by

change in carrier reservoir (photons)	=	carriers gained/lost due to abs. & radiative recomb.	-	photons lost	+	carriers gained due to spon. recomb.

By substituting the necessary values the following carrier number equations are generated

$$V_{qw}\frac{dN_{qw}}{dt}=\frac{I}{e}-\left(R_{qw}^{nr}+R_{qw}^{sp}\right)V_{qw}-(R_{qw}^{21}-R_{qw}^{12})V_{qw}-R_{qw}^{l}V_{qw} \tag{3.1}$$

$$V_{\alpha}\frac{dN_{\alpha}}{dt}=-\left(R_{\alpha}^{nr}+R_{\alpha}^{sp}\right)V_{\alpha}-(R_{\alpha}^{21}-R_{\alpha}^{12})V_{\alpha}-R_{\alpha}^{l}V_{\alpha} \tag{3.2}$$

$$V_{p}\frac{dS}{dt}=\left(R_{qw}^{21}-R_{qw}^{12}\right)V_{qw}+\left(R_{\alpha}^{21}-R_{\alpha}^{12}\right)V_{\alpha}-\frac{SV_{p}}{\tau_{s}}+R_{qw}^{sp}V_{qw}+R_{\alpha}^{sp}V_{\alpha} \tag{3.3}$$

where the subscripts qw and α represent values/processes within the active and absorber regions, respectively. The symbols V and N denote the volumes and carrier densities of the respective regions and V_p represents the volume occupied by the photons. The value S indicates the photon density generated within the structure whilst R denotes the rate of each process, for example R_{qw}^{21} represents the transition rate from band 2 (conduction band) to band 1 (valence band) in the active region. The photon lifetime, τ_s, is given by

$$\frac{1}{\tau_{s}}=v_{g}\left(\alpha_{i}+\frac{1}{L}\ln\frac{1}{R}\right). \tag{3.4}$$

where v_g, α_i, L and R denote the group velocity, intrinsic loss, cavity length and average facet reflectivity, respectively.

In addition to the transverse components the poor lateral carrier confinement must also be considered. To estimate the number of carriers that diffuse (laterally) out of the gain section (per unit time) the following equation is used [8]

$$V_{qw}\frac{dN_{qw\rightarrow\alpha}}{dt}=V_{qw}\frac{\left(N_{qw}-N_{\alpha}\right)}{T_{qw\rightarrow\alpha}} \tag{3.5}$$

where $T_{qw\to\alpha} = W^2/2D_n$ is a time constant with D_n denoting the material diffusion coefficient. Similarly, the number of carriers diffusing in the opposite direction during the same time period is given by [8]

$$V_\alpha \frac{dN_{\alpha\to qw}}{dt} = V_\alpha \frac{\left(N_\alpha - N_{qw}\right)}{T_{\alpha\to qw}} \tag{3.6}$$

where $T_{\alpha\to qw} = T_{qw\to\alpha}\left(V_\alpha/V_{qw}\right)$. Now the whole of the active region is continuously being pumped leading to a constant volume. This is not the case for the absorber as the time-dependent diffusion process changes its volume. Assuming a continuously varying lateral optical field an estimate for this volume may be calculated using the following equation [8]

$$V_\alpha = \frac{2dL}{\mathrm{Re}(\beta_2)} \tag{3.7}$$

where $\mathrm{Re}(\beta_2)$ represents the real part of the complex propagation constant within the active region.

Now, $R_{qw}^{21} - R_{qw}^{12} = v_g \times g(N_{qw}) \times S$ gives the photon generation due to stimulated radiative recombination in the active region where $g(N_{qw})$ represents the gain being generated in the active region. Similarly, the radiative recombination in the absorber section is given by $R_\alpha^{21} - R_\alpha^{12} = v_g \times g(N_\alpha) \times S$. The confinement factor, Γ, represents the fraction of the optical wave that exists in a specific region, as described in section 2.4.2. Substituting these values and the diffusion terms into the rate equations and dividing by the volumes results in the following carrier and photon density equations

$$\frac{dN_{qw}}{dt} = \frac{I}{eV_{qw}} - \left(R_{qw}^{nr} + R_{qw}^{sp}\right) - Sv_g g\left(N_{qw}\right) - R_{qw}^{l} - \frac{\left(N_{qw} - N_\alpha\right)}{T_{qw\to\alpha}} \tag{3.8}$$

$$\frac{dN_\alpha}{dt} = -\left(R_\alpha^{nr} + R_\alpha^{sp}\right) - Sv_g g\left(N_\alpha\right) - R_\alpha^{l} - \frac{\left(N_\alpha - N_{qw}\right)}{T_{\alpha\to qw}} \tag{3.9}$$

$$\frac{dS}{dt} = Sv_g \Gamma_{qw} g\left(N_{qw}\right) + Sv_g \Gamma_\alpha g\left(N_\alpha\right) - \frac{S}{\tau_s} + R_{qw}^{sp}\Gamma_{qw} + R_\alpha^{sp}\Gamma_\alpha \,. \tag{3.10}$$

A two-dimensional confinement factor is required due to the optical field consideration in both transverse and lateral directions. The confinement factor in the gain section is defined by $\Gamma_{qw}(x,y) = V_{qw}/V_p$ whilst a value for such an overlap factor

in the absorbing region is given by $\Gamma_\alpha(x,y) = V_\alpha / V_p$. The spontaneous emission generated in the absorber section, R_α^{sp}, is negligible so this term may be neglected. The photon density generated spontaneously in the gain section is given by βR_{qw}^{sp} where β is the fraction of the emission that enters the lasing mode. The carrier densities lost due to non-radiative recombination are denoted by $N_{qw,\alpha} / \tau_{qw,\alpha}$ where τ_{qw} and τ_α are the carrier lifetimes. Substituting these terms into the equations yields the following rate equation model

$$\frac{dN_{qw}}{dt} = \frac{J_{inj}}{e} - Sv_g g(N_{qw}) - \frac{N_{qw}}{\tau_{qw}} - \frac{J_{l,qw}}{e} - R_{qw}^{sp} - \frac{(N_{qw} - N_\alpha)}{T_{qw\to\alpha}} \tag{3.11}$$

$$\frac{dN_\alpha}{dt} = -Sv_g g(N_\alpha) - \frac{N_\alpha}{\tau_\alpha} - \frac{J_{l,\alpha}}{e} - \frac{(N_\alpha - N_{qw})}{T_{\alpha\to qw}} \tag{3.12}$$

$$\frac{dS}{dt} = Sv_g \Gamma_{qw} g(N_{qw}) + Sv_g \Gamma_\alpha g(N_\alpha) - \frac{S}{\tau_s} + \beta R_{qw}^{sp} \tag{3.13}$$

where J_{inj} represents the injection current density and J_l the leakage current density. By integrating equations (3.11)→(3.13) the time evolution of the carrier and photon densities within the cavity may be calculated. The three equations represent an initial value problem involving coupled first order differential equations and may be evaluated using the Runge-Kutta method [13].

3.3.3 Optical field estimate

To evaluate the rate equations in an accurate manner it is required to calculate the two-dimensional confinement factor, $\Gamma(x,y)$, as displayed in fig. 3.1. It is therefore necessary to calculate the optical field in two-dimensions as opposed to the one-dimensional system described in section 2.4.2. Assuming a single mode longitudinal component two methods may be used to evaluate the optical field.

The first estimate involves disregarding the $y\to\infty$ assumption that is made when evaluating the slab waveguide problem, leading to a scalar wave equation of the form [10]

$$\frac{\partial^2 E_y}{\partial x^2} + \frac{\partial^2 E_y}{\partial y^2} + \left(k_0^2 n^2 - \beta^2\right) E_y = 0. \tag{3.14}$$

The equation is then evaluated subject to boundary conditions in both lateral and transverse directions, yielding solutions for the modes propagating in the structure, allowing one to calculate a two-dimensional confinement factor.

Alternatively, the wave equation for a slab waveguide, i.e. equation (2.66), is considered separately in both directions, rotating the co-ordinates and assuming that the lateral dimension tends to infinity in both cases. This method yields mode components in both transverse and lateral dimensions, allowing one to calculate separate confinement factors for the TE_0 field. The two-dimensional estimate is then calculated using the equation [8]

$$\Gamma(x,y) = \Gamma(x)\Gamma(y). \tag{3.15}$$

As the field in the transverse (x) direction is reasonably stable this method is the easiest to implement.

In the lateral direction the field equation must be evaluated continuously for the case of a three-layer slab waveguide, taking the electrically pumped area as the active layer, yielding a time-dependent lateral confinement factor, $\Gamma(y)$. For an accurate estimate of the refractive index in the lateral direction complex notation must be used. Complex refractive indices of the form

$$n = n_{real} + in_{imag} = n_{real} + iK \tag{3.16}$$

enables dielectric waveguides composed of lossy media to be evaluated. The term K is known as the extinction coefficient and is caused by the absorption of radiation within the dielectric material. The value is calculated using the following equation

$$K = -\frac{\alpha}{2k_0} \tag{3.17}$$

where α is the attenuation coefficient per unit length and $k_0 = 2\pi/\lambda$ is the wave number. For a k-layered waveguide the refractive index of section j is given by [10]

$$n_j = n_{j,real} + n_{j,imag} = n_{j,0} + \alpha_p N_j(y) + \frac{g_j(N_j(y))}{2k_0} + iK_j \tag{3.18}$$

where $n_{j,0}$ is the bulk refractive index of layer j and α_p represents the free plasma coefficient [14]. The terms $N_j(y)$ and $g_j(N_j(y))$ denote the local carrier density and local gain, respectively, within the jth layer.

When the refractive index step between layers is small, as in the case of the

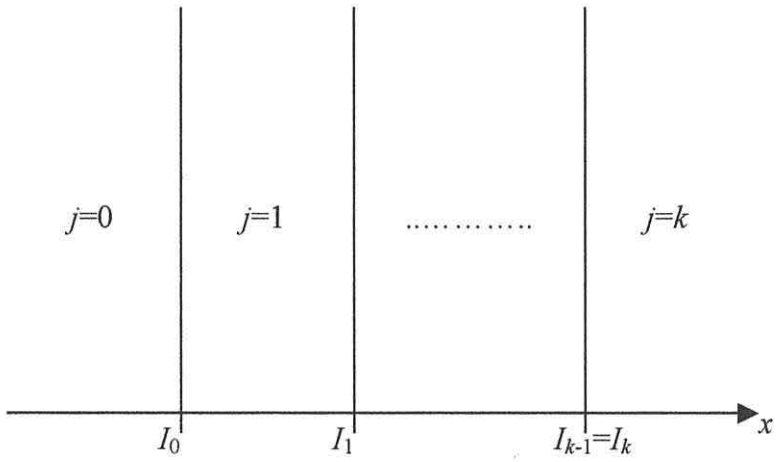

Fig. 3.2 *A multi-layered waveguide structure.*

lateral dimensions of a gain guided laser, the simple effective index estimate described in section 2.4.2, i.e. equation (2.71), becomes useless and a more thorough estimate of the optical field is required. Indeed, if the effective index approximation is used the error may be greater than the refractive index step resulting in numerous complications. So with this in mind, an alternative method of extracting solutions from the wave equation is required.

Consider a muti-layered dielectric waveguide, as displayed in fig. 3.2. By generalising equation (2.68), the TE field for the jth layer is described by

$$\frac{\partial^2 E_{y,j}(x)}{\partial x^2} + \left(k_0^2 n_j^2 - \beta^2\right) E_{y,j}(x) = 0 \tag{3.19}$$

where n_j is the complex refractive index of layer j. The propagation constant, β, may be used to determine the properties of the optical waves within the waveguide. A direct solution of the equation is difficult to obtain, so a general solution is used of the form

$$E_{y,j}(x) = A_j \exp\left(\left(x - I_j\right)\alpha_j\right) + B_j \exp\left(-\left(x - I_j\right)\alpha_j\right). \tag{3.20}$$

where I_j represents the interface of the jth layer as displayed in fig. 3.2, $\alpha_j = \sqrt{\beta^2 - k_0^2 n_j^2}$ and A_j and B_j are constants to be determined. It is therefore required to find a value for the propagation constant and a corresponding set of

coefficients α_j, A_j and B_j for which all field continuity conditions demanded by Maxwell's equations can be met at the layer interfaces, as described in appendix 1.

A popular method of solving such a problem involves constructing a matrix formulation, thus reducing the problem from $2N$ complex equations with $2N$ unknowns to a single complex equation with one complex unknown. The result is a single dispersion function whose zeros correspond to the propagation constants of the guided modes within the structure [15, 16], i.e.

$$m_{11}(\beta) = 0 . \tag{3.21}$$

A detailed description of the construction of such a formalism for a multi-layered waveguide is given in appendix 1. For example, a three-layered waveguide structure leads to the following dispersion relationship once the matrix has been multiplied out

$$m_{11}(\beta) = \left(1+\frac{\alpha_1}{\alpha_0}\right)\left(1+\frac{\alpha_2}{\alpha_1}\right)\exp(-\omega_1-\omega_2)+\left(1-\frac{\alpha_1}{\alpha_0}\right)\left(1-\frac{\alpha_2}{\alpha_1}\right)\exp(\omega_1-\omega_2) = 0 . \tag{3.22}$$

where $\omega_j = d_j\alpha_j$ and d_j represents the layer width. It is therefore the roots of this equation that yield solutions for the TE modes propagating within a three-layer waveguide.

When numerous modes exist, as displayed in fig. 3.3, a very powerful numerical technique can be used to extract all of the solutions using Cauchy integration and Riemann surfaces [15]. However, the short wavelength structures that are used in this thesis employ narrow active layers, so only a few lateral modes will propagate in the laser cavity. This allows a method developed by Schlereth and Tacke to be utilised [16], where the downhill method [17] is implemented to find the propagation constants. [*Note*: This method would be unsuitable (computationally inefficient) for multi-mode calculations.]

To find the roots of equation (3.21) using such a method requires an initial guess for the propagation constant, say β_0. This value may be calculated using equations (2.70) and (2.71), i.e. the propagation constant for the effective index of a symmetric waveguide with real refractive indices. For some predetermined value of Δ, the absolute square of the m_{11} matrix element is then evaluated, i.e.

$$F = |m_{11}|^2 , \tag{3.23}$$

for $\beta_0 \pm i\Delta$ and $\beta_0 \pm \Delta$. The value of β_0 that offers the smallest value of F is then chosen

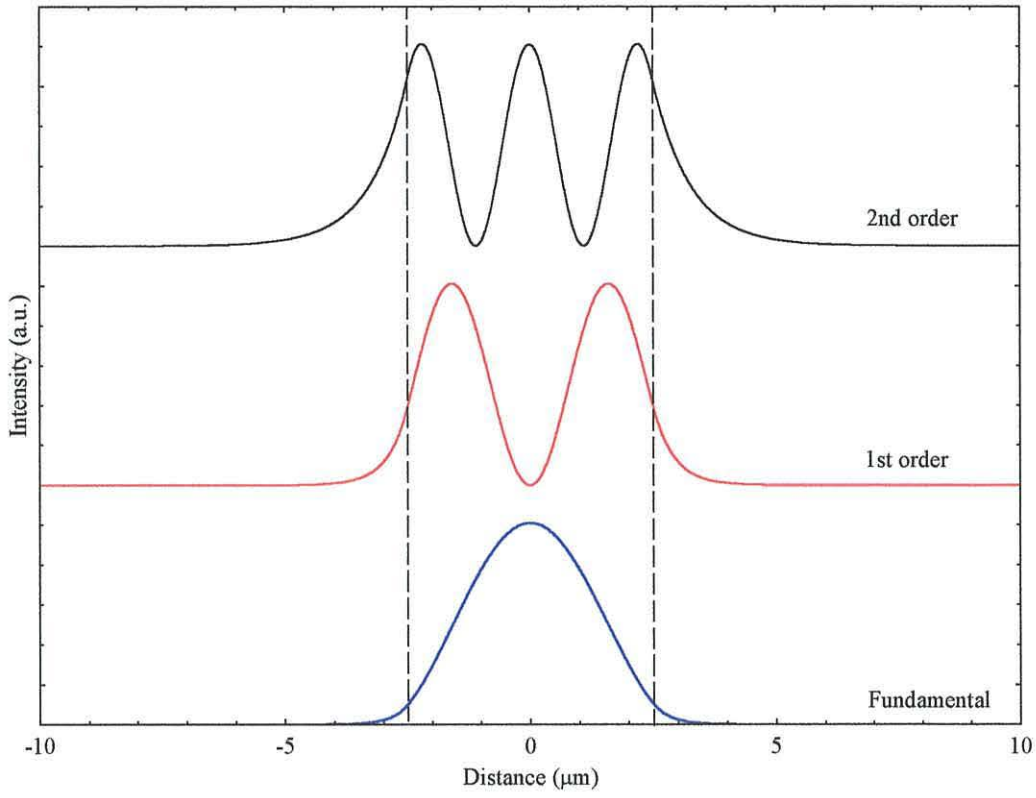

Fig. 3.3 *Intensity distribution for the fundamental, first and second order TE modes of a three-layer symmetric slab waveguide with a guiding layer thickness of 5 μm.*

as the next starting point. If the new starting point is the same as the old value then $\Delta=\Delta/2$. This process is repeated until some minimal value of Δ is found and it is the corresponding value of β that is chosen as the propagation constant. The field may then be plotted to determine which mode has been detected. If a mode higher than the fundamental is found, the program starts with a different initial guess until the TE_0 mode is discovered. Once the desired propagation constant is extracted a lateral confinement factor within the area of interest is calculated using equation (2.72). This estimate may then be entered into equation (3.15) to calculate a value for the two-dimensional confinement factor required for the rate equation analysis.

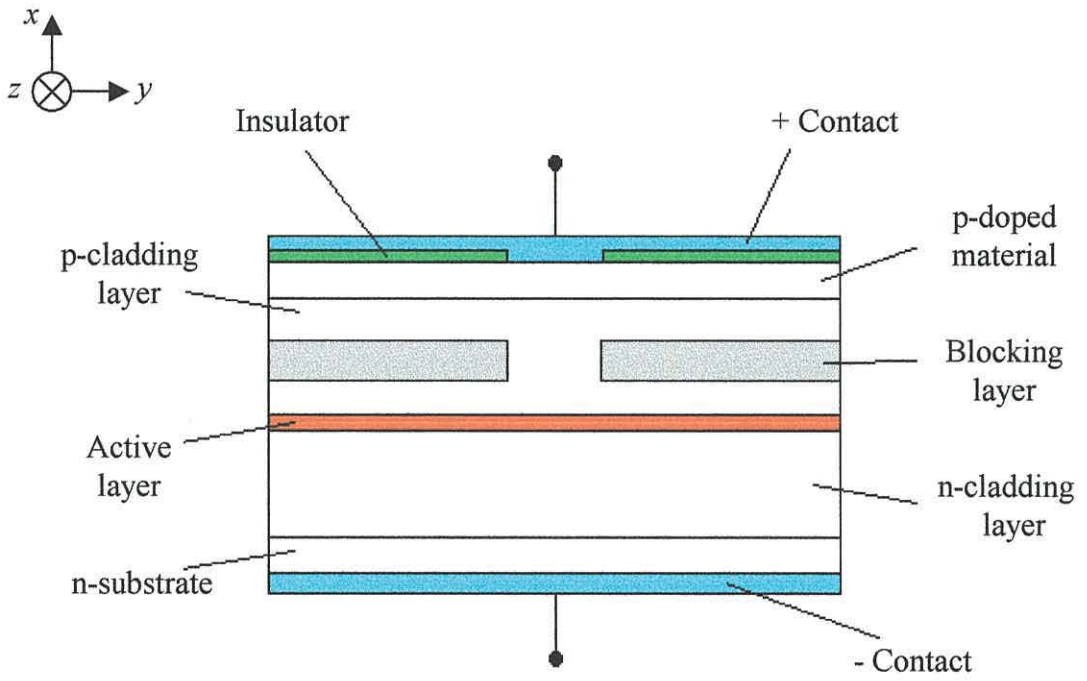

Fig. 3.4 *Schematic diagram of a ridge waveguide structure with current blocking layers.*

3.3.4 Real refractive index guided structure

Due to the poor confinement associated with a "purely" gain-guided laser, as one decreases the stripe width to achieve enough absorption for self-pulsation anti-guiding is frequently observed. This deleterious effect occurs when the carrier-induced lateral change in refractive index creates a scenario where the index in the absorbing region is greater than that in the gain section, creating a negative index step that cannot guide the lateral component of the optical field. As a result an unguided ray of light is emitted from the cavity. This carrier-induced effect is therefore particularly distinctive in gain-guided lasers due to the poor carrier confinement in the *y*-direction.

To avoid this problem a modified structure is required that offers a "built-in" lateral refractive index step such that the carrier-induced changes that occur during emission don't give rise to any anti-guiding. One method involves introducing current blocking layers into the p-doped cladding layer, as displayed in fig. 3.4, thereby creating a weakly index guided laser [18]. These layers are of different composition to both active and cladding regions. The resulting structure usually provides a sufficient built-in index step such that anti-guiding only becomes problematic in extreme

circumstances, e.g. very high operating currents. Other properties are also improved with a more stable transverse optical field being a notable benefit [19, 20]. For certain stripe widths self-pulsation is still attainable with the unpumped sections of the active layer, i.e. beneath the blocking layers, acting as an absorber [10, 11].

Depending on the material system being used the blocking layer material is usually designed to offer improvements in both carrier and optical confinement. Some structures use n-doped blocking layers of high refractive index (when compared with the remainder of the structure) which is optically absorbing at the lasing wavelength. Oscillations are favoured in the lateral fundamental mode, with high power emission also being observed [20]. For self-pulsation purposes a slightly different cavity design has been proposed [10, 11]. In such a structure the blocking layers are composed of a material of lower refractive index than the surrounding layers. Whilst still achieving sufficient carrier confinement this "real refractive index guided" device provides improvements in optical confinement resulting in stable transverse mode operation [10, 11, 19, 21]. Furthermore, the band-gap associated with the blocking layer material is wide, resulting in negligible optical loss, allowing high internal efficiency and low threshold currents.

This modified narrow stripe laser therefore offers three variables that may be investigated to determine optimum self-pulsation, as displayed in fig. 3.5. These variables are the stripe width, W, blocking layer thickness, d_b, and the thickness of the p-cladding layer that separates the two, d_p, or optical confinement layer as it will be known from now on. In such a structure the width of the area being pumped, or stripe width, W, is comparable to the lateral blocking layer separation, S, as displayed in fig. 3.5. [*Note*: To link these two values and estimate the effects of lateral current spreading various methods have been proposed [22]. However, in this thesis the p-cladding materials being considered have poor hole transport properties [23] allowing the assumption that the values are reasonably equal.]. It is also worth noting that it is the changes in d_b and/or d_p that alter the time-independent built-in properties whilst alterations in the stripe width varies the time-dependent, carrier-induced characteristics.

With the addition of such low index, wide band-gap blocking layers and subsequent changes in the emission the mathematical model for the narrow stripe laser must be modified. The lateral changes that occur as one varies the stripe width

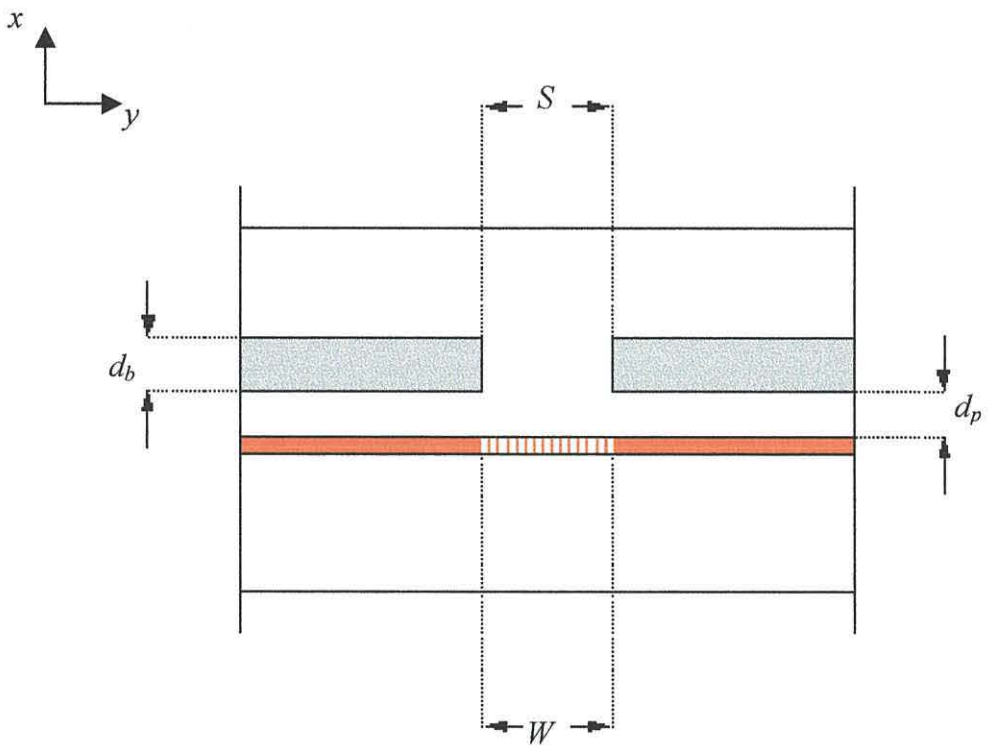

Fig. 3.5 *The cavity variables associated with the real refractive index guided device.*

are already considered, however, the time-independent components are neglected and must be included. Firstly, the built-in lateral index step must be calculated and added to equation (3.18). Secondly, the changes in the transverse optical field component must be evaluated by associating a confinement factor to both gain and absorber regions, as shown in fig. 3.6, thereby modelling the optical influence of the blocking layers.

For given values of d_p and d_b all of these built-in components may be calculated by considering the gain and absorber sections as two different waveguiding structures [19]. The area experiencing gain is evaluated as a five-layer waveguide whilst the absorber section is considered as a seven-layer structure, i.e. due to the inclusion of the blocking layers and subsequent introduction of the optical confinement layer. A propagation constant, β, is then calculated for the TE_0 mode of each section using the technique described in section 3.3.3. These complex values are used to calculate two distinct effective indices using the following equation

$$n_{eff}^{i} = \frac{\beta_i}{k_0} \tag{3.24}$$

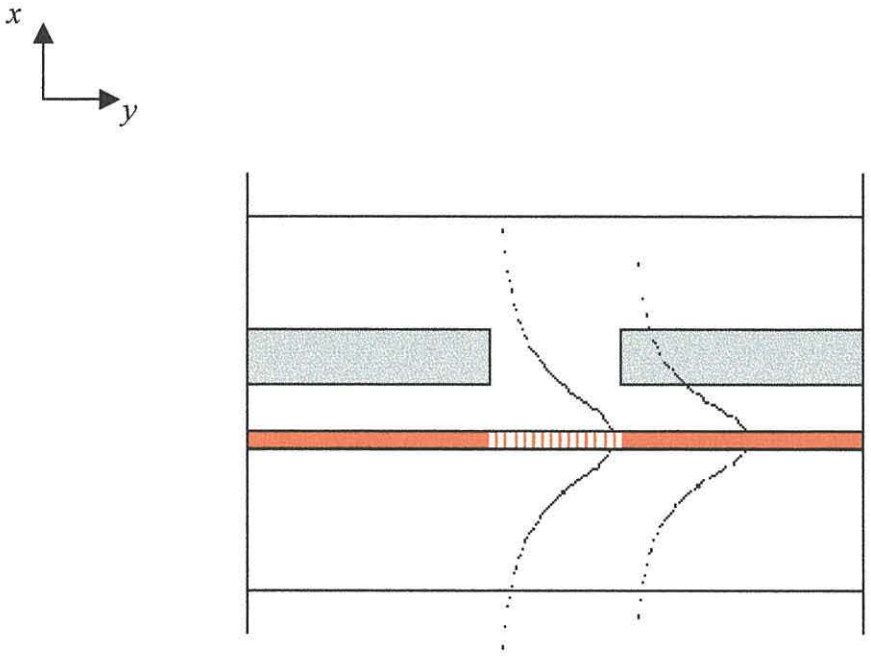

Fig. 3.6 *The transverse field profile of the real refractive index guided structure.*

where i=qw or α and $k_0 = 2\pi/\lambda$, which are in complex form as described in equation (3.16).

Now this real refractive index guided structure is characterised by a small amount of optical loss. This indicates that the imaginary part of the effective index is very small and may therefore be neglected [19]. The built-in refractive index step, Δn, is then calculated by considering the difference in the real part of the refractive indices through the following equation

$$\Delta n = n_{eff}^{qw} - n_{eff}^{\alpha}. \tag{3.25}$$

The propagation constant values may then be entered into equation (2.70) to calculate the two transverse confinement factors. Entering these calculations and the index step into the rate equation model gives an accurate assessment of the time-independent structural modifications associated with the blocking layers. The carrier-induced changes may then be calculated during the implementation of the rate equation model. [*Note*: To model the dynamics of the real refractive index guided laser a number of equations must be evaluated. An outline of the sequence of the numerical analysis is displayed in appendix 2, section A2.1.]

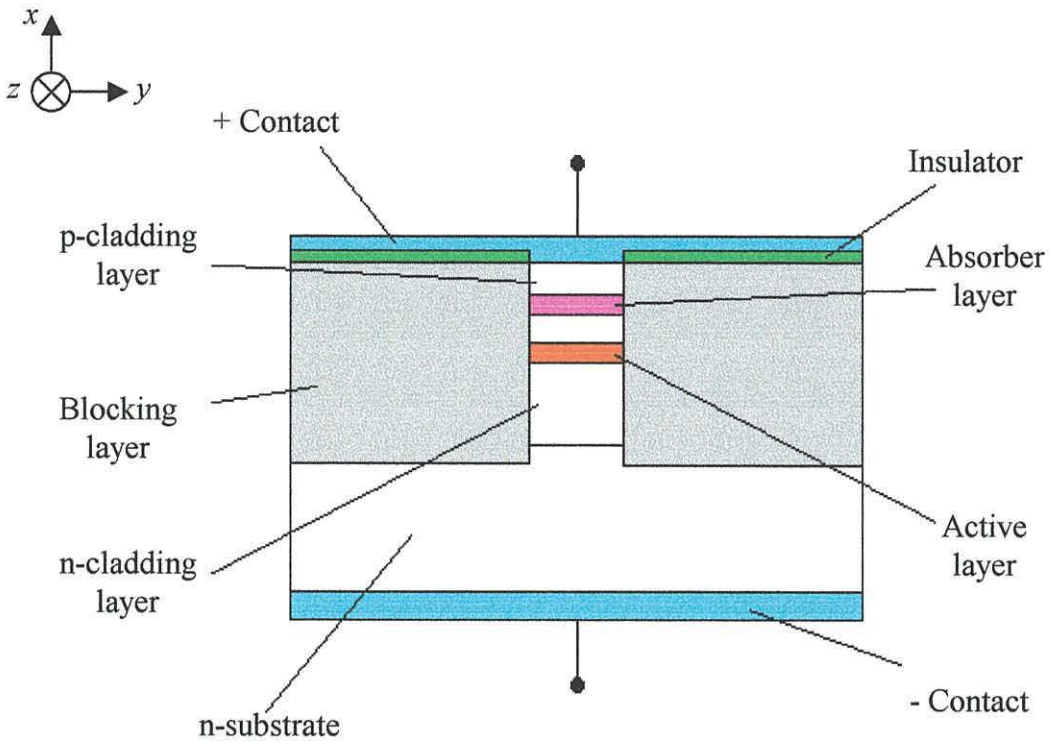

Fig. 3.7 *Schematic diagram of a buried stripe laser with an epitaxial absorber layer.*

3.4 Laser diode with epitaxial absorber layers

3.4.1 Structure

The most advanced self-pulsating device is the laser diode with epitaxial absorber layers. Originally developed for the GaAs material system, the structure makes use of an epitaxial layer of different composition to the active region to incorporate the saturable absorption required for self-pulsation [9]. The self-pulsation is then characterised by the interplay between the gain and the absorption at the operating wavelength. As a result a more flexible, "design-friendly" absorber is offered, with characteristics that can be engineered via the band-gap, thickness and position of the absorber layer(s).

This particular laser diode can be fabricated as a buried stripe laser, providing strong index guiding in the lateral direction. The structure is therefore designed such that the thickness of the active, absorber and cladding layers within the cavity are laterally non-uniform, as displayed in fig. 3.7. In this case only the substrate is

continuous, whilst thick blocking layers are used to inhibit lateral current spreading. The laser therefore provides good all round confinement allowing one to neglect the influence of the longitudinal (z) and lateral (y) optical field patterns when modelling the device [24], i.e. the consideration of lateral diffusion can be neglected due to the improvement in optical and carrier confinement.

3.4.2 Derivation of the rate equation model

As a new layer is added in the transverse (x) direction, the rate equation model must be adapted for this structure. Three equations are required, two carrier density equations, i.e. one for the active layer and the other for the absorber, and a single photon rate equation. It must also be stressed that the lateral diffusion can now be neglected due to the improvements in the optical and carrier confinement in the lateral direction. So, following the method outlined in section 3.3.2 a derivation of a rate equation model may be started by using the following carrier number rate equations [12]

$$V_{qw}\frac{dN_{qw}}{dt} = \frac{I}{e} - \left(R_{qw}^{nr} + R_{qw}^{sp}\right)V_{qw} - (R_{qw}^{21} - R_{qw}^{12})V_{qw} - R_{qw}^{l}V_{qw} \tag{3.26}$$

$$V_{\alpha}\frac{dN_{\alpha}}{dt} = R_{qw}^{l}V_{qw} - \left(R_{\alpha}^{nr} + R_{\alpha}^{sp}\right)V_{\alpha} - (R_{\alpha}^{21} - R_{\alpha}^{12})V_{\alpha} - R_{\alpha}^{l}V_{\alpha} \tag{3.27}$$

$$V_{p}\frac{dS}{dt} = \left(R_{qw}^{21} - R_{qw}^{12}\right)V_{qw} + \left(R_{\alpha}^{21} - R_{\alpha}^{12}\right)V_{\alpha} - \frac{SV_{p}}{\tau_{s}} + R_{qw}^{sp}V_{qw} + R_{\alpha}^{sp}V_{\alpha} \tag{3.28}$$

where the subscripts qw and α represent values/processes within the active and absorber layers, respectively, whilst the symbols are as given in section 3.3.2. All carriers "leaking out" of the gain section due to the thermally activated leakage current now enter the quantum wells in the absorber section, as indicated in equation (3.27). This is an important addition to the model as carrier leakage can significantly influence the high temperature performance of the device.

Now $R_{qw}^{21} - R_{qw}^{12} = v_g \times g(N_{qw}) \times S$ gives the photon generation due to radiative recombination in the active region and the radiative recombination in the absorber section is given by $R_{\alpha}^{21} - R_{\alpha}^{12} = v_g \times g(N_{\alpha}) \times S$. The confinement factor, Γ, is now only "transverse dependent", so two values are required using the equation $\Gamma_{qw,\alpha}(x) = V_{qw,\alpha}/V_p$. Substituting these expressions into equations (3.26)→(3.28) and dividing by the volumes gives the following carrier and photon density equations

$$\frac{dN_{qw}}{dt} = \frac{I}{eV_{qw}} - \left(R_{qw}^{nr} + R_{qw}^{sp}\right) - Sv_g g\left(N_{qw}\right) - R_{qw}^{l} \tag{3.29}$$

$$\frac{dN_{\alpha}}{dt} = \frac{R_{qw}^{l} V_{qw}}{V_{\alpha}} - \left(R_{\alpha}^{nr} + R_{\alpha}^{sp}\right) - Sv_g g\left(N_{\alpha}\right) - R_{\alpha}^{l} \tag{3.30}$$

$$\frac{dS}{dt} = Sv_g \Gamma_{qw} g\left(N_{qw}\right) + Sv_g \Gamma_{\alpha} g\left(N_{\alpha}\right) - \frac{S}{\tau_s} + R_{qw}^{sp} \Gamma_{qw} + R_{\alpha}^{sp} \Gamma_{\alpha} \ . \tag{3.31}$$

As the carrier density in the gain wells far outnumber the carriers in the absorber layers, the expression for the carrier leakage out of the absorber, R_{α}^{l}, may be left out. The spontaneous emission in the absorber section, R_{α}^{sp}, is negligible so this term may also be neglected.

By including the spontaneous and non-radiative terms the following rate equations are obtained

$$\frac{dN_{qw}}{dt} = \frac{J_{inj}}{e} - Sv_g g(N_{qw}) - \frac{N_{qw}}{\tau_{qw}} - \frac{J_l}{e} - BR_{qw}^{sp} \tag{3.32}$$

$$\frac{dN_{\alpha}}{dt} = -Sv_g g(N_{\alpha}) - \frac{N_{\alpha}}{\tau_{\alpha}} + \frac{J_l}{e}\frac{V_{qw}}{V_{\alpha}} \tag{3.33}$$

$$\frac{dS}{dt} = Sv_g \Gamma_{qw} g(N_{qw}) + Sv_g \Gamma_{\alpha} g(N_{\alpha}) - \frac{S}{\tau_s} + \beta R_{qw}^{sp} \tag{3.34}$$

where $\tau_{qw,\alpha}$ denote the carrier lifetimes in the respective layers. By integrating equations (3.32)→(3.34) the time evolution of the respective carrier densities may now be calculated using the Runge-Kutta method [13], as summarised in appendix 2, section A2.2. This rate equation system is very similar to the narrow stripe model described in section 3.4.2; however, the computational speed of this "laterally confined" model is far superior. Now the narrow stripe device requires a single calculation for the two transverse (x) confinement factors combined with a continuous estimate of the changing lateral (y) optical field making the calculation speed quite slow. The laser with epitaxial absorber layers allows one to neglect the lateral components of the device, requiring only two transverse confinement factors, as displayed in fig. 3.8. These values may be calculated using the transfer matrix technique for a five-layer waveguide and need only be calculated at the start of the computer program then set constant as the transverse optical field is reasonably stable. This explains why the calculation speed is so much quicker.

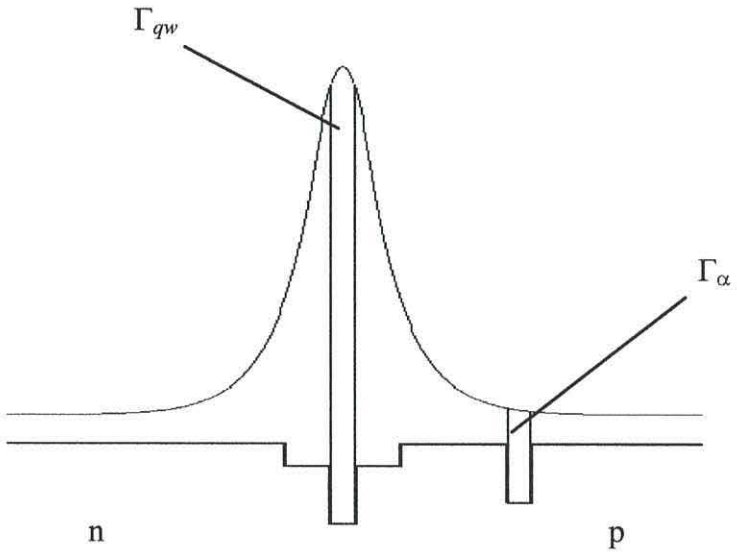

Fig. 3.8 *Band-gap profile of the self-pulsating laser diode and the corresponding transverse optical mode within the waveguide.*

3.5 Leakage current equation

Both rate equation models derived in sections 3.3 and 3.4 include a leakage current term, the inclusion of which is essential for some material systems, e.g. AlGaInP [23, 25, 26]. Leakage currents arise when carriers "escape" out of the active region into the cladding layers, resulting in a reduction of the lasers internal quantum efficiency. The magnitude of this carrier overflow is essentially dependent on two factors, namely the carrier confinement, which is dependent on the active region design, and the energy of the carriers, which increases with operating temperature. If carriers are poorly confined, this process can therefore have a significant influence on the high temperature performance of the device. Numerous operating characteristics can be affected, however, the most significant change is probably observed through the increase in threshold current. Now the threshold current density of a laser diode, J_{th}, varies with operating temperature, T, as follows [23]

$$J_{th} \propto \exp\frac{T}{T_0} \tag{3.35}$$

where T_0 represents the characteristic temperature, i.e. the temperature sensitivity of

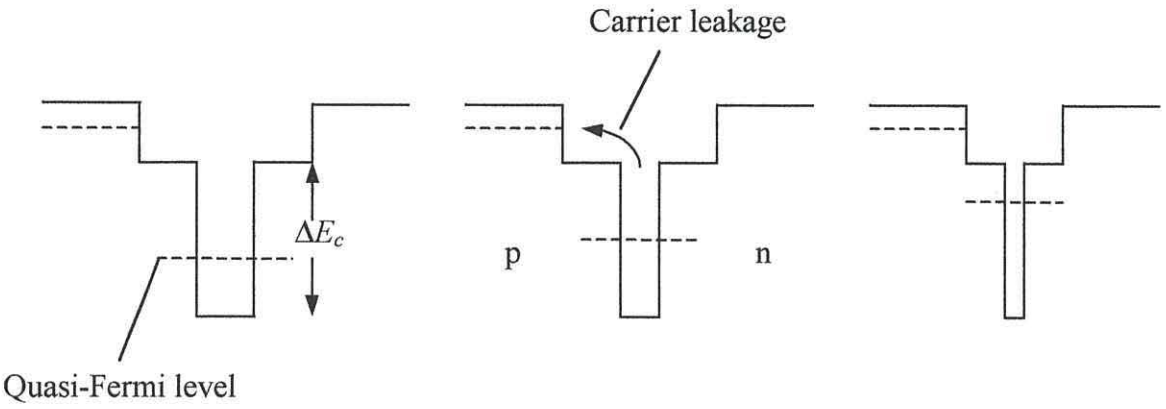

Fig. 3.9 *Changes in the conduction band due to a reduction in well width.*

the structure. This relationship indicates that the threshold current density increases with temperature. However, when carriers are poorly confined the characteristic temperature decreases quickly after room temperature, primarily due to the influence of the leakage current, causing an exponential-like increase in the threshold current. Equation (3.35) therefore indicates the importance of a structure that offers good carrier confinement if low threshold current performance is to be realised at high temperatures.

To minimise the characteristic temperature of a device it is important to optimise the dimensions of the quantum well active region. A decrease in well width causes an upward shift in energy states available to the electrons (downward shift in the valence band) as can be seen in fig. 3.9. These higher states not only change the emission wavelength but also make it easier for carriers to leak out of the wells contributing to an increase in carrier leakage. However, the high band offsets, ΔE_c (conduction band) and ΔE_v (valence band), available in some material systems can significantly decrease the amount of carrier overflow, indicating that a high band offset combined with a wide quantum well is usually desirable to maximise carrier confinement.

The wide band-gap materials that will be used in this work can all give rise to unwanted leakage currents, so an accurate estimate of the process is required. Now the total leakage current comprises of the carriers drift and diffusion components. The drift current arises when the charge carriers are accelerated by an electric field. When

this happens electrons acquire energy and a velocity, resulting in a net mean velocity in the opposite direction to the field. The electron drift current density is given by

$$J_{n,drift} = \frac{I_n}{A} = e\mu_n N\xi = \sigma_n \xi \tag{3.36}$$

where μ_n is the electron mobility indicating the ease with which the electron moves through the lattice. The symbol N represents the electron density, ξ is the electric field intensity and σ_n denotes the conductivity. An analogous equation may be derived for the hole drift current density.

When collections of particles are free to move in a random manner there exists areas of high and low particle concentration, i.e. a concentration gradient of carriers. In general, carriers will move away from the region of high concentration at a rate proportional to the concentration gradient. This diffusion of electrons is represented by a current density given by

$$J_{n,diffusion} = -eD_n \nabla N \tag{3.37}$$

where D_n is a constant of proportionality, usually called the diffusion coefficient (the minus sign is required to cancel the negative value of the gradient). The diffusion coefficient depends upon the collision processes that carriers experience in the material. Again, a similar equation can be derived for the hole diffusion current density. The diffusion length, L_n, represents the average distance an electron will diffuse before it recombines with a hole. This distance depends on the materials diffusion constant and recombination time and can be linked to the diffusion coefficient via the relationship $L_n = \sqrt{D_n \tau_n}$.

Now that the main components of the leakage current have been introduced an equation for the electron leakage current out of the quantum well active region can be derived. Consider a single quantum well (SQW) device. An expression is required that calculates the amount of electrons escaping out of the highest sub-band of the conduction band into the p-cladding layer of the structure. To acquire the leakage equation the minority carrier densities in the cladding layer at the barrier/cladding interface must be found, then the drift and diffusion currents. At the interface, the minority electron density is given by [25, 26]

$$N_l = 2\left(\frac{m_n^* kT}{2\pi\hbar^2}\right)^{3/2} \exp\left(-\frac{E_l - E_f}{kT}\right) \tag{3.38}$$

where

$$E_f = E_i + kT \ln\left[\exp\left(\frac{NL_x \pi \hbar^2}{m_n^* kT}\right) - 1\right] \tag{3.39}$$

is the electron quasi-Fermi level within the quantum well and barrier for a single sub-band. E_l , E_i and L_x represent the energy of the conduction band offset, the energy level of the lowest sub-band and the width of a single quantum well, respectively.

The minority carrier diffusion equation in the p-cladding layer in the presence of an electric field, ξ, is then solved using equations (3.36) and (3.37), i.e. [27]

$$J_l = -eD_n \frac{dN}{dx} + e\mu_n N\xi \tag{3.40}$$

where x is the length from the interface. Boundary conditions are $N(x=0) = N_l$ at the barrier/cladding interface and $N(x=w_c) = 0$ at the p-side contact where w_c is the width of the p-cladding layer. Solving the equation, subject to the boundary conditions, gives the following expression for the total leakage current density out of a SQW active region [26, 28]

$$J_l = J_{diffusion} + J_{drift} = \frac{eD_n N_l}{L_x}\left\{\sqrt{\frac{1}{L_n^2} + \frac{1}{4z^2}}\coth\left[\sqrt{\frac{1}{L_n^2} + \frac{1}{4z^2}}w_c\right] + \frac{1}{2z}\right\} \tag{3.41}$$

where z is a length characteristic of drift leakage which is described by the equation

$$z = \left(\frac{kT}{e}\right)\frac{\sigma_p}{J_t} \tag{3.42}$$

with $\sigma_p = ep\mu_p$ denoting the electrical conductivity of the p-cladding layer and J_t the total current density. Equation (3.41) can therefore be included in the two rate equation models to give an accurate estimate of the leakage current that will inevitably affect the high temperature performance of either device.

3.6 Mechanism for self-pulsation

Self-pulsation is observed when saturable absorption is introduced into the laser cavity, leading to the characteristic interplay between the regions experiencing gain and absorption. For a full understanding of this unstable process one must investigate

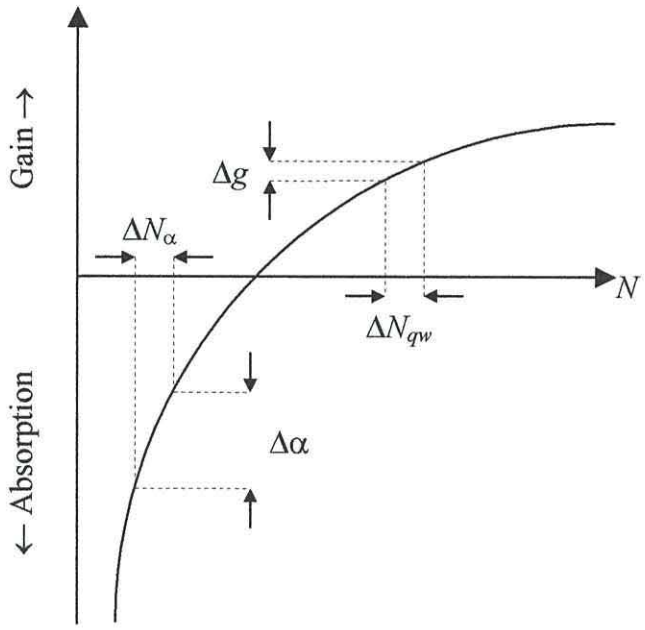

Fig. 3.10 *The sub-linear optical gain/absorption relationship with injected carrier density, N, that is required for self-pulsation.*

the optical gain and its functional dependence on carrier concentration [24, 29]. If the gain related to the system is linearly dependent on carrier density then no increase in net gain would occur, i.e. after the absorption of photons the laser has the same net gain as before, resulting in no self-pulsation. Pulsed emission can therefore only occur if there is sufficient non-linearity of the gain function. In particular, a sub-linear dependence is required where a small change in carrier density affects the absorption more strongly than the gain. A super-linear dependence leads to a stabilising effect that results in no pulsation [3].

Consider a sub-linear gain-current density relationship, as shown in fig. 3.10. Let N_α represent the average carrier density in the absorbing region and N_{qw} the average carrier density that experiences gain. Now an increase in photon emission produces a decrease in the carrier density in the amplifying section by ΔN_{qw}. This in turn causes a reduction in gain by a small amount, Δg. To maintain equilibrium the carrier density in the absorber section increases by an amount ΔN_α, reducing the absorption by $\Delta\alpha$. Due to the non-linearity of the gain/absorption curve the differential gain and absorption are different, so the following condition holds true [24, 30]

$$\eta_E \frac{d\alpha}{dN_\alpha} \geq \frac{dg}{dN_{qw}} \tag{3.43}$$

where η_E represents the transfer efficiency. Since the decrease in gain is less than the reduction in absorption the net gain after saturation is larger than the amount of gain required for steady state lasing. An unbalanced system is therefore created and self-pulsation will arise.

In addition to the required non-linear gain/carrier density relationship the self-pulsation characteristics can also be influenced by the time response of the carriers within the system. It is known that the carrier lifetime in the absorber section, τ_α, must be small compared to the carrier lifetime in the amplifying section, τ_{qw}, for self-pulsation to proceed [4, 31]. This indicates that the time-dependent change in absorption must be greater than that of the gain to create the required unstable system. This time dependence coupled with the non-linear feedback mechanism therefore gives rise to the following expression [30, 32]

$$\frac{1}{\tau_\alpha}\frac{d\alpha}{dN_\alpha} \geq \frac{1}{\tau_{qw}}\frac{dg}{dN_{qw}}, \tag{3.44}$$

a condition that must be carefully considered when designing a self-pulsating laser diode.

3.7 Conclusions

The work presented in this chapter has offered an insight into the modelling techniques that may be used to simulate the dynamical attributes of the self-pulsating laser diode. Having outlined how the self-pulsating laser has evolved over the past thirty years, two sets of rate equations have been derived, one for the real refractive index guided laser and the other for a laser diode with epitaxial absorber layers. The important influence of the thermally activated leakage current has also been studied and included in the rate equation analysis. An assessment of the dynamical properties required for successful self-pulsation was then given with time-dependent changes in the gain characteristics coupled with a non-linear feedback mechanism being of particular importance. These equations will now be used in the remainder of the thesis

to investigate the emission of the above-mentioned lasers for optical storage applications.

References

[1] E. S. Yang, P. G. McMullin, A. W. Smith, J. Blum and K. K. Shih, "Degradation-induced microwave oscillations in double-heterostructure injection lasers," *Appl. Phys. Lett.*, vol. 24, pp. 324-326, 1974.

[2] N. G. Basov, "Dynamics of injection lasers," *IEEE J. Quantum Electron.*, vol. 4, pp. 855-864, 1968.

[3] C. Harder, K. Y. Lau and A. Yariv, "Bistability and pulsations in semiconductor laser with inhomogeneous current injection," *IEEE J. Quantum Electron.*, vol. 18, pp. 1351-1361, 1982.

[4] M. Ueno and R. Lang, "Conditions for self-sustained pulsations and bistability in semiconductor lasers," *J. Appl. Phys.*, vol. 58, pp. 1689-1692, 1985.

[5] H. Kawaguchi and G. Iwane, "Bistable operation in semiconductor lasers with inhomogeneous excitation," *Electron. Lett.*, vol. 17, pp. 167-168, 1981.

[6] J. P. van der Ziel, "Pulsating output of separate confinement buried optical guide lasers due to the deliberate introduction of saturable loss," *Appl. Phys. Lett.*, vol. 39, pp. 376-378, 1981.

[7] M. Kuznetsov, "Pulsations of semiconductor lasers with proton bombarded segment: Well-developed pulsations," *IEEE J. Quantum Electron.*, vol. 21, pp. 587-592, 1985.

[8] M. Yamada, "A theoretical analysis of self-sustained pulsation phenomena in narrow-stripe semiconductor lasers," *IEEE J. Quantum Electron.*, vol. 29, pp. 1330-1336, 1993.

[9] R. C. P. Hoskens, T. G. van de Roer, C. J. van der Poel and H. P. M. Ambrosius, "Self-pulsating lasers with quantum well saturable absorber," *Appl. Phys. Lett.*, vol. 67, pp. 1343-1345, 1995.

[10] M. Yuri, S. Harris, T. Takayama, O. Imafuji, H. Naito, M. Kume, K. Itoh and T. Baba, "Two-dimensional analysis of self-sustained pulsation for narrow-stripe AlGaAs lasers," *IEEE J. Select. Topics Quantum Electron.*, vol. 1, pp. 473-479, 1995.

[11] T. Takayama, O. Imafuji, M. Yuri, H. Naito, M. Kume, A. Yoshikawa and K. Itoh, "800 mW peak-power self-sustained pulsation GaAlAs laser diodes," *IEEE J. Select. Topics Quantum Electron.*, vol. 1, pp. 562-568, 1995.

[12] S. W. Corzine and L. A. Coldren, *Diode Lasers and Photonic Integrated Circuits*, John Wiley and Sons, 1995.

[13] R. K. Nagle and E. B. Saff, *Fundamentals of Differential Equations*, Addison-Wesley, 1993.

[14] H. C. Casey Jr. and M. B. Panish, *Heterostructure Lasers (Part A)*, Academic Press, 1978.

[15] R. E. Smith, S. N. Houde-Walter and G. W. Forbes, "Mode determination for planar waveguides using the four-sheeted dispersion relation," *IEEE J. Quantum Electron.*, vol. 28, pp. 1520-1526, 1992.

[16] K. H. Schlereth and M. Tacke, "The complex propagation constant of multilayer wave-guides – an algorithm for a personal computer," *IEEE J. Quantum Electron.*, vol. 26, pp. 627-630, 1990.

[17] J. H. Mathews, *Numerical Methods For Mathematics, Science, and Engineering*, Prentice-Hall International Editions, 1992.

[18] G. P. Agrawal and N. K. Dutta, *Long-Wavelength Semiconductor Lasers*, Van Nostrand Reinhold, 1986.

[19] O. Imafuji, T. Takayama, H. Sugiura, M. Yuri, H. Naito, M. Kume and K. Itoh, "600mW *cw* single-mode GaAlAs triple-quantum-well laser with a new index guided structure," *IEEE J. Quantum Electron.*, vol. 29, pp. 1889-1894, 1993.

[20] D. P. Bour, R. S. Geels, D. W. Treat, T. L. Paoli, F. Ponce, R. L. Thornton, B. S. Krusor, R. D. Bringans and D. F. Welch, "Strained $Ga_xIn_{1-x}P/(AlGa)_{0.5}In_{0.5}P$ heterostructures and quantum-well laser diodes," *IEEE J. Quantum Electron.*, vol. 30, pp. 593-607, 1994.

[21] O. Imafuji, T. Fukuhisa, M. Yuri, M. Mannoh, A. Yoshikawa and K. Itoh, "Low operating current and high-temperature operation of 650-nm AlGaInP high-power laser diodes with real refractive index guided self-aligned structure," *IEEE J. Select. Topics Quantum Electron.*, vol. 5, pp. 721-728, 1999.

[22] W. T. Tsang, "The effects of lateral current spreading, carrier out-diffusion, and optical mode losses on the threshold current density of GaAs-$Al_xGa_{1-x}s$ stripe-geometry DH lasers," *J. Appl. Phys.*, vol. 49, pp. 1031-1044, 1979.

[23] P. Zory Jr., *Quantum Well Lasers*, Academic Press, 1993.

[24] R. W. Dixon and W. B. Joyce, "A possible model for sustained oscillations (pulsations) in (Al,Ga)As double-heterostructure lasers," *IEEE J. Quantum Electron.*, vol. 15, pp. 470-474, 1979.

[25] H. D. Summers and P. Rees, "Thermal limitation of self-pulsation in 650 nm AlGaInP laser diodes with an epitaxially integrated absorber," *Appl. Phys. Lett.*, vol. 71, pp. 2665-2667, 1997.

[26] D. P. Bour, D. W. Treat, R. L. Thornton, R. S. Geels and D. F. Welch, "Drift leakage current in AlGaInP quantum-well lasers," *IEEE J. Quantum Electron.*, vol. 29, pp.1337-1343, 1993.

[27] N. K. Dutta, "Calculated temperature dependence of threshold current of GaAs-$Al_xGa_{1-x}s$ double heterostructure lasers," *J. Appl. Phys.*, vol. 52, pp. 70-73, 1981.

[28] S. R. Chinn, P. S. Zory Jr. and A. R. Reisinger, "A model for GRIN-SCH-SQW diode lasers," *IEEE J. Quantum Electron.*, vol. 24, pp. 2191-2214, 1988.

[29] T. Ohmi and S. Yamazaki, "A limitation on repetition rate of pulsations of junction lasers due to the repetitively q-switched mechanism," *IEEE J. Quantum Electron.*, vol. 9, pp. 366-374, 1973.

[30] C. H. Henry, "Theory of defect-induced pulsations in semiconductor injection lasers," *J. Appl. Phys.*, vol. 51, pp. 3051-3061, 1980.

[31] H. Kawaguchi, "Optical bistability and chaos in a semiconductor laser with a saturable absorber," *Appl. Phys. Lett.*, vol. 45, pp. 1264-1266, 1984.

[32] H. D. Summers and P. Rees, "High temperature operation of 650-nm wavelength AlGaInP self-pulsating laser diodes," *IEEE Photon. Technol. Lett.*, vol. 10, pp. 1217-1219, 1998.

Chapter 4

Red self-pulsating real refractive index guided laser diode

4.1 Introduction

This chapter aims to investigate an AlGaInP real refractive index guided laser for high temperature self-pulsation, i.e. ≥70 °C, and therefore offer a cheap and efficient mechanism of reading data from an optical disc. This weakly index guided structure has already been described in a more generalised form in section 3.3.4. It is now intended to study the self-pulsation characteristics of the laser at an operating wavelength of 650 nm and tailor the device for use in DVD systems (with a 4.7 Gbyte storage capacity). The rate equation model and gain equations presented in previous chapters will therefore play significant roles in providing an accurate model of the dynamical output of the device.

The chapter starts with a brief section discussing the material properties associated with the AlGaInP material system, showing why the thermally activated leakage current plays such an important part in determining the operating characteristics of the device. A description of the real refractive index guided

structure is then given combined with a summary of the various design parameters that may be varied to try and optimise the self-pulsating emission. The rate equation model and gain calculations are then implemented and the design parameters studied. The latter part of the chapter therefore investigates the suitability of the self-pulsation for optical storage purposes. Parameters are varied in an attempt to achieve sufficient gain/absorption interaction over a wide operating temperature and current range. Once the design parameters have been studied in detail a summary of the results will be given, outlining the suitability of the structure for use in DVD systems.

4.2 AlGaInP: material information

4.2.1 Historical developments

The band-gaps available from alloys grown in the AlGaInP material system offer lasing in the 600 - 700 nm wavelength range. Since the first epitaxial growth of AlGaInP onto lattice matched GaAs substrates by molecular beam epitaxy (MBE) in 1982 [1] the understanding of devices fabricated in this material system has increased dramatically. In 1985 *cw* operation was achieved using double heterostructure (DH) active regions [2, 3] with shorter wavelengths being available by adding aluminium to the active region [4]. Subsequent research led to further understanding of the red laser, e.g. [5], in an attempt to lower the high threshold current and increase the characteristic temperature, T_0.

Once the DH lasers were well understood quantum well devices were fabricated with immediate success [6, 7]. Indeed, the quantum confined active region proved to be the ideal solution in not only reducing the threshold current of the device but also improving the temperature sensitivity and lowering the wavelength. Advances in strained quantum wells led to a further decrease in threshold [8, 9], with optimised structures approaching the thresholds of GaAs devices [8].

Research during the 1990's has primarily concentrated on optimising the structure, in an attempt to overcome some of the negative properties associated with the material system. By now there exists a good understanding of the characteristics of the red laser diode with detailed research leading to an in depth knowledge of the design parameters on offer. This allows the crystal grower to design a structure that

maximises T_0 leading to a more efficient laser diode; however, the material properties still severely limit the device performance.

4.2.2 Material properties

Typical red emitting structures make use of GaInP quantum wells grown alongside various AlGaInP layers to offer the best carrier and optical confinement. The materials are very closely lattice matched, so there is a large flexibility in the choice of structures available to the crystal grower. These lasers tend to emit at higher threshold currents in comparison with their GaAs counterparts. This is due to the higher density of states and higher effective mass [10], creating a laser with a low characteristic temperature, T_0, that becomes increasingly inefficient as the operating temperature, T, is increased, i.e. T_0 decreases as T increases [11, 12].

Usually a decreasing characteristic temperature is caused by changes in carrier confinement and/or Auger recombination. The dominance of Auger recombination decreases with decreasing wavelength [13], so it is the carrier confinement that is weak in AlGaInP devices, giving rise to a thermally activated leakage current. This carrier overflow is a consequence of the material properties that hinder the design of the active region [14]. For example, the high effective mass decreases the energy separation between the sub-bands (in comparison with GaAs), allowing thermally excited carriers to occupy higher energy bands with relative ease. Indeed, it is this weak confinement coupled with a small energy difference between the quasi-Fermi level of the GaInP quantum wells and the indirect X-band of the AlGaInP barrier layers that gives rise to this unwanted leakage current. Methods of improving the carrier confinement must therefore be investigated if high temperature operation is to be achieved.

Numerous methods have been used to try to suppress the leakage current in an attempt to maximise the effective energy barrier between layers and make it as difficult as possible for carriers to "escape" the quantum well active region. Some attempts have employed a multi-quantum barrier (MQB) where alternating thin layers of wide and narrow gap materials act as a multi-layer electron reflector [15, 16]. Unfortunately no striking improvements have been reported to date, possibly due to the difficulties in growing repeatable layers of such thin films. With such novel

techniques still in their infancy it is very important that the cavity design is optimised to offer maximum carrier confinement. This is done by optimising the well layer dimensions such that the quasi-Fermi levels are as deep as possible within the well and by maximising the energy difference between the quasi-Fermi level and the indirect X-gap.

Strained quantum wells achieve the lowest threshold currents in both compressive [8, 9, 17-23] and tensile [22, 24] domains, offering variations in active material band-gap and therefore allowing shorter wavelengths and improvements in carrier confinement. In particular, an active region consisting of compressively strained $Ga_yIn_{1-y}P$ quantum wells, i.e. $y<0.51$, offer the best performance [8, 9, 18]. Although no longer lattice matched to the AlGaInP barriers, the lattice compresses and modifies the band structure, as described in chapter 2, resulting in a reduced threshold current and higher differential gain. Higher barriers are also available, with an increase in indium content increasing the barrier height [10], resulting in an improvement in the suppression of the leakage current. The lowest threshold currents of all AlGaInP devices have been achieved using compressively strained SQW structures [8, 17, 18]. However, strained MQW active regions have been effective in achieving shorter wavelengths, higher gain and minimising the carrier leakage per well [12, 20-23].

The quantum well active region is usually grown within a separate confinement heterostructure (SCH). The difference between the refractive indices in the quantum well and SCH layers creates a waveguiding effect that is essential for efficient lasing. The optimum heterostructure configuration is the one which maximises the overlap between the optical field and the quantum well active region whilst still providing strong carrier confinement. This is a difficult balance to achieve. As the concentration of aluminium increases within the heterostructure, the carrier confinement improves whilst optical confinement becomes weak (and the converse is also true) [10]. A compromise between optical and carrier confinement must therefore be made if one is to construct an efficient laser. This is an important point and must be considered when optimising the structure for specific applications.

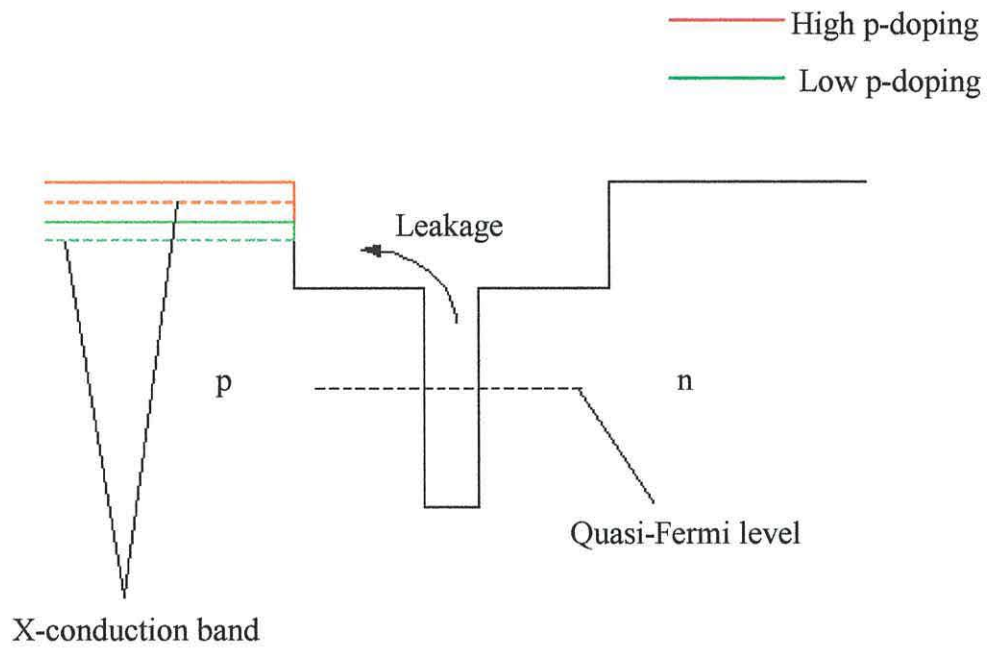

Fig. 4.1 *Schematic diagram of the electron leakage current and the effects of doping the p-cladding layer.*

Once the gain generating wells and SCH have been designed it is important to use a suitable cladding layer composition. For adequate carrier confinement, one would suspect that a high aluminium content would be desirable to maximise the barrier height. However, research has indicated that the X-gap is relatively insensitive to aluminium composition, so the indirect X-band is similar in both barrier and cladding materials [14]. High aluminium alloys also give rise to a hole conductivity that is unacceptably low, with a small mobility value limiting the hole concentration within the layers [25, 26]. It is therefore difficult to achieve a satisfactory p-cladding composition to maximise the effective barrier height and therefore minimise the carrier leakage, as displayed in fig 4.1. Indeed, difficulties in achieving a sufficiently high p-doping density gives rise to an electric field across the cladding layers, causing the drift component to dominate the leakage process. Unlike diffusion, the drift current is dependent on temperature and proportional to the total injection current [12]. This causes an increase in drift leakage with temperature that is much more rapid than the increase of diffusive leakage, indicating that it is the drift process that

must be controlled to minimise carrier overflow and obtain high temperature performance when using the AlGaInP material system [12].

To partially overcome this problem it is desirable to highly dope the p-cladding layer, thus, increasing the hole concentration and decreasing the resistance in the region. This process increases the effective barrier height (see fig. 4.1) and reduces the electric field in the cladding layer (reducing the drift current) resulting in a reduction in the leakage current and an improvement in high temperature performance. [*Note*: The leakage of holes into the n-cladding layers isn't as much of a problem due to the holes' lower mobility, diffusion length and the availability of a higher n-doping density all contributing to an improvement in conductivity and a higher barrier [10].]

Over the years improvements in growth techniques have allowed higher p-doping densities to be utilised. Materials such as zinc [5], beryllium [27] and magnesium [28] have been used as acceptor atoms to increase the hole concentration and improve the thermal conductance. However, there exists an upper doping limit available to all material systems and this is particularly true for AlGaInP where a maximum p-doping density of around $1\times10^{18}cm^{-3}$ is available.

4.3 AlGaInP real refractive index guided laser

4.3.1 Structure

Using the material information presented in the previous section it is now possible to design this modified AlGaInP narrow stripe device. Fig. 4.2 shows a schematic drawing of the structure. Now the cladding layers are grown onto lattice-matched GaAs substrates, a material of reasonably high conductivity that is attached to the metal contact layers. As one moves towards the active region the aluminium composition of the $(Al_xGa_{1-x})_{0.51}In_{0.49}P$ layers decreases in order to achieve the desired carrier and optical confinement. However, two current blocking layers composed of $Al_{0.51}In_{0.49}P$ are also included in the p-cladding section (separated by a distance *S*, see

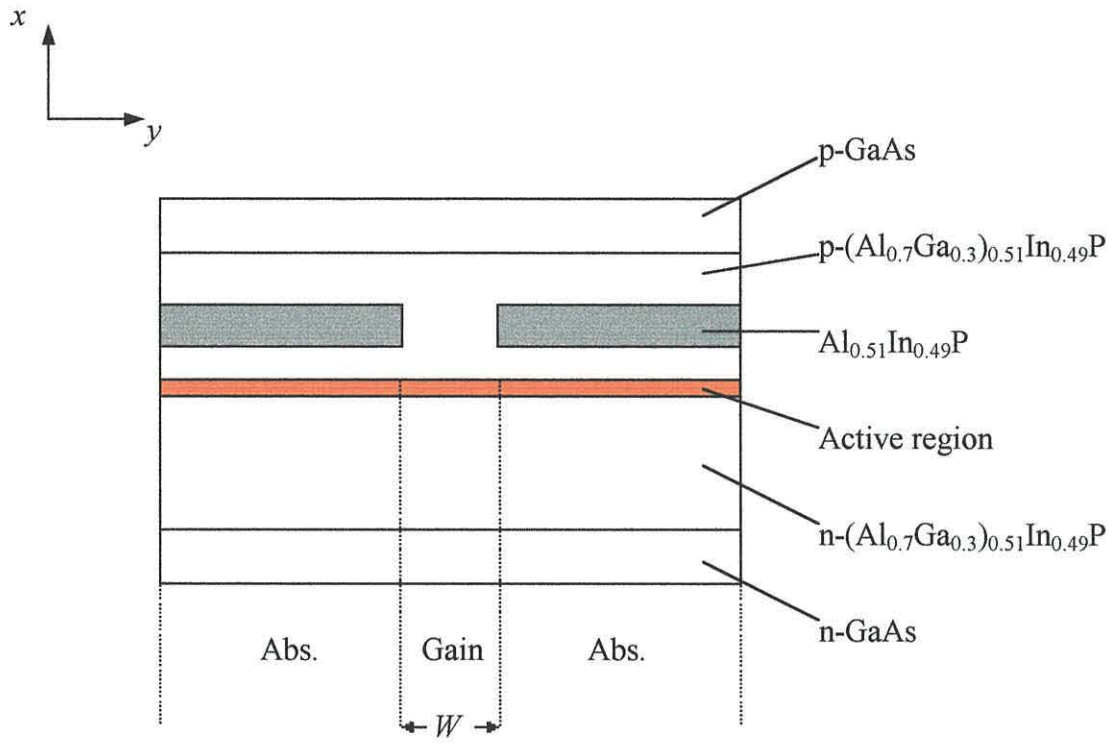

Fig. 4.2 *Schematic diagram of the AlGaInP real refractive index guided laser.*

fig. 3.5), thereby providing a sufficient index discontinuity to give superior transverse mode stability (in comparison with conventional ridge waveguide structures). A controllable amount of absorption is therefore on offer with a reduced operating current available if *cw* emission is required [29, 30]. Table 4.1 summarises the thickness and refractive index of each layer.

A schematic diagram of the active region is displayed in fig. 4.3. As has already been mentioned it is important to optimise the design such that the leakage current is suppressed at high temperatures. With this in mind the device has an active layer consisting of 3×70 Å $Ga_{0.48}In_{0.52}P$ quantum wells separated by 100 Å $(Al_{0.4}Ga_{0.6})_{0.51}In_{0.49}P$ wide barriers. These layers are then set within a 0.2 μm $(Al_{0.4}Ga_{0.6})_{0.51}In_{0.49}P$ waveguide core with $(Al_{0.7}Ga_{0.3})_{0.51}In_{0.49}P$ cladding layers for optimum carrier confinement. This structure has been proven to give optimum gain per injection current in a 650 nm laser [32], as is required here, offering good optical

Layer	Material	Thickness (μm)	Ref. Index
1	p-GaAs	0.5	3.60
2	p-$(Al_{0.7}Ga_{0.3})_{0.51}In_{0.49}P$	0.6	3.33
3	$Al_{0.51}In_{0.49}P$	d_b	3.25
4	p-$(Al_{0.7}Ga_{0.3})_{0.51}In_{0.49}P$	d_p	3.33
5	$(Al_{0.4}Ga_{0.6})_{0.51}In_{0.49}P$ SCH	0.1	3.40
6	$Ga_{0.48}In_{0.52}P$ QW	0.007	3.52
7	$(Al_{0.4}Ga_{0.6})_{0.51}In_{0.49}P$ SCH	0.1	3.40
8	n-$(Al_{0.7}Ga_{0.3})_{0.51}In_{0.49}P$	1.5	3.33
9	n-GaAs	0.5	3.60

Table 4.1 *Material properties of the different layers that form the real refractive index guided laser (from references [10, 29, 31]).*

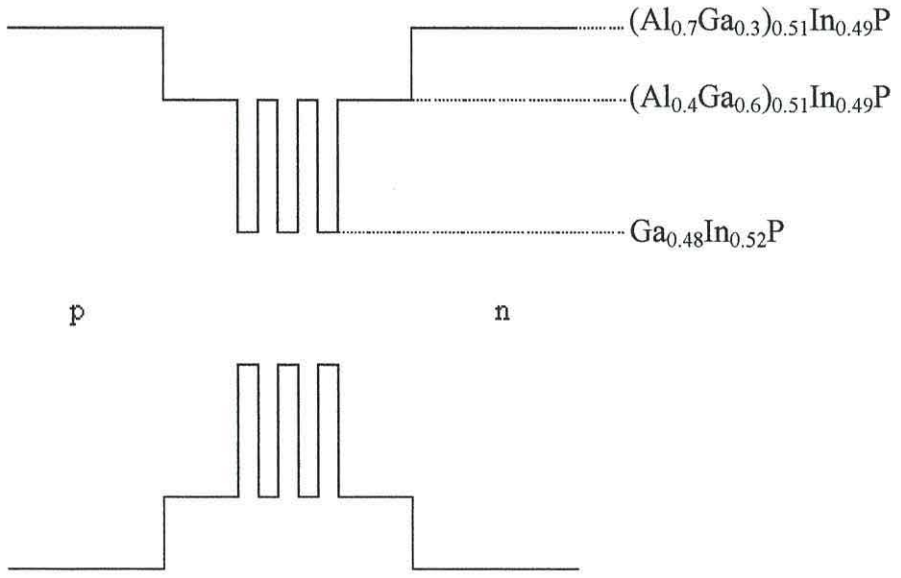

Fig. 4.3 *Schematic diagram of the active region used within the AlGaInP real refractive index guided laser diode.*

and carrier confinement subject to the design constraints mentioned in the previous section.

The most important factor that determines whether self-pulsation is achieved is the gain/absorption interaction. It is important that this concept is investigated fully to attain the optimum cavity design so three parameters are varied, i.e. the stripe width, W, the blocking layer thickness, d_b, and the thickness of the optical confinement layer, d_p (see fig. 3.5), to study the emission characteristics of the device. A variation in one of these values changes the key differential gain/absorption characteristics (at turn-on) and therefore determines the dynamical output of the device. If the structure is to be optimised for self-pulsation purposes one must find the optimum three-variable combination.

During emission the carrier densities in both sections will fluctuate. This will inevitably create a carrier-induced refractive index change in the lateral direction. It is therefore important to design a cavity that provides an adequate built-in refractive index difference such that the carrier-induced change is insufficient to disrupt the lateral waveguiding, i.e. $n_{qw}>n_{\alpha}$ must hold throughout the emission. Of the three variables on offer it is the blocking and optical confinement layer thicknesses that change the optical field in the transverse direction. An alteration in either variable will modify the built-in refractive index step and the transverse optical confinement in the absorber section, $\Gamma_{\alpha}(x)$. It has already been shown in chapter 3 how the index discontinuity may be evaluated, so an effective index value must be calculated for both gain and absorber regions.

Using the refractive index information in table 4.1 and the method described in section 3.3.4 (culminating with equation (3.25)) the built-in refractive index step as a function of blocking layer and optical confinement layer thickness is displayed in fig. 4.4 (a). From these results it is evident that a wide-ranging step is available, allowing one to design the cavity so that the deleterious effects of carrier-induced anti-guiding may be avoided. The graph also shows the importance of the thickness of optical confinement layer. This value determines the influence of the material properties of the blocking layers. As a result, the rate of change in the index step is very sensitive to the thickness of this p-doped section with the refractive index difference reducing as one increases d_p.

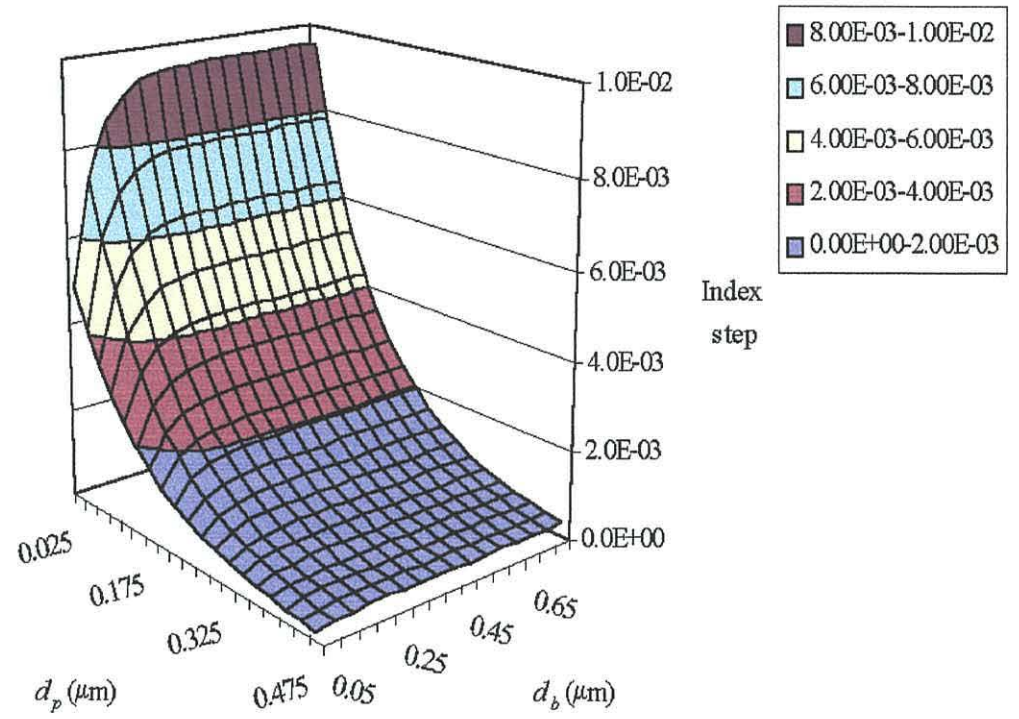

(a)

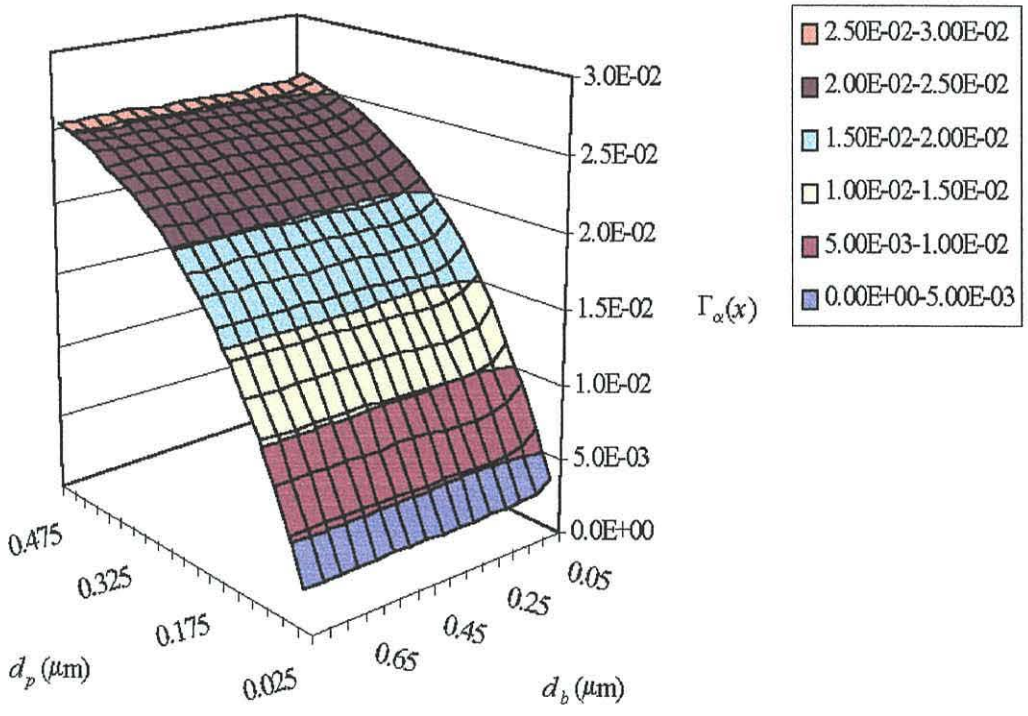

(b)

Fig. 4.4 *Calculated results of the (a) refractive index step and (b) transverse absorber confinement factor as a function of blocking and optical confinement layer thickness.*

The optical field is also a function of both blocking and optical confinement layer thicknesses and must therefore be evaluated if one is to vary the initial index step. Fortunately the transverse component of the optical field remains reasonably constant in the active region due to the exclusion of the blocking layers and the small changes in the thickness of d_p. However, this is not the case in the absorbing regions where the small refractive indices associated with the blocking layers influence the profile of the optical field. Using the propagation constant calculations that were obtained when evaluating the index step, the changes in transverse absorber confinement factor, $\Gamma_\alpha(x)$, are shown in fig. 4.4(b). It is very noticeable that a wide range of absorption is on offer with the amount of absorption increasing as one increases the thickness of the optical confinement layer. As in the case of the index step, this is due to its dominance over d_b, giving rise to confinement factor values that are far more dependent on d_p.

As one examines the graphs displayed in fig. 4.4 it is clear that the built-in properties will play a key role in determining whether or not self-pulsation will be observed. In the ranges being considered a significant index step is available, however, this corresponds to a small amount of absorption. A slight variation in either d_b or d_p could therefore be enough to change the emission from *cw* to self-pulsation, so a detailed investigation is required to obtain the best combination.

4.3.2 Gain calculations

Now that the design of the device has been completed it is important to obtain gain calculations for the strained quantum well active region that was introduced in fig. 4.3.1. Using equations (2.55) and (2.60) and the necessary parameters [10, 33] typical results for the TE gain are shown in fig. 4.5, displaying the changes that arise as one varies the carrier density and temperature within the device. [*Note*: These calculations were generated using a model developed by Dr P. Rees.]. At a temperature of 0 °C fig. 4.5(a) shows how the peak gain increases with carrier density with a value of approximately 5×10^{18} cm^{-3} required to generate gain. However, this is the material gain, i.e. the calculations do not include any loss terms. It is therefore suffice to say that a higher carrier density will be required to generate sufficient gain to overcome the losses within the laser.

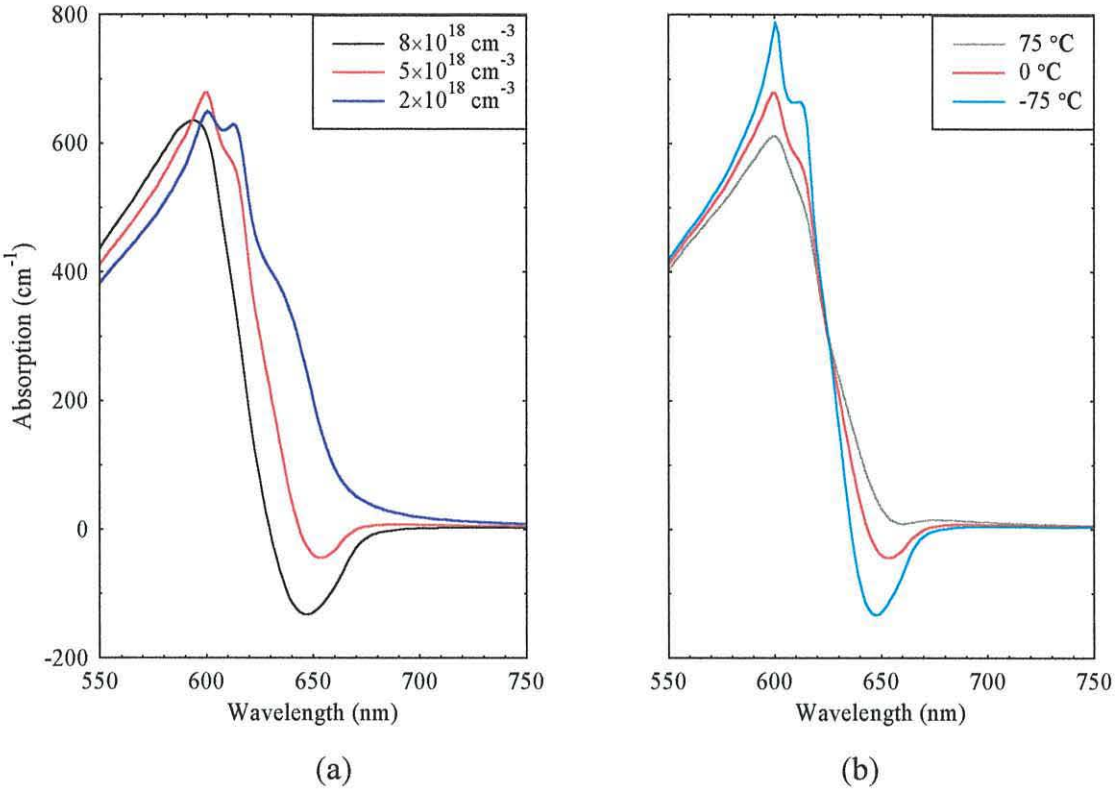

Fig. 4.5 *Typical modal gain spectrum for the 3×70 Å quantum well active region at (a) three different operating carrier densities at 0 ℃ and (b) three different temperatures for a carrier density of* 5×10^{18} cm^{-3}.

The influences of the many-body effects are also displayed. Coulomb enhancement causes a peak in the absorption spectrum at low carrier densities which "smoothes out" at higher values as the exciton lifetime diminishes due to collisions with other particles [34]. Band-gap renormaliation is also observed causing the "shift" in the peak gain to dampen somewhat (when compared to the free carrier case) as one increases the carrier density. In the single mode rate equation analysis the peak gain is taken for every iteration, so a slight change in wavelength will occur as the operating current is altered. [*Note*: Spectral broadening is harder to characterise, however, it does reshape the gain curve, especially when scattering events are dominant, and may be observed by comparing free-carrier and many-body gain curves [10, 34].]

Fig. 4.5(b) illustrates how the material gain changes with temperature. The

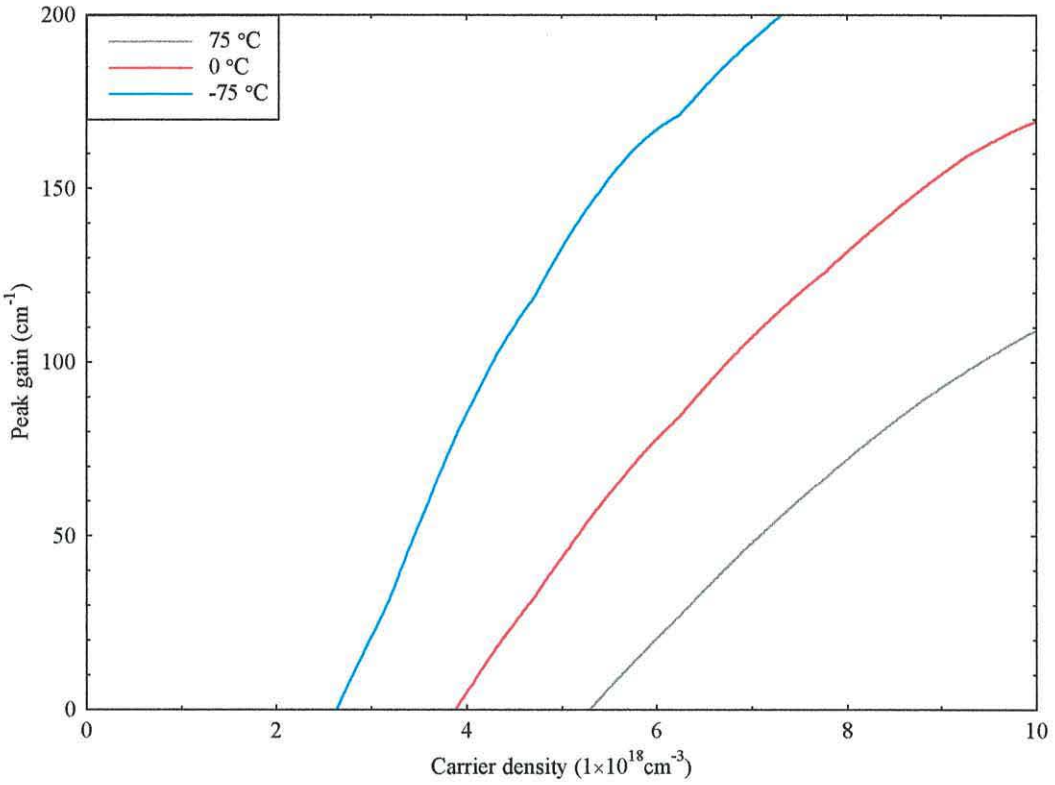

Fig. 4.6 *Calculated modal peak gain versus injected carrier density for the 3×70 Å quantum well active region at three different temperatures.*

results display how thermal effects dampen the gain spectrum, with the peak gain and absorption decreasing with temperature. This is a consequence of two factors. Firstly, the temperature dependence of the Fermi-Dirac distribution causes carriers to occupy higher energy levels and therefore decrease the probability of recombination. Secondly, the thermal dependence of some of the many-body effects, e.g. carrier-carrier scattering, modifies the gain profile. Coulomb enhancement is therefore reduced at high temperatures, i.e. the peak in the absorption curve disappears, whilst band-gap renormalisation is observed as it contributes towards the changes in the wavelength of the peak gain.

The changes in the peak gain due to variations in carrier density and temperature are displayed in fig. 4.6. As generalised in fig. 4.5, the graph indicates that the peak gain is at its highest at low temperatures and high carrier densities, giving rise to a slight reduction in the wavelength of the emission. The diagram also

gives a good indication of the changes in the differential gain, which is an important factor in determining self-pulsation with a change in sub-band being observed at -75 °C, i.e. the "kink" in the curve at N=6×10^{18} cm^{-3}. Now it is apparent that the sub-linear nature of the curves decrease with temperature. This suggests that the chances of self-pulsation should increase with temperature, however, the corresponding alterations in the differential absorption and the problematic nature of the leakage current will no doubt significantly modify these simple, initial ideas.

4.4 Initial results

4.4.1 Operating regimes

By applying the rate equations derived in section 3.4.2 it is now possible to model the dynamics of the device. The equations are solved using the method outlined in appendix 2, section A2.1, by applying the parameter values displayed in table 4.2, the built-in properties calculated in section 4.3.1 and the necessary gain/absorption calculations. To assess whether or not self-pulsation is observed the simple conditions set out in appendix 3 are used.

To gain "a feel" of the results that will be displayed in the remainder of the chapter it is useful to introduce the operating regimes that are observed as one varies the current at a given temperature. Starting at a very low current the first typical photon emission is displayed in fig. 4.7(a). At this point not enough gain is available to overcome the losses within the cavity so an incoherent stream of spontaneous emission is produced. As one increases the current similar output is observed until threshold is achieved, resulting in either self-pulsation or *cw* emission as shown in fig. 4.7(b). The type of output is dependent on the differential absorption on offer, i.e. dependent on whether condition (3.44) holds true. So, as one increases the proportion of absorption within the cavity, e.g. decrease the stripe width, the threshold current density will increase.

At a certain operating current the emission ceases and anti-guiding is observed, as displayed in fig. 4.7(c). This is a consequence of the carrier-induced

Symbol	Parameter name	Parameter value
α_i	Internal loss	10 cm^{-1}
R	Facet reflectivity	0.32
Γ_{qw}	Active layer confinement factor	0.048
β	Spontaneous emission coeff.	1×10^{-4}
τ_{qw}	Carrier lifetime in the active layer	1 ns
τ_{α}	Absorber carrier lifetime	0.3 ns
μ_n	Electron mobility in the p-cladding layer	60 $cm^2V^{-1}s^{-1}$
μ_p	Hole mobility in the p-cladding layer	7 $cm^2V^{-1}s^{-1}$
L_x	Well width of the MWQ in the active layer	70 Å
L	Laser cavity length	500 μm
V_{qw}	Volume of gain wells	Well no.×well width×W×L
m^*	X-band electron effective mass	0.23 m_0

Table 4.2 *Parameters used in the rate equation model (from references [35, 36]).*

changes in the refractive index and is a potential problem in any weakly index guided laser due to the poor lateral carrier confinement within the device. Once this anti-guiding threshold is achieved, all higher operating currents increase the negative index difference, so this anti-guiding regime is the last. The results in fig. 4.3 therefore indicate the importance of designing a cavity with a sufficient built-in refractive index step such that anti-guiding does not affect the current bounds within which self-pulsation takes place.

In general, there will exist three well-defined regimes that will vary as one changes the absorption, current and temperature within the cavity. The investigation will search for a suitable cavity design that offers self-pulsation at 70 °C for the lowest operating current. It is therefore crucial that the cavity design is optimised for such emission. [*Note*: It is only once the high temperature condition is satisfied that the power emission will be assessed.]

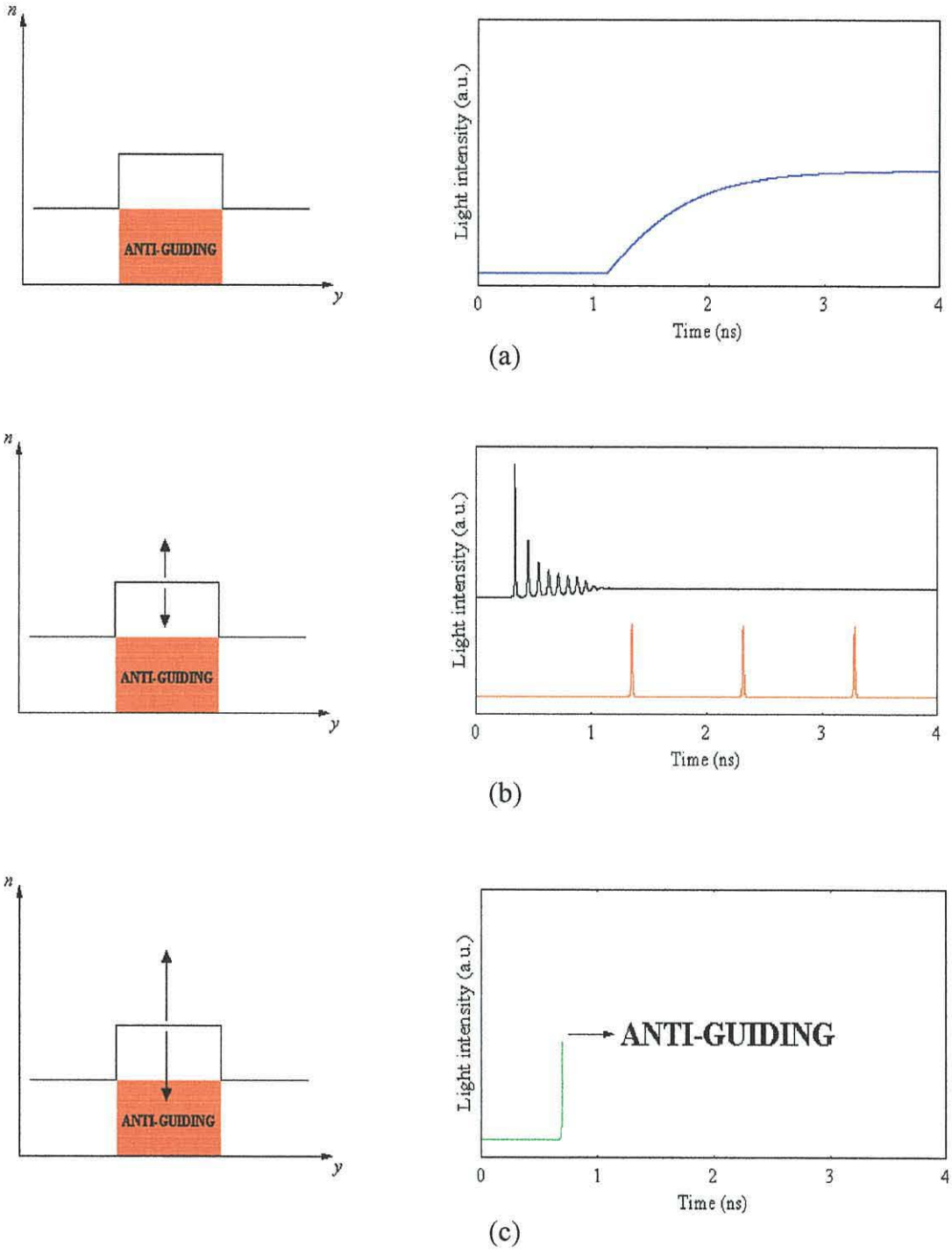

Fig. 4.7 *Fluctuations in the lateral refractive index during a pulse and the temporal behaviour for (a) low, (b) intermediate and (c) high operating currents at room temperature ($W=1\,\mu m$, $d_p=0.15\,\mu m$ & $d_b=0.4\,\mu m$).*

4.4.2 Importance of a time-varying lateral field calculation

In this weakly index guided device the carrier-induced changes in the lateral direction of the cavity play a key role in determining the characteristics of the emission. As a result, as one considers the optical field within the cavity the changes in the refractive index profile will inevitably vary the lateral component of the field. Early models of self-pulsating lasers neglected this factor, stating that the changes in the lateral field profile are negligible. A value for the confinement factor would then be calculated at turn-on then kept constant throughout the time range being investigated [37]. This method was regarded as being the standard way of modelling self-pulsation until Yuri et al. [38] suggested otherwise and gave strong evidence why a time-varying field should be included. Although more laborious to implement the carrier-induced changes in refractive index will often determine whether or not a pulse is emitted and must therefore be evaluated constantly when modelling the device.

The importance of the inclusion of a time-varying lateral optical field is shown in fig. 4.8 where the photon emission is displayed for two specific cases. Fig. 4.8(a) clearly shows that there exists a significant change in the lateral field during the emission as the carriers diffuse between the gain and absorbing regions. As a consequence a self-pulsating beam is emitted from the cavity. Part (b) illustrates the photon emission for the same cavity design and operating current when the confinement factor is kept constant, i.e. at a value calculated at threshold. It is clear that the emission is very different, offering output that would not be deemed self-pulsating when assessed using the conditions stated in appendix 3. As a result of these differences the intensity of the emission, frequency and power output would all differ from those values calculated using the model in part (a). A time-varying lateral field profile must therefore be continuously calculated if one is to accurately assess the self-pulsation characteristics from such a weakly index guided device.

4.4.3 Frequency of emission

The linear relationship between the operating current and the frequency of the self-pulsation is shown in fig. 4.9(a). This trend can be explained by considering the recovery rate of the carrier densities after depletion by a pulse. If the duration of the

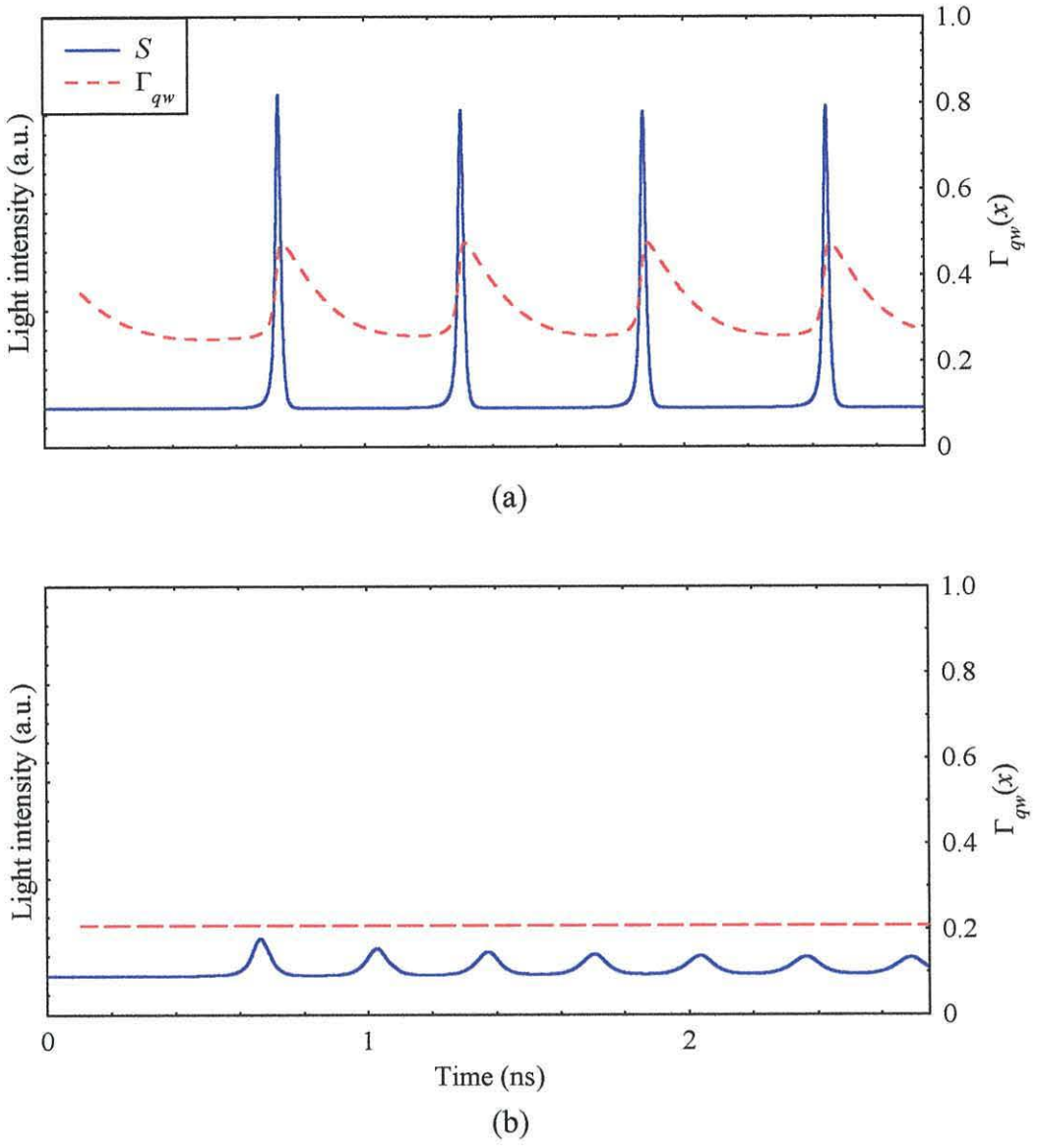

Fig. 4.8 *Typical temporal evolution of the photon emission at room temperature when the time-varying lateral optical field is (a) included and (b) omitted from the simulation (I=50 mA, W=1 μm, d_p=0.15 μm and d_b=0.4 μm).*

pulse, t_d, is short compared to the recovery time, t_p, (as displayed in fig. 4.9(b)) then a large-signal modulation regime is observed where the pulse frequency is determined by the simple relationship [39]

$$f_p \approx \frac{1}{t_p}. \tag{4.1}$$

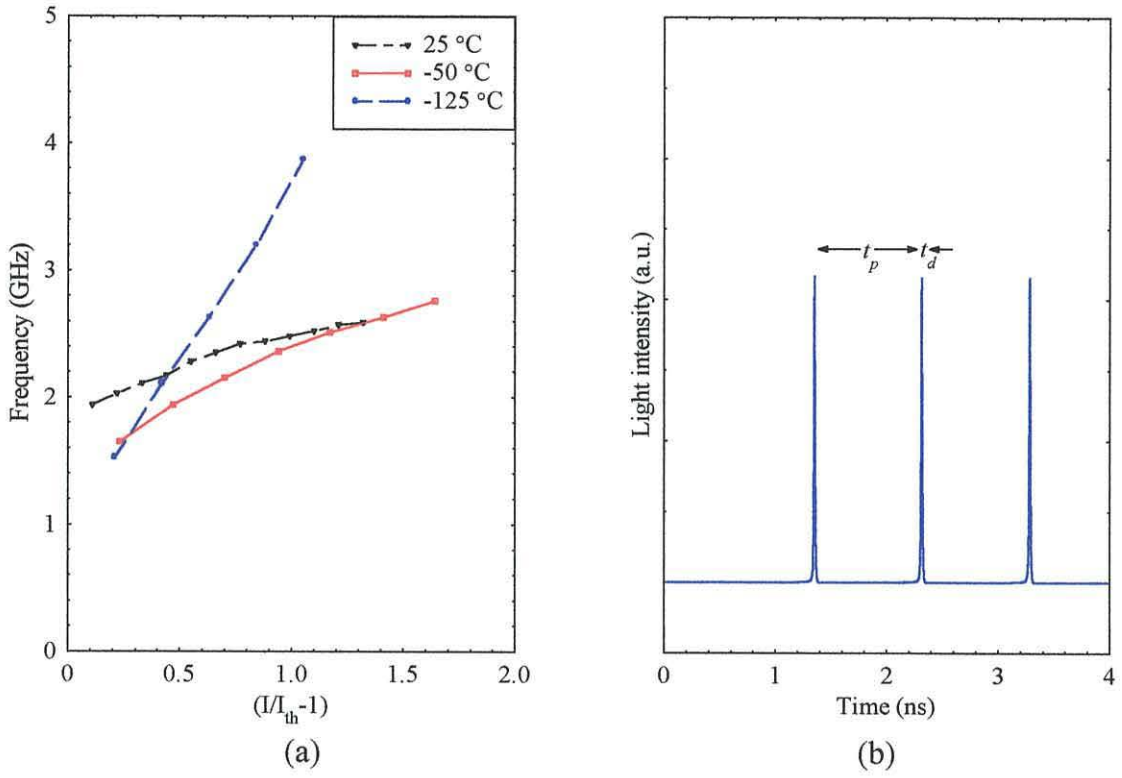

Fig. 4.9 *(a) The frequency of the self-pulsating emission at three different temperatures and (b) a typical illustration of the time evolution of the output at room temperature ($W=1\,\mu m$, $d_p=0.15\,\mu m$ & $d_b=0.4\,\mu m$).*

In this regime the frequency is dependent on the time required to replace the depleted carriers in the gain wells, i.e. [40]

$$t_p \propto \frac{dN_{inj}}{dt} \propto I_{inj}. \tag{4.2}$$

This leads to a linear relationship between the pulse frequency and injection current, as approximated by the following equation [39]

$$f_p \propto \left(\frac{I}{I_{th}} - 1\right), \tag{4.3}$$

which holds for the three temperatures being investigated in fig. 4.9(b). The results also show that the rate of change of the pulsation frequency (with respect to the operating current) decreases with temperature. This is a consequence of the leakage

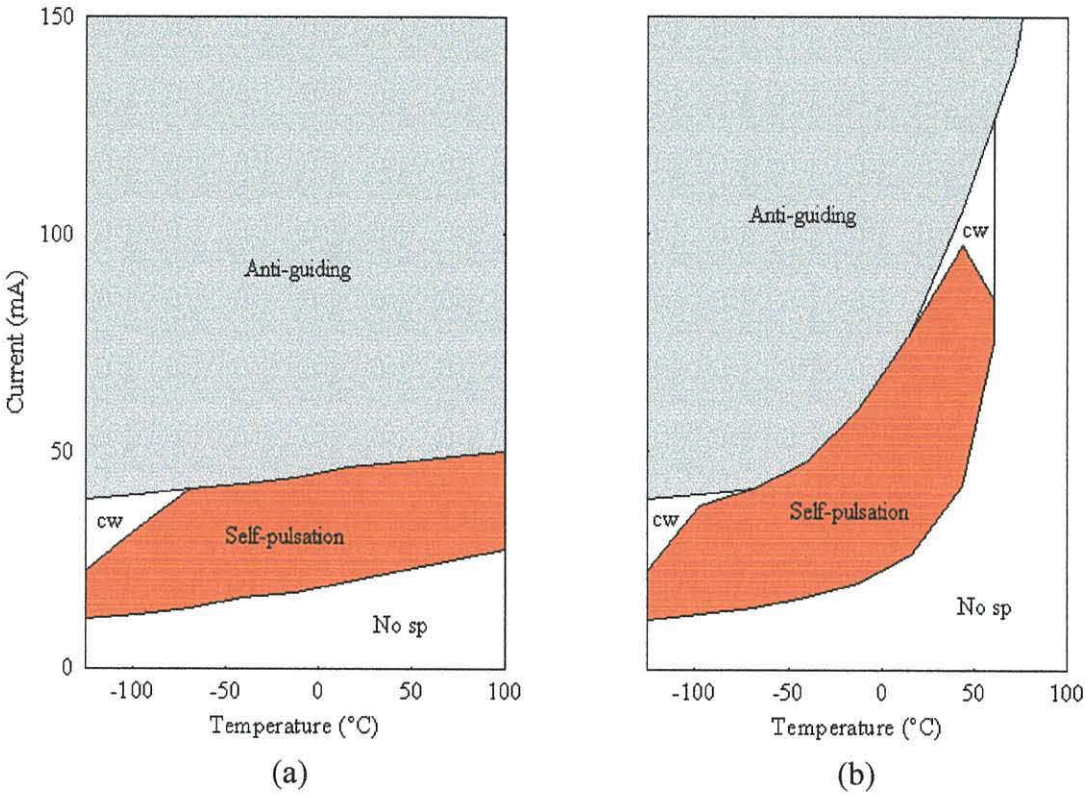

Fig. 4.10 *Operating bounds when the leakage current equation is (a) omitted then (b) included in the rate equation model ($W=1\,\mu m$, $d_p=0.15\,\mu m$ & $d_b=0.4\,\mu m$).*

current. Not only does this deleterious effect increase the threshold current it also affects the time required to replenish the carriers consumed in generating a pulse which consequently reduces the slope of the curves displayed in fig. 4.9(a).

4.4.4 Leakage effects

Even after optimising the design of the active region some undesirable properties associated with the AlGaInP material system indicate that a certain amount of leakage is inevitable. The problematic nature of this carrier overflow is illustrated in fig. 4.10 where a search for self-pulsation is conducted when the leakage equation, i.e. equation (3.41), is omitted then included in the rate equation model. As will be done throughout this chapter, the emission is examined between temperatures of -125 and 100 °C. In both cases the three typical operating regimes are realised, with a band of *cw* emission following the self-pulsation at low temperatures. This is to be expected

due to the high differential gain at low temperatures ensuring that equation (3.44) holds for a short range of operating currents.

Despite using a strained active region to maximise the carrier confinement the leakage current has a noticeable effect on the self-pulsation with both current and temperature bounds being altered. When the carrier overflow is neglected a "band" of self-pulsation is detected that increases with temperature due to the thermal temperature dependence of the diffusion term and the Fermi-Dirac distribution of carriers. Minimal changes in the emission characteristics are observed as self-pulsation is offered throughout the temperature range being investigated.

The inclusion of the leakage equations causes an "exponential-like" increase in the various boundaries as the thermally activated leakage current reduces the recombination efficiency within the active region. The carrier overflow becomes evident at approximately -70 °C then increases until the self-pulsation ceases at 42 °C. At this point (and beyond) the efficiency of the active region is very low with the subsequent changes in carrier and optical confinement affecting the gain and absorption characteristics. This creates a situation in which the differential gain term increases and the differential absorption decreases to a point where self-pulsation is no longer observed, i.e. equation (3.44) no longer hold true. For the cavity configuration under consideration this change in the differential gain/absorption relationship takes time to develop with the current range gradually decreasing once the carrier overflow is initiated. As a result a combination of *cw* emission and self-pulsation is observed as the differential gain/absorption interaction begins to weaken. The inclusion of a leakage equation is therefore of paramount importance when assessing the performance of an AlGaInP laser, especially when considering emission at room temperature (and beyond).

The effectiveness of a high p-doping density in the p-cladding layer is shown in fig. 4.11 where the density is gradually increased up to its maximum available value of 1×10^{18} cm^{-3}. The results indicate how the barrier height increases with doping density and therefore suppresses the leakage current in an increasingly effective manner. As a consequence both current and temperature bounds for self-

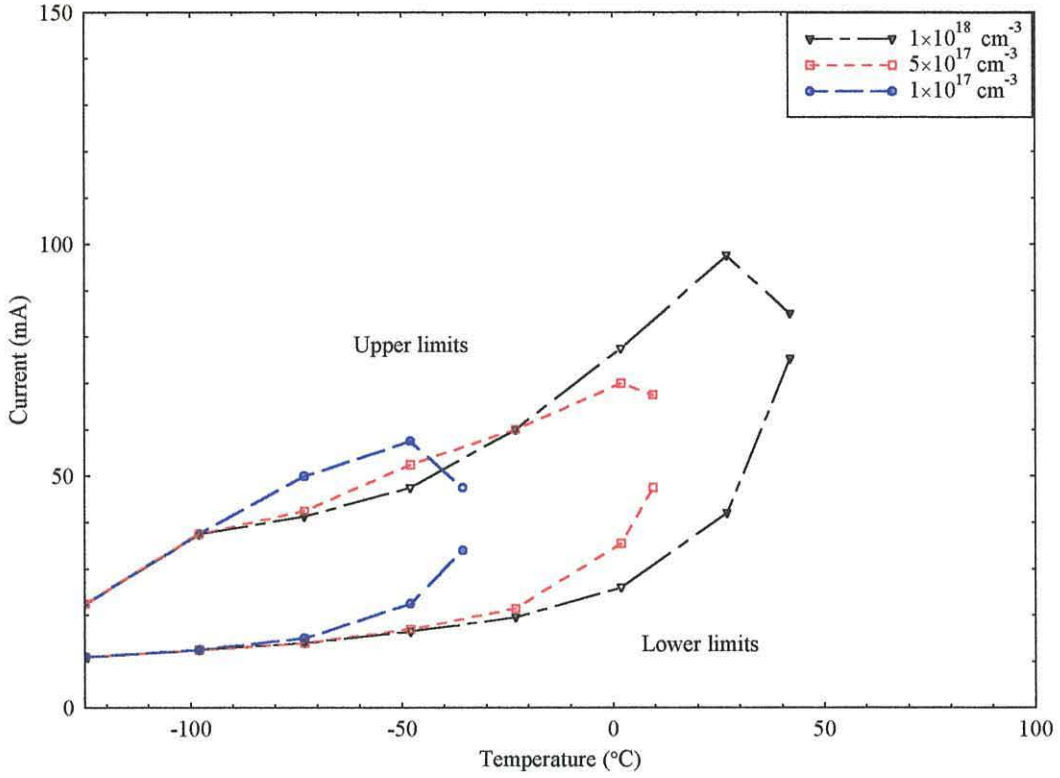

Fig. 4.11 *The upper and lower current bounds for self-pulsation versus temperature using three different p-cladding doping levels (W=1 μm, d_p=0.15 μm & d_b=0.4 μm).*

pulsation are improved with the "exponential shift" associated with the thermally induced carrier overflow taking longer to develop. With these points in mind the p-doping density will be kept constant at a value of 1×10^{18} cm^{-3} throughout this chapter.

4.5 Changes in absorption

The previous section used the same cavity configuration, i.e. W=1 μm, d_p=0.15 μm and d_b=0.4 μm, to give an insight into the characteristics of the self-pulsation. Now the work in this thesis aims to optimise the emission for optical storage purposes. The key factor that must be satisfied (before any other) is that the laser must self-pulsate at 70 °C. The previous results failed to achieve this temperature threshold by quite a margin. The three variables must therefore be investigated thoroughly in an attempt to

improve the maximum operating temperature whilst minimising the operating current of the device.

Investigations for a similar structure using the GaAs material system gives an indication of the stripe widths required for self-pulsation [38, 41]. However, a change in wavelength and a reduction in the diffusion length in particular [29] suggests that smaller stripe widths must be used if the device is to be fabricated in the AlGaInP material system. With this in mind values between 0.5 and 2.5 μm are tested at intervals of 0.5 μm. The blocking and optical confinement layer thicknesses are varied within the limits set out in figs. 4.4. The search for self-pulsation is then conducted. For a good indication of the configurations that combine satisfactorily to achieve self-pulsation, an initial search is performed at 0 °C. As demonstrated in fig. 4.10, this particular temperature offers a minimal leakage current and a small differential gain, resulting in self-pulsation over a wide range of operating currents.

Unfortunately the 0.5 and 2.5 μm stripe widths fail to emit any self-pulsation whatsoever. For the blocking and optical confinement layers being investigated both cases offer combinations of differential gain and absorption that are unsatisfactory, resulting in the absence of self-pulsation at turn-on. When the blocking layers are 2.5 μm apart an insufficient amount of carriers experience absorption. As a result, the differential gain at turn-on is too high ensuring *cw* emission at 0 °C. The output over a wide operating current is therefore the same as a conventional laser, i.e. no lasing→*cw*→anti-guiding. The reasonably small amount of absorption within the cavity therefore supports a low threshold current density [38, 41]. The "failure" of the 0.5 μm stripe to generate any self-pulsation is a consequence of too much absorption. The small width results in a high threshold current density for self-pulsation at low temperatures, so when the leakage current takes effect the increase in threshold is enough to give rise to carrier-induced anti-guiding before turn-on at 0 °C.

The combinations that offer self-pulsation for the three remaining stripe widths are shown in fig. 4.12. The clearest observation is the sensitivity of the emission to the cavity design. In the three cases only a limited number of configurations offer the desired relationship between differential gain and absorption to achieve self-pulsation. It is apparent that this sensitivity increases with stripe width

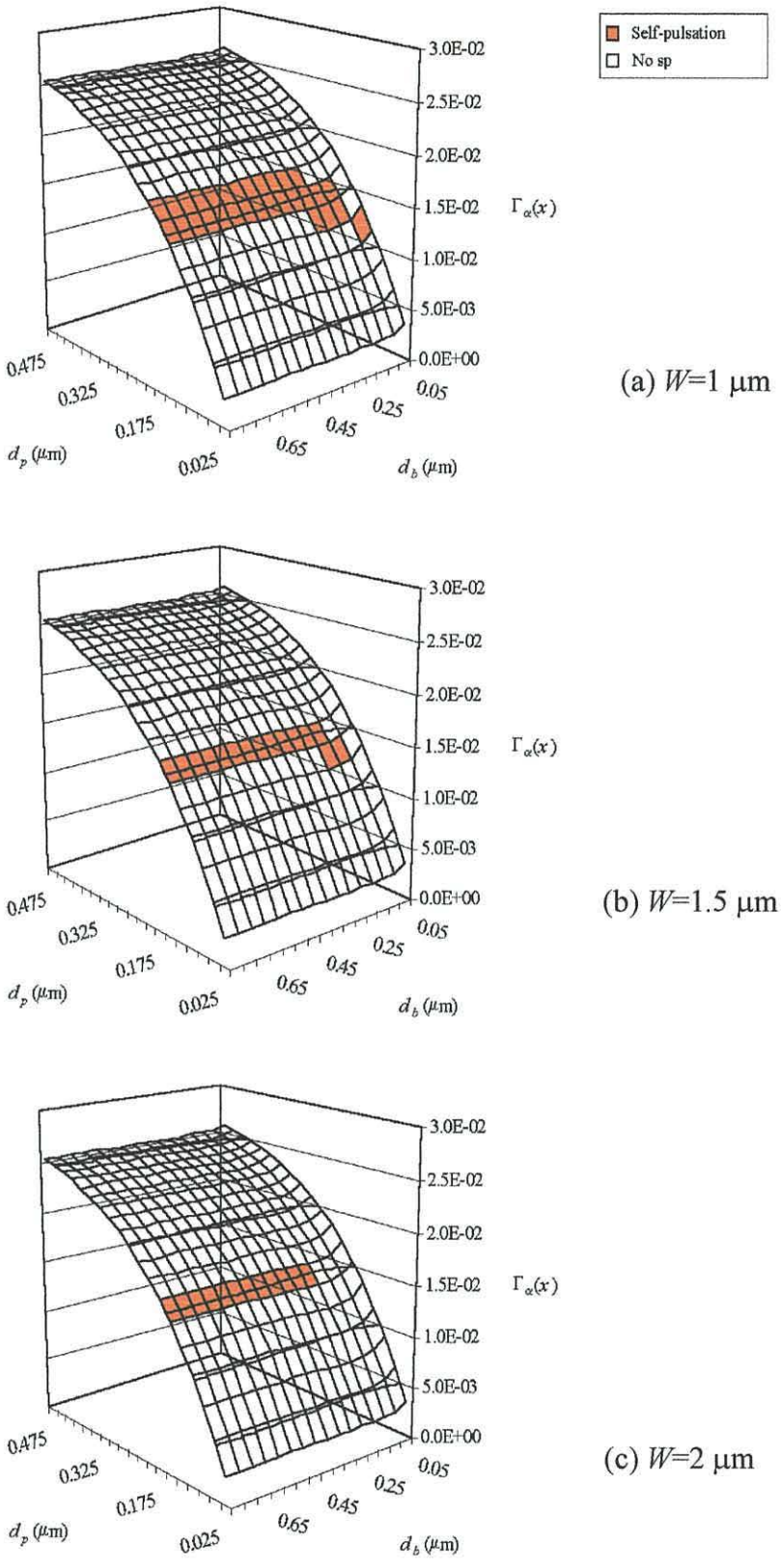

(a) W=1 μm

(b) W=1.5 μm

(c) W=2 μm

Fig. 4.12 *Self-pulsation bounds as a function of blocking and optical confinement layer thickness for stripe widths of (a) 1, (b) 1.5 and (c) 2 μm at 0 ℃.*

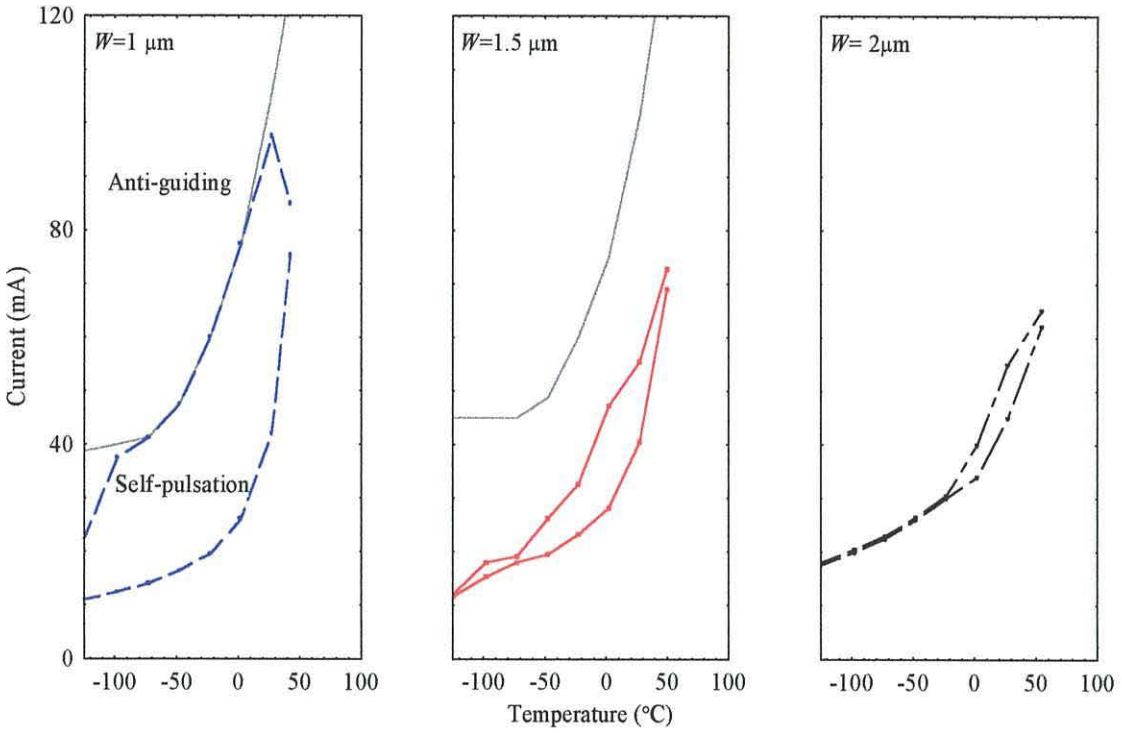

Fig. 4.13 *Current bounds for self-pulsation (and anti-guiding boundary if observed) versus temperature for three different stripe widths (d_p=0.15 μm & d_b=0.4 μm).*

with the optical confinement layer, d_p, behaving in a far more influential manner than the blocking layer thickness, d_b, due to its position next to the active layer. It is also worth noting that the number of combinations of d_b and d_p offering self-pulsation increases with a decreasing stripe width. A slight reduction in the lateral dimension of the gain section therefore gives rise to a decrease in the differential gain (in the active region) and/or increase in differential absorption (in the absorber) at turn-on, which increases the probability of achieving self-pulsation.

Now that it is known which combinations of variables provide the desired emission at 0 °C it will be of interest to study how a change in stripe width affects the current and temperature bounds for self-pulsation. Setting the blocking and optical confinement layer thicknesses at constant values, the results are displayed in fig. 4.13. The most notable observation is the significant reduction in the bounds of the operating current. This is a further consequence of the variation in the differential gain/absorption relationship with the interaction "weakening" as one increases the

gain within the cavity. It is also worth noting that the anti-guiding limit for a particular temperature increases with the stripe width as a higher proportion of the carriers injected into the device enter the absorber, i.e. reducing the index discontinuity. As a result when the stripe is 1 μm wide the majority of the current bounds are limited by the anti-guiding effect whilst the current bounds for the wider stripes are limited by the changes in the differential gain/absorption relationship at turn-on. [*Note*: When the stripe is 2 μm wide not enough carriers enter the absorber to cause any index discontinuity, so no anti-guiding bounds are observed.]

At low temperatures fig. 4.13 illustrates how the threshold current, I_{th}, increases with the stripe width as the reduction in gain and increase in absorption causes the absorption-induced effects to become more dominant. However, a decrease in the amount of absorption per unit volume is observed (with increasing W), leading to a reduction in the threshold current density, J_{th} (as $I_{th} \propto W J_{th}$). At higher temperatures the leakage current dominates the emission with an increase in the stripe width now causing a decrease in the threshold current whilst also increasing the maximum operating temperature of the self-pulsation. It is therefore apparent that the leakage current takes longer to affect the wider widths.

This trend may be explained by considering the quantity of absorption within the device for a given current. It is known that as one decreases the stripe the amount of absorption per unit volume increases, thus increasing the threshold current density of the device. As a results the amount of leakage per unit volume is also increased, thereby disrupting the emission and stopping self-pulsation at lower temperatures due to the changes in the differential gain/absorption interaction. At low temperatures it is solely the variation in absorption per unit volume (due to W) that decreases the separation between the threshold current bounds. However, once the leakage current begins to dominate these trends suddenly change as the deleterious effects of the carrier overflow takes longer to affect the wider stripe widths. As a consequence the wider stripe offers the lowest current and current density thresholds for self-pulsation whilst also emitting at the highest temperatures, however, 70 °C emission isn't available.

Fig. 4.14 shows how a change in the thickness of the blocking layer affects the

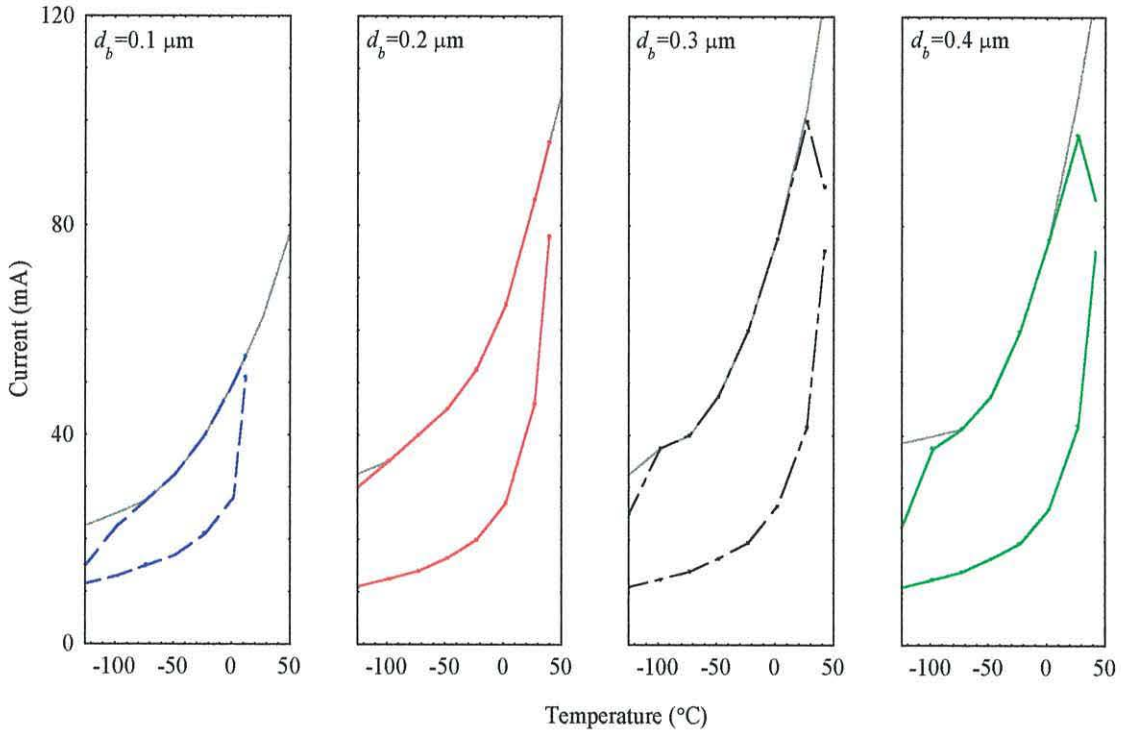

Fig. 4.14 *Anti-guiding bounds and the self-pulsation operating limits for four different blocking layers (W=1 μm & d_p=0.15 μm).*

temperature and current bounds. Taking constant values for the stripe width and the thickness of the optical confinement layer, variations in the bounds are now a consequence of the changes in the built-in refractive index step and the amount of absorption on offer. This point is emphasised as one compares figs. 4.4 and 4.14. Now fig. 4.4 shows that the rate of change of the built-in refractive index step and absorption decreases as one increases the blocking layer thickness as both values "flatten out" when d_b is set above approximately 0.3 μm (for a constant d_p). As a result the current bounds for self-pulsation for the thicker blocking layers are very similar with more pronounced changes observed as one reduces the value to 0.2 and 0.1 μm, as displayed in fig. 4.14. As a consequence a thick optical confinement layer provides an obvious improvement in the operating current range with the upper bound for self-pulsation being limited by the anti-guiding bound which increases with d_b.

More subtle improvements are observed for the threshold current and

maximum temperature limits with both being improved as one increases the blocking layer thickness. The lower threshold current is attributed to the decreasing amount of absorption, as summarised in fig. 4.4(b), however, the increase in the maximum operating temperature is more complicated. For the case of the 1 μm stripe width were there exists a wide operating current range the maximum temperature for self-pulsation is limited by two different effects, dependent on the thickness of the blocking layers.

For small values, i.e. ≤0.2 μm, the built-in refractive index step is small so the anti-guiding bounds occur at low operating currents. As a consequence, once the leakage current is activated the maximum temperature is limited by the anti-guiding boundary, i.e. at the point where the lower bound for self-pulsation meets the anti-guiding limit. For thicker blocking layers, i.e. ≥0.3 μm, the anti-guiding boundary is increased. As a result the lower bounds for self-pulsation are always less than this anti-guiding threshold. Now the leakage current is a function of current density, J, through equation (3.44). So, for the two configurations displayed in fig. 4.14, i.e. d_b=0.3 and 0.4 μm, an increase in the maximum temperature operation is due to the reduction of the thermally activated leakage current, thereby allowing the differential gain/absorption interaction to hold at higher temperatures. The changes in the current and temperature limits due to a varying blocking layer thickness are therefore quite subtle. However, it still appears that 70 °C self-pulsation is unattainable.

By setting the optical confinement layer thickness as a variable and keeping the stripe width and blocking layer values constant the influence of the optical confinement layer is shown in fig. 4.15. The results displayed in fig. 4.12 indicate that the significant rate of change in index step and absorption contribute to very few configurations offering self-pulsation at 0 °C (for a given W and d_b). As a consequence any change in d_p has a notable effect on the temperature and current bounds for self-pulsation, as displayed in fig. 4.15. As is to be expected, as one thickens the optical confinement layer an increase in absorption and subsequent increase in the threshold current is observed. In theory the operating current range should also improve as the differential absorption in the cavity increases. This is indeed true for the smaller thicknesses, however, as one increases d_p the built-in

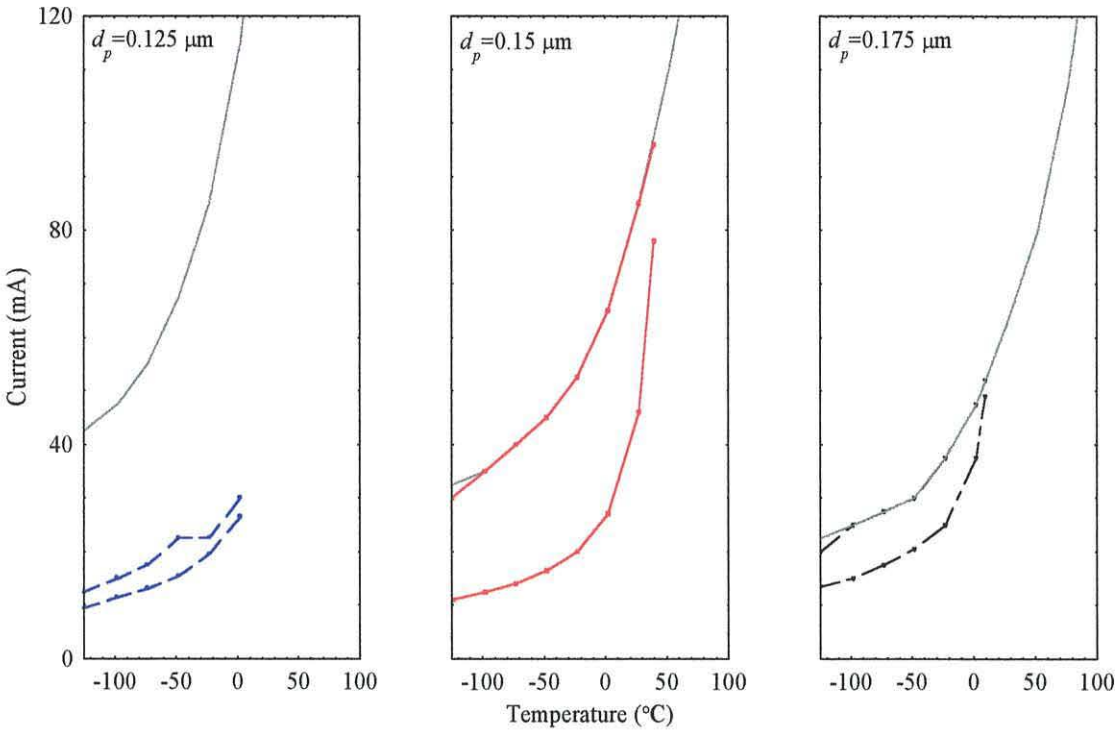

Fig. 4.15 *Anti-guiding bounds and the self-pulsation operating limits for three different optical confinement layers (W=1 μm & d_b=0.2 μm).*

refractive index step decreases and therefore becomes more influential. As a result the anti-guiding bound limits the self-pulsation causing the range to be reduced, as observed when $d_p \geq 0.15$ μm.

As the influence of the anti-guiding bound becomes more pronounced changes in the maximum operating temperature are observed. For the narrowest optical confinement layer a small amount of absorption is on offer combined with a sufficiently large built-in refractive index step. The thermally activated leakage current and the differential gain/absorption relationship therefore limit the operating temperature. For the larger values the carrier overflow and the anti-guiding bounds limit the maximum operating temperature, as was mentioned when discussing fig. 4.14. Due to the changes in these limiting factors the highest temperature for self-pulsation occurs when d_p is 0.15 μm thick, i.e. offering emission at 39.5 °C, however, the 70 °C threshold is still not available.

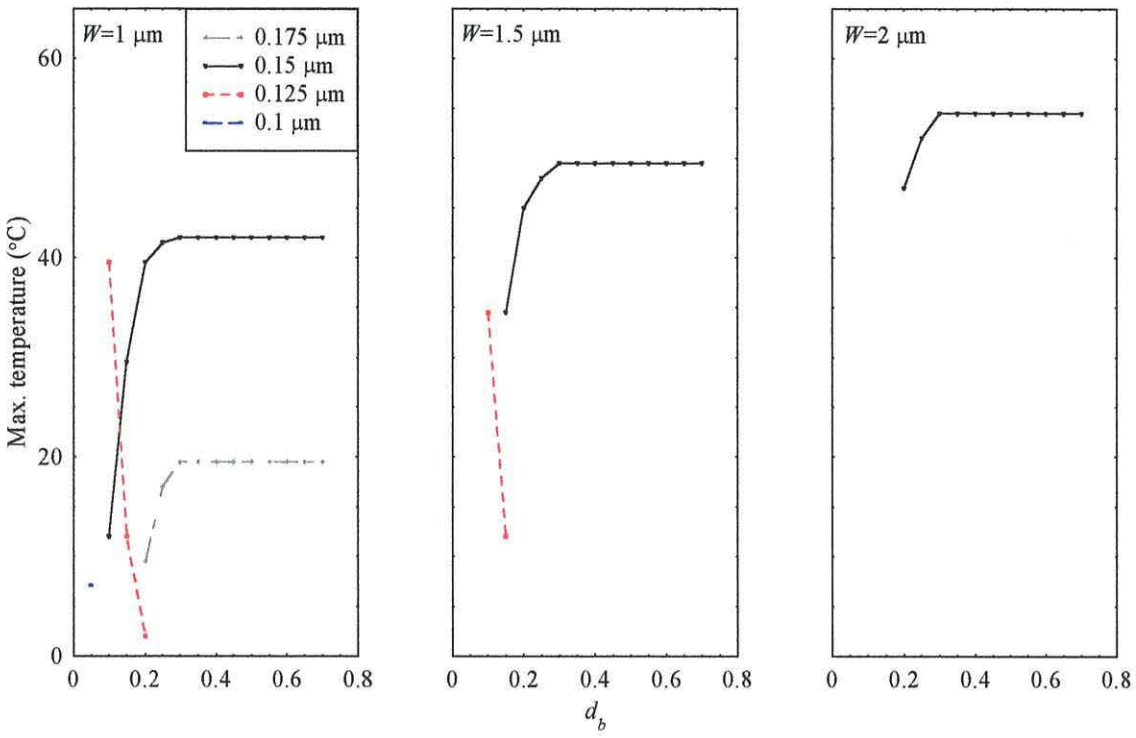

Fig. 4.16 *Maximum operating temperatures of the configurations that offer self-pulsation above 0 °C.*

All of the results presented in figs. 4.14 and 4.15 are for a stripe width of 1 μm. These diagrams illustrate the sensitivity of the self-pulsation to changes in absorption and the built-in refractive index step (particularly at high temperatures) with the temperature threshold being unattainable in all cases. Fig. 4.13 indicates that anti-guiding is less of a problem when using a wider stripe (due to the diminishing influence of the carrier-induced changes in the refractive index step), with self-pulsation being available at higher temperatures due to the suppression of the leakage current.

With this in mind, a general summary of the maximum operating temperature is shown in fig. 4.16 for all configurations that offer self-pulsation, i.e. those displayed in fig. 4.12. The graphs give an indication of the different limiting factors that affect the self-pulsation at high currents and high temperatures. For a thick optical confinement layer, i.e. ≥0.15 μm, the maximum temperature is limited by the anti-guiding and leakage effects. A change in the blocking layer thickness therefore

causes the maximum temperature to vary in proportion with the changes in the index step, as displayed in fig. 4.4(a). For a narrower d_p, i.e. ≤0.125 μm, an adequate built-in refractive index step is on offer. As one varies d_b the maximum operating temperature is now limited by the leakage current and absorption. As a result the upper temperature bounds now vary in proportion with the absorption, as displayed in fig. 4.4(b).

Although displaying some interesting physics the results displayed in fig. 4.16 indicate that no combination gives rise to self-pulsation anywhere near the temperature range required for optical storage purposes. Although the laser offers a method of achieving low threshold current emission once the leakage current is initiated the diffusion of carriers into the absorber is severely effected and therefore affects the self-pulsation. Following the trends observed in fig. 4.16 it is evident that a wide width and/or narrow optical confinement layer would be required for self-pulsation at 70 °C. However, as one increases the stripe width beyond 2 μm, the combinations of d_p and d_b combine poorly with the lateral diffusion characteristics of the active region, resulting in a small amount of absorption and no self-pulsation. Indeed, the small diffusion length associated with the AlGaInP material system [29] plays a fundamental role in this process as it limits the amount of carriers that experience absorption, i.e. in comparison to a GaAs device less carriers diffuse into the absorber (for a given carrier density) [38]. As for the case of a small optical confinement layer it is clear that such a value gives rise to an insufficient amount of absorption to achieve any self-pulsation. A real refractive index guided device grown in the AlGaInP material system is therefore very unlikely to achieve the high temperature self-pulsation that is required for optical storage devices.

4.6 Conclusions

The work in this chapter has investigated the self-pulsating characteristics of the real refractive index guided laser diode for optical storage applications. In order to achieve emission at 650 nm a simulation of a device fabricated in the AlGaInP material system was presented. As a consequence a thermally activated leakage

current is inevitable so the active region was designed to maximise carrier confinement. A key property of this particular laser is the wide-ranging amount of absorption that is on offer due to the weak lateral carrier confinement. For an accurate estimate of these changes the built-in properties of the cavity were modelled for variations in the blocking and optical confinement layer thicknesses.

The results have shown that the AlGaInP real refractive index guided laser is unsuitable for self-pulsation at high temperatures (so an investigation involving the power and operating current conditions wasn't required). Using three variables to study the built-in and dynamical properties of the laser only certain configurations combine sufficiently with the small diffusion length to offer self-pulsation at 0 °C. In most cases, at approximately room temperature the deleterious effects of the thermally activated leakage current come to the fore, with self-pulsation stopping before the 70 °C threshold.

The problems are primarily caused by the severe leakage out of the active layer at high temperatures (with the gain section in particular) creating a highly inefficient laser that is characterised by an "exponential-shift" in the current bounds. As a result the differential gain/absorption relationship is disrupted, stopping the self-pulsation at approximately room temperature. Due to the weakly index guiding nature of the device anti-guiding can also arise. In most cases a sufficient built-in refractive index step is provided, so this carrier-induced problem only hampers the performance of the laser at very high operating currents. However, there are occasions, e.g. W=1 μm, d_p=0.175 μm and d_b=0.2 μm, where the carrier-induced refractive index combines with a small index step to limit the current and temperature bounds, i.e. through anti-guiding, thereby disrupting the emission before any leakage induced effects.

The results outlined above indicate that the real refractive index guided laser is unsuitable for high temperature self-pulsation when fabricated in the AlGaInP material system. Unless improvements in carrier confinement are achieved, e.g. through research into multi-quantum barriers, the carrier overflow out of the active region will severely limit the high temperature performance of the device. It is therefore apparent that an alternative structure is required to evoke 70 °C emission, i.e. a more flexible self-pulsating laser that is affected less by the leakage current.

References

[1] H. Asahi, Y. Kawamura and H. Nagai, "Molecular beam epitaxial growth of InGaAlP on (100) GaAs," *J. Appl. Phys.*, vol. 53, pp. 4928-4931, 1982.

[2] M. Ikeda, Y. Mori, H. Satoh, K. Kaneko and N. Watanabe, "Room-temperature continuous-wave operation of an AlGaInP double-heterostructure laser grown by atmospheric-pressure metalorganic chemical vapor-deposition," *Appl. Phys. Lett.*, vol. 47, pp. 1027-1028, 1985.

[3] K. Kobayashi, S. Kawata, A. Gomyo, I. Hino and T. Suzuki, "Room-temperature *cw* operation of AlGaInP double-heterostructure visible lasers," *Electron. Lett.*, vol. 21, pp. 931-932, 1985.

[4] K. Kobayashi, S. Kawata, A. Gomyo, I. Hino and T. Suzuki, "661.7 nm room-temperature *cw* operation of AlGaInP double-heterostructure lasers with aluminium-containing quaternary active layer," *Electron. Lett.*, vol. 21, pp. 1162-1163, 1985.

[5] K. Kobayashi, I. Hino, A. Gomyo, S. Kawata and T. Suzuki, "AlGaInP double heterostructure visible-light laser-diodes with a GaInP active layer grown by metalorganic vapor-phase epitaxy," *IEEE J. Quantum Electron.*, vol. 23, pp. 704-711, 1987.

[6] M. Ikeda, A. Toda, K. Nakano, Y. Mori and N. Watanabe, "Room-temperature continuous-wave operation of a GaInP/AlGaInP multiquantum well laser grown by metalorganic chemical vapor-deposition," *Appl. Phys. Lett.*, vol. 50, pp. 1033-1034, 1987.

[7] H. Tanaka, Y. Kawamura, S Nojima, K. Wakita and H. Asahi, "InGaP/InGaAlP double-heterostructure and mutiquantum-well laser diodes grown by molecular-beam epitaxy," *J. Appl. Phys.*, vol. 61, pp. 1713-1719, 1987.

[8] T. Katsuyama, I. Yoshida, J. Shinkai, J. Hashimoto and H. Hayashi, "Very low threshold current AlGaInP/$Ga_xIn_{1-x}P$ strained single quantum-well visible laser diode," *Electron. Lett.*, vol. 26, pp. 1375-1377, 1990.

[9] T. Katsuyama, I. Yoshida, J. Shinkai, J. Hashimoto and H. Hayashi, "High-temperature (>150°C) and low threshold current operation of AlGaInP/$Ga_xIn_{1-x}P$ strained multiple quantum-well visible laser diodes," *Appl. Phys. Lett.*, vol. 59, pp. 3351-3353, 1991.

[10] P. Zory Jr., *Quantum Well Lasers*, Academic Press, 1993.

[11] D. P. Bour, N. W. Carlson and G. A. Evans, "Characteristic temperature of GaInP/AlGaInP single quantum well lasers," *Electron. Lett.*, vol. 25, pp. 1243-1245, 1989.

[12] D. P. Bour, D. W. Treat, R. L. Thornton, R. S. Geels and D. F. Welch, "Drift leakage current in AlGaInP quantum-well lasers," *IEEE J. Quantum Electron.*, vol. 29, pp.1337-1343, 1993.

[13] P. S. Zory Jr., A. R. Reisinger, R. G. Waters, L. J. Mawst, C. A. Zmudzinski, M. A. Emanuel, M. E. Givens and J. J. Coleman, "Anomalous temperature dependence of threshold for thin quantum well AlGaAs diode lasers," *Appl. Phys. Lett.*, vol. 49, pp. 16-18, 1986.

[14] A. Miller, M. Ebrahimzadeh and D. M. Finlayson, *Semiconductor Quantum Optoelectronics: From Quantum Physics to Smart Devices*, SUSSP Publications, 1999.

[15] K. Kishino, A. Kikuchi, Y. Kaneko and I. Namura, "Enhanced carrier confinement effect by the multiquantum barrier in 660 nm GaInP/AlInP visible laser," *Appl. Phys. Lett.*, vol. 58, pp. 1822-1824, 1991.

[16] H. Hamada, R. Hiroyama, S. Honda, M. Shono, K. Yodashi and T. Yamaguchi, "AlGaInP strained multiple-quantum-well visible laser diodes ($\lambda_L \leq 630$ nm band) with a multiquantum barrier grown on misorientated substrates," *IEEE J. Quantum Electron.*, vol. 29, pp. 1844-1850, 1993.

[17] J. Hashimoto, T. Katsuyama, J. Shinkai, I. Yoshida and H. Hayashi, "High-performance of AlGaInP/GaInP visible lasers by strain induced effects," *Electron. Lett.*, vol. 27, pp. 2028-2030, 1991.

[18] J. Hashimoto, T. Katsuyama, J. Shinkai, I. Yoshida and H. Hayashi, "Effects of strained-layer structures on the threshold-current density of AlGaInP/GaInP visible lasers," *Appl. Phys. Lett.*, vol. 58, pp. 879-880, 1991.

[19] M. Mannoh, J. Hoshina, S. Kamiyama, H. Ohta, Y. Ban and K. Ohnaka, "High-power and high-temperature operation of GaInP/AlGaInP strained multiple quantum-well lasers," *Appl. Phys. Lett.*, vol. 62, pp. 1173-1175, 1993.

[20] S. Kamiyama, T. Uenoyama, M. Mannoh, Y. Ban and K. Ohnaka, "Analysis of GaInP/AlGaInP compressive-strained multiple-quantum-well laser," *IEEE J. Quantum Electron.*, vol. 30, pp. 1363-1369, 1994.

[21] A. T. Menney, A. D. Prins, A. F. Phillips, J. L. Sly, E. P. O'Reilly, D. J. Dunstan and A. R. Adams, "Determination of the band structure of disordered AlGaInP and its influence on visible-laser characteristics," *IEEE J. Select. Topics Quantum Electron.*, vol. 1, pp. 697-706, 1995.

[22] P. Blood and P. M. Smowton, "Strain dependence of threshold current in fixed-wavelength GaInP laser-diodes," *IEEE J. Select. Topics Quantum Electron.*, vol. 1, pp. 707-711, 1995.

[23] P. Blood and P. M. Smowton, "GaInP-(Al_yGa_{1-y})InP quantum-well lasers for high-temperature operation," *IEEE J. Quantum Electron.*, vol. 31, pp. 2159-2164, 1995.

[24] D. F. Welch, T. Wang and D. R. Scifres, "Low threshold current lasers emitting at 637 nm," *Electron. Lett.*, vol. 27, pp. 693-695, 1991.

[25] Y. Ohba, M. Ishikawa, H. Sugawara, M. Yamamoto and T. Nakanisi, "Growth of high quality InGaAlP epilayers by MOCVD using methyl metalorganics and their application to visible semiconductor lasers," *J. Crystal Growth*, vol. 77, pp. 374-379, 1986.

[26] Y. Ohba, Y. Nishikawa, C. Nozaki, H. Sugawara and T. Nakanisi, "A study of p-type doping for AlGaInP grown by low pressure MOCVD," *J. Crystal Growth*, vol. 93, pp. 613-617, 1988.

[27] H. Asahi, Y. Kawamura and H. Nagai, "Molecular-beam epitaxial-growth of InGaAlP visible laser-diodes operating at 0.66-0.68 μm at room temperatures," *J. Appl. Phys.*, vol. 54, pp. 6958-6964, 1983.

[28] I. Hino, S. Kawata, A. Gomyo, K. Kobayashi and T. Suzuki, "Continuous wave operation (77-K) of yellow (583.6 nm) emitting AlGaInP double heterostructure laser-diodes," *Appl. Phys. Lett.*, vol. 48, pp. 557-558, 1986.

[29] O. Imafuji, T. Fukuhisa, M. Yuri, M. Mannoh, A. Yoshikawa and K. Itoh, "Low operating current and high-temperature operation of 650-nm AlGaInP high-power laser diodes with real refractive index guided self-aligned structure," *IEEE J. Select. Topics Quantum Electron.*, vol. 5, pp. 721-728, 1999.

[30] O. Imafuji, T. Takayama, H. Sugiura, M. Yuri, H. Naito, M. Kume and K. Itoh, "600mW *cw* single-mode GaAlAs triple-quantum-well laser with a new index guided structure," *IEEE J. Quantum Electron.*, vol. 29, pp. 1889-1894, 1993.

[31] H. Tanaka, Y. Kawamura and H. Asahi, "Refractive indices of $(Al_{0.7}Ga_{0.3})_{0.51}In_{0.49}P$ lattice matched to GaAs," *J. Appl. Phys.*, vol. 59, pp. 985-986, 1986.

[32] H. D. Summers, P. Blood and P. Rees, "Gain-current characteristics of strained AlGaInP quantum-well lasers," *Appl. Phys. Lett.*, vol. 63, pp. 2792-2794, 1993.

[33] P. M. Smowton, H. D. Summers, P. Rees and P. Blood, "Optimization of 670-nm strained-quantum-well laser-diodes for high-temperature operation," *IEE Proc. Optoelectronics*, vol. 141, pp. 136-140, 1994.

[34] W. W. Chow, S. W. Koch and M. Sargent III, *Semiconductor Laser Physics*, Springer-Verlag, Berlin, 1994.

[35] H. D. Summers and P. Rees, "Thermal limitation of self-pulsation in 650 nm AlGaInP laser diodes with an epitaxially integrated absorber," *Appl. Phys. Lett.*, vol. 71, pp. 2665-2667, 1997.

[36] D. R. Jones, P. Rees, I. Pierce and H. D. Summers, "Theoretical optimization of self-pulsating 650-nm-wavelength AlGaInP laser diodes," *IEEE J. Select. Topics Quantum Electron.*, vol. 5, pp. 740-744, 1999.

[37] M. Yamada, "A theoretical analysis of self-sustained pulsation phenomena in narrow-stripe semiconductor lasers," *IEEE J. Quantum Electron.*, vol. 29, pp. 1330-1336, 1993.

[38] M. Yuri, S. Harris, T. Takayama, O. Imafuji, H. Naito, M. Kume, K. Itoh and T. Baba, "Two-dimensional analysis of self-sustained pulsation for narrow-stripe AlGaAs lasers," *IEEE J. Select. Topics Quantum Electron.*, vol. 1, pp. 473-479, 1995.

[39] R. W. Dixon and W. B. Joyce, "A possible model for sustained oscillations (pulsations) in (Al,Ga)As double-heterostructure lasers," *IEEE J. Quantum Electron.*, vol. 15, pp. 470-474, 1979.

[40] H. D. Summers, C. H. Molloy, P. M. Smowton, P. Rees, I. Pierce and D. R. Jones, "Experimental analysis of self-pulsation in 650-nm-wavelength AlGaInP laser diodes with epitaxial absorbing layers," *IEEE J. Select. Topics Quantum Electron.*, vol. 5, pp. 745-749, 1999.

[41] T. Takayama, O. Imafuji, M. Yuri, H. Naito, M. Kume, A. Yoshikawa and K. Itoh, "800 mW peak-power self-sustained pulsation GaAlAs laser diodes," *IEEE J. Select. Topics Quantum Electron.*, vol. 1, pp. 562-568, 1995.

Chapter 5

Red self-pulsating laser diode with epitaxial absorber layers

5.1 Introduction

Having studied the performance of the real refractive index guided laser in the previous chapter it is clear that such a weakly index guided structure is unsuitable for 70 °C self-pulsation at 650 nm. The main problems arise above room temperature when the leakage current within the AlGaInP device reduces the efficiency of the active region. As a result the self-pulsation mechanism is disrupted leading to changes in the differential gain/absorption interaction and/or the lateral refractive index profile which consequently stops the pulsed emission.

Due to the problems encountered in the previous chapter an alternative cavity design is required which is affected less by the carrier overflow and therefore provides high temperature self-pulsation. With this in mind the laser diode with epitaxial absorber layers will now be investigated. In such a device the necessary absorption is supplied by growing quantum wells of suitable composition in the p-

cladding layer, offering a more flexible "designer" absorber. The inclusion of the saturable absorber in the barrier minimises the leakage of carriers out of the active region into the absorbing region allowing self-pulsation to occur at high temperatures. Carrier and optical confinement is improved allowing one to neglect the lateral properties of the device. As a consequence many problems encountered in the previous chapter, e.g. anti-guiding, are avoided.

Having already described the properties of this particular device in chapter 3, the chapter is set out in the following manner. To start, a description of the structure is given, using the AlGaInP material system to achieve 650 nm emission. The rate equations are then implemented and used to optimise the self-pulsation subject to the absorber design parameters that are on offer. The cavity length and reflectivity parameters are then studied in an attempt to optimise the laser even further. An optimum cavity design is then presented, outlining the desirable configurations that offer high temperature emission at the designated power thresholds.

5.2 Laser structure

A schematic diagram of the laser diode with epitaxial absorber layers is displayed in fig. 5.1. To obtain self-pulsation at high temperatures it is essential that the gain section offers maximum carrier confinement in order to minimise the thermally activated leakage current. With this in mind the active region is the same as that outlined in chapter 4, providing optimum gain per injection current at 650 nm for a structure without any absorber layers [1].

To achieve self-pulsation it is important to maximise the differential absorption in the absorber relative to the differential gain in the active region. To achieve this condition narrow $Ga_{0.39}In_{0.61}P$ quantum wells with high compressive strain are placed in the p-doped cladding layer [1-3] at a distance of 0.115 μm away from the active region. Fig. 5.1 shows an absorber section comprising of three quantum wells, however, an investigation to find the best absorber configuration will be given later in an attempt to optimise the self-pulsation characteristics. To ensure

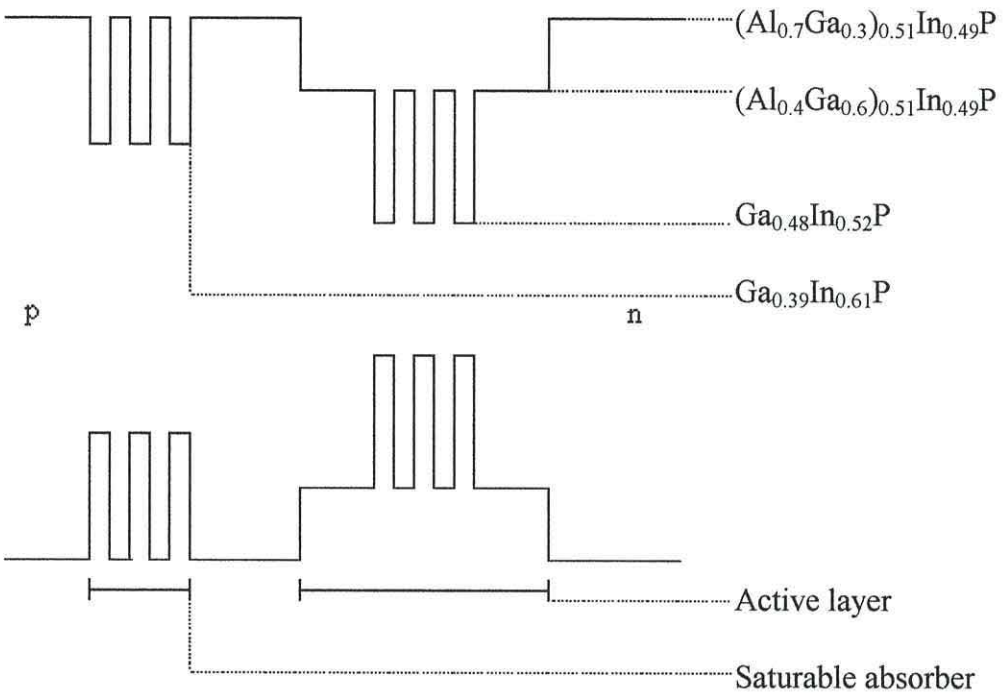

Fig. 5.1 *Schematic diagram of the AlGaInP laser diode with epitaxial absorber layers.*

that the inequality described in equation (3.44) holds true the carrier lifetime in the absorber section must be shorter than that in the gain wells to maximise *dS/dt* in equation (3.34). This is achieved by highly p-doping the absorber wells and has been measured using time resolved photoluminescence (PL), giving a value of 0.3 ns [4].

5.3 Initial results

5.3.1 Operating regimes

Using the rate equation model derived in section 3.4.2 it is now possible to simulate the emission of this particular laser. The parameters displayed previously in table 4.3 (combined with a stripe width of 5 μm) and the necessary gain/absorption calculations are entered into the rate equations then this coupled system is solved

using the procedure outlined in appendix 2, section A2.2. The photon emission is studied for self-pulsation subject to the conditions stipulated in appendix 3.

Fig. 5.2 shows the typical output at room temperature where three operating regimes are observed. For a low current density the amount of gain produced by the active region is not sufficient to overcome the high amount of loss within the cavity. Self-pulsation is therefore not achieved and an increase in injection current is required. As the current density increases more gain is generated and the difference between optical gain and loss gradually decreases until self-pulsation is detected at a certain threshold current density. At this stage the differential gain/absorption interaction, i.e. from equations (3.44), is sufficient to offer the desired emission. At room temperature the pulse frequency operates in a large-signal regime and is determined solely by the injection current owing to the temperature dependence of the threshold current [3].

Once threshold is achieved, an increase in current density increases the frequency of the emission [3]. However, the differential gain/absorption ratio gradually changes until self-pulsation stops at a current density "upper bound", i.e. at an operating current where the differential gain overcomes the differential absorption, forcing equation (3.44) to fail. At this point the final operating regime is observed, beyond which self-pulsation will not occur, only *cw* emission. [*Note*: For an absorber offering the correct amount of absorption (relative to the gain produced by the active region) the above process will be detected. However, there are situations where an insufficient amount of absorption can be offered. This leads to behaviour similar to a standard laser where the self-pulsation stage is omitted.]

5.3.2 Leakage current considerations

Although a compressively strained active region has been used to minimise the leakage current this non-radiative process still affects the self-pulsation characteristics at high temperatures. This point is emphasised in fig. 5.3 where an absorber configuration of three 40 Å quantum wells (denoted from now on as 3×40 Å) is used. As will be the case throughout this chapter, the emission is examined for self-pulsation at temperatures between -125 and 100 °C. The diagram displays the upper

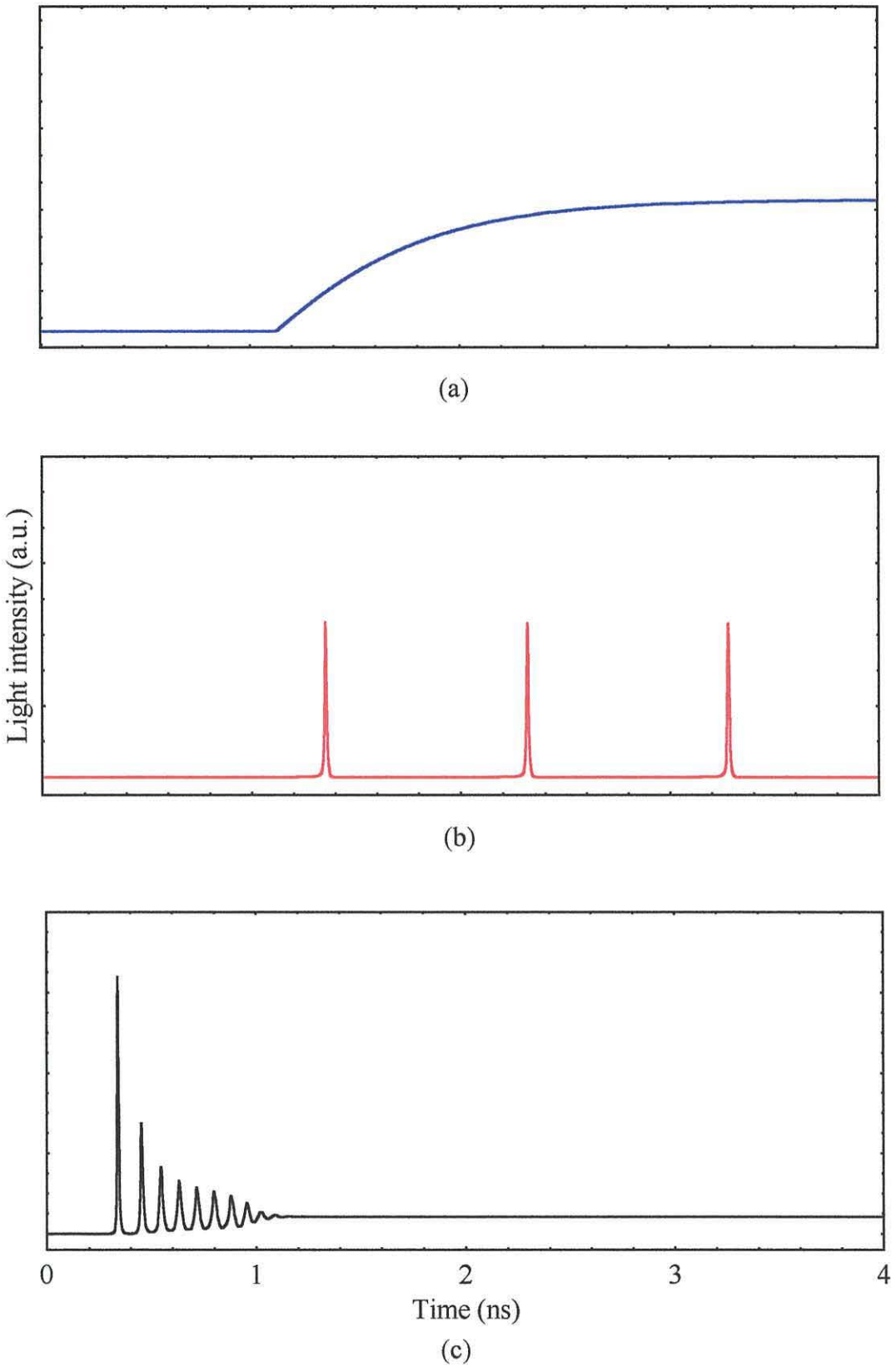

Fig. 5.2 *Temporal behaviour of the photon emission for (a) low, (b) intermediate and (c) high operating currents at room temperature (for an absorber section of 3×55 Å quantum wells).*

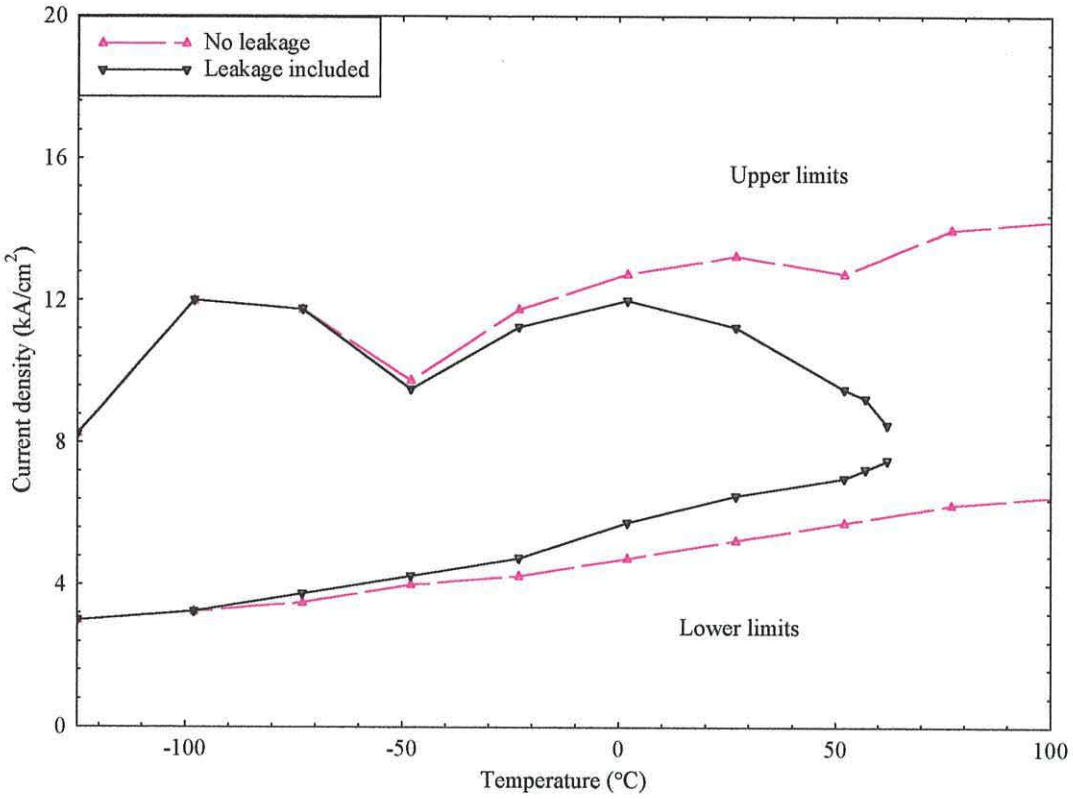

Fig. 5.3 *Self-pulsation bounds with and without leakage for an absorber section of 3×40 Å quantum wells.*

and lower bounds for self-pulsation when the leakage equation is included and omitted from the model, i.e. J_l=0. The results show how the leakage current increases with temperature, not only increasing the threshold current due to carriers escaping from the active region but also decreasing the current density range over which self-pulsation occurs. The emission is effected as the overflowing carriers bleach the absorber wells, disrupting the amount of absorption, and thus influencing the self-pulsation characteristics. An increase in carriers entering the absorber wells damps the non-linear interaction between the gain and absorber regions, i.e. via equation (3.44), and limits the capacity for self-pulsation. When fully bleached no absorption exists in the cavity and therefore no pulsation is seen. As a result of this process self-pulsation stops at approximately 67 °C, whilst the model without leakage continues beyond 100 °C.

The thermally activated leakage current will inevitably arise at high temperatures, causing a rapid change in slope for both upper and lower bounds. There exists a similar occurrence at approximately -50 °C, however, changes in the upper bounds are observed in both cases, i.e. when the leakage is on and off, which indicates that this is not caused by the deleterious effects of the carrier overflow. One may explain this development by considering the sub-bands within the quantum well active region. As one increases the temperature a slight increase in operating current is required to achieve self-pulsation. As a consequence, above -50 °C a large amount of optical gain is required to overcome the absorption. Sufficient gain can only be achieved on the second sub-band optical transition, thereby lowering the wavelength in comparison to the first transition. At this wavelength the absorption in the cavity is different so a change in the threshold current bounds is observed. Two separate processes therefore cause a narrowing of the operating bounds, however, it is the absorber bleaching that one must be wary of if high temperature emission is to be achieved.

The effect of varying the p-doping level is displayed in fig. 5.4, showing the pulsation range as a function of temperature for a structure with 3×40 Å absorber wells. At low temperatures, where current leakage is negligible, this doping density has no effect on the pulsation range. As the temperature increases the higher doping levels are the most effective in suppressing the leakage current, allowing improved self-pulsation characteristics. This example demonstrates the importance of a high p-density, not only to reduce the threshold current but also to achieve self-pulsation at high temperatures. A maximum value of 1×10^{18} cm^{-3} is available and will therefore be used throughout the chapter.

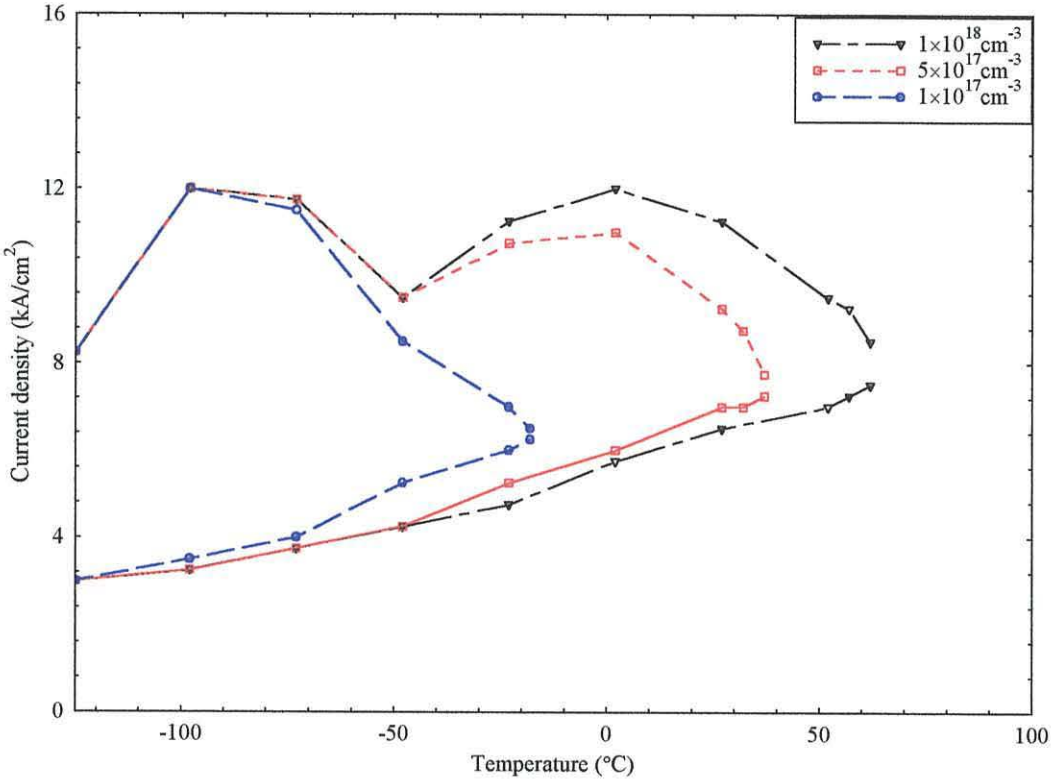

Fig. 5.4 *The upper and lower current density bounds for self-pulsation versus temperature for structures including 3×40 Å absorber wells using three different p-cladding doping levels.*

5.4 Optimisation of the absorber section

5.4.1 Variation in well configuration

The purpose of this chapter is to optimise the self-pulsating laser for optical storage applications. The main factor that determines whether or not self-pulsation is produced is the differential gain/absorption interaction, so the quantum well configuration in the absorber section is a key factor in determining optimum emission characteristics. In this section the absorber structure will be optimised by considering well widths of 25, 40, 55, 70 and 85 Å and well numbers between 1 and 5. The absorber confinement factor, Γ_α, will then be varied accordingly, as displayed in fig.5.5. So, as the well width is increased, the amount of absorption in the system

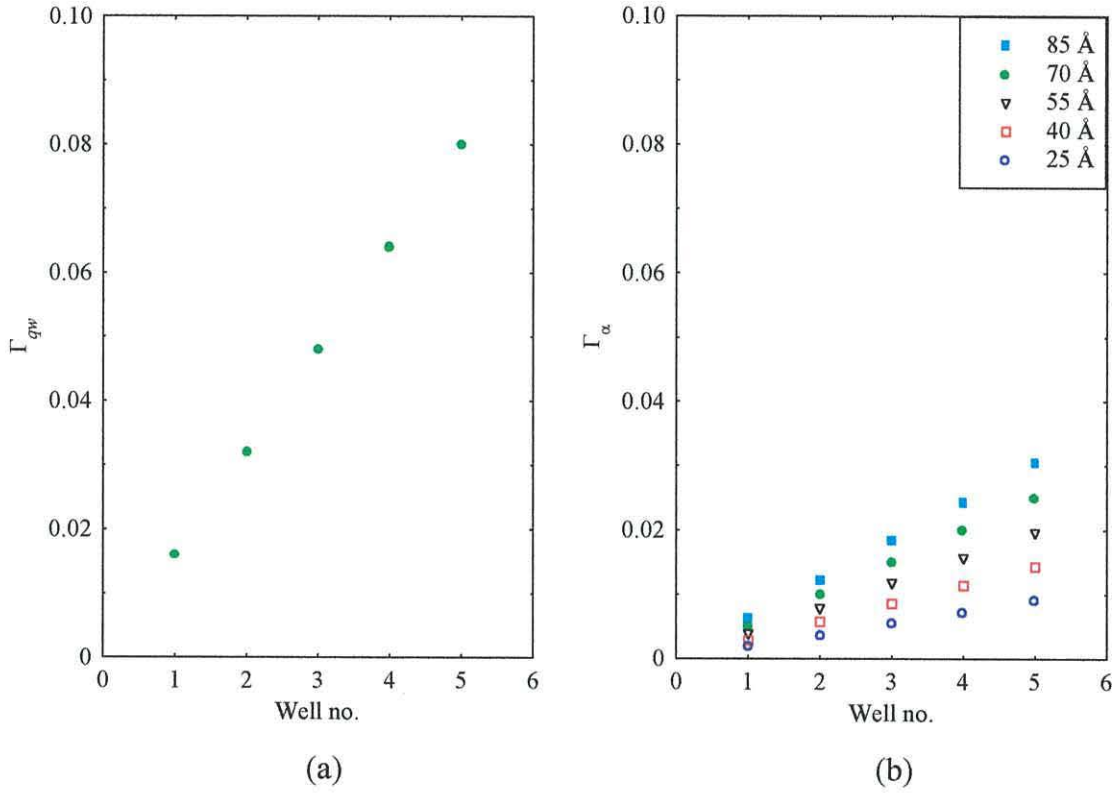

Fig. 5.5 *Transverse confinement factor calculations for a changing quantum well configuration in the (a) gain and (b) absorber sections of the AlGaInP laser diode.*

increases due to the larger overlap with the optical field at the operating wavelength. [*Note*: The linear relationship between well no. and Γ (per well width) stems from the fact that the quantum wells are very small when compared to the optical field.]

When using a single absorber, pulsation is observed for all well widths except for the structure with the 25 Å quantum well. Indeed, no self-pulsation was observed for any of the 25 Å absorber configurations due to the negligible amount of absorption providing insufficient differential absorption characteristics at turn-on. The results for the other absorber structures are shown in fig. 5.6, where the current density at which pulsation begins, together with the upper limit where pulsation is lost, are plotted versus temperature. The lower limits occur at reasonably low currents due to the small amount of absorption offered by the single quantum wells. The current range over which pulsation occurs is very narrow especially for the thinner

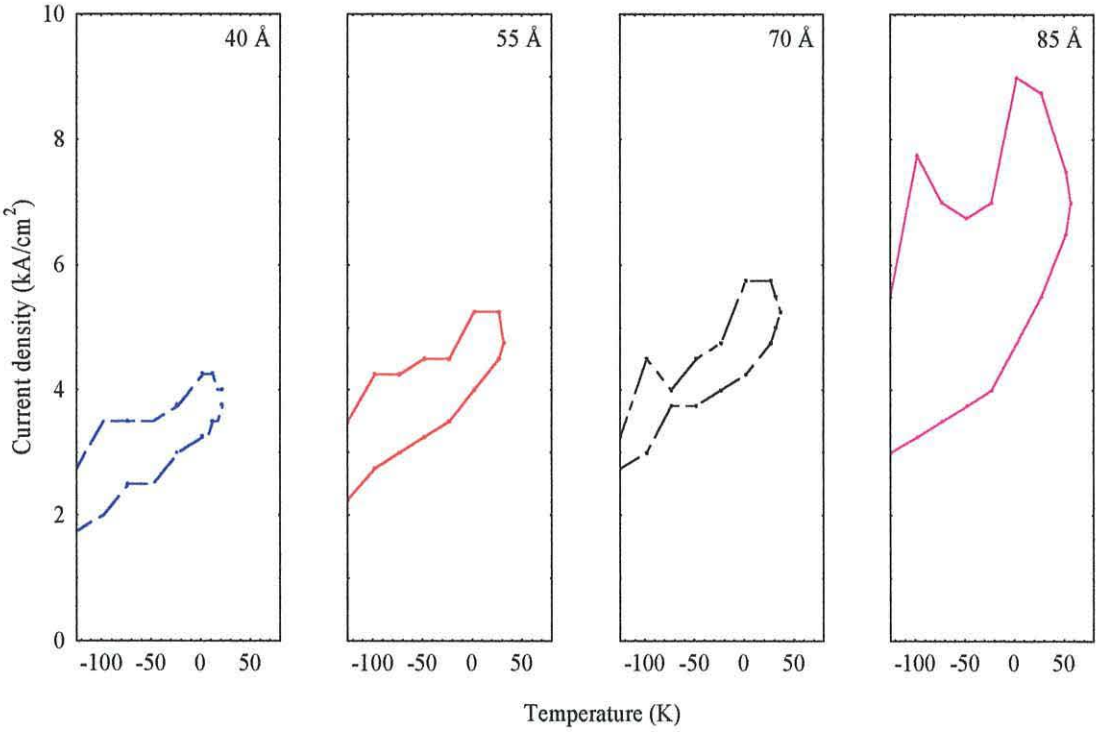

Fig. 5.6 *Upper and lower current density bounds for self-pulsation as a function of temperature for structures including a* ***single*** *40, 55, 70 and 85 Å absorber well.*

wells whilst in all cases the emission ceases well before the 70 °C temperature threshold. This is due to the thermally activated leakage current from the three gain wells being captured in the single absorber well thus bleaching the absorber very effectively at high temperatures. This effect also causes the narrowing of the range of currents over which pulsation is observed at higher temperatures.

For two quantum wells in the absorber section pulsation is observed using the 40, 55, 70 and 85 Å absorber wells as shown in fig. 5.7. The extra absorption due to the additional well increases the current density at which the laser self pulsates and also extends the range of currents over which pulsation is observed. There is a clear trend of increasing threshold current with increasing well width due to the additional absorption. As the well width increases the maximum temperature operation also increases, approaching 80 °C for the 2×85 Å absorber configuration. This is due to the larger volume offered by the wider wells, requiring more carriers to saturate the absorption, therefore offering a higher tolerance to the leakage current as the temperature is increased.

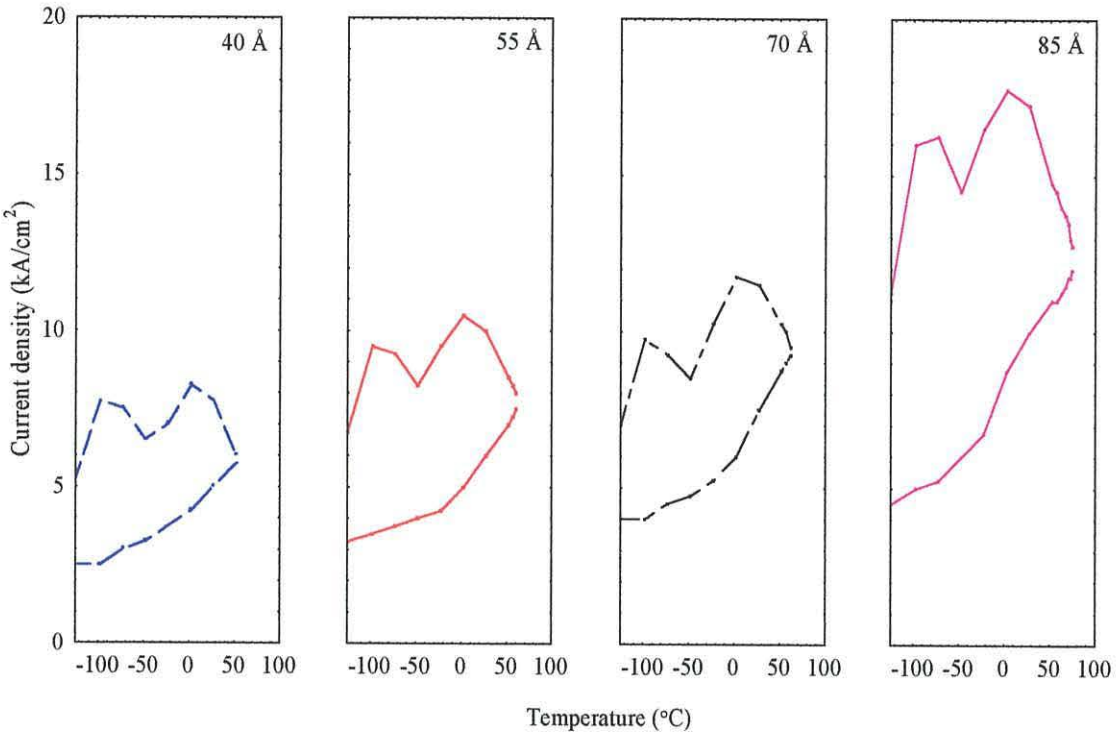

Fig. 5.7 *Current density bounds for self-pulsation as a function of temperature for structures including* ***two*** *40, 55 , 70 and 85 Å absorber wells.*

Fig. 5.8 shows the current density limits for structures including three absorber wells. As in the case of the previous results the lower limit increases due to the additional absorption. However, no self-pulsation is observed for three 85 Å wells as there is too much absorption and the interplay between the gain and absorption fails to materialise, i.e. the amount of gain/absorption at the threshold current density equates to an insufficient differential gain/absorption relationship. The presence of three absorber wells reduces the number of carriers captured per well, therefore bleaching is dramatically reduced and pulsation is now observed at higher temperatures (in comparison to previous results). This indicates that at least three absorber wells are required to achieve self-pulsation at 70 °C but this imposes the penalty of an increased operating current. Further evidence is shown in fig. 5.9. When four wells are placed in the absorber layer the threshold current and maximum temperature operation of the 40 and 55 Å structures increase again whilst the 70 and 85 Å wells provide too much absorption for self-pulsation.

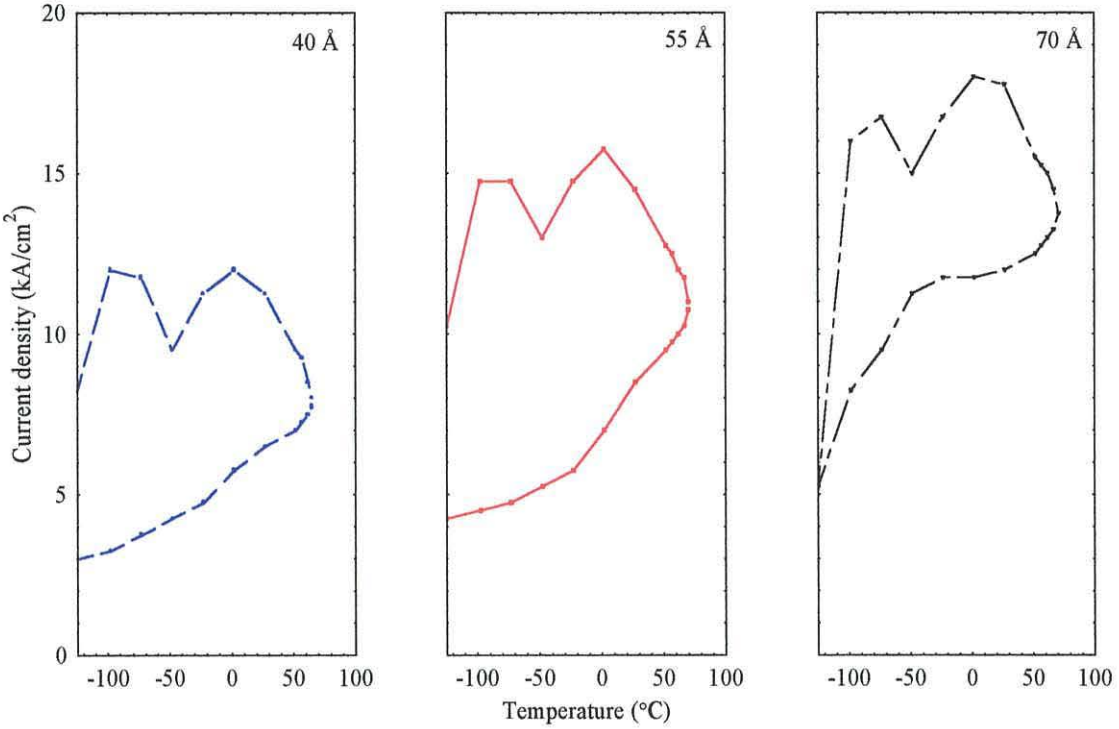

Fig. 5.8 *Current density bounds for self-pulsation as a function of temperature for structures including* ***three*** *40, 55 and 70 Å absorber wells.*

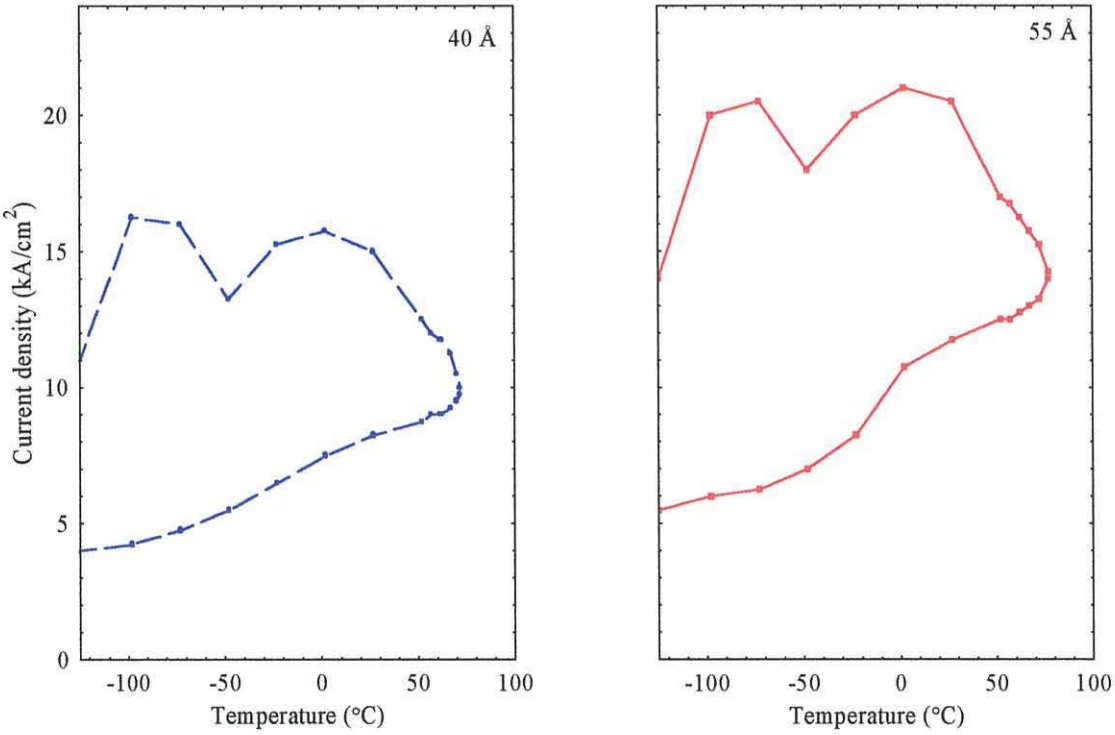

Fig. 5.9 *Current density bounds for self-pulsation as a function of temperature for structures including* ***four*** *40 and 55 Å absorber wells.*

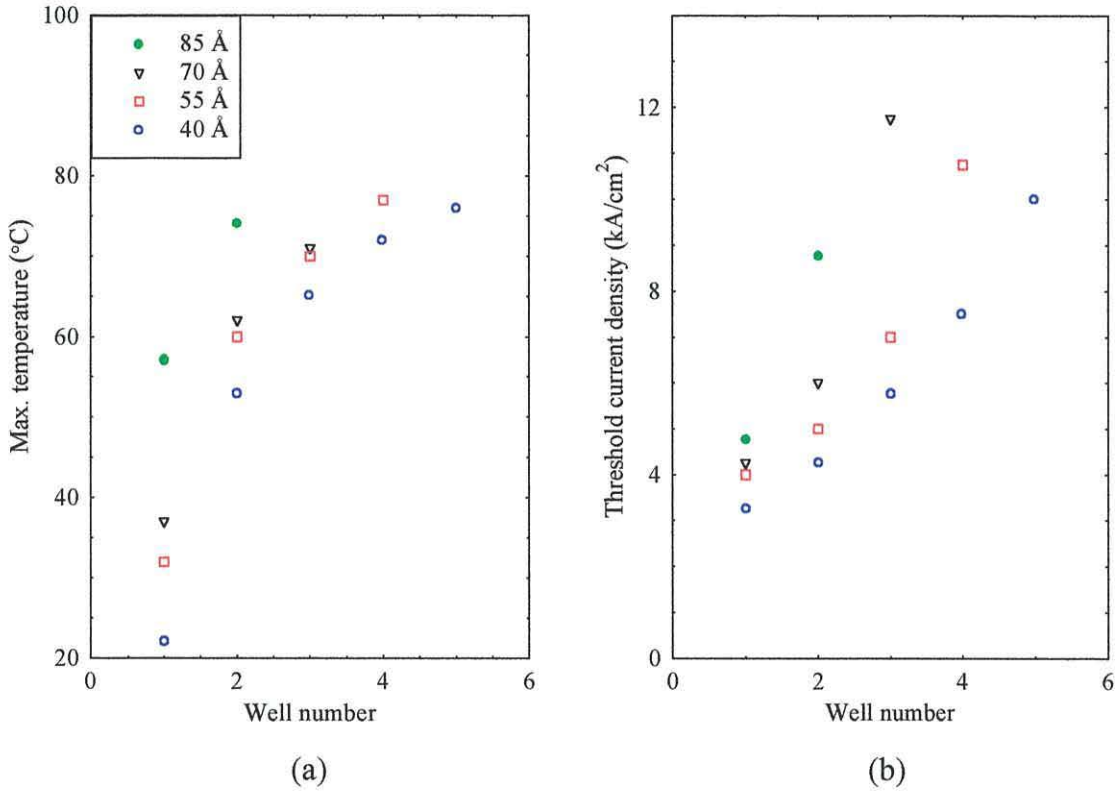

Fig. 5.10 *(a) Maximum temperature operation and (b) threshold current density at 0 °C as a function of absorber well number for four different well widths.*

A summary of the results is shown in fig. 5.10. Part (a) displays the maximum temperature operation per absorber structure. As described earlier, there exists a maximum amount of absorption beyond which self-pulsation will cease. This is evident in the diagram, indicating that only the 40 Å absorber gives rise to any pulsation when the well number increases to five. The effects of absorber bleaching is also apparent, showing further that the thicker well widths offer higher temperature operation. Fig. 5.10(b) summarises how an increasing absorber volume increases the threshold current density for self-pulsation. By studying these two diagrams and considering the results presented so far it is clear that an absorber section of 4×40 Å quantum wells gives rise to the most desirable operating characteristics, achieving high temperature self-pulsation, i.e. >70° C at the lowest possible threshold currents [5].

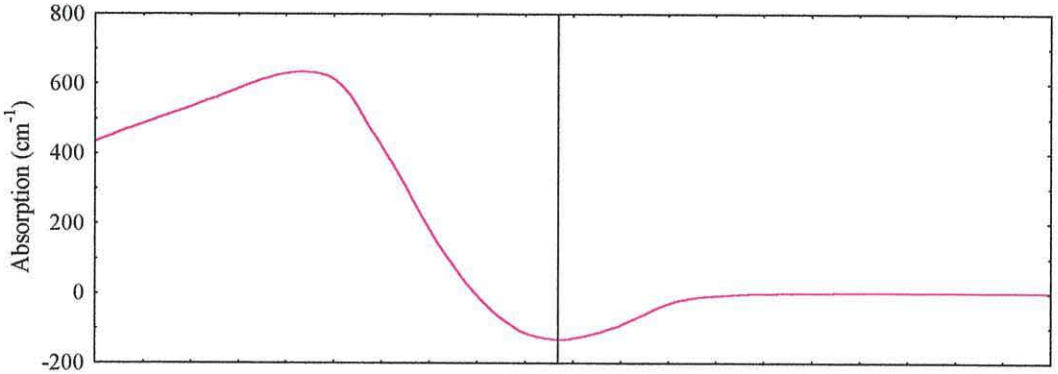

(a)

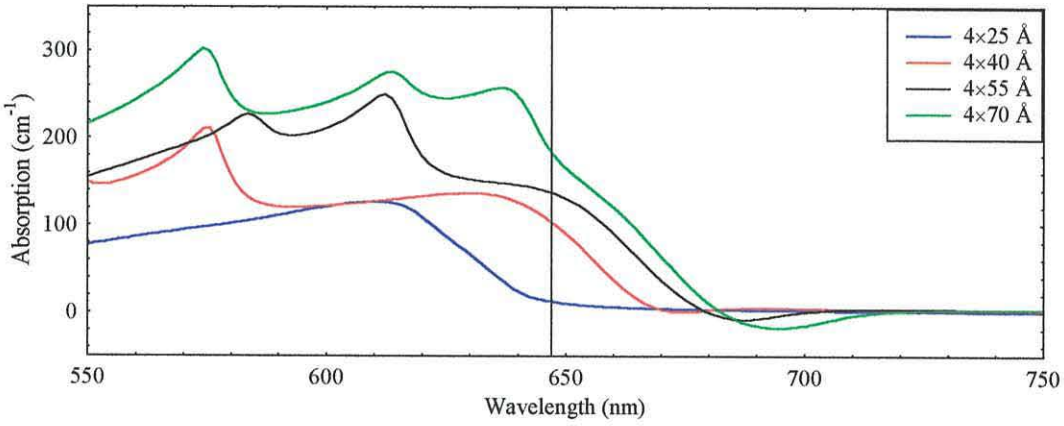

(b)

Fig. 5.11 *(a) Modal gain spectrum at a typical operating carrier density for the 3×70 Å quantum well active region together with (b) the corresponding modal absorption seen in 4 different absorber structures (T=0 ℃).*

The self-pulsation characteristics can be explained in terms of the changing absorption in the absorber layers of different thickness. Fig. 5.11 shows the modal gain for the 3×70 Å quantum well active region and the corresponding modal absorption in the 4×25, 40, 55 and 70 Å absorber quantum wells. The carrier densities are typical of those at the time of emission of an output optical pulse. The lasing wavelength occurs at the peak of the gain in the laser cavity. For the 3×70 Å quantum well active region, it occurs at 648 nm (marked by the vertical line in fig. 5.11) and, hence, it is at this wavelength that the absorption needs to be considered. It can be seen that if 25 Å wells are employed there is very little absorption available at the lasing wavelength due to the confined sub-band energies being higher in these narrow

wells and therefore it is impossible to obtain self-pulsation, even with four wells. For the 70 Å absorber wells the sub-band energy levels are quite low and so a large amount of absorption is seen at the lasing wavelength. This explains why self-pulsation is observed up to three wells but for the four well structure there is too much absorption and so lasing cannot be achieved. In between these extremes the 40 and 55 Å wells give an adequate amount of absorption (at the gain peak) to give rise to self-pulsation which is easily bleached during an output pulse, a characteristic required for self-pulsation.

To analyse the average optical power output of a pulse the following equation is used [6]

$$P = S_{av} h\nu V_p v_g \alpha_m \tag{5.1}$$

where S_{av} gives the average photon density during a single pulse, $h\nu$ describes the energy per photon and V_p represents the cavity volume occupied by the photons. The symbol v_g describes the group velocity and $\alpha_m=(1/L)\ln(1/R)$ gives a value for the mirror losses where L and R represent the cavity length and facet reflectivity respectively. Fig. 5.10(a) indicates that only six absorber configurations achieve self-pulsation above the 70 °C temperature threshold so the power output of these six cases will be studied.

The effect that the operating temperature has on the current density bounds and power output is shown in figs. 5.12(a) and 5.12(b), respectively. The diagrams illustrate how the maximum power varies in proportion with the current density range for self-pulsation. The two graphs are taken for an absorber structure of 4×40 Å quantum wells but the trend is consistent for all the absorber configurations under investigation. The physical reason for this occurrence is fairly trivial – the more carriers entering the active region after turn-on, the greater the power. The results also show the problems of high power operation at high temperatures [5]. As the 70 °C limit is approached leakage effects come to the fore causing the current density range to decrease until pulsed emission ceases at 72 °C when the self-pulsation condition, i.e. equation (3.44), no longer holds true (due to the effects of bleaching). As a result the range-dependent maximum power output also decreases making high power emission a difficult proposition. However, for this particular structure the 5 mW threshold is available at 70 °C.

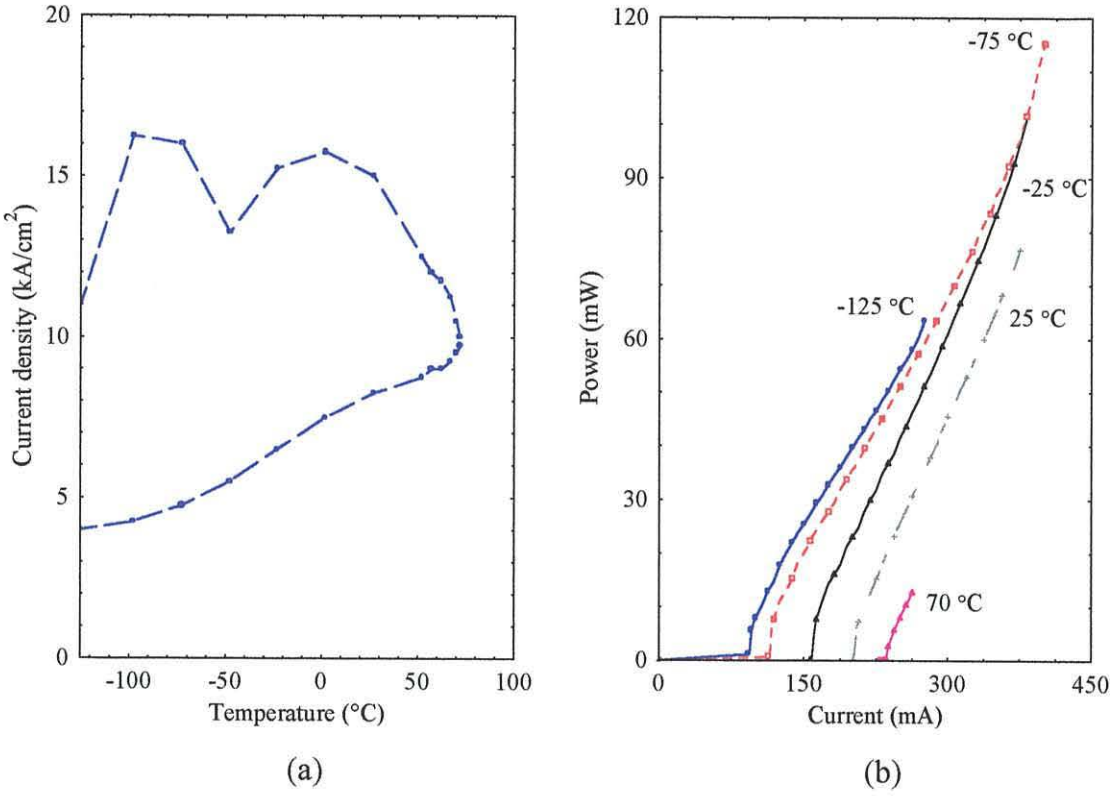

Fig. 5.12 *(a) Operating bounds and (b) the power output for self-pulsation for a laser diode with an absorber section of 4×40 Å quantum wells (L=500 μm & W=5 μm).*

Above room temperature the current density range decreases with temperature until pulsation stops. It is therefore desirable for self-pulsation to be available well above 70 °C if the 30 mW power threshold is to be achieved at high temperatures. This point is observed in fig. 5.13 where the six absorber configurations that self-pulsate beyond 70 °C are considered. The highest power is detected for the absorbers that provide self-pulsation at the greatest temperatures, thus offering the highest current density range (at a given temperature). The diagram indicates that 5 mW operation is available when using all six absorber configurations. However, the 4×40 Å absorber gives rise self-pulsation at the lowest operating current, as this particular structure offers the least amount of absorption.

Fig. 5.13 illustrates the benefits of using narrow absorber wells, with the improvements in the differential absorption giving rise to superior operating

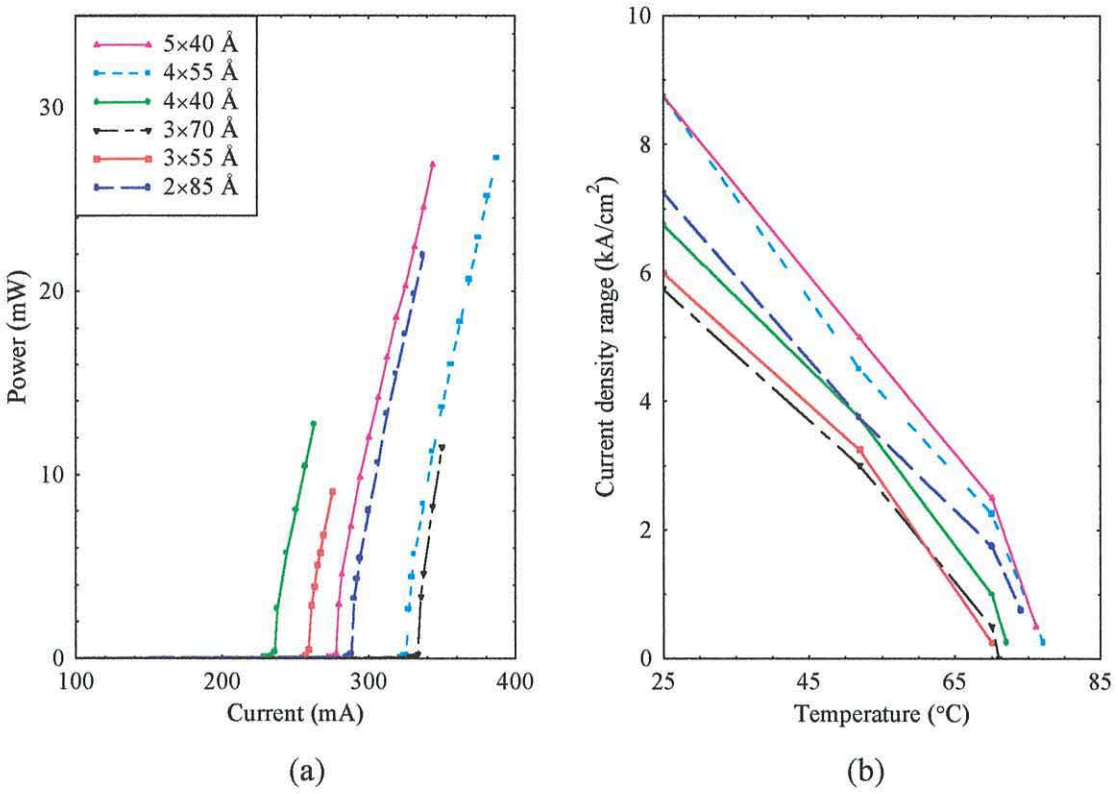

Fig. 5.13 *(a) Maximum power output at 70 °C and (b) current density range for self-pulsation for the six absorber configurations that pulsate beyond 70 °C.*

characteristics (for a given volume), as was mentioned when discussing figs. 5.6 to 5.9. From this evidence it is clear that such a narrow well absorber configuration is desirable for low current and high temperature operation. With this in mind, the 4×40 Å structure is very close to offering optimum 5 mW self-pulsation. However, further work is required to achieve 30 mW operation.

5.4.2 Variation in absorber position

Throughout the investigation the position of the absorber quantum wells in the cladding layer has remained constant, i.e. d_{sep}=0.115 μm, with the confinement factor varying with the number of wells and the well width. In this section it is intended to study the effects of changing the position of the absorber wells. This will be done by varying the confinement factor, Γ_α, for an absorber consisting of 4×40 Å wells; an

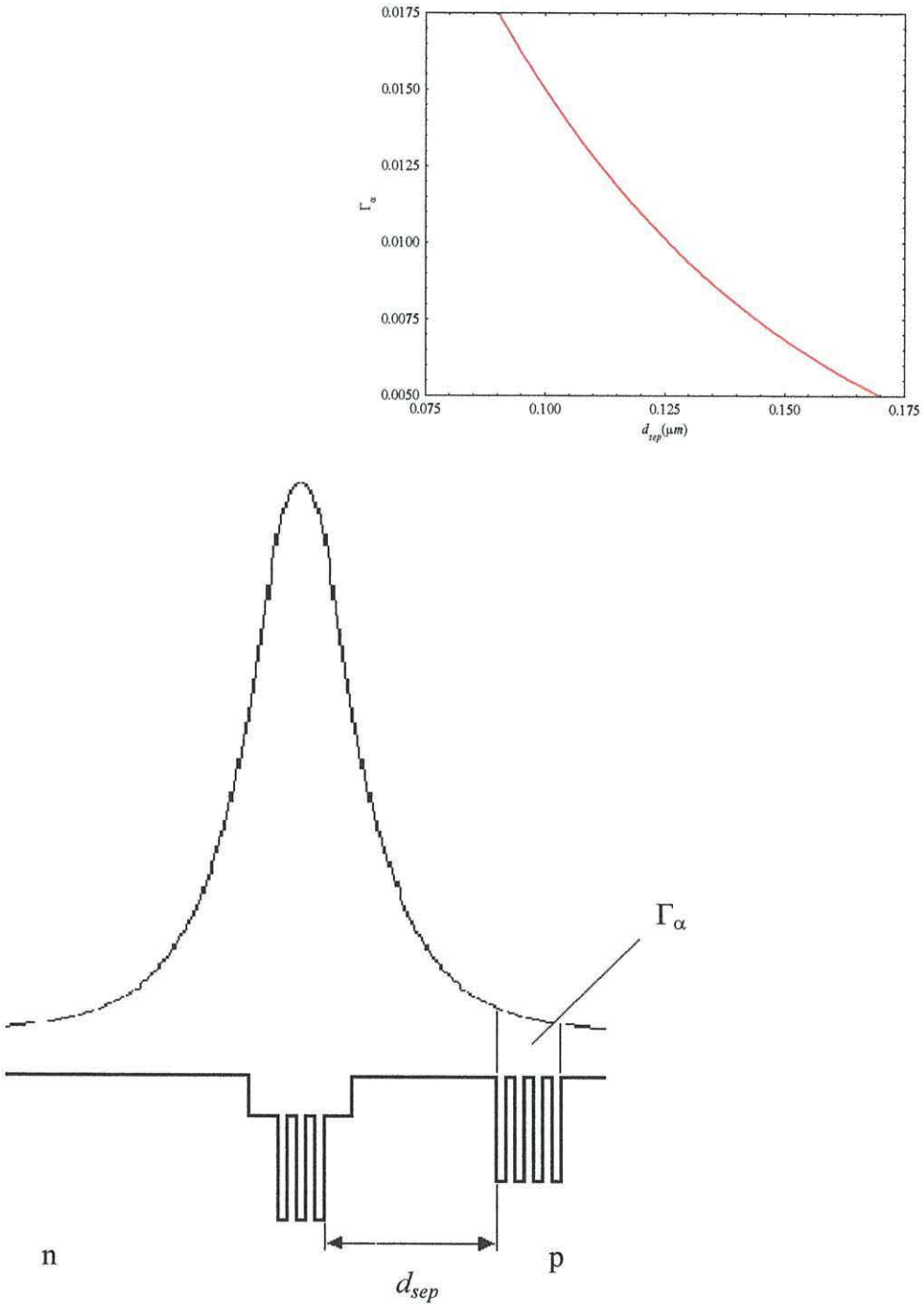

Fig. 5.14 *Schematic diagram of the self-pulsating laser diode and the corresponding optical mode within the waveguide. (Inset) The relationship between the absorber confinement factor, Γ_α, and the distance between the absorber and gain regions, d_{sep} (for the 4×40 Å quantum well absorber).*

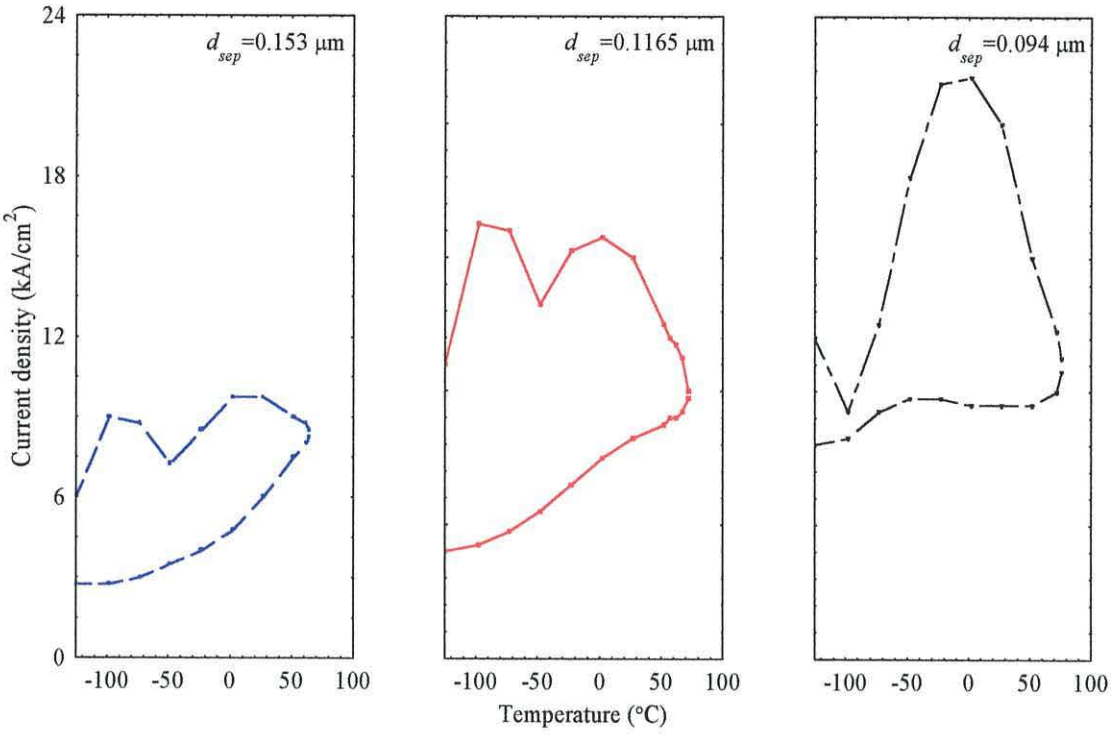

Fig. 5.15 *Self-pulsation bounds for a laser with an absorber layer consisting of 4×40 Å wells for three different absorber positions.*

increase in Γ_α arising from a movement towards the active region and a reduction in the value indicating a movement away, as summarised in fig. 5.14. Absorber confinement values between 0.0065 and 0.0165 (d_{sep}=0.153→0.094 μm) are tested at intervals of 0.00125. Only variations in this range are examined as an absorber position too close or too far away from the active region will fail to give any self-pulsation, i.e. the amount of absorption will be unsatisfactory. It is worth noting that in this model the absorber confinement value, Γ_α, and separation distance, d_{sep}, are dependent only on each other.

Fig. 5.15 shows how a change in distance between active region and absorber layer can affect the current density bounds at various temperatures. In the three cases self-pulsation ceases at around 75 °C, showing the negative influence of the leakage current as it bleaches the absorber until self-pulsation stops. The most striking observation from the three diagrams is the considerable increase in the threshold

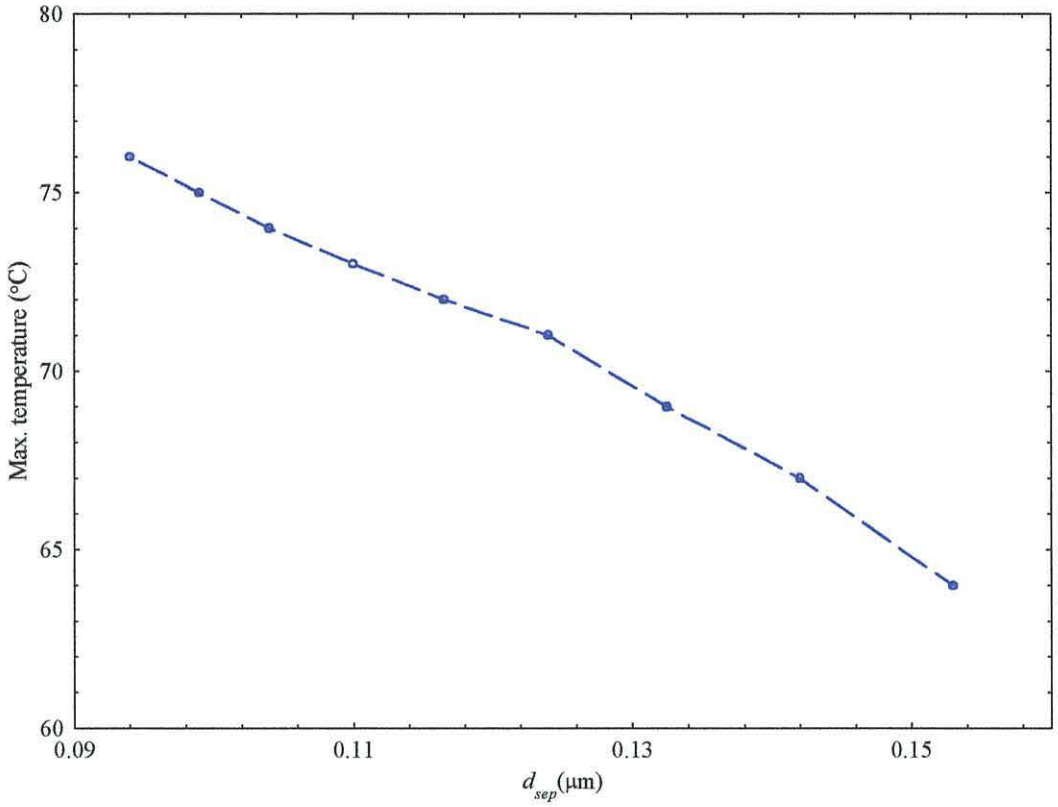

Fig. 5.16 *Maximum operating temperature for self-pulsation as a function of distance between absorber and active region, d_{sep}.*

current density and operating range as the absorber layer moves closer to the active region. As the interaction with the optical field is stronger with decreasing separation this is to be expected, i.e. the greater the amount of absorption the higher the threshold current density. However, the extent of the changes with only a slight variation in position shows how influential the absorber position is on the self-pulsation characteristics [7]. Also note that the shape of the lower limit curve alters as the amount of absorption varies. The changing slope of the curve indicates a probable change in sub-band emission, as described in section 5.3.2.

Looking closer at the variation in maximum operating temperature with changing absorber position it is evident that the maximum temperature for self-pulsation increases with the amount of absorption, as shown in fig. 5.16. This is further evidence of the high temperature/low threshold trade-off observed in previous

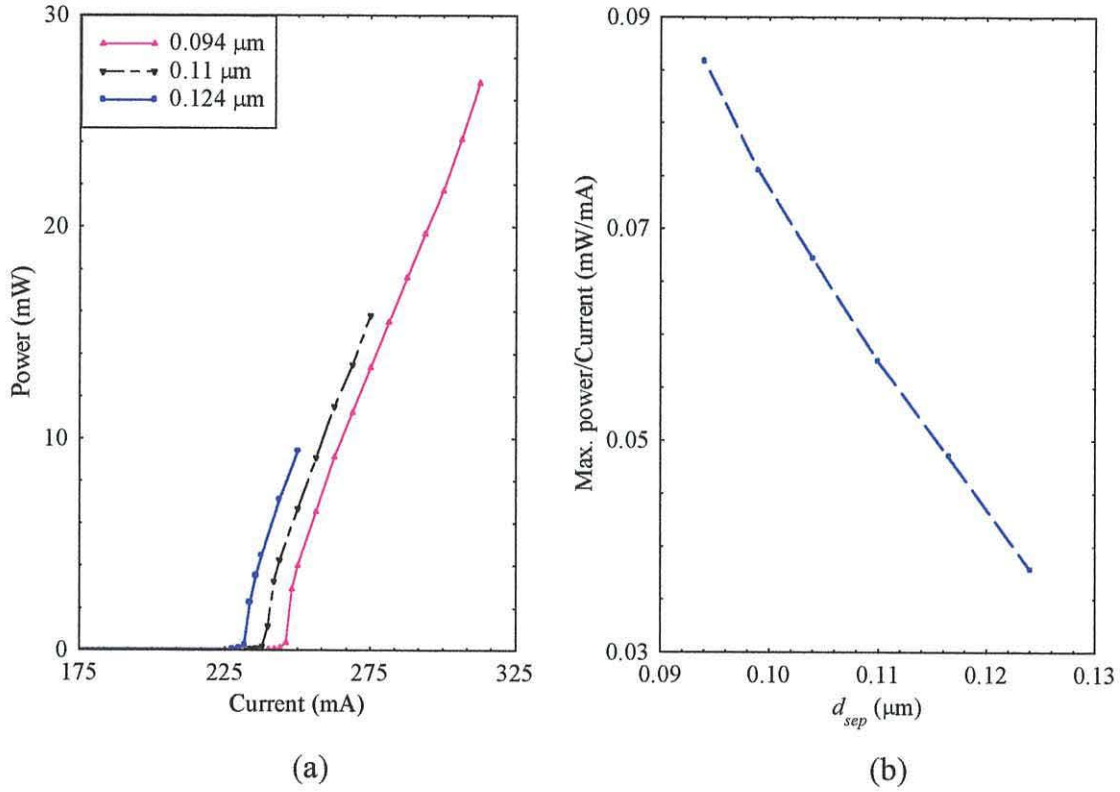

Fig. 5.17 *(a) The average pulse power output and (b) the maximum power/current ratio for three different absorber positions at 70 °C.*

results. It is worth noting that the change in temperature operation is far less substantial than the alteration in current density bounds observed in fig. 5.15. This observation shows that it is the absorption that has the dominant influence on the current density bounds whilst it is the leakage current that controls the high temperature operation of self-pulsation [7].

Fig. 5.17 displays how a change in the position of the absorber layer affects the output power of the pulses at a temperature of 70 °C. Only distances less then 0.124 μm (Γ_α>0.01025) gives rise to self-pulsation above this temperature threshold as displayed earlier in fig. 5.16. Fig. 5.17(a) illustrates the influence that the upper current density bound has on self-pulsation. As the absorber section moves nearer to the active region a higher average power output is observed due to the larger current density range on offer (as was explained in the previous section). This factor enables the maximum power output to increase as the distance between the absorber and

active region decreases. However, a penalty of a slight increase in operating current is noticed.

Fig. 5.17(b) displays how the power output decreases in efficiency as the absorber section moves away from the gain region. These results show that the most efficient laser in terms of power output at 70 °C is that which provides the most absorption due to the effective suppression of the leakage current. The two diagrams therefore illustrate the maximum power/efficiency trade-off that is a characteristics of this particular device. It is also worth noting that the 5 mW power threshold is easily achieved but the 30 mW output required for the read/write DVD system is still unattainable. As was mentioned earlier, an absorber distance less than 0.094 μm (Γ_α=0.0165) provides too much absorption resulting in no self-pulsation whatsoever. This indicates that other cavity parameters need be varied in an attempt to increase the power output to 30 mW.

5.5 Changes in cavity losses for further optimisation

Previous work has investigated the structure of the epitaxial absorber layers to satisfy the temperature, power and operating current conditions stipulated in section 1.3.2. It was observed that the best structures failed to reach the 30 mW power threshold required for a read/write device. In this section the computer simulation will be used to investigate the design parameters further by optimising the laser cavity design, primarily trying to achieve the high power threshold. By doing so a further insight into obtaining an optimum structure will be presented in an attempt to satisfy the emission criteria.

The threshold gain for the self-pulsating laser, described by the equation

$$G_{th} = \Gamma_{qw} g_{qw} \approx \alpha_i + \alpha_m + \Gamma_\alpha g_\alpha$$

$$\approx \alpha_i + \frac{1}{L}\ln\left(\frac{1}{R}\right) + \Gamma_\alpha g_\alpha, \qquad (5.2)$$

expresses the condition that the gain due to pumping must balance the total losses. In this particular laser a high threshold is observed due to the additional absorption

supplied by the absorber quantum wells. The equation consists of the intrinsic loss, α_i, which is given by [8]

$$\alpha_i = (1-\Gamma_{qw})\alpha_{pg} + \Gamma_{qw}\alpha_{fc} + \alpha_{sc} \tag{5.3}$$

where α_{pg} represents the losses in the passive regions of the waveguide and in the cladding and α_{fc} and α_{sc} denote the free carrier loss and scattering loss, respectively. Whilst the intrinsic loss value doesn't fluctuate much (the value is set at 10 cm^{-1} in the model [1]), the transmission loss through the mirrors, α_m, can be varied in an attempt to lower the threshold current and influence the high temperature operation of the device. The mirror loss is usually a few times greater than the intrinsic loss, so, the reflectivity, defined by [8]

$$R = \sqrt{R_1 R_2} \tag{5.4}$$

(where R_1 and R_2 are the two facet reflectivities) and cavity length, L, can be varied to optimise the emission (Γ_{qw} and Γ_α can also have an effect, however these parameters have already been studied). In conventional lasers changes in the mirror losses have been studied extensively [8-12]. However, the performance of the AlGaInP laser diode is influenced by a leakage current at high temperatures, so a detailed study of the cavity design is required if the all round performance of the device is to be improved. [*Note*: The spontaneous emission has been neglected from equation (5.2). Once threshold is achieved this effect is minimal, so the approximation is adequate.]

For high temperature operation saturation of the absorber due to carrier leakage must be minimised [1, 13]. It was found in a previous section that a MQW absorber region is desirable for such an application. This was achieved using an absorber configuration of four quantum wells, giving optimum current density and temperature performance when the well widths were set at 40 Å [5]. Unfortunately the maximum power output was only 12.74 mW with other structures offering improved power characteristics at a cost of higher threshold current density. In this investigation the 4×40 Å absorber and the original gain-absorber distance, d_{sep}, of 0.115 μm will be used to study the trends that are observed when varying the cavity parameters. Unless otherwise stated, cavity length values between 200 and 950 μm will be examined at intervals of 150 μm. Reflectivities between 0.12 and 0.92 will also be studied at intervals of 0.2. The findings will then be combined with previous results in an attempt to achieve the desired self-pulsation characteristics.

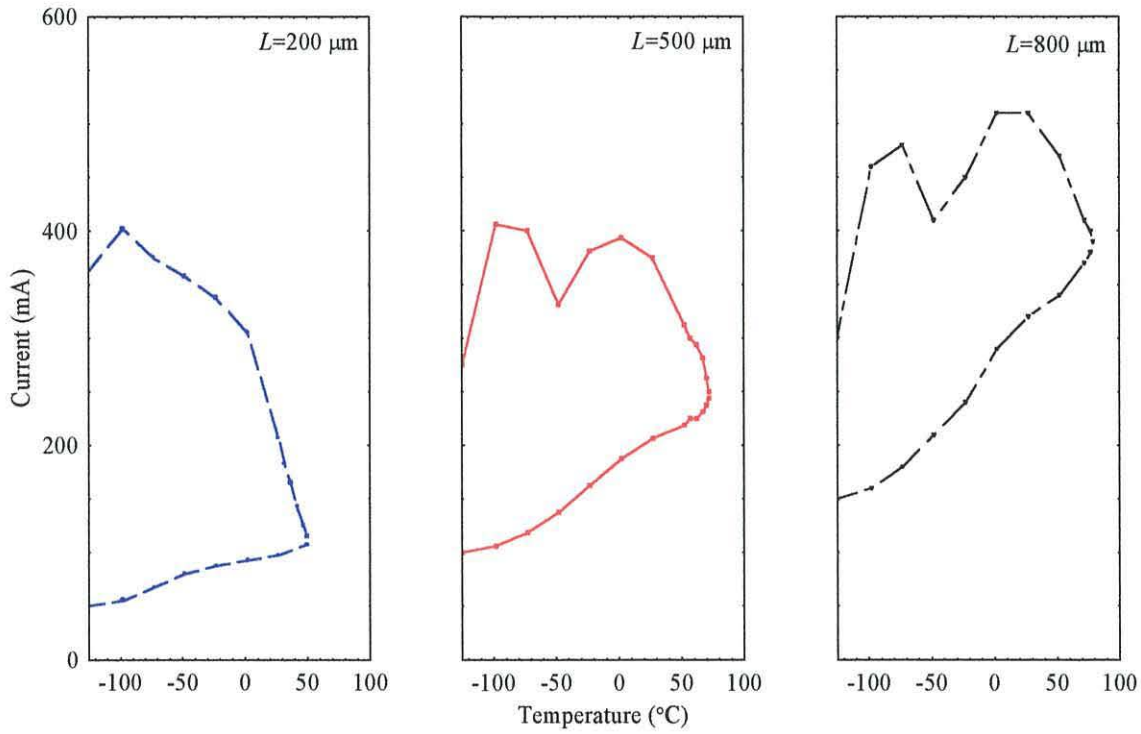

Fig. 5.18 *Self-pulsation bounds for a laser with an absorber section of 4×40 Å quantum wells for three different cavity lengths (R=0.32).*

5.5.1 Operating current and temperature considerations

The threshold current and threshold current density are related by the equation

$$I_{th} = J_{th}WL \tag{5.5}$$

where L is the cavity length and W is the stripe width. As the cavity length increases, the amount of gain required to overcome the loss decreases, as given by equation (5.2), so the threshold current density, J_{th}, should decrease with length as is apparent in equation (5.5). However, in this section the cavity length is being varied and the threshold current, I_{th}, is of primary interest. So, from equations (5.5) it is clear that the amount of optical loss is scaled by the WL term, i.e. the cavity area. This process is evident in fig. 5.18 where the reflectivity value is kept constant and the cavity length is varied. In the length range being investigated, the amount of loss increases with extending cavity (as the area term increases), resulting in an increase in threshold current. However, the amount of loss per unit length decreases, resulting in the above-mentioned trend in the threshold current density. Also note that the current range over

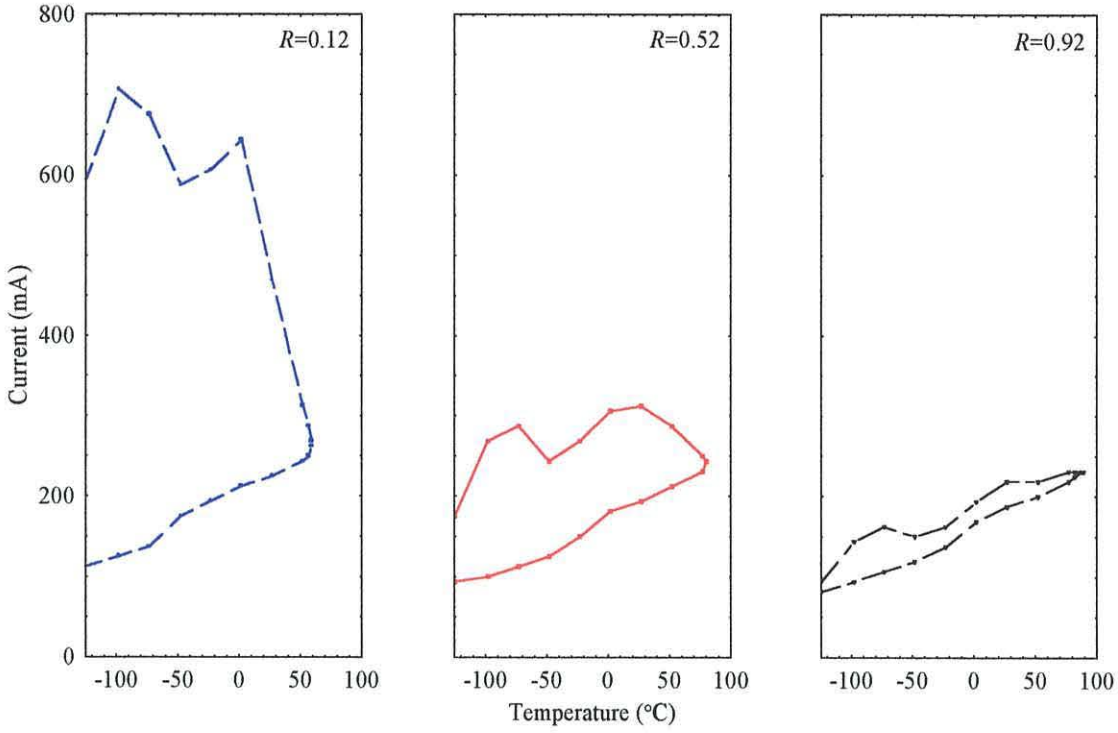

Fig. 5.19 *Self-pulsation bounds for a laser with an absorber layer consisting of 4×40 Å wells for three different facet reflectivities (L=500μm).*

which self-pulsation occurs doesn't vary much. This could change if the length bounds went beyond those being investigated but for the temperature and power conditions to be satisfied the length range being studied is adequate as will be shown later.

The effects of varying the reflectivity are shown in fig. 5.19. In this case the length is kept constant, so the area scaling value behaves as a constant and only one variable is being changed unlike two in the previous case. This explains why the threshold current decreases with increasing reflectivity, resulting from a decrease in optical loss (see equation (5.2)). The change in the current density bounds for self-pulsation in this case is interesting. Now the condition for self-pulsation was stipulated in equation (3.44). The diagrams show how the condition holds over a wider range of operating currents when the reflectivity value is at its lowest. A change in reflectivity changes the operating carrier density. As a result a decrease in

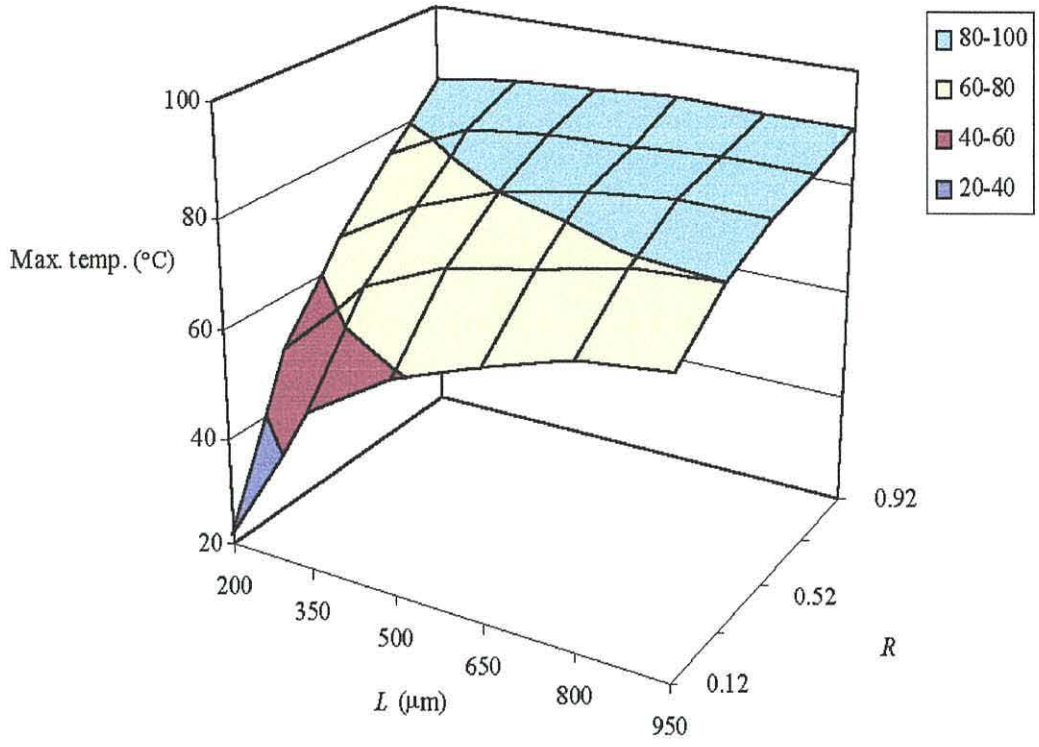

Fig. 5.20 *Maximum temperature operation for self-pulsation versus cavity length, L, and facet reflectivity, R, for an absorber configuration of 4×40 Å quantum wells.*

reflectivity increases the differential gain/absorption at turn-on. However, the change in the differential gain/absorption in the gain section is different to that observed in the absorber, e.g. exciton peaks affect the absorption spectrum. As a result, an increase in the reflectivity reduces the difference between the differential gain and absorption at the operating wavelength, leading to a smaller operating range for self-pulsation, as displayed in fig. 5.19.

Changes in the maximum temperature operation due to variations in length and reflectivity are displayed in fig. 5.20. The diagram shows that not all configurations achieve the 70 °C threshold required for optical storage applications. As mentioned previously, it is the leakage current that causes the self-pulsation to cease as the absorber wells are bleached at high temperatures. As the same absorber arrangement is being used throughout this section it is clear that at a given temperature the contribution of this carrier overflow becomes increasingly influential as one decreases either parameter, thereby increasing the amount of loss per unit

length within the cavity. Although values are only displayed for the 4×40 Å absorber structure this is a trend that is observed for all absorber configurations.

Fig. 5.21 summarises how a variation in length and reflectivity affects the threshold current at three different temperatures. The graphs are used to show how the threshold current changes when the leakage effects are minimal (-75 °C), moderate (25 °C) and high (70 °C). For the three cases, an increasing reflectivity and decreasing length reduces the threshold current due to a reduction in the amount of loss, as stipulated when discussing figs. 5.18 and 5.19. For this work the minimum length was lowered to 150 μm in order to show the sudden increase in threshold once the cavity length decreases below some optimum value, as displayed in fig. 5.21(a). This happens for small lengths when the $1/L$ loss term begins to dominate the threshold gain equation, i.e. equation (5.2), taking over from the area scaling term that dominates for longer lengths. The point at which the minimum occurs can be manipulated to generate an equation for an optimum length that offers the minimum threshold current [8, 9]. However, 70 °C self-pulsation cannot be achieved at any optimal cavity design, i.e. <200 μm, due to the deleterious effects of the leakage current (see fig. 5.20).

Fig. 5.21 therefore summarises the threshold current trends that were mentioned earlier as well as further evidence of the failure to achieve self-pulsation for some configurations at 70 °C. The results also show a more subtle effect that needs some explanation. At low temperatures, the threshold current for all cavity length and reflectivity configurations are reasonably low, due to the negligible influence of the leakage current. As the temperature increases this carrier overflow begins to dominate the device performance at different magnitudes dependent on the amount of loss. Looking at figs. 5.20 and 5.21 it is clear that self-pulsation stops at the lowest temperatures for small lengths and low reflectivities. However, the slope of the curves in figs. 5.21(a) to (c) increase with temperature, indicating that the magnitude of leakage is highest for long cavity lengths in particular. These observations verify that the amount of leakage per unit length is at its minimum for the long length and high reflectivity combinations, thus taking longer for carrier bleaching to affect the device performance, resulting in higher temperature operation.

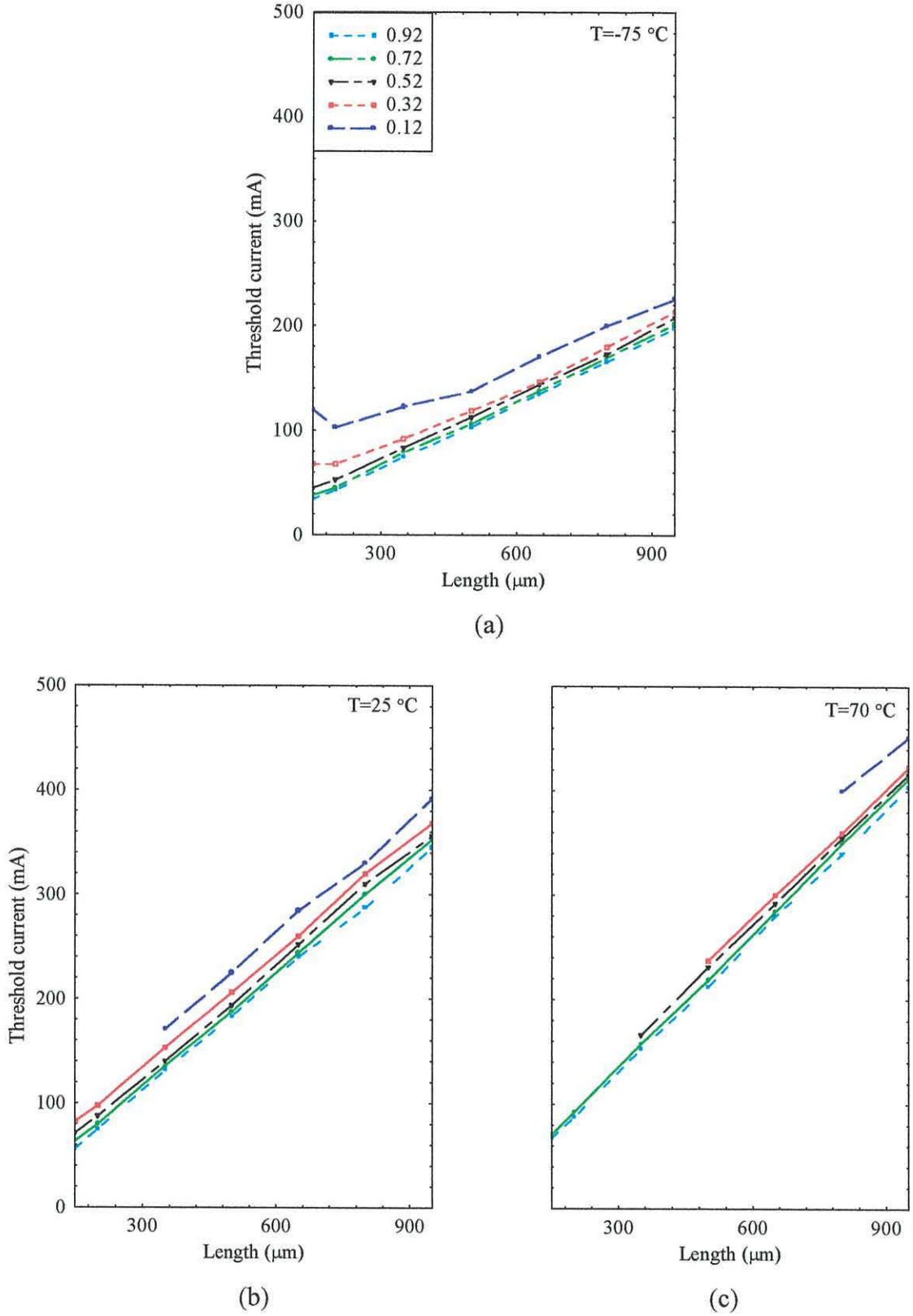

Fig. 5.21 *Threshold current values for self-pulsation for varying cavity lengths and reflectivities at (a) -75, (b) 25 and (c) 70 °C.*

5.5.2 Power output

Now that the current and temperature characteristics have been investigated a detailed study of the power of the self-pulsation is required (for varying cavity parameters). To start, the reflectivity will be kept constant (R=0.32) and the cavity length will be varied for the three different temperatures, as shown in fig. 5.22. Below room temperature (-75 °C) the influence of the leakage current is negligible causing the maximum power emission to decrease with increasing length as the current density range decreases in a manner similar to that shown in fig. 5.12. Also note that the slope efficiency decreases with length as the amount of loss increases [12].

As the temperature increases the leakage current per unit length is greatest within the smaller cavities, resulting in a reduction of the upper current density bound. This leads to a "role reversal" in terms of power at 25 and 70 °C; i.e. the maximum power increases with an extending cavity due to the reduction in leakage current per unit length. This leakage reduction results in the highest power being emitted from the longest cavity at high temperatures and no self-pulsation whatsoever for some of the smaller lengths at 70 °C. A decrease in the slope efficiency with an increasing length is still observed due to its dependence on the magnitude of loss. [*Note*: The slope efficiency for a particular length decreases with temperature (this is not obvious, as the "maximum power" scales are different) as the carrier leakage gradually decreases the efficiency of the laser.]

Fig. 5.23 shows how the power output changes as the reflectivity values varies for a constant length of 500 μm. As the length is kept constant the threshold current is not scaled by the area term in equation (5.2). This causes the threshold current to increase with decreasing reflectivity due to the increasing amount of optical loss. In this case, the higher the threshold current, the greater the amount of energy stored within the cavity at turn-on. As a consequence, as the reflectivity decreases the slope efficiency increases. The decreasing current range caused by the changes in differential gain/absorption is also apparent as the maximum power output varies with current bounds. These factors enable a laser with the highest threshold to achieve certain power values at the smallest injection current. The influence of the leakage current is also observed, stopping self-pulsating at 70 °C for the cavity configurations that offer too much loss.

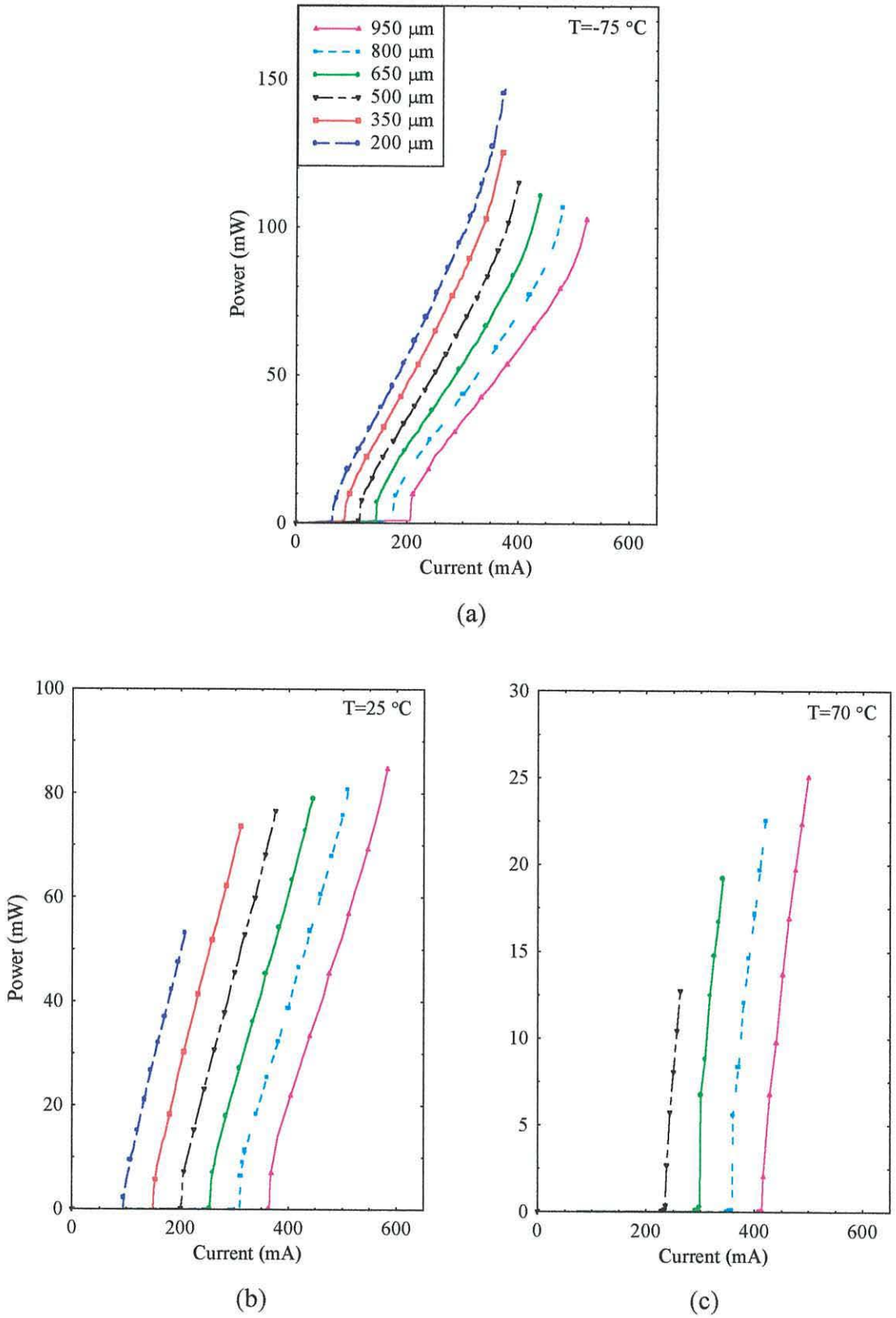

Fig. 5.22 *The average pulse power output for six different cavity lengths at (a) -75, (b) 25 and (c) 70 ℃ for an absorber structure of 4×40 Å wells (R=0.32).*

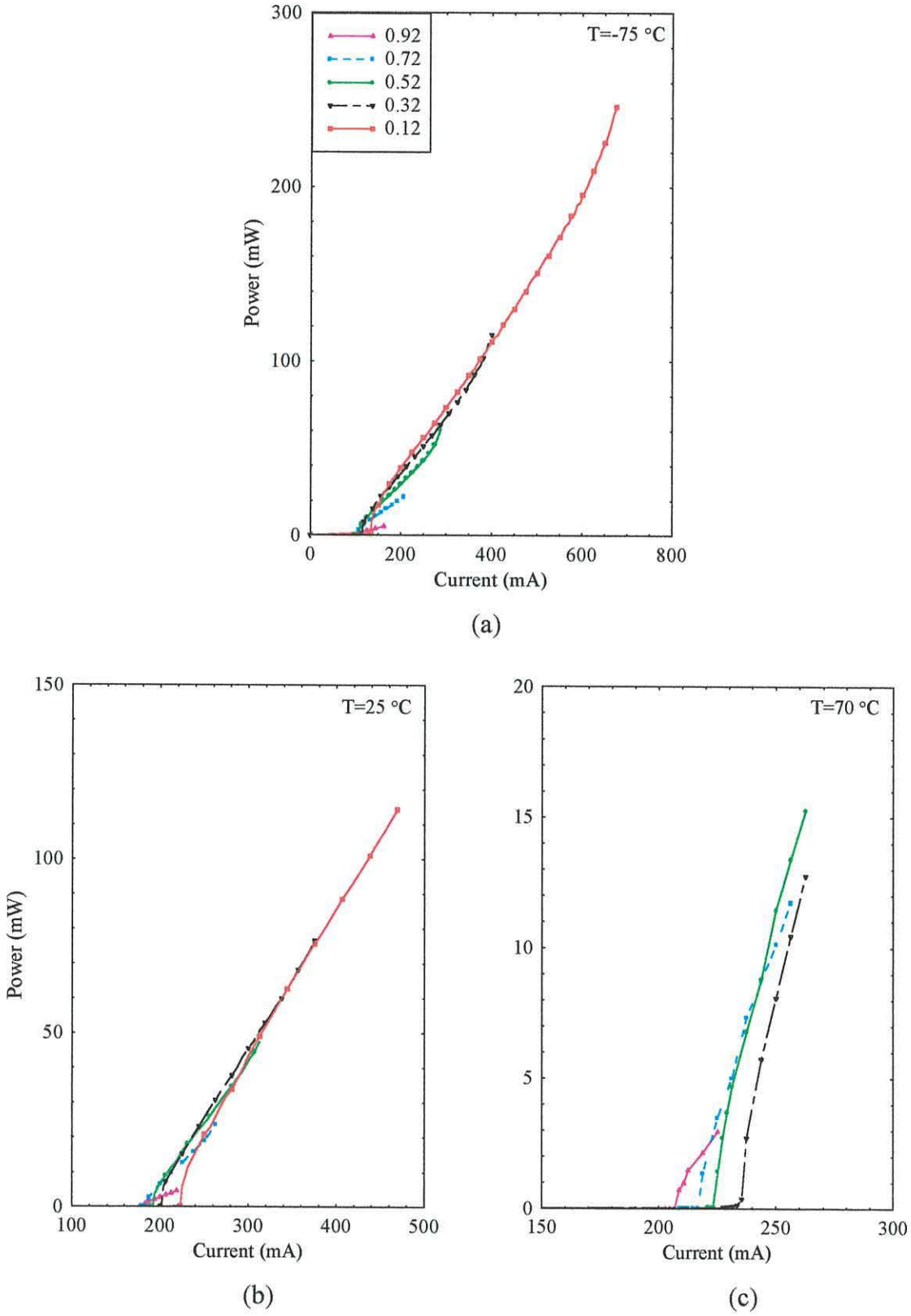

Fig. 5.23 *The average pulse power output for five different facet reflectivities at (a) -75, (b) 25 and (c) 70 °C for an absorber structure of 4×40 Å wells (L=500 μm).*

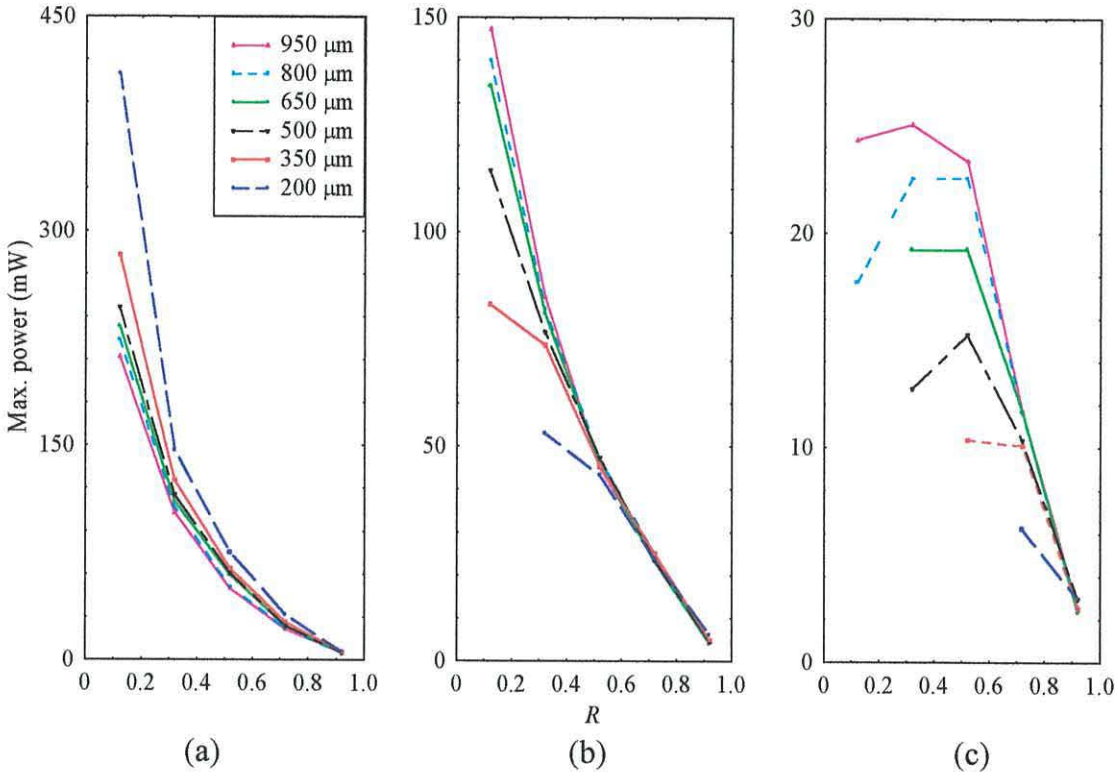

Fig. 5.24 *The maximum average pulse power output for varying lengths and reflectivities at (a) -75, (b) 25 and (c) 70 °C (absorber structure of 4×40 Å wells).*

Fig. 5.24 summarises how a variation in length and reflectivity affects the maximum power output at three different temperatures. The results show primarily how the leakage current affects the maximum power operation. At -75 °C, where the carrier overflow is minimal, a small reflectivity and small cavity length provides the least amount of loss resulting in the highest power. Once the leakage current becomes evident at 25 °C the optimum configuration changes with a long length and small reflectivity offering the best performance as the amount of leakage per unit length decreases with an increasing cavity. At 70 °C the $1/L$ term begins to dominate the mirror loss value when a particular configuration is close to maximum loss (relative to the amount of gain being offered) creating a downward turn in the curve.

At 70 °C a maximum power of 25.07 mW is emitted, indicating that 30 mW self-pulsation is still not available for the 4×40 Å quantum well absorber structure due to the deleterious effects of the leakage current. Power and operating temperature

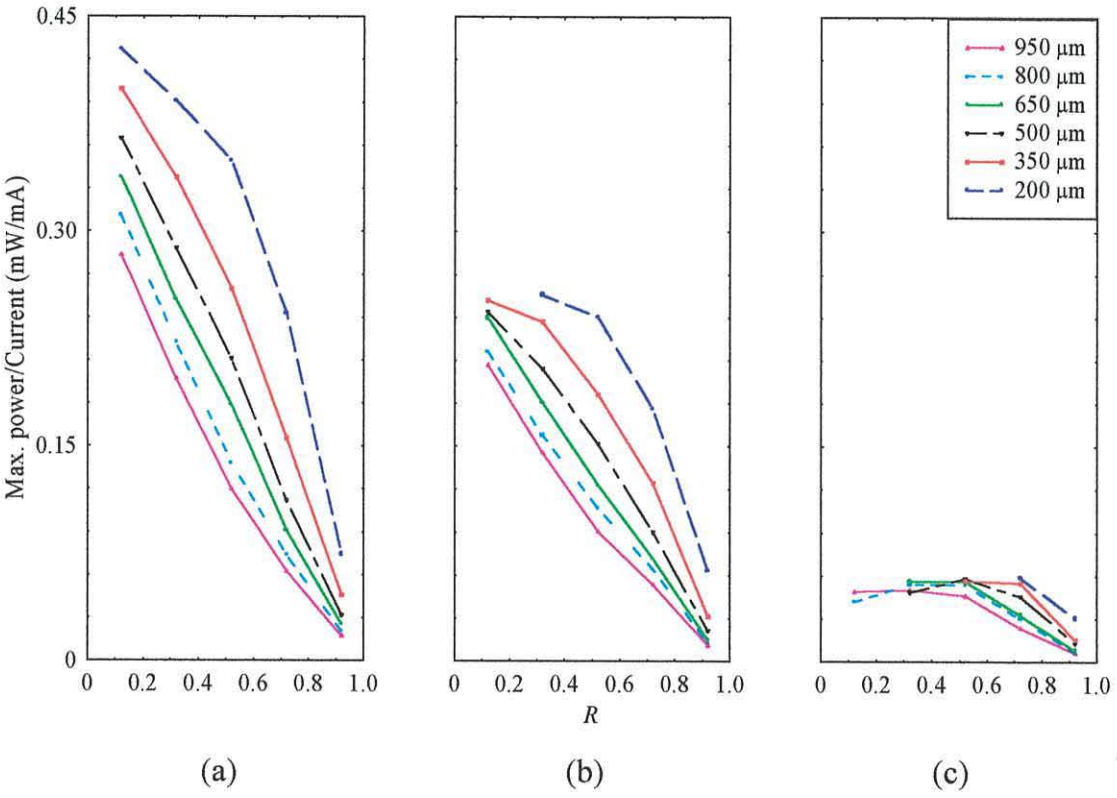

Fig. 5.25 *The maximum power/current ratio for varying lengths and reflectivities at (a) -75, (b) 25 and (c) 70 °C (absorber structure of 4×40 Å wells).*

improvements come at a cost of increasing the injection current. Keeping this value low is essential in commercial devices. The trade-offs between high temperature, high power and low current operation therefore hamper the optimisation process, indicating that a desirable high power self-pulsating device is difficult to obtain.

The efficiency of the maximum power output is show in fig. 5.25. For temperatures below 25 °C, the best power output per injection current is consistently offered by the shortest cavity as it generates the least amount of loss. A small reflectivity is also desirable, providing a reduction in differential gain and an increase in the current range, as was discussed earlier (see fig. 5.19). These results show that the cavity that offers the maximum power emission is not necessarily the most efficient, especially at high temperatures when the leakage current becomes dominant. This thermal effect is shown as the slope of each curve decreases with increasing temperature. At 70 °C, when the $1/L$ term begins to dominate the mirror

losses the power emission ratio suffers as the threshold current rises and the maximum power output decreases. However, the maximum power configuration stipulated when discussing fig. 5.24, i.e. L=950 μm and R=0.32, unfortunately offers the least efficient power emission.

5.5.3 Summary

In this section an investigation of the reflectivity and length parameters has been presented. The work has shown how the leakage current affects the self-pulsation characteristics at high temperatures and how it may be minimised using the cavity parameters. Results indicate that the lowest threshold current occurs when a small length and large reflectivity is used, thus, minimising the amount of loss, as summarised in fig. 5.21. Using this configuration a minimal threshold current can be achieved at 70 °C. Unfortunately a different combination is required to optimise the power output. Fig. 5.24 shows that a long length combined with a reasonably small reflectivity gives rise to the maximum power. However, for this amount of power to be generated a large injection current is required and the power output is fairly inefficient. A number of trade-offs therefore exist between the cavity parameters, something that must be carefully considered when optimising the device.

5.6 Optimum structure

Now that the absorber structure and cavity have been thoroughly investigated it is desirable to finish the chapter with two optimally designed laser diodes that satisfy the temperature, power and operating current conditions stated in section 1.3.2. From the investigation it is apparent that the 4×40 Å quantum well absorber structure suppresses the leakage current very effectively. The design must then be optimised around this absorber section. What is also clear from the work are the numerous trade-offs, in particular the requirement that the maximum temperature operation increases with absorption, thus increasing the threshold current of the device.

For 5 mW operation at 70 °C a length of 200 μm combined with a large

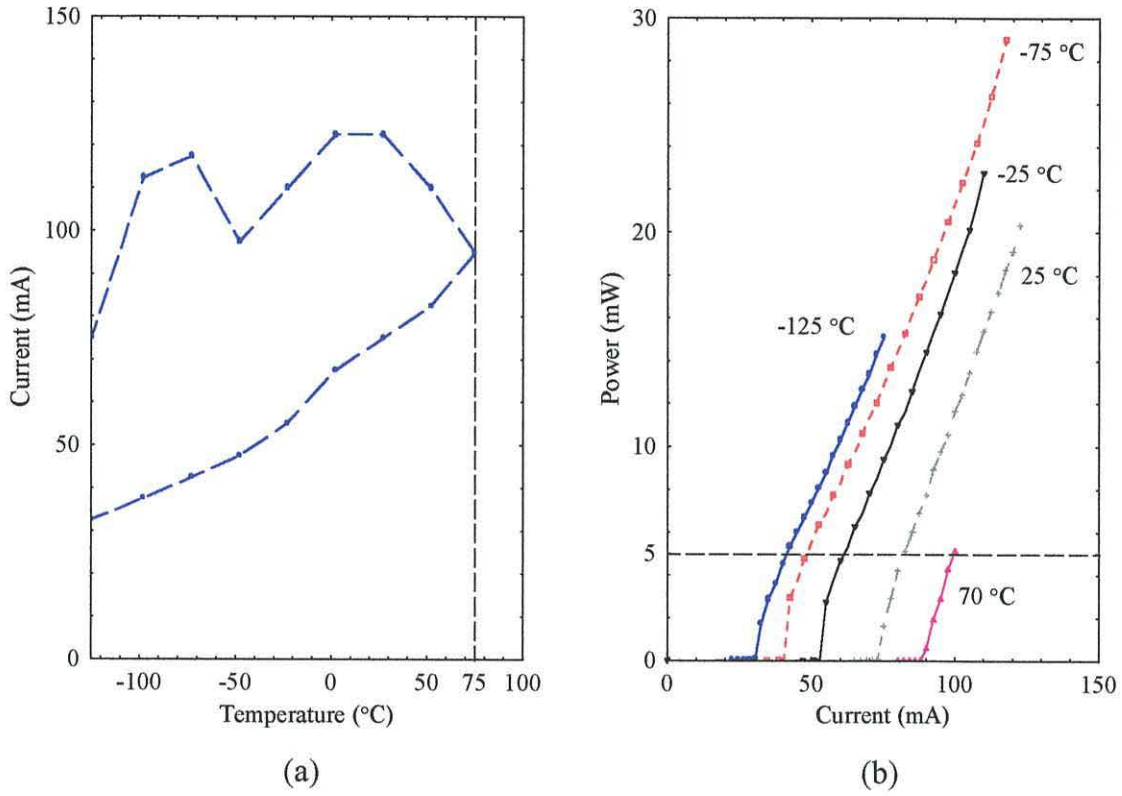

Fig. 5.26 *(a) Operating bounds and (b) power output for the optimum 5mW self-pulsating laser, i.e. 4×40 Å absorber, L=200 μm, R=0.72 and* d_{sep}*=0. 1245 μm.*

reflectivity offers desirable operating characteristics. All smaller lengths that operate at lower threshold currents fail to achieve 5 mW self-pulsation. Ideally a reflectivity of 0.32 would be desirable, thereby making use of the refractive index change between the cavity/air interface for reflectivity purposes and reducing costs. Unfortunately a longer length would be required to achieve pulsation at the temperature threshold which would increase the operating current to unsuitable levels.

As shown in fig. 5.24, a reflectivity of 0.92 combined with the above-mentioned length fails to achieve self-pulsation at the desired power threshold due to the small operating range that is offered by the structure. Even after decreasing the gain-absorber separation distance, d_{sep}, to its limit, 5 mW self-pulsation failed to develop. Fortunately, a reflectivity of 0.72 offers an improvement in efficiency, as indicated in fig. 5.25, so the desired power output can be achieved. To lower the

threshold current, the separation distance can be increased, with an optimum distance of 0.1245 μm giving 5 mW self-pulsation at approximately 100 mA. The characteristics of this particular laser diode are shown in fig. 5.26.

Due to the numerous trade-offs between high power and low threshold current operation the 30 mW self-pulsation is more difficult to obtain. To achieve the power threshold an increase in absorption is required. To do so two options are available. The first is to increase the volume of the absorber wells then optimise the structure, as was done for the 5 mW emitter. The second option is to keep the 4×40 Å absorber structure, use a long cavity, relatively small reflectivity then increase the gain-absorber distance beyond 0.115 μm. Unfortunately both options result in a vast increase in threshold current, leading to a device that self-pulsates at a current that is far too high, i.e. >500 mA. One can therefore conclude that an AlGaInP laser diode of this type can be adapted for a read/write DVD system but would require an unrealistic amount of current to operate within a commercial device. [*Note*: These results are based on a stripe width of 5 μm. Further reductions in operating current could be achieved by lowering this particular value.]

5.7 Conclusions

The purpose of this chapter was to model and optimise a 650 nm self-pulsating laser diode with epitaxial absorber layers for optical storage applications. The first, and most important conclusion is that high temperature self-pulsation can be achieved. However, the influence of the thermally activated leakage current has a deleterious effect on the emission, causing the threshold current to increase and current density range to decrease once fully initiated, i.e. at approximately room temperature.

Various design parameters have been investigated to optimise the self-pulsation. Firstly, the configuration of the absorber section was studied. By varying the quantum well number (1→5) and width (25→85 Å) it was shown that only certain combinations offer the desired amount of absorption at the operating wavelength to achieve self-pulsation. Within this "range", as the volume of the absorber increases the threshold current also increases due to the growing influence of the absorption.

However, this has a positive effect on the maximum operating temperature, which is extended due to the more resistive nature of the absorber to the incoming leakage current, i.e. as the volume of the absorber increases an increasing carrier density is required to bleach the absorber and stop the self-pulsation. This threshold current/maximum temperature trade-off therefore limits the device performance. For a typical absorber volume (that offers self-pulsation) the use of narrow quantum wells improves the differential absorption characteristics and therefore increases the maximum operating temperature, due to the absorbers greater tolerance to bleaching. As a result, the performance of the laser with a 4×40 Å quantum well absorber provides some very desirable operating characteristics.

Once the absorber configuration was optimised the position of the structure in the p-cladding layer was investigated. The results indicated that the separation distance between absorber and gain regions can be used to "fine tune" the optimisation. Such changes can significantly affect the current density limits, range and power output whilst having a more subtle influence on the maximum operating temperature.

After the optimum absorber structure was determined the cavity losses were studied via the cavity length and reflectivity parameters in order to achieve the previously unattainable high power, i.e. 30 mW, self-pulsation. As both parameters increase, the maximum temperature operation increases due to an effective suppression of the leakage current (per unit length in the case of the length parameter). A small length and high reflectivity is required to minimise the amount of optical loss and offer the lowest threshold current at a particular operating temperature. The results also indicated that the combination of a long cavity and a reasonably small reflectivity is required to minimise the amount of loss per unit length to produce maximum power output. This comes at a cost of a reduction in efficiency, which is another trade-off that must be considered when optimising the cavity design.

Having investigated the most influential design parameters it may be concluded that suitable emission for a read-only device is achievable for a number of absorber configurations with an optimum structure having been stated in section 5.6. Unfortunately the 30 mW self-pulsation that is required for a read/write device is

more difficult to obtain with all the desirable configurations requiring an unrealistic amount of injection current to achieve this power threshold. However, a reduced stripe width could improve these operating characteristics somewhat.

References

[1] H. D. Summers and P. Rees, "Thermal limitation of self-pulsation in 650 nm AlGaInP laser diodes with an epitaxially integrated absorber," *Appl. Phys. Lett.*, vol. 71, pp. 2665-2667, 1997.

[2] D. R. Jones, P. Rees, I. Pierce and H. D. Summers, "Theoretical optimization of self-pulsating 650-nm-wavelength AlGaInP laser diodes," *IEEE J. Select. Topics Quantum Electron.*, vol. 5, pp. 740-744, 1999.

[3] H. D. Summers, C. H. Molloy, P. M. Smowton, P. Rees, I. Pierce and D. R. Jones, "Experimental analysis of self-pulsation in 650-nm-wavelength AlGaInP laser diodes with epitaxial absorbing layers," *IEEE J. Select. Topics Quantum Electron.*, vol. 5, pp. 745-749, 1999.

[4] H. D. Summers, C. H. Molloy, P. M. Smowton, P. Rees, I. Pierce and D. R. Jones, "High temperature self-pulsation in 650-nm, AlGaInP lasers with an epitaxially integrated saturable absorber," *Proc. 16th IEEE Semiconductor Laser Conf.*, Nara, Japan, 1998, pp. 145-146.

[5] D. R. Jones, P. Rees, I. Pierce and H. D. Summers, "Power output of 650-nm self-pulsating AlGaInP laser diodes for optical storage applications," submitted to *IEEE J. Quantum Electron.*.

[6] S. W. Corzine and L. A. Coldren, *Diode Lasers and Photonic Integrated Circuits*, John Wiley and Sons, 1995.

[7] D. R. Jones, P. Rees, I. Pierce and H. D. Summers, "Investigation of changes in absorber position in the 650-nm AlGaInP self-pulsating laser for optical storage applications," *IEE Proc. Optoelectronics*, vol. 148, pp. 65-68, 2001.

[8] P. Zory Jr., *Quantum Well Lasers*, Academic Press, 1993.

[9] P. W. McIlroy, A. Kurobe and Y. Uematsu, "Analysis and application of theoretical gain curves to the design of multi-quantum-well laser," *IEEE J. Quantum Electron.*, vol. 21, pp. 1958-1963, 1985.

[10] A. R. Reisinger, P. S. Zory Jr. and R. G. Waters, "Cavity length dependence of the threshold behaviour in thin quantum well semiconductor lasers," *IEEE J. Quantum Electron.*, vol. 23, pp. 993-999, 1987.

[11] B. J. Thedrez and C. H. Lee, "A reassessment of standard rate equations for low facet reflectivity semiconductor-lasers using travelling wave rate-equations," *IEEE J. Quantum Electron.*, vol. 28, pp. 2706-2713, 1992.

[12] T. Makino, J. D. Evans and G. Mak, "Maximum output power and maximum operating temperature of quantum well lasers," *Appl. Phys. Lett.*, vol. 71, pp. 2871-2873, 1997.

[13] D. P. Bour, D. W. Treat, R. L. Thornton, R. S. Geels and D. F. Welch, "Drift leakage current in AlGaInP quantum-well lasers," *IEEE J. Quantum Electron.*, vol. 29, pp.1337-1343, 1993.

Chapter 6

Blue self-pulsating laser diode with epitaxial absorber layers

6.1 Introduction

Due to recent advances in short wavelength nitride laser diodes it is now possible to fabricate semiconductor lasers that emit in the visible range of the electromagnetic spectrum. Many areas in opto-electronics are set to take advantage of these developments. Applications include optical disc storage where a reduction in wavelength combined with improvements in optics and drive mechanics can significantly improve the storage capacity of the device. Indeed, a change from red to blue laser diodes would increase the storage capacity of current read-only DVD systems from 4.7 to 18 Gbytes. The benefits of using a self-pulsating laser in an optical storage device have already been stated. It is therefore conceivable that a blue self-pulsating laser diode will be a key component in any "next generation" optical storage system. With this in mind, the work in this chapter will concentrate on investigating the operating characteristics of such a laser.

It is known that a device grown in the GaN material system can give rise to a thermally activated leakage current at high temperatures [1]. The previous chapter showed the advantages of using the laser diode with epitaxial absorber layers for high temperature operation, especially when there exists any carrier overflow within the device. The work in this chapter will therefore investigate the performance of a 420 nm self-pulsating laser diode with epitaxial absorber layers for optical storage applications. The emission will be studied and optimised subject to the temperature, power and operating current conditions stipulated in section 1.3.2.

The chapter starts with a detailed description of the historical evolution of nitride light emitters combined with a general discussion about the associated material properties. The self-pulsating laser is then designed and optimised for gain/absorption interaction to achieve the strict temperature, current and power thresholds. This is followed by an investigation of the cavity design in order to improve the laser diodes operating characteristics even further. The work concludes with a detailed description of the optimum structure subject to the above-mentioned constraints. The parameters that will be varied are the same as those encountered when studying the laser in the previous chapter, so the trends that were observed for the AlGaInP device will be of some help during the optimisation process.

6.2 GaN: material information

6.2.1 History of wide band-gap light emitters

Since the commercialisation of the first red AlGaInP laser diodes in the mid 1980's the search has been on for a blue emitting semiconductor laser. Different wide band-gap materials have been studied in an attempt to produce blue light for two main reasons. One is the short wavelength (≈400 nm) that allows the laser beam to resolve (read and write) more information than red laser diodes (operating at 650 nm). This would considerably increase the storage capacity of current optical disc devices, as already shown in chapter 1. The second reason is that blue light can be combined with red and green to produce any other colour, including white light. This would in turn

revolutionise the lighting industry, replacing the standard light bulb with a more reliable and efficient source of light in the form of a white LED.

The search for the first commercially viable blue semiconductor laser has advanced rapidly during the 1990's. The two material systems that have received most attention are zinc selenide (ZnSe), a II-VI compound, and the III-V compound gallium nitride (GaN). However, these materials could be described as semi-insulators, a name that highlights just one basic problem when using them in electronic devices.

The main advantage of the ZnSe compound is that it can be grown onto a GaAs substrate. This is due to similarities in the material lattice constants, minimising the amount of misfit dislocations. Unfortunately difficulties in p-doping (causing problems in the fabrication of a p-n junction) plagued ZnSe research in the 1980's. The problem was solved by incorporating nitrogen atoms into the system leading to the first blue and green laser diodes being reported in 1991 [2, 3]. However, many problems existed such as difficulties in obtaining *cw* operation and the inability to emit at high temperatures. The fragility of the material was also a cause for concern - a single defect can cause others to propagate, disrupting the weak bonding and causing device failure. Extensive research has subsequently led to an operating lifetime of around 100 hours [4] which is insufficient for practical applications, i.e. a lifetime of 10,000 hours is usually required for a commercially viable device.

More dramatic developments have taken place using the GaN material system. In the late 1980's researchers had nearly given up hope of fabricating nitride light emitters. They knew that nitride materials offered the desired band-gap for blue emission but growth problems using conventional techniques and difficulties in p-doping the material hindered development. However, in 1988 Hiroshi Amano from Nagoya University in Japan produced p-type gallium nitride by doping the compound with magnesium [5]. Other doping techniques were subsequently developed leading to Shuji Nakamura and colleagues producing high quality indium gallium nitride (InGaN) films for the first time in 1992 [6]. The addition of some indium to GaN decreases the energy band-gap, enabling the crystal grower to fabricate InGaN quantum wells that emit in the blue region of the spectrum. This compound is the only nitride compound that can produce light strong enough for practical devices, so

the fabrication of InGaN was a significant milestone in the realisation of blue light emission.

Nakamura reduced the amount of growth defects by modifying the metal–organic chemical vapour deposition (MOCVD) growth technique. Conventional MOCVD methods create semiconductors by flowing reactant gases over a substrate, parallel to its surface. Nakamura's technique used a system in which gases flow in two directions rather than one, cooling the temperature of the reactant gases on the substrate just before reaction. This in turn leads to more stable reactions, improving the quality of the material [7].

Once these fabrication problems were resolved the first InGaN LED was reported in 1993 [8], then commercialised by Nichia within two years [7]. Similar to device developments using other material systems, once the LED had emerged it didn't take long for the first laser diode to be produced – the first laser with an InGaN MQW active region was reported by Nakamura *et. al.* in 1996 [9]. Subsequent investigations have led to blue semiconductor laser diodes with lifetimes greater than 10,000 hours (at room temperature) being released onto the market [10].

The GaN material system has therefore become the dominant blue light emitting material. Indeed, the gulf between GaN and ZnSe opto-electronic technology seems to be increasing with light sources based on nitride compounds improving at a much faster rate. It is therefore apparent why the work in this chapter will use the GaN material system (and associated alloys) to study self-pulsation at a wavelength of 420 nm.

6.2.2 Properties of nitride materials

Typical nitride light emitters are grown onto sapphire or silicon carbide substrates [11, 12]. Sapphire has been the most commonly used material, however, silicon carbide offers improvements in both lattice matching and conductivity and therefore looks to be the more suitable substrate for use in future nitride-based devices. The epitaxial layers are then constructed to offer suitable carrier and optical confinement, thereby forming an efficient laser diode. Barrier and cladding layers are usually grown using AlGaN or GaN materials with InGaN quantum wells being used as an active region. The inclusion of the InGaN alloy is essential to improve luminescence

efficiency and provide the desired band-gap for low wavelength emission [13]. As with other most material systems a small amount of strain is usually employed within the active layers, thereby modifying the band structure and subsequently improving the operating characteristics of the emission.

Nitride materials are characterised by high carrier effective masses and small radiative recombination matrix elements ($\propto^{-1}E_g$). The subsequent high density of states indicates that a large amount of carriers are required for population inversion, hence high lasing threshold currents are predicted. Low levels of gain are achieved compared to other smaller band-gap alloys. However, as the wavelength decreases the confinement factor for a specific well width increases. Unfortunately this trade-off is not enough, so high threshold currents are still required with a typical GaN laser achieving a modal gain that is roughly half of that offered by an AlGaInP laser diode [14-16].

Even though a vast amount of work has been achieved in a relatively short period of time numerous material and optical properties associated with the nitrides are still not fully understood. Although new growth processes have enabled lasing to be realised, large amounts of dislocations still exist within the epitaxial layers. This has led to a wide-ranging debate over some of the basic characteristics, even the radiative recombination process is not fully understood. Structural defects typify some of these strange properties. The dislocation density in the active layer of a typical nitride device is approximately 10^{10} cm^{-2} due to the large lattice mismatch between the nitride and substrate materials [17]. A dislocation density of around 10^6 cm^{-2} is usually enough for device failure in typical III-V semiconductor devices as the defects behave as non-radiative recombination centres and reduce the optical output. In spite of a very large density of defects this doesn't happen in nitride lasers. Indeed, some reports have indicated that the efficiency of a nitride-based device is similar to that offered by some AlGaInP light emitters [12].

Recent experiments have shown that the indium composition within InGaN films is not uniformly distributed [18, 19]. The weak temperature dependence of the emission spectra in InGaN has subsequently led to suggestions that radiative recombination is due to localised excitons in these indium-rich clusters [19]. These areas of high indium concentration therefore act as quantum dots and confine carriers,

resulting in a high efficiency of emission even when dislocations are present. However, there are studies that do no support this hypothesis. There exists an argument that the spectral density of states of these localised states is not high enough to provide the gain for lasing [20, 21]. Sun et al. suggested that the radiative process is dominated by free carrier recombination at room temperature [22], whilst another argument stated that the recombination mechanism is due to an electron-hole plasma in quantum dots [23]. The radiative recombination mechanism in InGaN quantum wells is therefore still a hot subject of debate. However, the band-to-band gain model being used in this thesis has offered some encouraging results so the gain calculations will be used with confidence throughout this chapter. [14, 15]. [*Note*: Indium compositional fluctuations are not considered in the gain model.]

In general, the binding energy in semiconductor materials tends to increase with an increasing band-gap. As a result Coulomb enhancement plays a key role in the calculation of the material gain of nitride alloys [16]. Excitons cause peaks in the absorption spectrum with the strength of these peaks being much stronger in quantum wells than in bulk materials due to the stronger overlap between the electron and hole wavefunctions [24]. Now the large binding energy associated with the GaN material system permits these electron-hole pairs to exist at low carrier densities even at room temperature. The Coulombic interaction between electrons and holes therefore has a strong influence on the absorption spectrum even at high temperatures. To model these effects accurately a gain model that considers many-body effects is essential [16, 24].

The cladding regions of a nitride-based laser diode typically consist of $Al_xGa_{1-x}N$ layers, so it is very important to be able to fabricate both p- and n-doped layers. Unfortunately a high p-doping density is difficult to achieve. A reasonably high aluminium (Al) mole fraction is required for sufficient carrier confinement, however, the conductivity rapidly decreases with an increase in Al, giving rise to a trade-off between p-doping density and Al mole fraction [1, 12]. As was explained earlier, this problem severely affected the progress of nitride-based electronics during the 1970's and 80's until suitable fabrication techniques allowed sufficiently doped p-type AlGaN layers. Magnesium has subsequently become the most commonly used

acceptor atom with recent reports indicating that a p-doping density of around 2×10^{17} cm^{-3} is available when the Al concentration is limited to 20% [25].

Thermally activated leakage currents can affect the high temperature performance of a laser diode [26]. GaN and associated alloys display a higher characteristic temperature, T_0, than AlGaInP [7] indicating better electron confinement. However, it has been reported that the performance of some nitride lasers can still degrade at high temperatures with carriers overflowing via the direct Γ-band [1]. The band offset values available to InGaN/GaN/AlGaN quantum wells have been investigated by several authors although different estimates have been given [27, 28]. One conclusion that can be deduced from the data is that the conduction band offsets are greater than those offered by AlGaInP materials. However, the difficulties of p-doping and the high threshold carrier densities associated with nitride lasers indicate that leakage currents are still a possibility.

Now the leakage path, i.e. the direct Γ-band, is sensitive to Al content. To overcome the problem of electron overflow it is recommended to maximise the p-doping density and Al composition in the p-cladding layer. However a trade-off between the two values does exist, so it is important to optimise the cavity design (and therefore minimise the leakage current) subject to the combinations that are on offer [1]. [*Note*: Hole overflow into the n-cladding layers is less of a problem due to the holes' lower mobility, diffusion length and the availability of a high n-doping density all contributing to an improvement in conductivity and a higher barrier [12].]

6.3 Laser structure

6.3.1 Design

Due to the ongoing debate about the dominant recombination mechanism in nitride laser diodes (and the difficulties of fabricating such lasers), research regarding the gain/current performance has been somewhat neglected. The amount of literature concerning this topic is therefore quite sparse. Recently some papers have been published regarding the performance of InGaN quantum well devices [1, 16, 22],

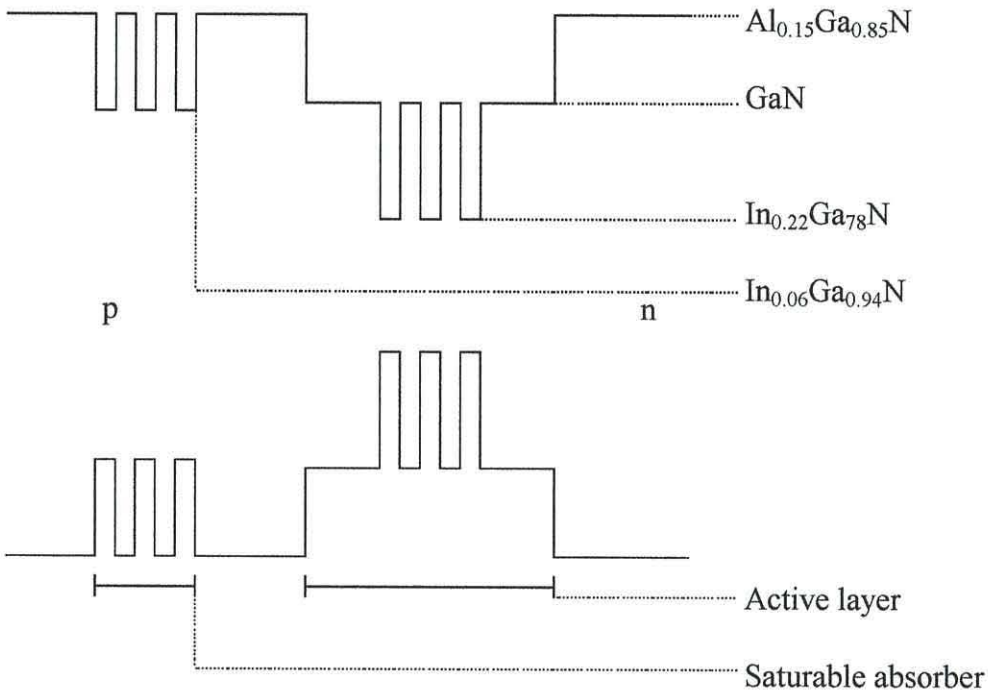

Fig. 6.1 *Schematic diagram of the InGaN self-pulsating laser diode.*

offering details about the well widths and cladding designs required for good gain/current characteristics and low threshold current performance. Using these results as a guide the device in this investigation will use an active region consisting of 35 Å wide $In_{0.22}Ga_{0.78}N$ quantum wells that are separated by 50 Å thick $In_{0.06}Ga_{0.94}N$ barriers, as displayed in fig. 6.1. This gain section is placed within a 0.1 μm wide GaN waveguiding layer (SCH) which is set alongside $Al_xGa_{1-x}N$ cladding layers. Unlike the AlGaInP structures described in the previous two chapters the quantum well number in the active region hasn't been optimised in the literature, so the well configuration of this gain generating section must be investigated.

When using an InGaN quantum well device leakage currents may cause deleterious effects if the structure isn't designed to offer sufficient carrier confinement, with carriers "leaking" out of the gain region via the direct Γ-band. The key design parameter to control this carrier overflow is the energy separation between the quantum well quasi-Fermi level and the Γ-band. Unlike the AlGaInP material system nitride-based devices can provide high barriers, thereby reducing the carrier overflow at high temperatures. To achieve such a structure it is recommended to use a

p-cladding layer with a large Al composition, i.e. around 15-20 % [1]. A high p-doping density is also desirable; however, this quantity is limited by the Al concentration. A p-cladding layer composition of $Al_{0.15}Ga_{0.85}N$ is achievable when combined with a p-doping density of 1×10^{17} cm^{-3} and will therefore be used throughout this chapter. A schematic of the laser design is shown in fig. 6.1.

To achieve the necessary absorption for self-pulsation a number of $In_{0.06}Ga_{0.94}N$ quantum wells are placed in the p-doped cladding layer at a distance of 0.115 μm from the active region. These absorber layers are strained in order to maximise the differential absorption as is required for self-pulsation (see equation (3.44)). Well widths of 15, 25, 35 and 45 Å will be investigated as will the absorber well number in order to obtain the optimum differential gain/absorption interaction.

6.3.2 Gain calculations

Using the necessary parameters [7, 11, 12] and the gain/absorption calculations presented in section 2.3, fig. 6.2 displays the results for the TE gain within a 3×35 Å quantum well active region. [*Note*: These calculations were generated using a model developed by Dr P. Rees.]. As predicted, the carrier densities required to achieve gain are high with the modal peak gain approximately half of that generated by the AlGaInP material system, i.e. when compared to fig. 4.6. Having described the properties associated with nitride materials it is apparent that many-body effects play a key role in determining the material gain of the structure. This point is emphasised even further in the diagrams. Apart from displaying the general trends associated with many-body effects, i.e. exciton peak in the absorption spectrum at low carrier densities and spectral broadening and band-gap renormalisation at high carrier densities, the magnitude of these changes are significantly greater than those displayed for the GaInP active region. Indeed, peaks in the absorption spectrum (caused by excitons) are observed at 0 °C even at high carrier densities.

The changes in the peak gain due to variations in carrier density and temperature are displayed in fig. 6.3. As expected, a high carrier density is required to generate gain at any of the three temperatures, with the differential gain (for a carrier density) reducing with temperature in a similar manner to that of the GaInP active

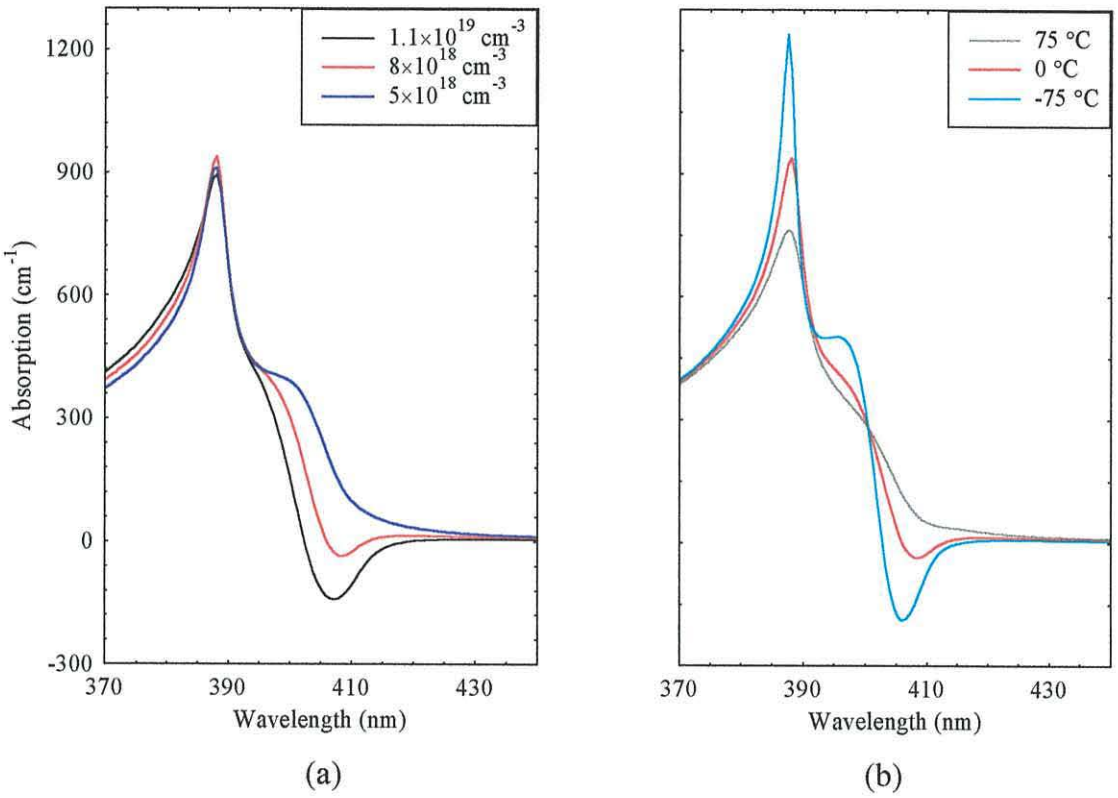

Fig. 6.2 *Typical modal gain spectrum for a 3×35 Å quantum well active region at (a) three different operating carrier densities at 0 °C and (b) three different temperatures for a carrier density of 8×10^{18} cm^{-3}.*

region. A sub-band transition is observed at 0 °C. When compared to the AlGaInP material more frequent sub-band changes are to be expected due to the smaller amount of gain per sub-band that is on offer. It is also worth noting that the changes in peak gain due to alterations in the operating temperature, i.e. the gaps between the curves, are significantly increased indicating the more dominant influence of the many-body effects. As a result, a larger shift in the operating wavelength (for a given carrier density) is observed.

6.3.3 Initial results

Now that the structure and gain properties of this nitride self-pulsating laser have been determined it is possible to model the dynamics of the device using the rate equations derived in section 3.4.2. After entering the parameters displayed in table 6.1

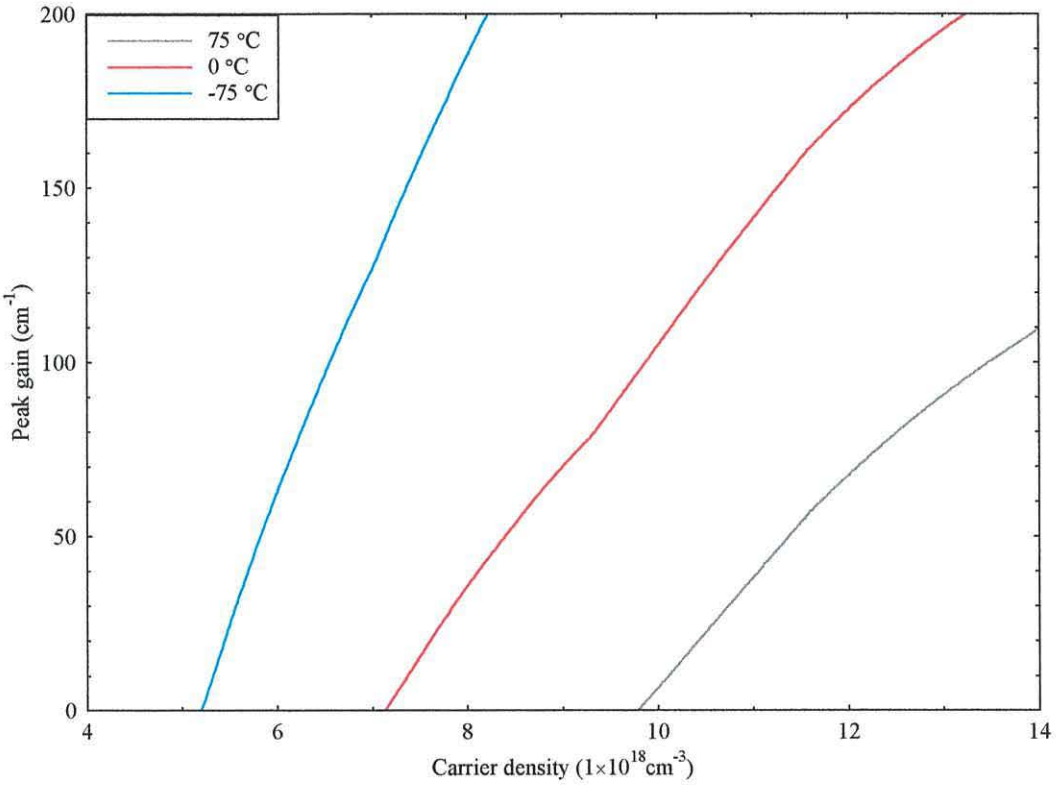

Fig. 6.3 *Calculated modal peak gain versus injected carrier density for a 3×35 Å quantum well active region at three different temperatures.*

and the gain/absorption values (at the operating wavelength) into this coupled system the equations are solved using the procedure outlined in appendix 2, section A2.2. The time evolution of the carrier densities in the gain and absorber sections and the photon generation in the waveguide may then be investigated, with self-pulsation being deemed as the emission that satisfies the conditions stated in appendix 3. The vast amount of defects that are a characteristic of nitride structures result in small non-radiative lifetimes, so the key value of the absorber carrier lifetime is given as 0.1 ns [1].

Initial results indicate that the structure is able to suppress the carrier overflow enough to allow self-pulsation throughout the temperature range being investigated, i.e. -125→100 °C, as displayed in fig. 6.4. Indeed, the diagram shows that for the 3×35 Å active region the leakage current doesn't influence the operating

Symbol	Parameter name	Parameter value
α_i	Internal loss	40 cm^{-1}
n_1	Ref. index of the $Al_{0.15}Ga_{0.85}N$ cladding layers	2.46
n_2	Ref. index of the GaN SCH	2.54
n_3	Ref. index of the $In_{0.06}Ga_{0.94}N$ QWs	2.56
n_4	Ref. index of the $In_{0.22}Ga_{0.78}N$ QWs	2.66
R	Facet reflectivity (coated)	0.32
β	Spont. emission coeff.	1×10^{-5}
τ_{qw}	Carrier lifetime in the active layer	1 ns
τ_α	Absorber carrier lifetime	0.1 ns
μ_n	Electron mobility in the p-cladding layer	200 $cm^2V^{-1}s^{-1}$
μ_p	Hole mobility in the p-cladding layer	7 $cm^2V^{-1}s^{-1}$
L_x	Well width of the MQW in the active layer	35 Å
L	Laser cavity length	500 μm
W	Stripe width	5 μm
V_{qw}	Volume of gain wells	Well no.×well width×W×L
V_α	Volume of absorber wells	Well no.×well width×W×L
m^*	Γ-band electron effective mass	0. 22 m_0
w_c	Thickness of p-cladding layer	1 μm

Table 6.1 *Parameters used in the rate equation model (from references [1, 29, 30]).*

characteristics until around 25 °C. Even at this point the effects are minimal. The increase in operating current and reduction in range (relative to the model with no leakage) then continues to increase quite slowly until the very high temperatures, i.e. >80 °C, where the exponential nature of the leakage equation begins to dominate. It is therefore evident that leakage effects are negligible until after the 70 °C temperature threshold, a point that makes the optimisation process much easier to enforce.

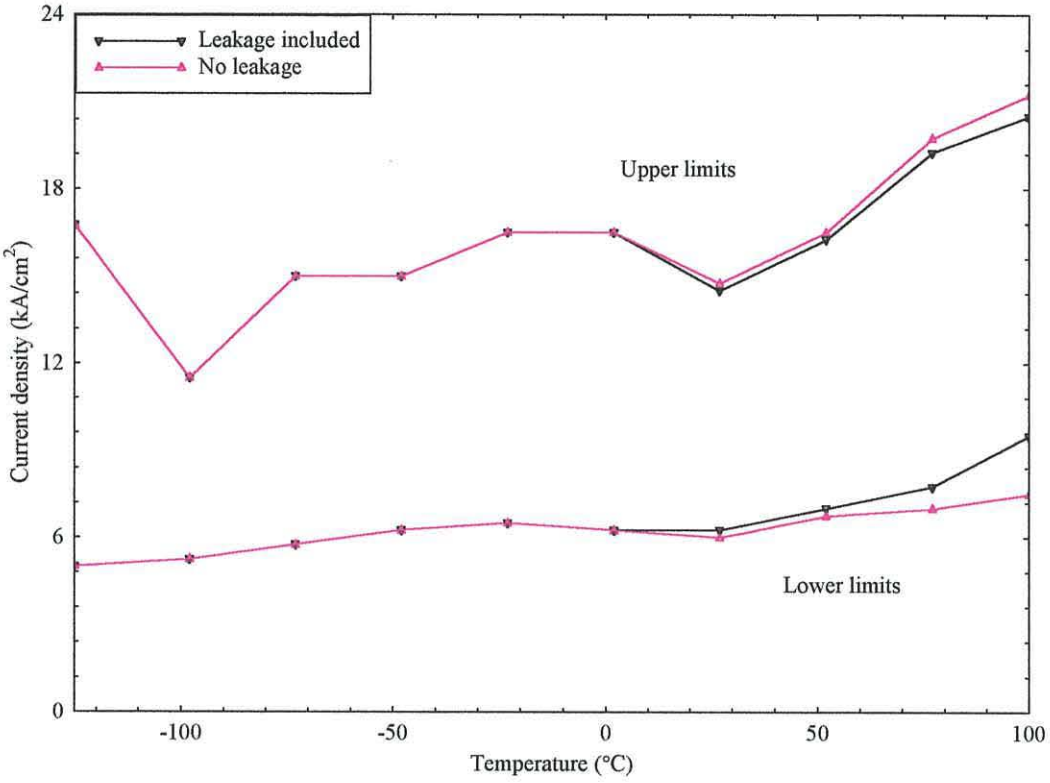

Fig. 6.4 *Self-pulsation bounds with and without leakage for a gain region with 3×35 Å quantum wells and an absorber section of 2×25 Å quantum wells.*

With this effective leakage suppression in mind the approach towards the optimisation of self-pulsation should be somewhat different to that proposed in the previous chapter. For the red emitting laser diode the emphasis was primarily on the high temperature performance of the device, and then the threshold current and power conditions. Now this structure allows self-pulsation throughout the temperature range being tested, so as long as self-pulsation can be achieved the 70 °C operating condition is already satisfied due to the leakage suppression. With this in mind, the temperature threshold should be less of a priority with the other emission criteria, i.e. the power and current conditions, being of greater cause for concern.

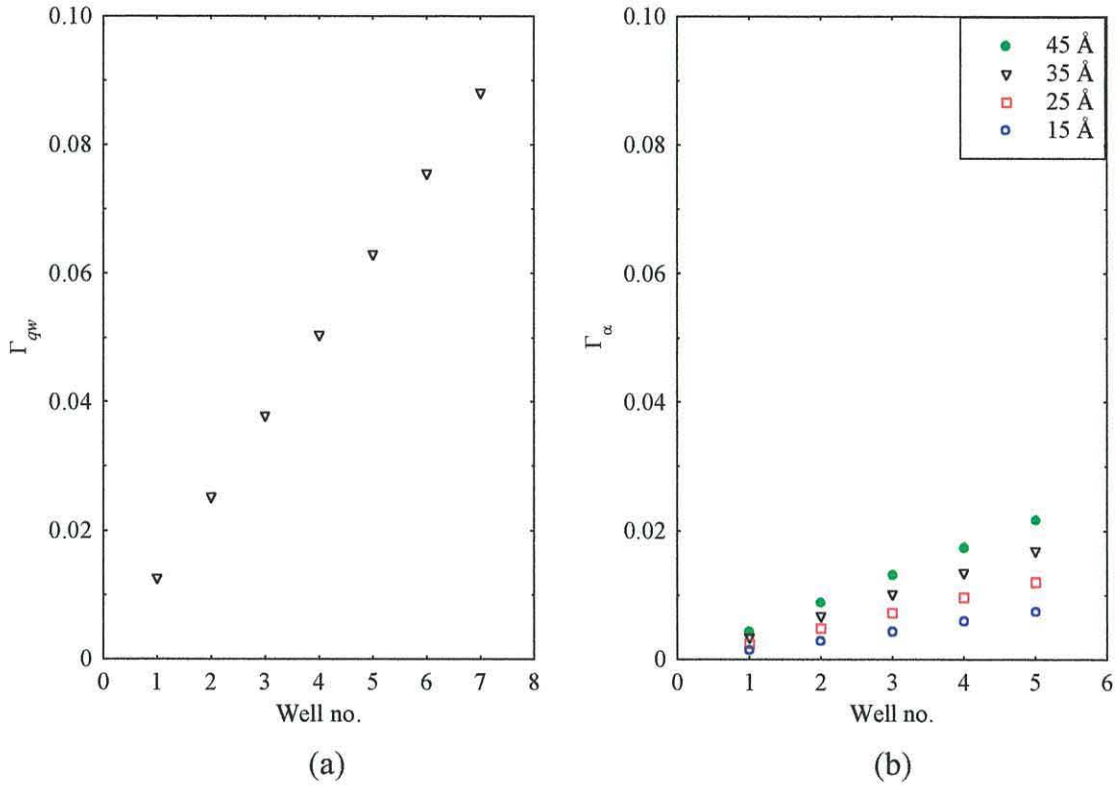

Fig. 6.5 *Transverse confinement factor calculations for a changing quantum well configuration in the (a) gain and (b) absorber sections of the InGaN laser diode.*

6.4 Optimum gain/absorption interaction for self-pulsation

6.4.1 Optimum gain region

In the previous chapter the active region was optimised for gain/current characteristics. For an $In_{0.22}Ga_{0.78}N$ quantum well gain section it is known that a 35 Å well width offers desirable properties [16]. However, the number of wells placed in the active region need to be investigated as this parameter can influence the differential gain and therefore affect the self-pulsation characteristics. So, in this section four well numbers will be studied, i.e. 1, 3, 5 and 7, in an attempt to seek the optimum gain configuration. The confinement factor, Γ_{qw}, will then be varied with the changing well number, as displayed in fig. 6.5(a).

It will be useful to investigate the properties of these active regions when operating alongside different absorber structures. Two cases are investigated. The

first being a study of the gain configuration in relation to a "small" amount of absorption, i.e. 2×25 Å quantum wells, and the second part involving an investigation with a "large" amount of absorption, i.e. 3×45 Å quantum wells. These generalisations are relative to the absorber layer widths that are on offer, as given in section 6.3.1.

Unfortunately the single 35 Å gain well fails to achieve self-pulsation when operating alongside either absorber structure. This active region provides the least amount of gain at the operating wavelength, so the threshold currents are high with the differential gain/absorption relationships at turn-on being unsuitable (to offer any self-pulsation). This active region would probably achieve self-pulsation when combined with thinner absorber wells, i.e. less absorption. However, for the well widths on offer in this chapter the performance is ineffective, so this single gain well configuration may be disregarded.

For the remaining active regions combined with a "small" amount of absorption, i.e. 2×25 Å quantum wells, the current density operating characteristics are displayed in fig. 6.6. The graphs show that for all gain generating configurations it is possible to suppress the leakage current sufficiently for self-pulsation up to 100 °C. The bleaching process experienced in the previous chapter is therefore negligible, however, beyond this temperature range leakage-induced effects are inevitable (as is observed when one extrapolates the curves in fig. 6.4).

It is also evident that the 3×35 Å gain section offers the lowest threshold currents. Now the higher the well number in the active region, the greater the differential gain. From equation (3.44) it is clear that an increase in differential gain will hinder the self-pulsation process. As a result, (for a given temperature) the differential gain/absorption relationship holds true for much longer amongst a specific sub-band transition when the number of wells in the gain section are at a minimum. A more stable transition process is therefore observed for the 3×35 Å structure resulting in a lower threshold current. This differential gain factor also causes the current density range of the emission to increase with decreasing well number, i.e. the differential gain/absorption relationship holds for much longer when the active region well number is minimised.

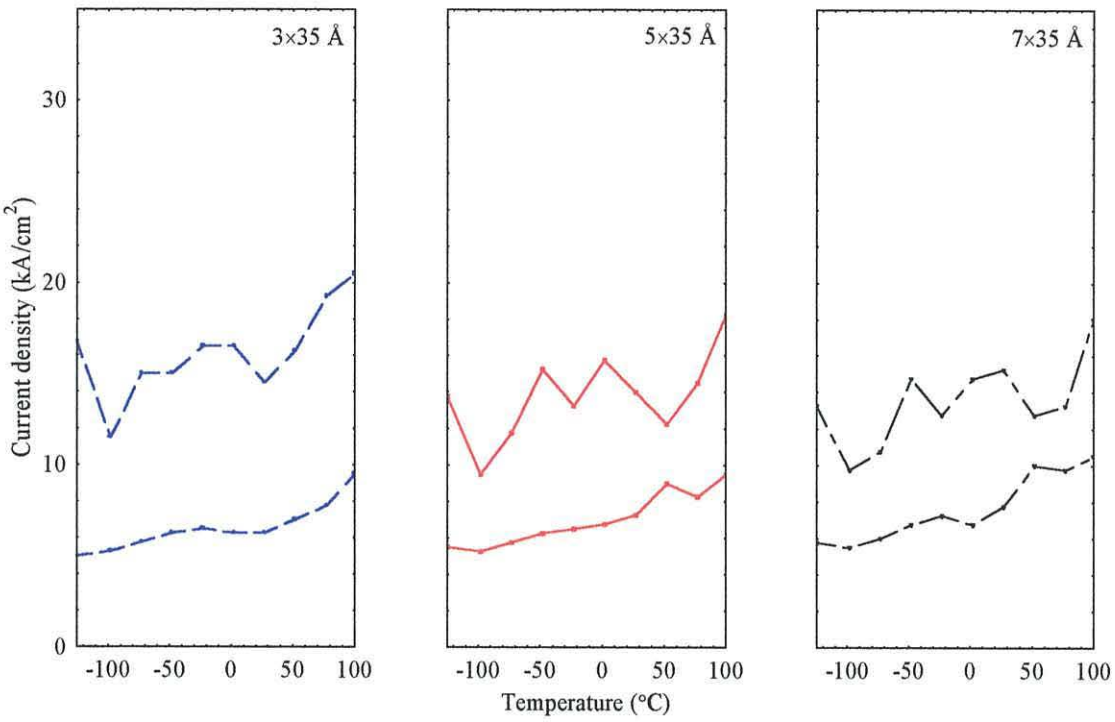

Fig. 6.6 *Self-pulsation bounds for three different gain region configurations with an absorber section of 2×25 Å quantum wells.*

This leads to the question of power output. The average optical power of a pulse is calculated using equation (5.1). As was mentioned in chapter 5, the greater the current density range for self-pulsation, the higher the power of the emission. Fig. 6.7 proves this point further, showing that when the leakage current is negligible (-25 °C) or at an influential level (75 °C) it is when the well number is at a minimum that the most efficient and highest power output is observed. The graphs would probably change at very high temperatures, i.e. >100 °C, when the leakage current becomes more problematic. However, at temperatures below 100 °C, when combined with this "small" amount of absorption the power output is best for the smallest gain generating well number, offering both 5 and 30 mW self-pulsation at the lowest possible current.

When a "large" amount of absorption is introduced, i.e. the 3×45 Å quantum wells, self-pulsation is only available over the full temperature range when using a

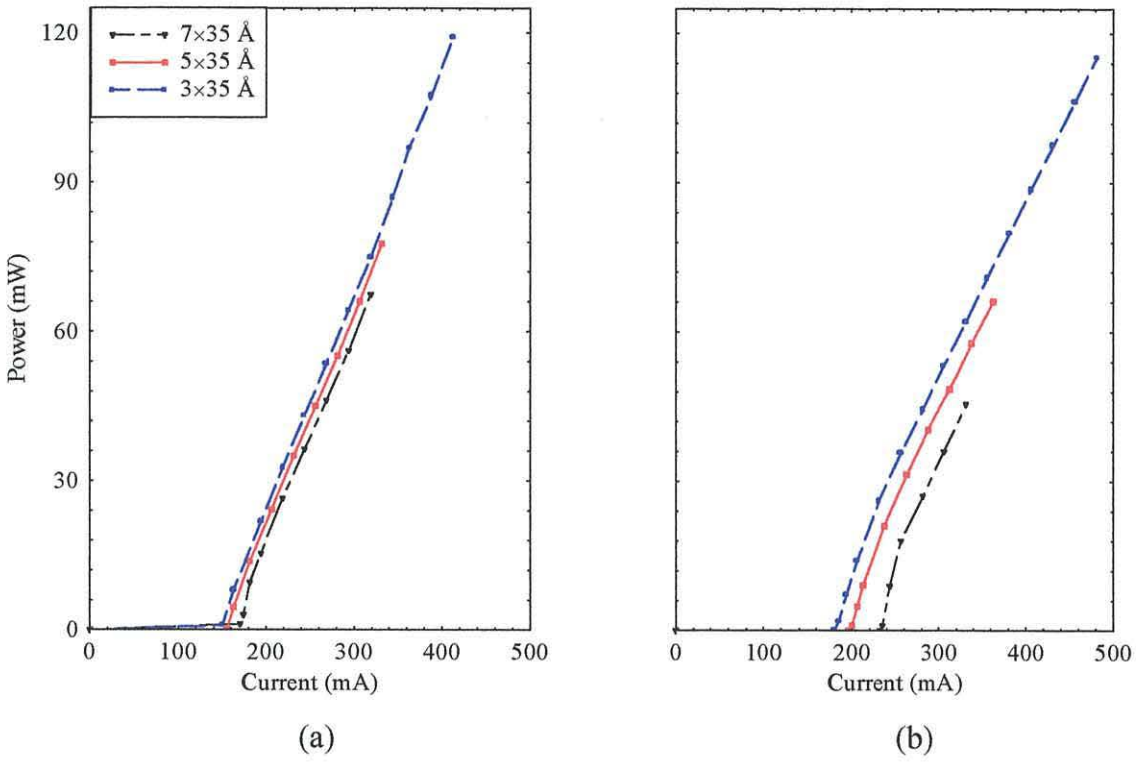

Fig. 6.7 *The average pulse power output for three different active regions with an absorber structure of 2×25 Å quantum wells at (a) -25 and (b) 75 °C.*

3×35 Å active region, as displayed in fig. 6.8. This indicates that the other two configurations generate too much differential gain at turn-on, causing equation (3.44) to fail at some optimum temperature. The "failure" of the self-pulsation cannot be due to the leakage current as the temperatures are too low (and the volumes of the absorber wells are too big to get bleached). The threshold current densities in all cases are very high owing to the large amount of absorption within the cavity, with the corresponding increase in differential absorption providing a wide operating range. This allows a very high power output in the case of the 3×35 Å gain section; however, the operating currents are too high for practical purposes, so the results aren't displayed.

The findings in this section provide clear evidence that the 3×35 Å quantum well active region offers the best performance at temperatures below 100 °C (subject to the generalised combinations of absorption). The amount of differential gain

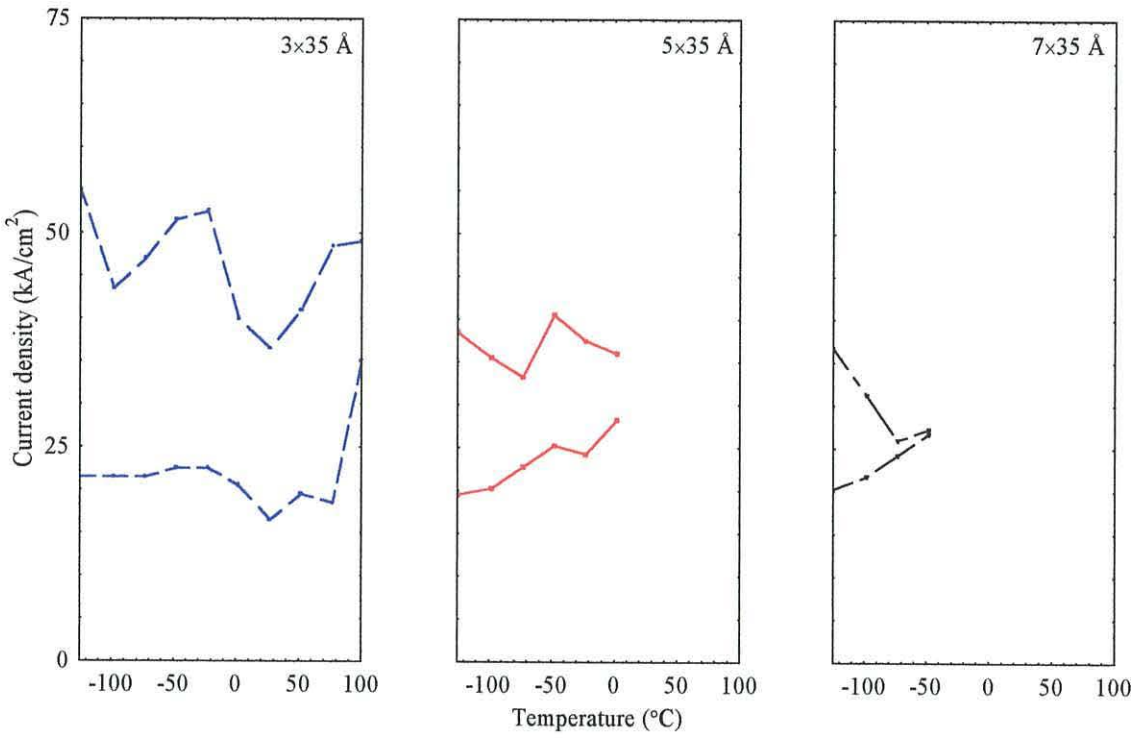

Fig. 6.8 *Self-pulsation bounds for three different gain region configurations with an absorber section of 3×45 Å quantum wells.*

available is small, so the conditions for self-pulsation holds over a wide temperature and current density range, leading to improvements in the threshold current density and power characteristics. So, in the remainder of this chapter this particular structure will be used in an attempt to create an optimised device for optical storage applications.

6.4.2 Optimum absorber configuration

Using the 3×35 Å quantum well active region the configuration of the absorber section will now be studied. A structure is required that offers sufficient differential absorption in relation to the differential gain from the active region to produce good self-pulsation characteristics. The absorber section will be optimised by considering well widths of 15, 25, 35, and 45 Å and well numbers between 1 and 5. The confinement factor, Γ_α, will therefore change with absorber configuration, as displayed in fig. 6.5(b), due to the varying overlap with the optical field.

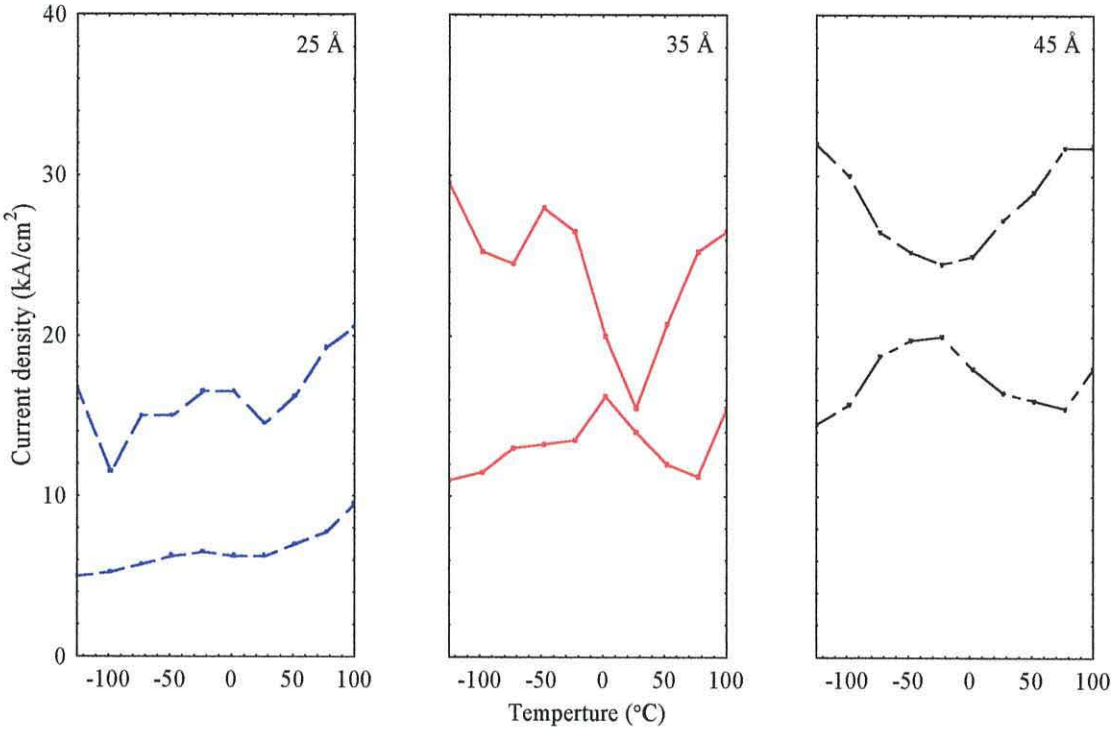

Fig. 6.9 *Current density bounds for self-pulsation as a function of temperature for structures including two 25, 35 and 45 Å absorber wells (and a 3×35 Å gain region).*

As was explained in section 6.3.3, due to the satisfactory suppression of the leakage current the intention is to minimise the threshold current and achieve the power thresholds of 5 and 30 mW. To achieve self-pulsation at a desirable threshold current, it is required to minimise the amount of absorption within the cavity. Unfortunately when a single absorber well is used all configurations, i.e. 1×15, 25, 35 and 45 Å, fail to emit any self-pulsation due to the unsatisfactory differential absorption characteristics at turn-on. Indeed, for the same reason, no self-pulsation is observed for any 15 Å quantum well configuration whatsoever.

An increase in absorption is therefore required. For the case of an absorber section with two quantum wells self-pulsation is available, as shown in fig. 6.9. The graphs display the expected trend of an increasing threshold current density with well width and confirmation that high temperatures can be achieved for all configurations. Changes in sub-band transitions are also very noticeable, represented by a minima in

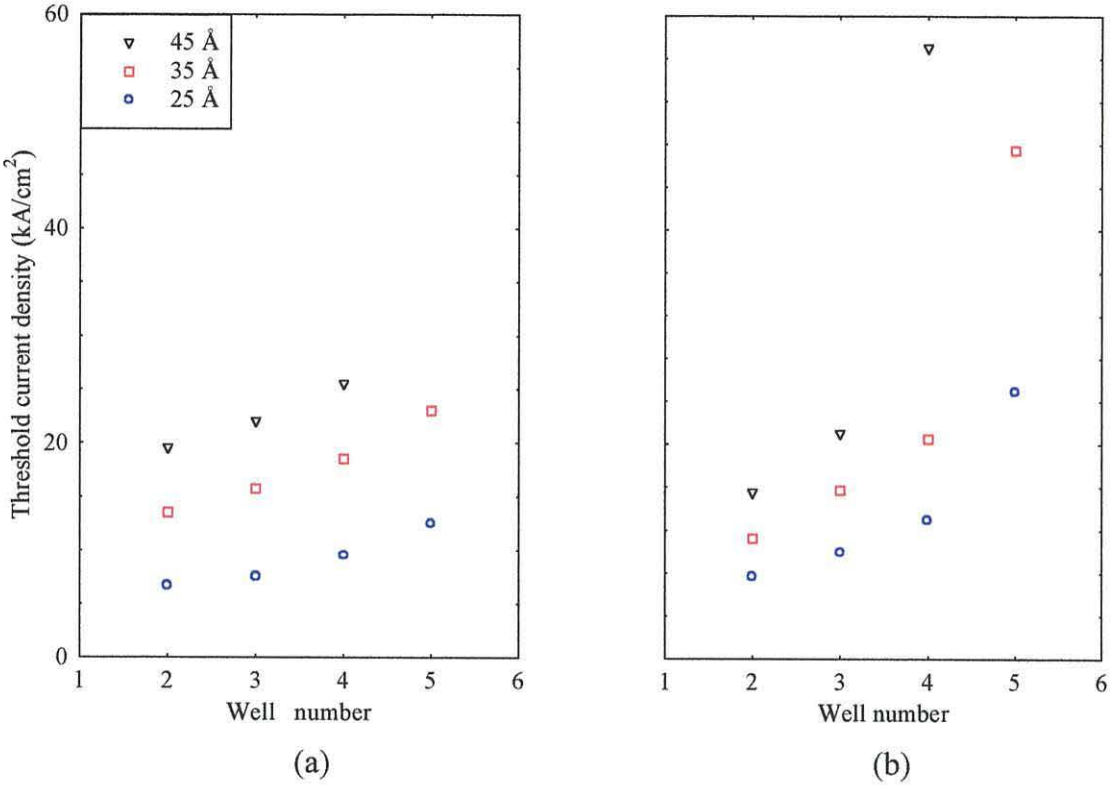

Fig. 6.10 *Threshold current density as a function of absorber well number at (a) -25 and (b) 75 ℃ for three different well widths (with a 3×35 Å gain section).*

the upper limit and a corresponding maximum in the lower limit curve, especially for the thicker absorber wells. The results indicate that the 2×25 Å quantum well absorber provides the least amount of absorption (relative to the amount of gain being generated) to achieve self-pulsation at the lowest possible threshold current.

Fig. 6.10 summarises the threshold current densities for self-pulsation for all the absorber structures under investigation at two different operating temperatures, i.e. before and after leakage takes effect. The results show that amongst the configurations being tested only the 5×45 Å structure offers too much absorption and is unable to generate any self-pulsation. The results also confirm that the 2×25 Å absorber generally gives rise to the lowest threshold currents, even at high temperatures, due to the effective suppression of the leakage current.

As one increases the temperature the most startling result is the significant change in the threshold current density per well configuration. It is the influence of

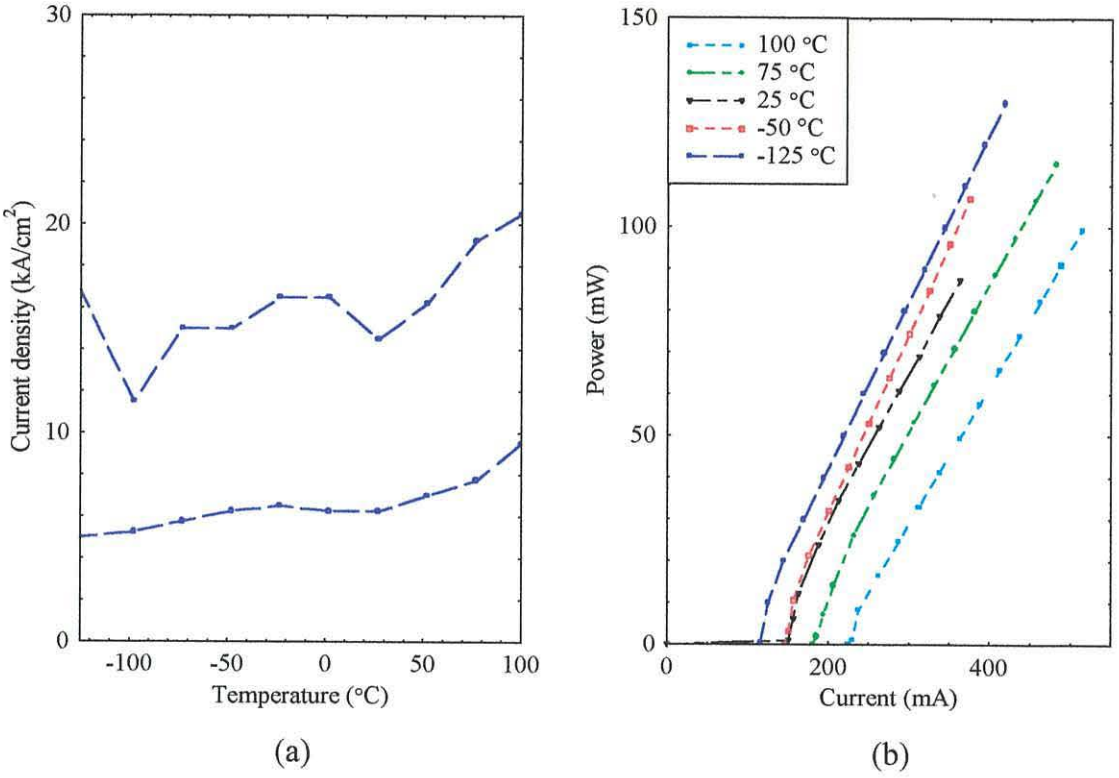

Fig. 6.11 *(a) Operating bounds and (b) the power output for self-pulsation for a laser diode with an absorber section of 2×25 Å quantum wells.*

changes in sub-band emission that cause this effect, not the leakage current. At -25 °C none of the structures have changed sub-bands hence the reasonably linear relationship between well number and threshold current density (per well width). When the temperature increases to 75 °C the sub-band emission within the gain wells have all shifted to higher transitions. However the varying amounts of absorption cause this "sub-band shift" to occur at different temperatures. When a sub-band change is experienced, the lower limit follows the path of a parabolic curve before changing to another sub-band, as displayed in fig. 6.9. The structures are therefore at different stages of this cycle, whilst at -25 °C all devices are experiencing emission on an upward part of the parabolic path. For numerous structures, lower threshold currents are then observed at 75 °C!

The previous results indicate that the 2×25 Å absorber offers the best performance in terms of threshold current, however the power output must also be investigated. Fig. 6.11 displays the current density bounds and corresponding power

output for such a laser, verifying the relationship between the maximum power and current density range that was mentioned previously (see fig. 6.7). It is evident that the wide operating range at temperatures below 100 °C allows the power output to increase beyond 100 mW in most cases. Both power thresholds are therefore available at temperatures above 70°C. The deleterious effects of the leakage current are also visible as the slope efficiency of the power curves decrease and the separation between curves increase with temperature, indicating a drop in the power/current ratio. However, these effects are negligible, so an absorber structure of 2×25 Å in combination with a 3×35 Å gain region can achieve the performance required for optical storage applications.

Fig. 6.12 shows the modal gain that is generated in the active region and four corresponding amounts of modal absorption that are on offer from various absorber well configurations. These curves are taken at carrier densities that are typical of those observed when a pulse is emitted. The wavelength of the emission is chosen such that the highest amount of gain is available, i.e. 408 nm, so it is at this point that the absorption is considered. If two 15 Å wells are used the sub-band energy levels are very high in comparison with the other well widths, resulting in a small amount of absorption that provides insufficient differential absorption characteristics at turn-on. For the other three cases self-pulsation is available. At the lasing wavelength the three structures offer lower sub-band energies, resulting in greater amounts of absorption. This leads to higher threshold currents; however, the differential absorption values are now sufficient to generate self-pulsation.

6.4.3 Separation distance between the gain and absorber layers

Now that a near optimum combination of gain and absorption has been achieved it is desirable to "fine-tune" the current density and power characteristics of the self-pulsation. A useful parameter that may be varied for just this purpose is the separation distance between the gain and absorber regions, d_{sep}, as displayed in fig. 5.14. The value has been set at 0.0115 μm throughout the previous sections which corresponds to a confinement factor, Γ_{α}, of approximately 0.0048 for the 2×25 Å absorber structure, as shown in fig. 6.5(b). Using this separation distance both power

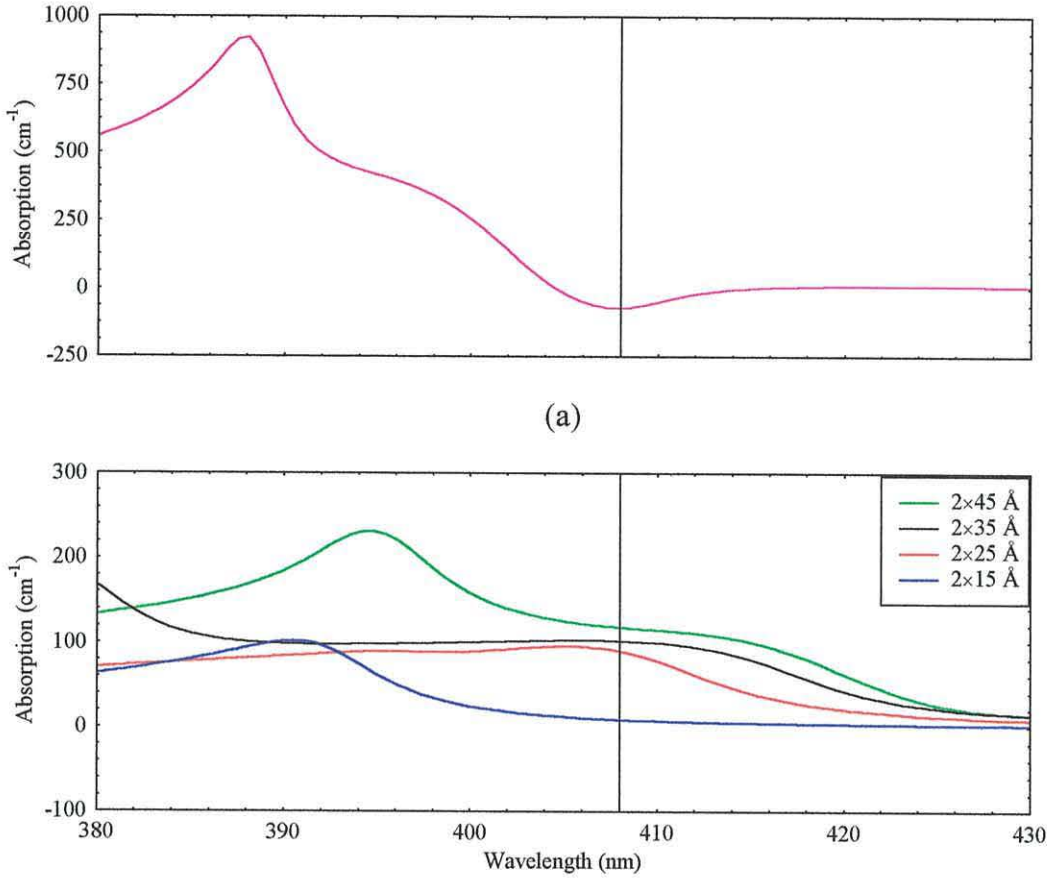

Fig. 6.12 *(a) Modal gain spectrum at a typical operating carrier density for the 3×35 Å quantum well active region together with (b) the corresponding modal absorption seen in 4 different absorber structures (T=0 °C).*

thresholds, i.e. 5 mW and 30 mW, can be achieved quite comfortably. It is therefore apparent that an absorber position further away from the gain region is desirable in order to reduce the threshold current density. This will result in a decrease in power, as was observed in the previous chapter. However, unlike the AlGaInP laser diode, the current structure offers over 100 mW of power at temperatures above 70 °C, so there exists plenty of leeway for optimisation purposes. In this investigation the absorber confinement value will be varied between 0.0048 and 0.0023 at intervals of 0.0005. This corresponds to a separation distance that is increasing, from 0.115 to 0.191 μm, as is summarised in fig. 6.13.

When the absorber quantum wells are at a distance of 0.191 μm away from

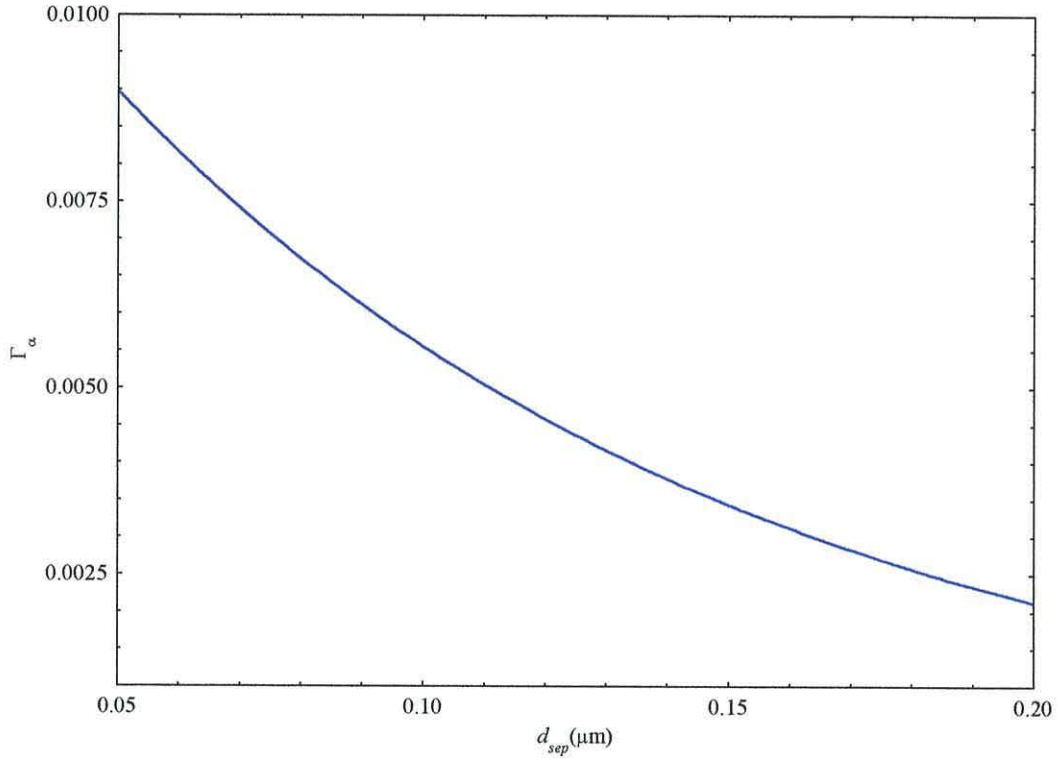

Fig. 6.13 *The relationship between the absorber confinement factor, Γ_α, and the distance between the absorber and gain regions, d_{sep} (for the 2×25 Å quantum well absorber).*

the active region no self-pulsation is observed, proving that an insufficient differential gain/absorption relationship exists at turn-on. For the other values being investigated the desired emission can be achieved, indicating a maximum separation distance of approximately 0.171 μm (Γ_α=0.0028). The current density bounds for three of these results are displayed in fig. 6.14. As was shown in the previous chapter, a movement away from the active region offers a reduction in threshold current and a decrease in the range of self-pulsation. In all cases the effects of the leakage current are negligible, so self-pulsation is achieved throughout the temperature range being investigated. The decreasing range causes a reduction in maximum output power, as is displayed in fig. 6.15. However, in all cases the 30 mW power threshold required for read/write devices is still on offer at 75 °C. This indicates that the maximum

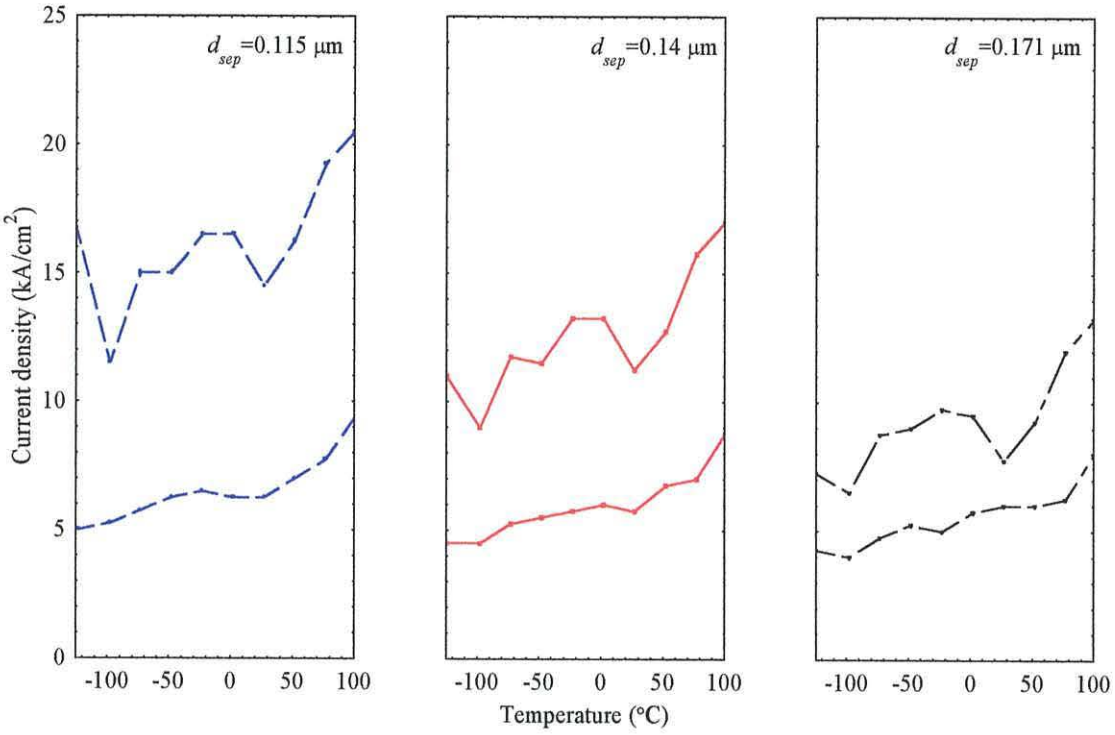

Fig. 6.14 *Self-pulsation bounds versus temperature for a laser with an absorber layer consisting of 2×25 Å wells for three different absorber positions.*

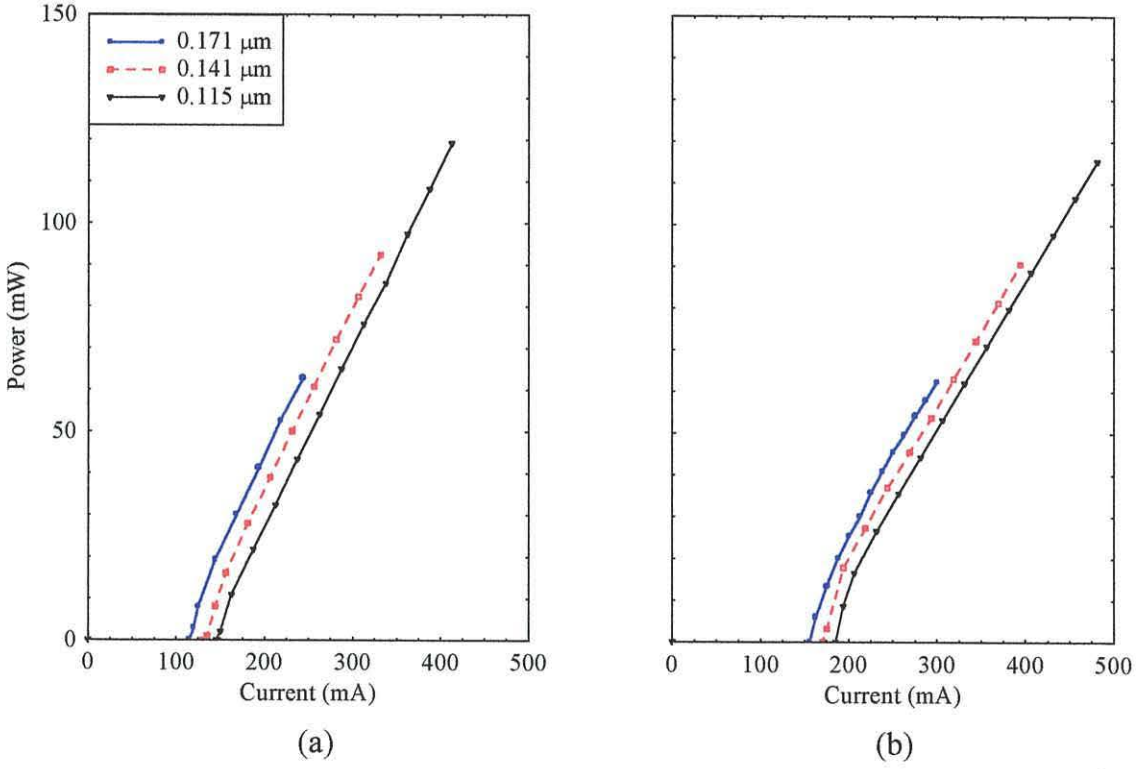

Fig. 6.15 *Power output of the self-pulsating laser with 2×25 Å absorber wells for three separation distances at (a) -25 and (b) 75 °C.*

separation distance of 0.171 μm results in a device that offers 5 and 30 mW operation at the lowest possible threshold current, regardless of the operating temperature (as long as it is below 100 °C).

Fig. 6.14 shows that the sub-band changes for the three separation distances occur at similar temperatures. The absorber wells are also of the same volume, so the bleaching effects are similar in the three cases. Due to these two factors the separation between the three power/current curves in fig. 6.15 do not fluctuate as the temperature is increased. However, thermal effects are observed as the slope efficiency decreases as the temperature changes from -25 to 75 °C.

6.5 Cavity design

From the previous sections it is clear that a 3×25 Å quantum well active region and a 2×25 Å quantum well absorber section separated by a distance of 0.171 μm offers self-pulsation that satisfies the optical storage conditions. These results were achieved using a cavity length of 500 μm and a (coated) reflectivity of 0.32, i.e. 32%. It is now desirable to optimise the structure even further by investigating the cavity design. This may be done by varying the length and reflectivity parameters. However, the current and power thresholds can be achieved quite easily indicating that it is acceptable to keep the reflectivity at 0.32, i.e. assuming a coated facet thereby increasing the reflectivity of the uncoated air/cavity interface. So, with this in mind the cavity optimisation will now be investigated by varying the length parameter only.

It is already known from the previous chapter that a decrease in the length provides a method of decreasing the threshold current. However, it is also known that a smaller cavity offers an increase in the amount of leakage current per unit length, thereby decreasing the maximum power output at high temperatures. Fortunately the power output from a 500 μm long cavity is quite high (even at high temperatures) and the leakage current is negligible, so there exists plenty of scope to reduce this length parameter. With this in mind six cavities are studied, i.e. 50, 100, 200, 300, 400 and 500 μm, in an attempt to optimise the structure.

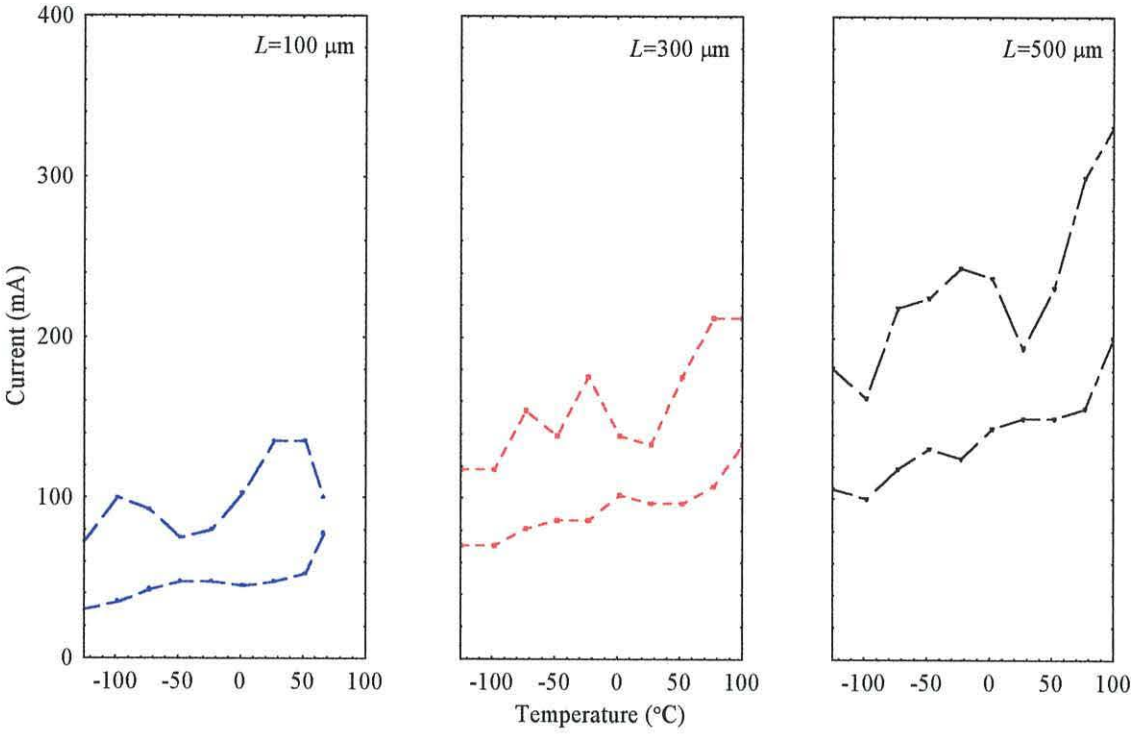

Fig. 6.16 *Self-pulsation bounds for a laser with an absorber layer consisting of 2×25 Å wells at a distance of 0.171 μm from the active region for three cavity lengths.*

Fig. 6.16 displays the current bounds for self-pulsation for three cavity lengths. No self-pulsation is observed for the 50 μm cavity, i.e. too much loss is on offer, so the results show the extremes of the range being investigated. The graphs display how the amount of optical loss is scaled by the cavity area, resulting in a threshold current that decreases with length. The most notable result is the reduced temperature range for the 100 μm cavity, i.e. self-pulsation stops at 67 °C. This indicates that the increase in leakage current per unit length influences the performance of the smaller cavities enough to affect the self-pulsation characteristics at high temperatures. So, in order to achieve the 70 °C temperature threshold a longer cavity length is required, providing evidence that a threshold current/high temperature trade-off exists even in this nitride laser diode.

The point is stressed even further in fig. 6.17 where the threshold currents for varying lengths and temperatures are displayed. These results show that all cavities

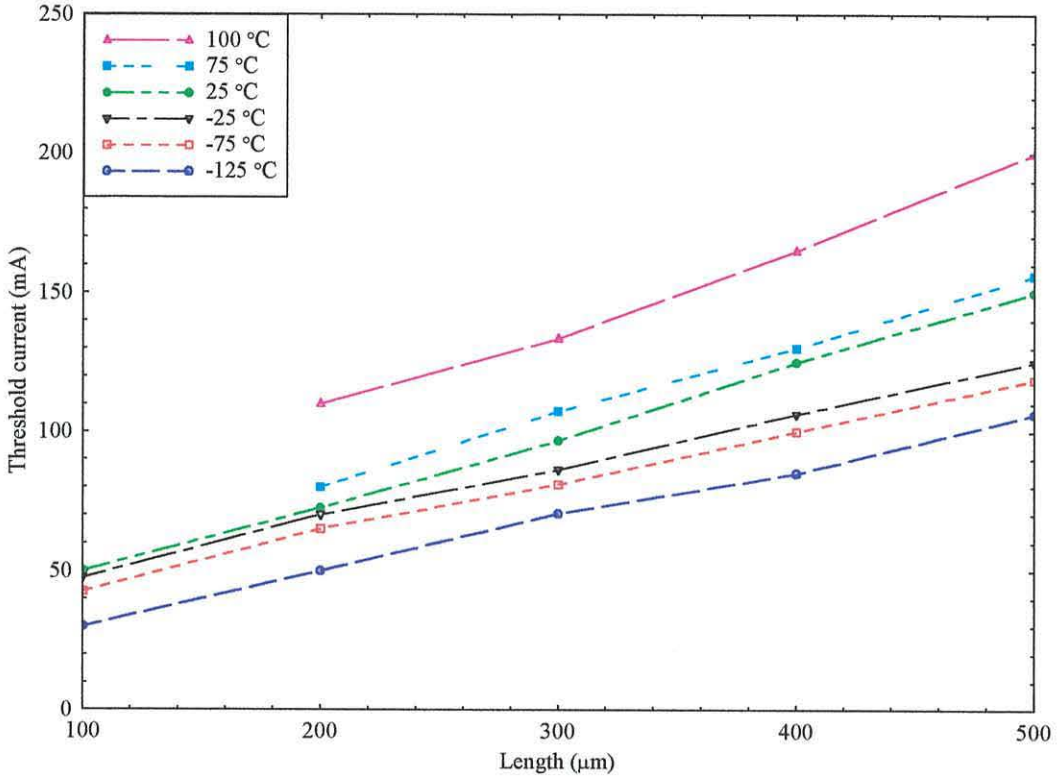

Fig. 6.17 *Threshold current values for self-pulsation for varying cavity lengths and temperatures.*

greater than 200 μm offer a sufficient suppression of the leakage current (per unit length) to allow self-pulsation up to (and beyond) 100 °C. The point at which the threshold current is scaled by the $1/L$ term rather than the area of the cavity (see equation (5.2)) cannot be reached, owing to the substantial amount of loss within the smaller cavities. This results in self-pulsation ceasing when the cavity length is at a value between 50 and 100 μm. So, for a minimal threshold current at temperatures greater than 70 °C a cavity length of roughly 200 μm offers the best performance.

Fig. 6.18 shows the power output of the self-pulsation for a varying cavity length. Again, the emission is investigated at two different temperatures to analyse the effects of the leakage current. Both graphs indicate that a decrease in length offers an improvement in the power/current ratio, due to the mirror loss term being scaled by the length of the device. For lengths greater than 100 μm, as one increases the temperature there exists a change in the maximum power output as the leakage

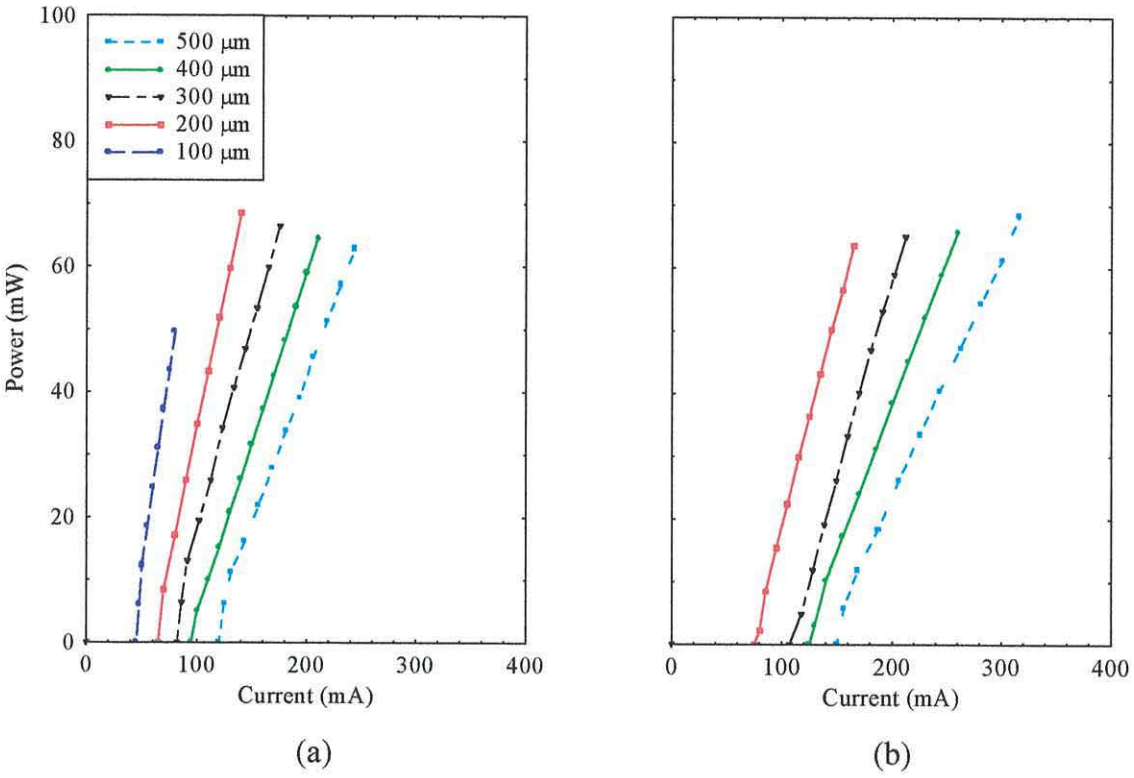

Fig. 6.18 *The average pulse power output for five different cavity lengths at (a) -25 and (b) 75 °C for an absorber structure of 2×25 Å quantum wells (R=0.32).*

current per unit length reduces with an increasing cavity (as observed in the previous chapter). All the cavities that self-pulsate at 75 °C offer maximum power outputs well beyond the desired thresholds, so it is desirable to choose the most efficient structure, i.e. the 200 μm device.

The curve that represents the 100 μm device behaves somewhat differently to the others; rather than emitting the highest maximum power at -25 °C, it emits the lowest! It is known that self-pulsation stops at 67 °C due to the leakage current, however, at -25 °C carrier overflow is negligible, so there exists another deleterious effect. This "buck in trend" cannot be a consequence of the $1/L$ term dominating the mirror loss value, as the power/current ratio hasn't been effected. It must therefore be a consequence of a change in sub-band transition. As is observed in fig. 6.16, at -25 °C the operating current range for the 100 μm cavity is very small, indicating that the active region is in the process of changing sub-band emission. The longer cavities offer a smaller amount of loss per unit length, so this sub-band change occurs at

higher temperatures. The current range that is made available to the 100 μm laser is therefore different to the other structures and restricts the maximum power output of the device.

The results presented in this section indicate that the optimisation of the cavity length can improve the performance of the nitride self-pulsating laser diode. In order to achieve 5 and 30 mW operation at the 70 °C temperature threshold it is evident that a cavity length of 200 μm provides the best performance. This structure allows self-pulsation to be realised at the lowest possible threshold current whilst offering emission throughout the temperature range being investigated.

6.6 Optimum structure

Using the work displayed in the previous sections it is now possible to suggest an optimum structure that offers self-pulsation suitable for optical storage applications. From the investigation it is apparent that a 3×35 Å quantum well active region generates sufficient gain (relative to the absorption on offer) to achieve self-pulsation over a wide operating range. It has also been found that an absorber section of 2×25 Å quantum wells placed at a distance of 0.171 μm away from the above-mentioned active region provides emission with desirable absorption characteristics. When this design is set within a 200 μm long cavity (32% reflectivity) the self-pulsating laser offers the characteristics observed in fig. 6.19. For 5 and 30 mW emission at 70 °C operating currents of 82 and 112 mA, respectively, are required thereby achieving the emission criteria at the lowest threshold currents. The effective suppression of the leakage current (per unit length) allows emission up to 100 °C, thus allowing plenty of scope for very high temperature operation if required.

6.7 Conclusions

The purpose of this chapter was to design a blue self-pulsating laser diode with epitaxial absorber layers and optimise the structure for optical storage applications. In

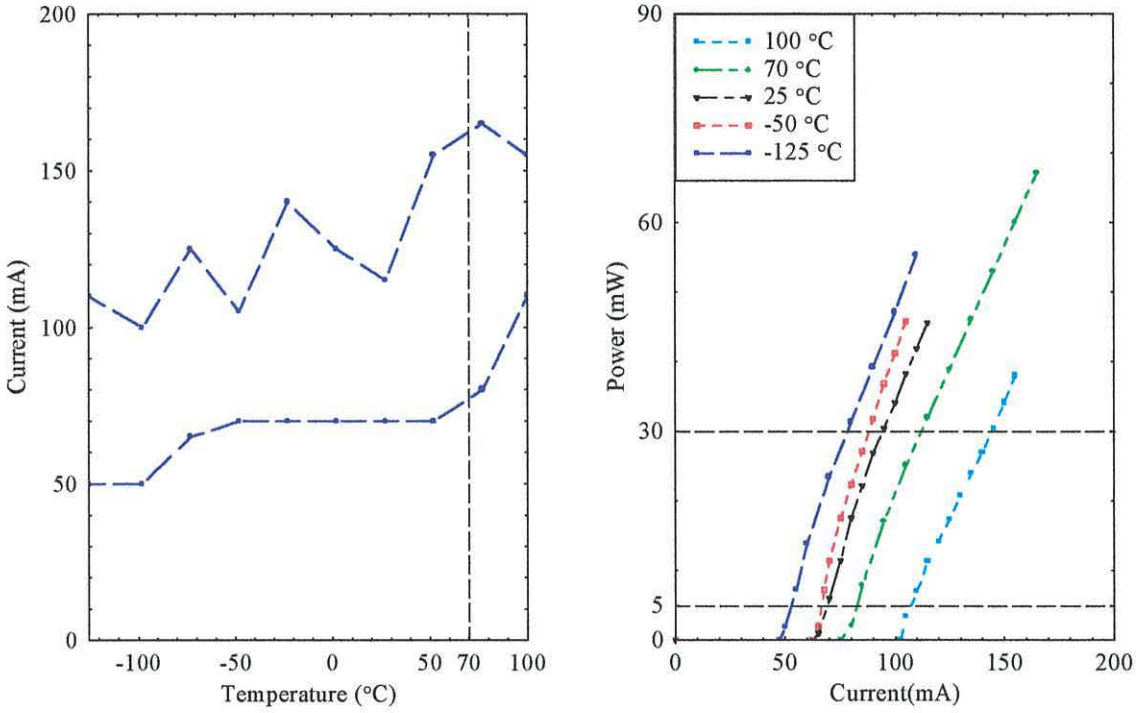

Fig. 6.19 *(a) Operating bounds and (b) the power output for the optimum 5 and 30 mW self-pulsating laser diode, i.e. 2×25 Å absorber, L=200 μm, R=0.32 and* d_{sep}*=0. 171 μm.*

order to achieve the desired operating wavelength the laser was fabricated in the GaN material system. Now it is known that an active region consisting of 35 Å wide quantum wells offers the lowest threshold current for an $In_{22}Ga_{0.78}N$ quantum well device [16]. By varying the well number the gain section was optimised subject to the absorber layers under investigation. It was found that a 3×35 Å quantum well active region generates a sufficient amount of gain to achieve self-pulsation. This design produces a relatively small amount of differential gain in relation to the typical differential absorption on offer, thus allowing self-pulsation over a large current density range. Carrier overflow into the cladding layers is also minimised, thus reducing the probability of absorber bleaching, allowing self-pulsation to be achieved at 70 °C with relative ease.

Due to the reduction in carrier overflow the design of the absorber structure concentrated on minimising the operating current at which the power thresholds could be achieved. It was stated that a minimal amount of absorption would be desirable.

Using the 3×35 Å active region no 15 Å absorber configurations give rise to any self-pulsation neither do any single well absorber structure. All the other multiple quantum well absorbers, apart from the 5×45 Å structure, give the desired output offering both 5 and 30 mW emission well beyond the temperature threshold. However, as the 2×25 Å absorber section provides the least amount of absorption and therefore the smallest threshold currents it was deemed the optimum absorber configuration.

Once the gain/absorption interaction was optimised, the separation distance between the two sections was investigated. It was found that a distance of 0.171 μm reduces the amount of absorption enough to minimise the threshold current whilst still achieving the power thresholds. It was also found that the optimum gain and absorber structures must be set within a 200 μm long cavity in order to minimise the operating current whilst allowing emission over a wide temperature range. [*Note*: These results are based on a stripe width of 5 μm. Further reductions in operating current could be achieved by lowering this particular value.]

It may be concluded that both power thresholds are available at 70 °C (and beyond) when using the above-mentioned optimised structure. The operating currents are far superior to those offered by the AlGaInP device due the effective suppression of the leakage current. As a result this nitride self-pulsating laser diode is desirable for use in a "next generation" DVD system.

References

[1] K. Domen, R. Soejima, A. Kuramata and T. Tanahashi, "Electron overflow to the AlGaN p-cladding layer in InGaN/GaN/AlGaN MQW laser diodes," *MRS Internet J. Nitride Semicond. Res.*, vol. 3, article 2, 1998.

[2] M. A. Hasse, J. Qiu, J. M. DePuydt and H. Cheng, "Blue-green laser-diodes," *Appl. Phys. Lett.*, vol. 59, pp. 1272-1274, 1991.

[3] Y. Guan, C. A. Zmudzinski, P. S. Zory Jr. and R. M. Park, "Photopumped antiguide blue lasers fabricated from molecular-beam epitaxial ZnSe on GaAs," *IEEE Photon. Technol. Lett.*, vol. 3, pp. 685-687, 1991.

[4] S. Itoh, K. Nakano and A. Ishibashi, "Current status and future prospects of ZnSe-based light-emitting devices," *J. Crystal Growth*, vol. 214, pp. 1029-1034, 2000.

[5] H. Amano, I. Akasaki, T. Kozawa, K. Hiramatsu, N. Sawaki, K. Ikeda and Y. Ishii, "Electron-beam effects on blue luminescence of zinc-doped GaN," *J. Lumin.*, vol. 40, pp. 121-122, 1988.

[6] S. Nakamura and T. Mukai, "High-quality InGaN films grown on GaN films," *Jpn. J. Appl. Phys. Part 2*, vol. 31, L1457-L1549, 1992.

[7] S. Nakamura and G. Fasol, *The Blue Laser Diode*, Springer-Verlag, Berlin, 1997.

[8] S. Nakamura, M. Senoh and T. Mukai, "p-GaN/n-InGaN/n-GaN double-heterostructure blue-light-emitting diodes," *Jpn. J. Appl. Phys. Part 2*, vol. 32, L8-L11, 1993.

[9] S. Nakamura, M. Senoh, S. Nagahama, N. Iwasa, T. Yamada, T. Matsushita, H. Kiyoku and Y. Sugimoto, "InGaN-based multi-quantum-well-structure laser diodes," *Jpn. J. Appl. Phys. Part 2*, vol. 35, L74-L76, 1996.

[10] S. Nakamura, M. Senoh, S. Nagahama, N. Iwasa, T. Yamada, T. Matsushita, H. Kiyoku, Y. Sugimoto, T. Kozaki, H. Umemoto, M. Sano and K. Chocho, "High-power, long-lifetime InGaN/GaN/AlGaN-based laser diodes grown on pure GaN substrates," *Jpn. J. Appl. Phys. Part 2*, vol. 37, L309-L312, 1998.

[11] S. J. Pearton, J. C. Zolper, R. J. Shul and F. Ren, "GaN: Processing, defects, and devices," *J. Appl. Phys.*, vol. 86, pp. 1-78, 1999.

[12] S. C. Jain, M. Willander, J. Narayan and R. Van Overtraenten, "III-nitrides: Growth, characterization, and properties," *J. Appl. Phys.*, vol. 87, pp. 965-1006, 2000.

[13] S. Nakamura, "The roles of structural imperfections in InGaN-based blue light-emitting diodes and laser diodes," *Science*, vol. 281, pp. 956-961, 1998.

[14] P. Rees, C. Cooper, P. Blood, P. M. Smowton and J. Hegarty, "Gain characteristics of GaN quantum wells including many-body effects," *Electron. Lett.*, vol. 31, pp. 1149-1150, 1995.

[15] P. Rees, C. Cooper, P. M. Smowton, P. Blood and J. Hegarty, "Calculated threshold currents of nitride- and phosphide-based quantum well lasers," *IEEE Photon. Technol. Lett.*, vol. 8, pp. 197-199, 1996.

[16] W. W. Chow, H. Amano, T. Takeuchi and J. Han, "Quantum-well width dependence of threshold current in InGaN lasers," *Appl. Phys. Lett.*, vol. 75, pp. 244-246, 1999.

[17] S. D. Lester, F. A. Ponce, M. G. Craford and D. A. Steigerwald, "High dislocation densities in high-efficiency GaN-based light-emitting-diodes," *Appl. Phys. Lett.*, vol. 66, pp. 1249-1251, 1995.

[18] P. G. Eliseev, P. Perlin, J. Y. Lee and M. Osinski, ""Blue" temperature-induced shift and band-tail emission in InGaN-based light sources," *Appl. Phys. Lett.*, vol. 71, pp. 569-571, 1997.

[19] Y. Narukawa, Y. Kawakami, M. Funato, S. Fujita, S. Fujita and S. Nakamura, "Role of self-formed InGaN quantum dots for exciton localization in the purple laser diode emitting at 420 nm," *Appl. Phys. Lett.*, vol. 70, pp. 981-983, 1997.

[20] Y. K. Song, M. Kuball, A. V. Nurmikko, G. E. Bulman, K. Doverspike, S. T. Shepperd, T. W. Weeks, M. Leonard, H. S. Kong, H. Dieringer and J. Edmond, "Gain characteristics of InGaN/GaN quantum well diode lasers," *Appl. Phys. Lett.*, vol. 72, pp. 1418-1420, 1998.

[21] A. Vertikov, A. V. Nurmikko, K. Doverspike, G. Bulman and J. Edmond, "Role of localized and extended electronic states in InGaN/GaN quantum wells under high injection, inferred from near-field optical microscopy," *Appl. Phys. Lett.*, vol. 73, pp. 493-495, 1998.

[22] C. K. Sun, S. Keller, T. L. Chiu, G. Wang, M. S. Minsky, J. E. Bowers and S. P. DenBaars, "Well-width dependent studies of InGaN-GaN single-quantum wells using time-resolved photoluminescence techniques," *IEEE J. Select. Topics Quantum Electron.*, vol. 3, pp. 731-738, 1997.

[23] K. Domen, A. Kuramata, R. Soejima, K. Horino, S. Kubota and T. Tanahashi, "Lasing mechanism of InGaN-GaN-AlGaN MQW laser diode grown on SiC by low-pressure metal-organic vapor phase epitaxy," *IEEE J. Select. Topics Quantum Electron.*, vol. 4, pp. 490-497, 1998.

[24] W. W. Chow, S. W. Koch and M. Sargent III, *Semiconductor Laser Physics*, Springer-Verlag, Berlin, 1994.

[25] I. Asakai and H. Amano, *GaN*, Academic Press, New York, 1998.

[26] G. P. Agrawal and N. K. Dutta, *Long-Wavelength Semiconductor Lasers*, Van Nostrand Reinhold, 1986.

[27] S. H. Wei and A. Zunger, "Valence band splittings and band offsets of AlN, GaN and InN," *Appl. Phys. Lett.*, vol. 69, pp. 2719-2721, 1996.

[28] G. Martin, A. Botchkarev, A. Rockett and H. Morkoc, "Valence-band discontinuities of wurtzite GaN, AlN and InN heterojunctions measured by x-ray photoemission spectroscopy," *Appl. Phys. Lett.*, vol. 68, pp. 2541-2543, 1996.

[29] S. Nakamura, "Characteristics of room temperature-*cw* operated InGaN multi-quantum-well-structure laser diodes," *MRS Internet J. Nitride Semicond. Res.*, vol. 2, article 5, 1997.

[30] M. S. Chung, N. M. Miskovsky, P. H. Cutler and N. Kumar, "Band structure calculation of field emission from $Al_xGa_{1-x}N$ as a function of stoichiometry," *Appl. Phys. Lett.*, vol. 76, pp. 1143-1145, 2000.

Chapter 7

Conclusions

7.1 Summary of the thesis

The first chapter summarised the demands for self-pulsating laser diodes in the optical storage industry. Starting with a brief outline of the historical development of the semiconductor laser the work then described the benefits of using such a laser in an optical storage device, specifying the advantages of short wavelength, i.e. 650 and 420 nm, pulsed emission. The output specifications were outlined, indicating that the laser diode must emit at 70 °C whilst offering a 5 mW power output for a read-only system and 30 mW operation for a read/write device. The most compact and economical method of achieving such operating characteristics involves using a self-pulsating laser, where saturable absorption is included in the cavity to create a dynamically unstable beam. Such a laser was introduced, followed by a description of the aims of the thesis, i.e. the work involved designing and optimising short wavelength self-pulsating laser diodes subject to the high temperature conditions that must be satisfied for use in optical storage devices.

The second chapter introduced the theory required to understand the material and optical properties of a semiconductor and how these properties are manipulated to construct a laser. The concept of quantum confinement was introduced, with a derivation of an equation for the material gain in quantum well structures. Many-body effects and strain were also described and included in the gain model. The

propagation of an optical field within a dielectric material was analysed, specifying the demands for waveguiding in a symmetric dielectric "slab". The chapter concluded by combining the material and optical components of the semiconductor to construct an equation for the threshold gain in a semiconductor laser.

The third chapter introduced the mathematical techniques required to investigate the dynamical properties of a self-pulsating laser diode. Starting with a description of the different structures that offer self-pulsation, two lasers were then studied in more depth, i.e. the real refractive index guided laser and laser diode with epitaxial absorber layers. In each case a derivation of a rate equation model was presented (combined with an assessment of the optical field within the cavity) so that the emission characteristics of either structure could be thoroughly investigated. The thermally activated leakage current was then presented, including a derivation of an equation to model this potentially problematic effect. The chapter concluded with an outline of the conditions for self-pulsation, with attention being paid to the key differential gain/absorption relationship that must be satisfied for the emission to self-pulsate.

The first three chapters introduced the theory required to study the material and dynamical properties of a self-pulsating laser. The final three chapters implemented the equations and studied three different self-pulsating lasers for use in optical storage devices, i.e. subject to the requirements stated in chapter 1. Chapter 4, used a rate equation model (and appropriate gain calculations) to simulate the output of a 650 nm real refractive index guided laser grown in the AlGaInP material system. Such a laser emits a self-pulsating beam by using the unpumped outer regions of the active layer as a saturable absorber. The desired emission is then achieved as carriers diffuse laterally between the gain and absorber sections, giving rise to self-pulsation if the cavity design offers sufficient gain/absorption characteristics. However, such a weakly index guided laser must be carefully designed to provide a sufficient "built-in" refractive index step (in the lateral direction) such that carrier-induced anti-guiding is avoided throughout the diffusion cycle.

After an initial description of the properties associated with the AlGaInP material system the laser was designed and investigated for optimum performance by varying the stripe width, blocking layer and optical confinement layer thicknesses,

thereby varying the gain/absorption interaction. The work showed that only certain configurations can generate the desired differential gain/absorption relationship combined with a sufficient lateral index step to achieve self-pulsation at 0 °C. However, all of these structures fail to self-pulsate at 70 °C as the deleterious effects of the leakage current came to the fore. The chapter concluded by stating that the AlGaInP real refractive index guided laser offers unsuitable self-pulsation characteristics for use in optical storage devices (due to the problematic nature of the leakage current).

Due to the poor high temperature performance of the above-mentioned laser chapter 5 studied the laser diode with epitaxial absorber layers for 650 nm self-pulsation subject to the optical storage constraints. Grown in the AlGaInP material system such a laser includes quantum well layers of different composition to the gain section to achieve the necessary absorption for self-pulsation. Placing the absorber wells in the p-cladding layer gives rise to a more flexible absorber, offering absorption characteristics that are independent of those offered by the gain section (as opposed to the previous laser). Indeed, the influence of the gain region only arises at high temperatures when the absorber wells are bleached by overflowing carriers, causing the self-pulsation to stop.

Using an optimised gain section, the high temperature self-pulsation was initially investigated by varying the design of the quantum wells in the absorber, i.e. the well width and well number. The results showed that 70 °C emission is available for a number of combinations due to the effective suppression of the leakage current. Two valuable relationships were found. Firstly, an increase in the volume of the absorber section increases the high temperature performance of the device as the number of carriers required to bleach the absorber (and stop self-pulsation) is increased. Secondly, for a constant absorber volume a large number of narrow wells gives rise to self-pulsation at higher temperatures than a small number of wider wells. These key results indicate that absorber bleaching (for a given temperature) is more rapid in the wide well configurations due to the smaller differential absorption on offer.

With the temperature threshold achieved the laser was then optimised to satisfy the temperature, current and power requirements by varying the gain-absorber

separation distance and the cavity parameters. It was found that 5 mW operation at 70 °C is attainable at a relatively satisfactory threshold current, however, 30 mW emission requires a significantly higher operating current, with the power threshold being achieved at impractical values. However, a 5 μm stripe width was used, so a smaller stripe (if available) could improve the operating currents to more manageable values.

Once 70 °C self-pulsation had been obtained using the red semiconductor laser chapter 6 investigated and optimised a blue self-pulsating laser diode subject to the constraints stipulated in chapter 1. Such a laser would be useful in a "next generation" DVD system, so an investigation of the feasibility of such a laser is invaluable. In order to emit at a wavelength of 420 nm it was decided to model a laser fabricated in the in the GaN material system with the material properties indicating that the active region could be effected by a thermally activated leakage current. With this in mind a laser diode with epitaxial absorber layers was investigated which had proven to offer a more "leakage resistant" self-pulsation than the real refractive index guided laser.

The laser was designed and optimised for self-pulsation (subject to the optical storage constraints) by investigating the gain/absorption interaction through the configuration of the gain and absorber quantum wells. The results showed that the leakage current is well suppressed (due to the careful design of the cladding layers) with 70 °C operation achievable with relative ease. As a result the priority of high temperature performance was relaxed with the power thresholds and the minimisation of the operating current taking precedence. Further studies involving the gain-absorber separation distance and cavity design resulted in two optimum configurations for 5 and 30 mW operation at 70 °C. With these results in mind, this nitride self-pulsating laser diode proves to offer sufficient operating characteristics for use in future DVD systems. Indeed, this investigation provided a step towards the realisation of a "next-generation" device.

7.2 Ongoing and future work

The work in this thesis has investigated and optimised the design of three different self-pulsating laser diodes for optical storage applications. The work indicated the difficulties in achieving 650 nm self-pulsation at high temperatures when using the most advanced laser diodes on offer, with high power emission, i.e. >30 mW, at suitable operating currents being a particular cause for concern. As a result 650 nm self-pulsation would only be a realistic option in a read-only DVD system. The problems stem from the thermally activated leakage current. Throughout the investigation a strained active region was utilised, providing optimum carrier and optical confinement in relation to the band-offsets and cladding layers on offer. However, the deleterious effects of the leakage current still caused problems indicating that confinement must be improved even further if an adequate suppression of the carrier overflow is to be achieved. At the moment multi-quantum barriers (MQB) seem to offer the best hope [1, 2]. Unfortunately research into such structures is still in its infancy. Until the necessary technology is developed the AlGaInP self-pulsating laser diode may not be utilised to its full potential, leading to alternative, more expensive methods of achieving the desired high power pulsation.

Whilst research into MQB technology is being conducted "next generation" DVD systems will also be in development, making use of laser diodes emitting in the blue range of the electromagnetic spectrum. The work in chapter 6 proved that 420 nm self-pulsation (subject to the emission criteria) is achievable due to the improvements in carrier confinement. However, the investigation used a laser diode with epitaxial absorber layers. It is known that the real refractive index guided laser is easy to fabricate and offers emission at low threshold currents [3], so it would be desirable to study the emission characteristics of such a laser grown in the GaN material system. It would also be of interest to simulate the output using a "diffusion model" where a second order partial differential equation is coupled with a simple photon rate equation to simulate the dynamical properties of the device. Such a system would enable one to expand the (lateral) "three-node" rate equation used in chapter 4, i.e. absorber-gain-absorber, by using a "multi-node" model that allows one to investigate the diffusion characteristics in a more accurate manner. During the past

few months such a simulation has been constructed and tested for the red real refractive index guided laser, making use of 80 nodes in the lateral direction. Unfortunately the computational speed is very slow, indicating a trade-off between accuracy and speed. However, with computer processors getting faster by the month such a technique could be utilised in the future in an attempt to model the dynamical properties of the blue real refractive index guided laser diode.

The benefits of blue emission will enable laser diodes grown in the GaN material system to play an important role in semiconductor laser research in the next few years. For successful models to be utilised some issues, such as the gain mechanism, must be resolved. Once such problems have been addressed and multi-dimensional quantum confined lasers are pushed to their full potential there is going to be a call for new quantum confined, self-pulsating structures. Different approaches to those evaluated in this thesis will have to be developed. As a result self-pulsating devices will continue to evolve with the demands of a "next generation" DVD playing the key role in these developments.

References

[1] K. Kishino, A. Kikuchi, Y. Kaneko and I. Namura, "Enhanced carrier confinement effect by the multiquantum barrier in 660 nm GaInP/AlInP visible laser," *Appl. Phys. Lett.*, vol. 58, pp. 1822-1824, 1991.

[2] H. Hamada, R. Hiroyama, S. Honda, M. Shono, K. Yodashi and T. Yamaguchi, "AlGaInP strained multiple-quantum-well visible laser diodes ($\lambda_L \leq 630$ nm band) with a multiquantum barrier grown on misorientated substrates," *IEEE J. Quantum Electron.*, vol. 29, pp. 1844-1850, 1993.

[3] M. Yuri, S. Harris, T. Takayama, O. Imafuji, H. Naito, M. Kume, K. Itoh and T. Baba, "Two-dimensional analysis of self-sustained pulsation for narrow-stripe AlGaAs lasers," *IEEE J. Select. Topics Quantum Electron.*, vol. 1, pp. 473-479, 1995.

Appendix 1

Transfer matrix formalism

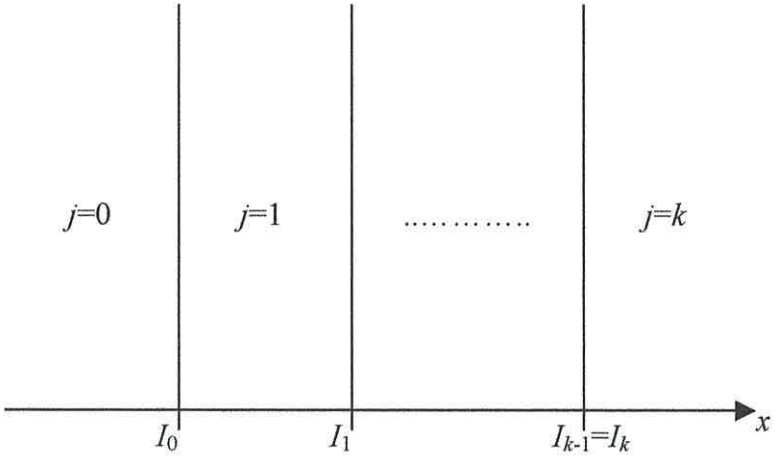

Fig. A1.1 *A multi-layered waveguide structure.*

Consider a multi-layered waveguide, as displayed in fig. A1.1. The TE field for the *j*th layer is given by

$$\frac{\partial^2 E_{y,j}(x)}{\partial x^2} + \left(k_0^2 n_j^2 - \beta^2\right) E_{y,j}(x) = 0 \qquad \text{(A1.1)}$$

where n_j is the complex refractive index of layer j. The propagation constant, β, may be used to determine the properties of the optical waves within the waveguide. A direct solution of the equation is difficult to obtain, so a general solution is used which is of the form

$$E_{y,j}(x) = C_j \exp\left(\pm\left(x - I_j\right)\alpha_j\right) \qquad \text{(A1.2)}$$

where I_j represents the interface of the jth layer, $\alpha_j = \sqrt{\beta^2 - k_0^2 n_j^2}$ and C_j is a constant to be determined. The sign ambiguity can be overcome by separating the equation into two parts giving

$$E_{y,j}(x) = A_j \exp\left((x - I_j)\alpha_j\right) + B_j \exp\left(-(x - I_j)\alpha_j\right). \tag{A1.3}$$

To find the modes propagating within the waveguide it is necessary to find the propagation constants that satisfy equation (A1.3) and some boundary conditions. For TE modes the boundary conditions stipulate that the field and its derivative must be continuous at the interface, i.e.

$$E_{y,j}(I_j) = E_{y,j+1}(I_j) \tag{A1.4}$$

$$\frac{\partial}{\partial x} E_{y,j}(I_j) = \frac{\partial}{\partial x} E_{y,j+1}(I_j). \tag{A1.5}$$

Substituting equation (A1.3) into the above gives

$$A_j + B_j = A_{j+1} \exp\left(-d_{j+1}\alpha_{j+1}\right) + B_{j+1} \exp\left(d_{j+1}\alpha_{j+1}\right) \tag{A1.6}$$

$$A_j - B_j = A_{j+1}\left(\frac{\alpha_{j+1}}{\alpha_j}\right)\exp\left(-d_{j+1}\alpha_{j+1}\right) - B_{j+1}\left(\frac{\alpha_{j+1}}{\alpha_j}\right)\exp\left(d_{j+1}\alpha_{j+1}\right) \tag{A1.7}$$

where d_j is the width of the jth layer. By combining these two equations it is possible to form a recursive relationship between the coefficients of the form

$$A_j = \frac{A_{j+1}}{2}\left(1 + \frac{\alpha_{j+1}}{\alpha_j}\right)\exp\left(-\omega_{j+1}\right) + \frac{B_{j+1}}{2}\left(1 - \frac{\alpha_{j+1}}{\alpha_j}\right)\exp\left(\omega_{j+1}\right) \tag{A1.8}$$

$$B_j = \frac{A_{j+1}}{2}\left(1 - \frac{\alpha_{j+1}}{\alpha_j}\right)\exp\left(-\omega_{j+1}\right) + \frac{B_{j+1}}{2}\left(1 + \frac{\alpha_{j+1}}{\alpha_j}\right)\exp\left(\omega_{j+1}\right) \tag{A1.9}$$

where $\omega_j = d_j \alpha_j$.

So, given a suitable initial condition it is possible to calculate A_j and B_j using the coefficients from a subsequent layer. Equations (A1.8) and (A1.9) can be written as a 2×2 matrix, T, giving

$$\begin{bmatrix} A_j \\ B_j \end{bmatrix} = T_j \begin{bmatrix} A_{j+1} \\ B_{j+1} \end{bmatrix} \tag{A1.10}$$

where

$$T_j = \begin{bmatrix} \left(1 + \frac{\alpha_{j+1}}{\alpha_j}\right)\frac{\exp\left(-\omega_{j+1}\right)}{2}, & \left(1 - \frac{\alpha_{j+1}}{\alpha_j}\right)\frac{\exp\left(\omega_{j+1}\right)}{2} \\ \left(1 - \frac{\alpha_{j+1}}{\alpha_j}\right)\frac{\exp\left(-\omega_{j+1}\right)}{2}, & \left(1 + \frac{\alpha_{j+1}}{\alpha_j}\right)\frac{\exp\left(\omega_{j+1}\right)}{2} \end{bmatrix}. \tag{A1.11}$$

This recursive relationship may then be generalised by the following matrix

$$m = \prod_{j=0}^{k-1} T_j. \tag{A1.12}$$

At the two end layers the field should decay to zero. So, in both cases one of the coefficients of the general solution (equation (A1.3)) must be zero. For the first layer the field must decay away from the interface in an exponential fashion. This happens when B=0. Similarly, at the final layer the exponential decay should be in the opposite direction, so A=0. The solutions of the bound modes therefore satisfy

$$\begin{bmatrix} 0 \\ B_0 \end{bmatrix} = \begin{bmatrix} m_{11}, m_{12} \\ m_{21}, m_{22} \end{bmatrix} \begin{bmatrix} A_{k-1} \\ 0 \end{bmatrix} \tag{A1.13}$$

or, when simplified

$$\begin{bmatrix} 0 \\ B_0 \end{bmatrix} = \begin{bmatrix} A_{k-1} m_{11} \\ A_{k-1} m_{21} \end{bmatrix}. \tag{A1.14}$$

In order to find the modes propagating within the waveguide it is therefore necessary to find the propagation constants that satisfy

$$m_{11}(\beta) = 0. \tag{A1.15}$$

For example, consider a three layer symmetric slab waveguide. By setting k=2 the product of only two matrices need to be considered, i.e.

$$m = \prod_{j=0}^{1} T_j = T_0 T_1. \tag{A1.16}$$

After multiplying the matrices out, the following expression must be solved

$$\left(1+\frac{\alpha_1}{\alpha_0}\right)\left(1+\frac{\alpha_2}{\alpha_1}\right)\exp(-\omega_1-\omega_2)+\left(1-\frac{\alpha_1}{\alpha_0}\right)\left(1-\frac{\alpha_2}{\alpha_1}\right)\exp(\omega_1-\omega_2)=0. \tag{A1.17}$$

It is therefore the roots of this equation that represent the modes propagating within the waveguide.

Appendix 2

Implementing the rate equation models

To continually assess the evolution of the photon emission from a particular laser diode a consistent method of evaluation is required to solve the two sets of rate equations derived in chapter 3. A summary of the procedures are outlined in the following sections, however, a number of attributes are the same from model to model.

In each simulation a maximum time of 10 ns is set. Whatever set of rate equations being used the equations are solved using the Runge-Kutta technique at time intervals of 5×10^{-13} s. Every iteration gives rise to a continuously changing carrier density. For a given temperature, the peak gain/absorption generated in the gain section is therefore assessed continuously. The gain/absorption is then evaluated in the absorber section at the operating wavelength. This method continuously solves the coupled rate equation whilst other parts, e.g. built-in refractive index step, are added to characterise the model for a particular structure.

A2.1 Sequence of numerical analysis for the real refractive index guided laser

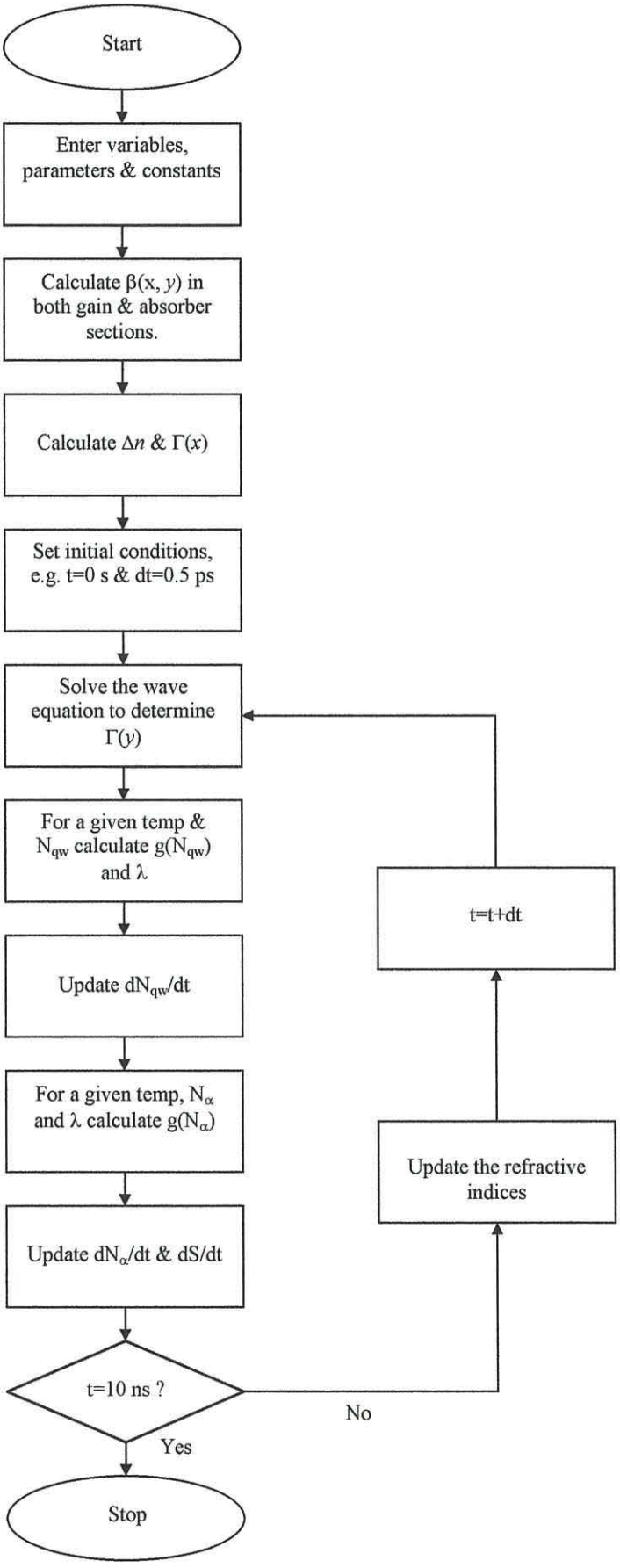

A2.2 Sequence of numerical analysis for the laser diode with epitaxial layers

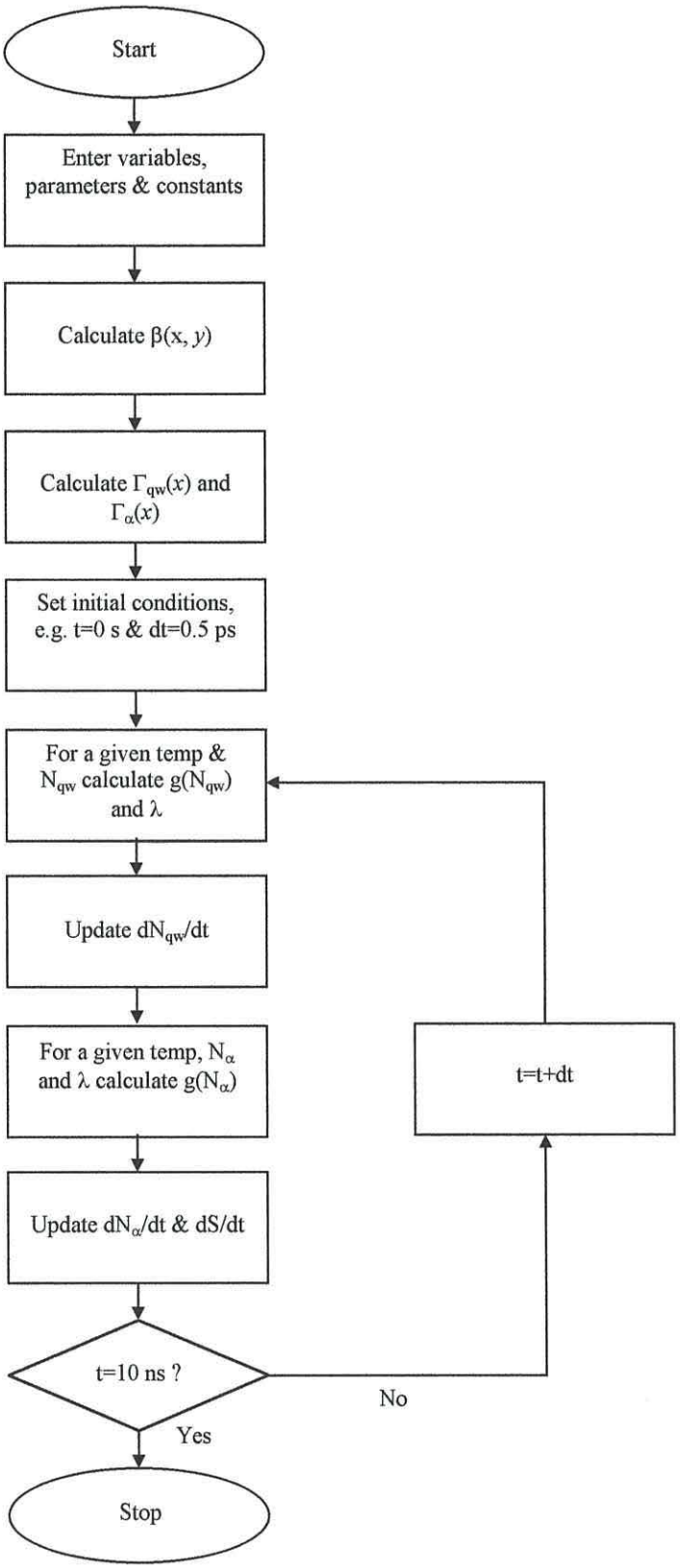

Appendix 3

Definition of self-pulsation

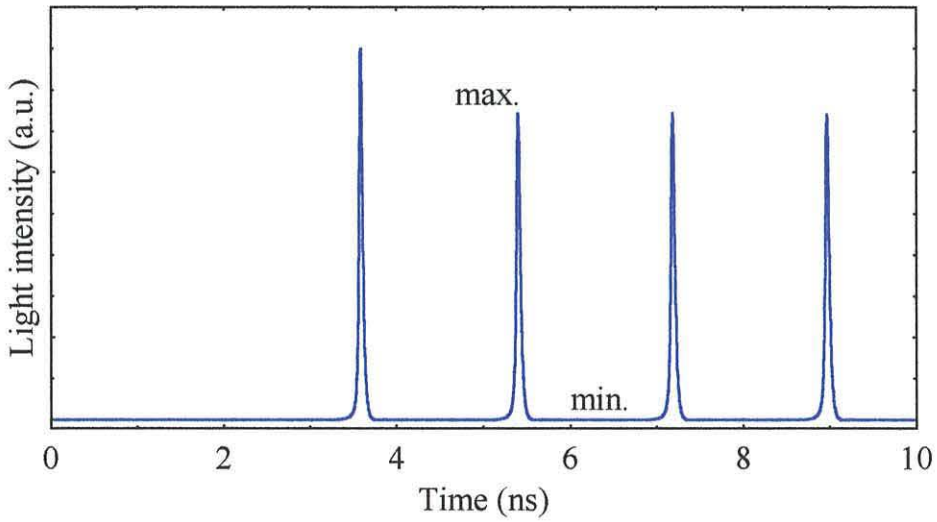

Fig. A3.1 *Typical temporal evolution of a self-pulsating laser diode.*

To consistently assess whether or not self-pulsation has been achieved it is important that the emission is compared to some clearly defined rules. For a given current density the output is considered over a time scale of 10 ns, as displayed in fig. A3.1. Now, in general, the first pulse is unstable as the spontaneous emission dominates in a similar manner to *cw* output. The emission is therefore considered after this "initial burst". Two of the most obvious traits of a pulse are its maximum and minimum points, so in order to determine whether or not a pulse has been emitted the following condition is applied

$$\text{max./min.} > 500. \qquad \text{(A3.1)}$$

The second pulse is assessed, then the third, and so on with the position of each pulse being noted.

To determine self-pulsation the frequency characteristics are considered after the 10 ns have elapsed. If the frequency from pulse to pulse is unstable, e.g. pulses dampen like *cw* emission, or no pulses are observed then the output is deemed not to self-pulsate. If a consistent frequency is emitted then self-pulsation is achieved and the characteristics of the emission are noted.

Appendix 4

List of publications

A4.1 Refereed journal papers

[1] D. R. Jones, P. Rees, I. Pierce and H. D. Summers, "Investigation of changes in absorber position in the 650-nm AlGaInP self-pulsating laser for optical storage applications," *IEE Proc. Optoelectronics*, vol. 148, pp. 65-68, 2001.

[2] D. R. Jones, P. Rees, I. Pierce and H. D. Summers, "Theoretical optimization of self-pulsating 650-nm-wavelength AlGaInP laser diodes," *IEEE J. Select. Topics Quantum Electron.*, vol. 5, pp. 740-744, 1999.

[3] H. D. Summers, C. H. Molloy, P. M. Smowton, P. Rees, I. Pierce and D. R. Jones, "Experimental analysis of self-pulsation in 650-nm-wavelength AlGaInP laser diodes with epitaxial absorbing layers," *IEEE J. Select. Topics Quantum Electron.*, vol. 5, pp. 745-749, 1999.

A4.2 Conference contributions

[4] D. R. Jones, P. Rees and I. Pierce, "Optimisation of InGaN narrow stripe self-pulsating laser diodes," Paper CWF98, CLEO/Europe 2000, Nice, France, September 2000.

[5] I. Pierce, P. Rees, D. R. Jones and H. D. Summers, "Multi-mode self-pulsation in laser diodes with epitaxially integrated saturable absorbers," Paper CWF78, CLEO/Europe 2000, Nice, France, September 2000.

[6] D. R. Jones, P. Rees and I. Pierce, "Power output of 650 nm self-pulsating laser diodes for optical disc storage applications," 14th Conference on Semiconductor and Integrated Optoelectronics (SIOE 2000), Cardiff, UK, April 2000.

[7] I. Pierce, P. Rees, D. R. Jones and H. D. Summers, "Multi-mode pulsation in AlGaInP laser diodes with epitaxially integrated saturable absorbers," 14th Conference on Semiconductor and Integrated Optoelectronics (SIOE 2000), Cardiff, UK, April 2000.

[8] P. Rees, D. R. Jones, I. Pierce and H. D. Summers, "Short wavelength laser diodes for optical storage applications," Paper SEMc.P2.3, Institute of Physics Condensed Matter and Materials Physics Conference (CMMP 99), Leicester, UK, December 1999.

[9] D. R. Jones, P. Rees, I. Pierce and H. D. Summers, "Theoretical investigation of GaN self-pulsating laser diodes for optical storage applications," Poster 1-24, Institute of Physics National Quantum Electronics Conference (QE '14), Manchester, UK, September 1999.

[10] I. Pierce, P. Rees, P. Spencer and D. R. Jones, "Effect of carrier temperature in chirp in directly modulated laser diodes," 13th Conference on Semiconductor and Integrated Optoelectronics (SIOE 2000), Cardiff, UK, April 1999.

[11] D. R. Jones, P. Rees, I. Pierce and H. D. Summers, "Theoretical investigation of short wavelength self-pulsating laser diodes for optical storage applications," 13th Conference on Semiconductor and Integrated Optoelectronics (SIOE 2000), Cardiff, UK, April 1999.

[12] D. R. Jones, P. Rees, I. Pierce and H. D. Summers, "Optimisation of digital video disc lasers operating at 650nm," Postgraduate Research in Electronics, Photonics and Related Fields (PREP '99), UMIST, Manchester, UK, January 1999.

[13] H. D. Summers, C. H. Molloy, P. M. Smowton, P. Rees, I. Pierce and D. R. Jones, "High temperature self-pulsation in 650 nm, AlGaInP Lasers with an epitaxially integrated saturable absorber," 16th IEEE Semiconductor Laser Conference, Nara, Japan, November 1998.

[14] D. R. Jones and P. Rees, "Effects of the inclusion of cross polarisation terms in the calculation of optical gain in semiconductors," 12th Conference on Semiconductor and Integrated Optoelectronics (SIOE 2000), Cardiff, UK, April 1998.

A4.3 Papers currently under consideration

D. R. Jones, P. Rees, I. Pierce and H. D. Summers, "Power output of 650-nm self-pulsating AlGaInP laser diodes for optical storage applications," submitted to *IEEE J. Quantum Electron.*.

D. R. Jones, P. Rees and I. Pierce, "Theoretical investigation of InGaN self-pulsating laser diodes for optical storage applications," submitted to *IEE Proc. Optoelectronics*.